On Charm and Beauty in Dielectron Measurements

Dielectron Production in p–Pb Collisions at $\sqrt{s_{\mathrm{NN}}} = 5.02$ TeV with ALICE at the LHC

Dissertation

zur Erlangung des Doktorgrades
der Naturwissenschaften

vorgelegt beim Fachbereich Physik
der Johann Wolfgang Goethe-Universität
in Frankfurt am Main

von
Horst Sebastian Scheid
aus Meisenheim

Frankfurt am Main 2024
(D 30)

Vom Fachbereich Physik
der Johann Wolfgang Goethe-Universität
als Dissertation angenommen.

Dekan:	Prof. Dr. Roger Erb
Gutachter:	Prof. Dr. Harald Appelshäuser
	Prof. Dr. Christoph Blume
Datum der Disputation:	8.11.2024

DILEPTONS OR DEATH

Abstract

One possibility to study the quark-gluon plasma created in ultra-relativistic heavy-ion collisions is to measure modifications of an established baseline and by this infer on the interaction of a given probe with the created medium. A prominent way to introduce this baseline is through measurements in pp collisions. However, it is known that the binding effects of the proton in a heavy nucleus can modify said baseline without the creation of a quark-gluon plasma. In order to study such cold nuclear matter effects one can study collisions with a smaller transverse size and density, such as proton-lead (p–Pb) collisions.
This thesis presents the analysis of dielectron production in p–Pb collisions at a collision energy in the centre of mass system of $\sqrt{s_{\mathrm{NN}}} = 5.02$ TeV as a function of the invariant mass and the momentum of the $\mathrm{e}^{+}\mathrm{e}^{-}$ pair. The main purpose of the analysis is to study modifications with respect to scaling expectations of the contribution of heavy-flavour production and their impact on the measured dielectron yield. This is done by measuring the dielectron yield in p–Pb collisions and comparing it to baseline expectations. The baseline for light flavour hadron decays is constructed based on measurements in p–Pb collisions at $\sqrt{s_{\mathrm{NN}}} = 5.02$ TeV. The heavy-flavour contribution uses the measured production cross sections of heavy quarks in pp collisions and assumes a scaling of the production cross section with the number of binary nucleon-nucleon collisions. It is found that the baseline constructed in this way is able to describe the data within the experimental uncertainties. To investigate the impact of a possible modification of the contribution of the charm hadron decays to the dielectron spectrum, model calculations based on globally available data are included in the charm baseline. This reduces the expected contribution and a tension starts to arise in the mass region dominated by the heavy-flavour contributions. The possibility of an additional source of dielectrons produced as thermal radiation from a hot and dense medium formed in p–Pb collisions is investigated by also including such a source in the comparisons. The conclusion drawn from the presented measurement and its comparisons to baseline calculations under different assump-

tions is that no significant suppression of the charm contribution due to cold nuclear matter effects is present in the dielectron spectrum. However, it is possible that the suppression could be present but is offset due to the presence of a thermal source of dileptons, keeping the overall dilepton rate constant. The discussion finishes with an outlook on future measurements that might be able to resolve this ambiguity.

Summary

The thesis starts with an introduction into the topic. Here, the peculiar features of quantumchromo dynamics as the description of the force that binds quarks into hadrons are discussed. Asymptotic freedom, confinement, and the spontaneous breaking of chiral symmetry are connected to the study of a state of matter called the quark-gluon plasma, i.e. a state in which the otherwise bound quarks and gluons are expected to roam free from the shackles of confinement. This state is expected to have existed in the early stages of the universe, in conditions that can be created in the laboratory today via the collision of heavy nuclei accelerated to ultra-relativistic velocities. Arguments to study such collisions by measuring electromagnetic probes, in particular, virtual photons that decay into a dielectron pair are summarised. The measurement of dielectrons has the striking advantage that, as electromagnetic probes, their interaction with the matter created in heavy-ion collisions is negligible, enabling direct access to information related to the early stages of those collisions. The introduction closes with a short statement about the experimental approach to establish effects of the medium to a baseline measured in pp and p–Pb collisions. In particular, p–Pb collisions are of interest, as they can be used to characterise effects that are rooted in the binding of the proton in a large nucleus.

After a short discussion of the production of thermal dielectrons, it is pointed out that two important parts are contained in the calculations of the thermal dilepton rate. On the one hand, a thermal contribution in the shape of a Bose-Einstein factor connects the rate to the medium temperature and on the other hand a connection to the electromagnetic spectral function which if measured precisely gives access to modifications of the vector mesons that can yield information on the restoration of chiral symmetry in a hot and dense medium. After a short introduction of the so-called Drell-Yan process which produces dileptons from quark anti-quark annihilation of the incoming projectiles, the discussion focuses on the dielectrons that stem from decays of hadrons that are produced in the collisions. The contribution from light-flavour hadron decays produces an e^+e^- pair either in a decay in which only

the two leptons are produced or in so-called Dalitz decays that include an internal conversion of a photon. The invariant mass of these e^+e^- pairs is only a fraction of the mass of the original hadron. The residual mass of the e^+e^- pair can in first order be calculated following the Kroll-Wada equation, however, the electromagnetic transition form factors determined by measurements needs to be taken into account. An additional source of dielectrons are the decays of open-heavy flavour hadrons. The approach to calculating the production cross section assuming a factorisation of the different involved processes is presented. While these hadrons only decay with one lepton in the final state they are produced in pairs and have rather large branching ratios in the semi-leptonic decay channels. This leads to pairs which are from two independent decays but the residual correlations and the global conservation of flavour leads to a signal in the dielectron channel. In the case of beauty hadron decays, different decay topologies can even produce a pair from one quark, or multiple pairs in the final state of the decays of the correlated hadrons. In particular, at high energies the understanding of these sources is necessary to single out the thermal signal.

After this introducing the subject of dielectron production, a discussion of previous results is presented. The first measurements discussed were carried out by the CERES (NA45) and the NA60 collaborations at the SPS at CERN. In the CERES measurement a modification of the dielectron spectrum around the ρ mass was observed that could not be explained by an enhancement of the ρ vacuum contribution. While it was clear that the source needed a modification to describe the shape of the excess spectrum, the nature of this modification was not clear. Two scenarios were discussed at the time of the measurement: one in which the mass of the ρ meson is reduced due to its interaction with the medium, the so-called Brown-Rho scaling or dropping mass scenario, and one in which the ρ mass shape is modified by collisional broadening of the resonance by the interaction with the surrounding medium. The measurement of dimuons by the NA60 collaboration resolved this ambiguity and confirmed a collisional broadening of the in-medium ρ mass shape. In addition, the extension of the measurement to higher masses was possible and a first measurement of the temperature of the partonic source could be carried out. This was mainly possible because the NA60 apparatus included a vertexing detector that could separate the prompt thermal radiation from the non-prompt background from heavy-flavour hadron decays. The next measurements discussed are the dielectron measurements by the PHENIX and STAR collaborations at Brookhaven National Laboratory's RHIC. With an increase of the collision energy by about a factor ten, the produced

medium is expected to be hotter and longer living than at the SPS. However, also the background from heavy-flavour hadron decays gets larger due to the growing cross section of heavy-flavour production. The experiments confirmed the CERES and NA60 findings concerning an enhancement in the mass region around the ρ mass. However, they were not able to extract a temperature of the partonic source because the mass region in which NA60 extracted the temperature is dominated by correlated heavy-flavour background and no experimental means were available to separate the prompt and non-prompt contributions. The spectra could be explained by the baseline constructed for the heavy-flavour measurements without any further modification or additional thermal radiation.

At the LHC at CERN, the ALICE experiment is dedicated to measurements of the properties of the medium created in Pb–Pb collisions. The collision energy is an order of magnitude larger than at RHIC and thus the background from heavy-flavour hadron decays is also larger. Measurements in Pb–Pb collisions at $\sqrt{s_{\mathrm{NN}}} = 5.02$ TeV show a hint of an enhancement in the mass region around the ρ, as observed before. The measurement in the intermediate mass region suffers from similar problems as the RHIC results concerning the separation of prompt and non-prompt contributions. However, using a technique similar to NA60 the ALICE collaboration shows that the limiting factor in their measurement is not the capability of the tracking detectors, but the limited statistical precision. Because the overwhelming background in the mass region relevant for the determination of the temperature in the early phase of the collision stems from the decays of heavy-flavour hadrons, a precise understanding of this background is mandatory for future measurements. This is why in this thesis a measurement of dielectron production in p–Pb collisions at $\sqrt{s_{\mathrm{NN}}} = 5.02$ TeV is performed to estimate possible modifications of the heavy-flavour dielectron background due to cold nuclear matter (CNM) effects.

After a short introduction of the ALICE detector and the sub-detector systems that are relevant for the tracking of charged particles and for the identification of electrons, the analysis itself is explained step by step. Firstly, the data set is described. This analysis utilised p-Pb collision data recorded in 2016. A peculiarity of the data is that two different triggers were used. The two triggers differed in the usage of two layers of the Inner Tracking System, which were disabled in one of the triggers due to their slower readout time. In order to ensure a uniform performance over the full data both triggers were reconstructed using the same software and detector conditions, i.e. even if the full ITS is available the hits in the layers missing in one dataset are omitted. Furthermore, selections on the reconstructed collisions are applied to

reject events that are not inelastic beam-beam events. After this, the selection of the tracks for analysis is discussed. Several observables are used to select tracks that are deemed good for analysis. In addition, some selections reject tracks that are most likely to originate in weak decays or photon conversions. In continuation, particle identification criteria are discussed. The specific energy loss of particles in the TPC is used together with the measurement of the time-of-flight system to identify electron candidates. The selection is validated in MC simulations. In order to ensure a good matching of the MC simulations to the data, a recalibration of the PID response of the TPC is carried out. After elaborating on how individual tracks are selected, the process of combining two tracks into a dielectron pair is discussed. Samples of unlike-sign (ULS) and like-sign (LS) spectra are constructed and the LS spectrum is corrected for different acceptances of LS and ULS spectra. The LS spectrum is then used to estimate the combinatorial background in the ULS spectrum. The raw signal can be determined by subtracting the LS from the ULS spectrum. In order to derive the dielectron yield per p–Pb collision, MC simulations are used to estimate the efficiency of the measurement and correct for it. Different MC productions are used to ensure good coverage of the phase space of the measurement and reduce statistical fluctuations in the correction. To estimate possible systematic biases in the measurement, different approaches depending on the source of the bias are studied. The overall systematic uncertainty of the measurement is determined as the quadratic sum of the single contributions. To interpret the data, a baseline is constructed to compare to it, the so-called hadronic cocktail. This cocktail is based on measurements and aims to reproduce the dielectrons that are produced in the decays of light and heavy-flavour hadrons. As one of the purposes of the measurement presented in this thesis is to evaluate possible modifications of the heavy-flavour contribution due to CNM effects, parametrisations of the CNM effects based on global fits are also included in the cocktail calculations. The comparison of the dielectron measurement in p–Pb collisions at $\sqrt{s_{\mathrm{NN}}} = 5.02$ TeV to the cocktails with and without the inclusion of CNM effects hints that possible modifications are small, if present at all. The possibility of an enhancement is also explored by including an additional source. Including such an additional dielectron source only shows a small expected modification of the spectrum, however, it would cancel a suppression that is expected for the heavy-flavour contribution due to CNM effects.

The thesis concludes with an outlook towards future measurements of dielectron production at the LHC with ALICE. The upgrades of the ALICE detector during the last long shutdown of the LHC will benefit the measurement of dielectrons in

two ways. The upgrade of the TPC readout chambers grants the possibility to integrate the full delivered luminosity of the LHC in continuous readout. This will drastically improve the statistical precision of the data. In addition, the upgraded ITS will help in the separation of the prompt and non-prompt dielectrons and thus contribute significantly to the measurement of the thermal radiation from the quark-gluon plasma. A further upgrade of the experiment in the 2030s will go another step in this direction. The proposal of the ALICE 3 detector foresees implementing the first tracking layers in a secondary vacuum as close as possible to the interaction point. This would greatly improve the possibility to measure the displacement of the electrons from heavy-flavour decays, and thus to separate a thermal contribution from the heavy-flavour background.

Acknowledgments

As the time of writing this thesis comes to an end, I would like to take the opportunity to thank the people who have made it possible. First and foremost, I would like to thank my supervisor, Prof. Dr. Harald Appelshäuser. For his scientific guidance and for always taking the time to discuss open points and questions concerning my analysis, but also for giving me all the opportunities I have had over the last few years. It is hard to find words to describe how grateful I am to you and I hope we can continue to discuss all sorts of things in the future.
As the person who guided me during my long time in the ALICE group and helped me become the scientist I am today, I would like to thank Dr. Raphaelle Bailhache-Römer. With your kind and calm nature and the hard work and precision you put into everything you do, I have learned a lot from you.
During my time at the institute, I always enjoyed coming into the office. The atmosphere in the group was always a friendly and constructive one. For this, I want to first thank my partners in crime in the dielectron group, in particular, Jerome Jung for the long discussions and opportunities to rant when things didn't work as planned. Not unmentioned should be Dr. Carsten Klein, Theo Bröker, and Dr. Patrick Reichelt who always had an open ear for all problems related to analysis and beyond. Besides the dielectron group, I want to thank the whole ALICE group in Frankfurt. I am happy that I spent the last years with people that are passionate about their work, but also could have fun otherwise. Be it at the summer excursions, the Christmas parties, the trips to the DPG spring meeting, or at the institute preparing experiments for lectures or the Night of Science. A special thanks I want to give at this point to my former office mate Fabian Pliquett and to Prof. Dr. Henner Büsching for all the conversations that made the difference in going to the institute from going to work. Also responsible for making the institute a place that I enjoyed coming to were my fellow PhD candidates, Mario Krüger, Joshua König, and Matthias Kleiner who I owe an apology to as they had to endure my mood over the last weeks before finishing this thesis.

I want to express my gratitude for all the help I received to Stefan Dittrich, Sylke Schneider, Tülay Bam, and Claudia Freudenberger. Without you, many of us would not be able to do the work we do.
Within the ALICE collaboration, I want to thank Dr. Nicolò Jacazio for the Thursday meetings during the writing of the ALICE 3 LoI and all the time we spent in Frankfurt, at CERN, and in Bologna. For the long calls during COVID and the preparation of our publication, I want to thank Dr. Aaron Capon. In a time that was difficult for all involved, I think we made the best of it. To the rest of the ALICE dielectron physics analysis crew, I want to say thank you for the constant support and the constructive discussions that we had in the weekly meetings, during conferences and at our annual workshops. I hope it was as much fun for everyone as it was for me. Not only me but whoever reads this thesis should thank Dr. David Chinellato and Dr. Fernando Flor for making sense of some of my writing and adding most of the commas. For the moral support during the writing of the bulk of this thesis, I want to thank Lars Bratrud, as well as Dr. Alba Soto-Ontoso, Dr. Samuel Abreu and the rest of the Geneva by Night crew and Samuel's Fire Juju.
Last but not least I want to express my gratitude to my parents Ingo, Claudia and Gernot. Without you, I would not be who I am. It would not have been possible to bring this part of my life to a successful end without you. Every single one of you supported me in your way, and all of them were necessary at times. Thank you.

Contents

Chapter 1

Introduction

"Where do we come from?" — A question asked by many throughout human existence and probably one of the biggest questions still to answer. Several approaches can be taken to address this question depending on the respective field of study.

The universe in today's state and the matter in it and its interactions can be described by gravity and the smaller parts by the standard model of particle physics. While gravity is used to describe the relations and interactions of objects on large scales as planets and galaxies, the standard model of particle physics describes the interplay of objects on the smallest scales. To do so, it combines the strong, electromagnetic and weak interactions that govern the interactions of the smallest particles known to date and organises them. According to the standard model, the building blocks of matter are the six quarks and six leptons and their anti-particles. Their interactions are mediated by the exchange of the gauge bosons. By coupling to the Higgs field, the particles gain their mass. While all particles interact via the weak force, mediated by the Z and W bosons, only the electrically charged leptons e, μ and τ as well as the quarks interact on the electromagnetic level via γ exchange. The third interaction is via the so-called strong force that couples to the colour charges of the quarks and is mediated by the gluons (g) which also carry a colour charge. The strong interaction is responsible for binding the quarks into charge-neutral states known as hadrons. The colour charge neutral states can be achieved by either binding three quarks with different charges (red, blue, green) equivalent to the colour theory of light or binding a quark with an anti-quark to a colour/anti-colour state. The fundamental theory describing the strong interaction is named quantum chromodynamics (QCD), as it describes the interactions of colour-charged elementary objects [1, 2]. The formulation of QCD as a non-abelian gauge theory in the

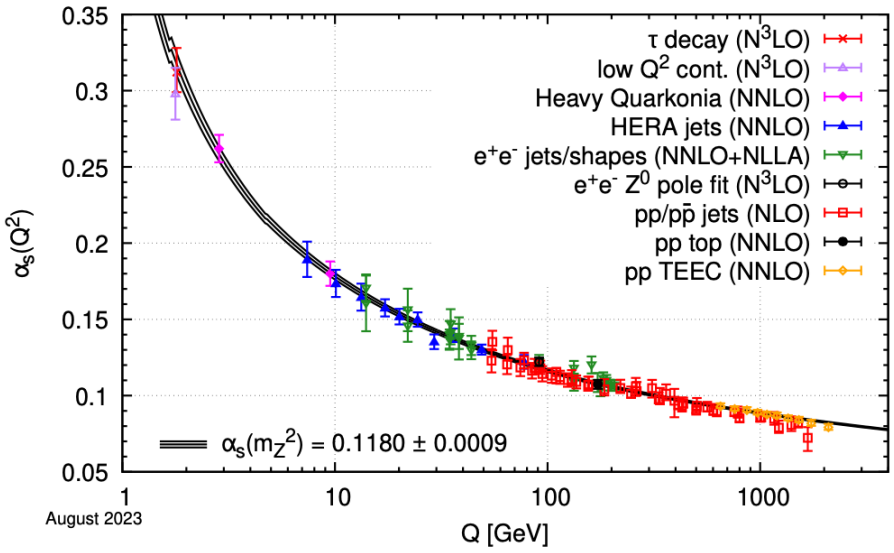

Figure 1.1.: Summary of α_S measurements as a function of the scale Q [3].

SU(3) symmetry group opened the possibility of understanding many phenomena in physics that to that point were explained in effective models and led to the Nobel prizes for David Gross, Frank Wilczek, and David Politzer. The phenomenology of QCD shows some peculiar features that should be discussed next. The bound states that are formed are always colour-neutral, meaning their open colour charges are never observed. This imprisonment of colour-charged objects is called confinement. It can be understood as a consequence of the fact that the gluons themselves carry a colour charge which leads to an interaction between the gauge bosons mediating the interaction. This also means that the colour-charged quarks are never observed in an unbound state. Another feature of QCD to introduce is the so-called running coupling. In quantum field theory, the strength of the interaction of a gauge boson with the charge is determined by the respective coupling "constant". In the electromagnetic interaction, this is given by the fine structure constant α_{EM}. In QCD the label of the strong coupling (α_S) as a coupling constant might be misleading as α_S depends strongly on the scale at which it is probed as illustrated in Fig. 1.1 [3]. The coupling strength of QCD decreases with a larger momentum transfer Q. The momentum transfer can also be interpreted as the inverse of the probed distance of the interaction or the time of the interaction. The larger Q, the smaller the distance, the shorter the time of the interaction. This behaviour of the coupling lead to the idea of asymptotic freedom. One can interpret the fact that quarks only exist in bound states as a consequence of a strong coupling at normal conditions (i.e. smaller

Q, large distances, long interaction times). However, the decrease of the coupling α_S at large Q indicates that the binding should weaken and at small enough α_S, the quarks should behave as if they were not bound, or quasi-free.

The last feature of QCD that should be briefly introduced is related to the masses of the quarks as building blocks of matter and the mass of the hadrons. Compound states of either a quark-antiquark pair or three quarks called a meson or a baryon, respectively. When looking at the expected masses of the quarks based on lattice QCD (lQCD) calculations, masses of a few MeV $/c^2$are expected for the light quarks (up and down). However, the bound states of these quarks are of a few 100 MeV$/c^2$. This can be understood as a process in which the mass of the bound states is generated as a dynamical quantity emerging from the interaction of the quarks and gluons confined in the compound objects. A more detailed comparison of states that have the same contents and differ only in their parity or chirality. Examples for this are the $\pi(140)$ and the $f_0(500)$, the $\rho(770)$ and the $a_1(1250)$. The number in parentheses is the approximate mass of the meson in MeV$/c^2$ taken from [3]. The only difference in the particles is a parity transformation from $J^{PC} = 0^{-+}$ states to 0^{++} states. The parity transformation can be seen as a mirroring of the particle while keeping all other attributes the same. The change in parity, also known as handedness introduces a drastic change in the mass of the particles. This phenomenon is known as the spontaneous breaking of chiral symmetry. It should be noted that the finite quark masses also introduce an explicit breaking of this symmetry in the Lagrangian of QCD, however as the masses are small the symmetry can be seen as approximate and no large effects are expected. This spontaneous breaking of chiral symmetry in QCD suggests a strong coupling between the left-handed quarks (q_L) and the right-handed anti-quarks ($\bar{q}_R$) that form a non-vanishing condensate $\langle q_L \bar{q}_R \rangle \neq 0$ in the vacuum.

Coming back to the initial question "Where do we come from?" after this venture into QCD. The answer most physicists would give is: The Big Bang. An explosion that brought the universe into existence and created space and time. The observation that the universe expands leads to the idea that it once came from one place. Consequently, there must have existed a hot and dense phase shortly after the Big Bang. With the above considerations, this would mean that the scales of QCD are at values in which the coupling gets weak. Consequently, a state would emerge in which the quarks and gluons cannot be considered bound states anymore; the so-called quark-gluon plasma. The small coupling between q_L and $\bar{q}_R$ should melt the chiral condensate resulting in a restoration of chiral symmetry.

The study of matter under such extreme conditions is the subject of (ultra) relativistic heavy-ion collisions. Heavy nuclei are accelerated in laboratories and brought to collision to create energy densities and create a state of matter that should resemble conditions in the early universe, liberate the quarks and gluons from their hadronic prisons, and form a quark-gluon plasma. Hence the term Little Big Bang for heavy-ion collisions in the laboratory. After pioneering experiments at the Lawrence Berkeley National Laboratory Bevalac and in Dubna the next generation of experiments were installed at the Alternating Gradient Synchrotron in Brookhaven and at the Super Proton Synchrotron (SPS) in Geneva. The first claim of a discovery of a new state of matter came from the lead beam program at CERN started in 1994 in which several experiments took part [4–17]. In the beginning of 2000 the claim was made that a new state of matter was discovered [18] which however did not exactly match the expectation of a weakly interacting plasma in which the quarks and gluons roam with only small interaction. Measurements at the relativistic heavy ion collider (RHIC) at the Brookhaven National Laboratory (BNL) then followed up and established that while a quark-gluon plasma is formed it is indeed a strongly interacting medium that shows properties of an almost perfect liquid instead of a weakly interacting gas [19–22].

It should be clear from the number of references that led to these findings that there is not a single measurement that presents itself as a smoking gun to any properties of the emerging QGP. A moment should be taken to elaborate where in the field the analysis presented in this thesis is contributing. As the title suggests an analysis of dielectron production in p–Pb collisions is presented in this manuscript. The choice of p–Pb collisions might seem odd in the context of the prior discussed effects. Nevertheless, a precise understanding of effects that are not related to the QGP is necessary. For this, reference measurements need to be carried out, such as the one presented. The measurement of dielectrons was already part of the programs at SPS and at RHIC. In the following subsection, the advantage of such measurements and their sensitivity to QGP properties are discussed.

1.1 Probing strongly interacting matter with dielectrons

When thinking about the creation of the Little Big Bang in the laboratory by colliding heavy nuclei at ultra relativistic velocities, different stages of these collisions

can be identified in which different physics is at work. In the first and most violent initial collisions, the partons of the nuclei will deposit energy in the collision zone. After this, the system will start to build up a medium which will approach thermal equilibrium and form a plasma of quarks and gluons at a thermal scale of some hundred MeV. With time, this system will expand and cool, around a pseudo-critical temperature $T_{\mathrm{pc}} = 154 \pm 9$ MeV [23] the medium will go through a cross-over and confinement will force the quarks and gluons into hadrons. While further cooling down these hadrons will continue interacting for a short time. First, the inelastic interactions will cease fixing the hadron chemistry, and then no more elastic scattering of each other will occur manifesting the momentum distributions of the hadrons. The widely used terminology in the field describes these points in time as chemical and kinetic freeze-out which can both be connected to a temperature of the medium. Finally, the debris of the collision will be measured in the detector. In short, an initial phase of a pre-equilibrium is expected, from which a quark-gluon plasma emerges. The QGP cools down and a hadronic medium is formed. Further cooling leads to a cease of the interactions in the hadronic medium and the particles and their decay products are registered in the detector.

Given that electromagnetic probes, like photons and/or dileptons, do not interact strongly, a natural question could challenge the thought of using them to study and understand QCD phenomena. After all, they do not interact strongly. And therein lies the beauty. While hadronic observables will always be obscured by interactions with the later stages of the collision, electromagnetic probes will carry their information to the detector unscathed. In addition, the energy scales of the interactions producing direct photons change with time, and the measured spectra change as well. This means that the low transverse momentum (p_{T}) region will be populated mainly by the later emitted thermal photons from the hadronic phase. Going up in p_{T} then the photons produced in the QGP are the most abundant while at higher momenta then the contribution from the pre-equilibrium would dominate. In the case of virtual direct photons, in addition to a selection in p_{T}, the invariant mass of the dielectron pair can separate the different contributions. This gives the possibility to measure the average temperature of the emitting photon source. In the picture of an equilibrated thermal source producing the photons, the spectrum should depend on the size and the temperature of the source. While the absolute yield then depends on the space-time volume of the source, the inverse slope of the spectrum only depends on the temperature (T). Here the differences in the measurement of real and virtual direct photons should be noted. In the case of

real photons, the energy of the photon measured in the detector is blue-shifted due to the expanding source. For the virtual direct photons, such a blue shift is not present since the Lorentz invariant mass of the virtual photons is observable. In the terminology, this is reflected by measuring an effective temperature in the real direct photon measurements. In addition, a measurement of the decays of the vector mesons in their electromagnetic channel could give access to a modification of the vector mesons in a hot medium, which can reveal a possible approach to the restoration of chiral symmetry. Proposals to measure dilepton spectra to access the early stages of the collision were formulated by several authors [24–29] with the emergence of the field. In the following chapter, the different production mechanisms of dielectrons will be discussed.

Chapter 2

Dielectron Sources

This chapter gives an overview of the different production processes that result in a correlated e^+e^- pair. Starting with the production of dielectrons from a hot thermal medium, the physics connected to the measurement is introduced. The different sources that produce additional e^+e^- pairs via their decays are discussed to illustrate the complexity of the interpretation of the measurement.

2.1 Thermal Production of Dielectrons

The production of dielectrons from a hot quark-gluon plasma in a space-time volume at rest and in (local) thermal equilibrium was derived by McLarren and Toimela [30] in 1985 as

$$\frac{\mathrm{d}N_{\mathrm{ee}}}{\mathrm{d}x^4\mathrm{d}q^4} = \frac{\alpha_{\mathrm{EM}^2}}{\pi^3 m_{\mathrm{ee}}^2} f^{\mathrm{BE}}(q_0, T)\mathrm{Im}\Pi_{\mathrm{EM}}(m_{\mathrm{ee}}, q, \mu_{\mathrm{B}}, T), \tag{2.1}$$

with the fine-structure constant α_{EM}, the dielectron invariant mass (m_{ee}), the baryochemical potential (μ_{B}) and the temperature of the fluid cell T. Furthermore the Bose-Einstein occupation factor

$$f^{\mathrm{BE}}(q_0, T) = \frac{1}{e^{q_0/T} - 1} \tag{2.2}$$

and the imaginary part of the electromagnetic current-current correlator ($\mathrm{Im}\Pi_{\mathrm{EM}}$) are relevant for the calculation. The imaginary part of the current-current correlation function is directly connected to the spectral function. This was measured in its vacuum state in e^+e^- collisions by the ratio of hadronic to leptonic production

$$R = \frac{\sigma(\mathrm{e^+e^-} \to \mathrm{hadron})}{\sigma(\mathrm{e^+e^-} \to \mu^+\mu^-)}. \tag{2.3}$$

A compilation of measurements of R at different collision energies by the particle data group is shown in Fig. 2.1 [3]. The ratio of hadronic to leptonic final states is

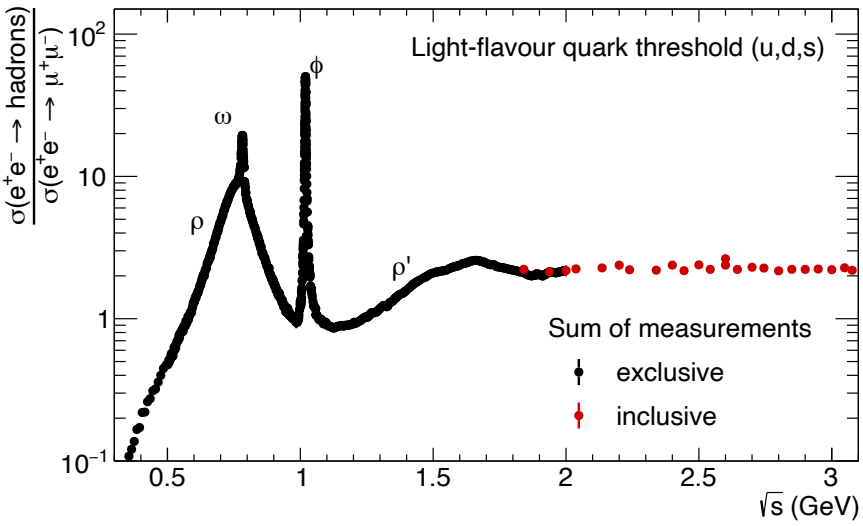

Figure 2.1.: Compilation of data on the ratio of hadronic to leptonic final states in e^+e^- collisions as a function of $\sqrt{s}$. Data taken from [3].

shown as a function of the energy in the centre of mass system of the collision of the two electrons, which directly translates to the momentum transfer in the collision and in the case of the process $\gamma\gamma \to \mu^+\mu^-$ to the mass of the virtual photon and consequently the $\mu^+\mu^-$ pair. The vacuum spectral function can be separated into two regions. Collision energies below 1.5 GeV show a clear structure connected to the vector mesons ρ, ω and ϕ. The annihilation of the e^+e^- pair can be understood to be moderated instead of a virtual photon by an intermediate vector meson with the same quantum numbers, the so-called vector-meson dominance model (VDM) [31–34]. At higher collision energies a structureless continuum emerges. The strong connection between the electromagnetic spectral function to the vector-meson spectral function implies that a precise measurement of the dielectron spectrum from a hot and dense medium can give direct information about possible modifications of the vector-meson spectral shape. At higher masses, however, the spectrum is sensitive directly to the medium temperature. As seen in Fig. 2.1, the spectral function is structureless, while the occupation term going with $e^{-q_0/T}$ indicates that the inverse slope of the spectrum should be directly proportional to the temperature of the medium.

2.2 The Drell-Yan process

A different process that produces a dielectron pair which is not connected to a thermal medium is the so-called Drell-Yan process [35]. It describes the annihilation of a quark from one incoming nucleon with an anti-quark from the other nucleon. The momentum transfer of the process is connected to the fraction of the momentum of the nucleon that is carried by the quark and anti-quark (x). The pair mass is then given by the process' momentum transfer as $m_{\mathrm{ee}} = Q^2 = x_1 x_2 s$, with $\sqrt{s}$ the collision energy, and x_1 and x_2 the momentum fractions carried by the quark or anti-quark.

2.3 Dielectrons from Hadronic Decays

The main source of correlated $\mathrm{e^+e^-}$ pairs that are measured in the detector are unfortunately produced by the decays of different hadrons that are created in the high energy collisions. The most abundant are the so-called light-flavour hadrons which are used to address all hadrons that are built from up (u), down (d) and strange (s) quarks. Hadrons containing a heavy charm (c) or beauty (b) quark are referred to as heavy-flavour hadrons. In particular, differentiating between the hadrons which contain one heavy, and one or two light quarks (open heavy flavour) and those that are made up of a heavy quark-anti-quark pair which are also called quarkonia. These are then again subdivided into charmonium and bottomonium, depending on the type of heavy quark. In the following, the contributions of all the different types of hadrons to the dielectron signal are discussed.

2.3.1 Light-Flavour Hadrons

The most abundant particles that decay with a dielectron in the final state are the light-flavour hadrons, to be more precise light-flavour mesons. Compound $q\bar{q}$ states that contain u, d and s quarks. The relevant mesons that decay with a $\mathrm{e^+e^-}$ pair in the final state are summarised in Tab. 2.1. They are listed with their mass, angular momentum (J), parity (P) and charge-parity (C) configuration as well as the decays with an $\mathrm{e^+e^-}$ pair in the final state with the respective decay probability or branching ratio (BR) [3]. The combination of J^{PC} and the conservation in the decays is relevant for the possible decay channels of the particle. While all particles show an odd parity ($-$), the angular momentum as the sum of the spin (S) and the

Particle	Mass (MeV/c^2)	J^{PC}	Decays	Branching Ratio
π^0	134.9768 ± 0.0005	0^{-+}	$e^+e^-\gamma$	$(1.174 \pm 0.035) \cdot 10^{-2}$
			$e^+e^-e^+e^-$	$(3.34 \pm 0.16) \cdot 10^{-5}$
η	547.862 ± 0.017	0^{-+}	$e^+e^-\gamma$	$(6.9 \pm 0.4) \cdot 10^{-3}$
η'	957.78 ± 0.06	0^{-+}	$e^+e^-\gamma$	$(4.91 \pm 0.27) \cdot 10^{-4}$
			$e^+e^-\omega$	$(2.0 \pm 0.4) \cdot 10^{-4}$
			$e^+e^-\pi^+\pi^-$	$(2.42 \pm 0.10) \cdot 10^{-3}$
ρ	775.26 ± 0.23	1^{--}	e^+e^-	$(4.72 \pm 0.005) \cdot 10^{-5}$
ω	782.66 ± 0.13	1^{--}	e^+e^-	$(7.38 \pm 0.23) \cdot 10^{-5}$
			$e^+e^-\ \pi^0$	$(7.7 \pm 0.6) \cdot 10^{-4}$
ϕ	1019.461 ± 0.016	1^{--}	e^+e^-	$(2.979 \pm 0.033) \cdot 10^{-4}$
			$e^+e^-\ \eta$	$(1.08 \pm 0.04) \cdot 10^{-4}$
			$e^+e^-\ \pi^0$	$(1.3^{+0.07}_{-0.10}) \cdot 10^{-5}$

Table 2.1.: Light-flavour neutral mesons with their mass, angular momentum, parity and chrage partiy (J^{PC}) and the most significant decay topology with a dielectron in the final state and the respective decay branching ratio [3].

orbital momentum (L) is 0 in the case of π^0, η, η' and 1 for ρ, ω, ϕ. In case of $J = 0$ the spin states of the two component quarks are in a configuration in which they compensate each other ($\uparrow\downarrow, \downarrow\uparrow$). In the nomenclature the $J = 0$ mesons with odd parity are labeled pseudoscalar mesons. A state of $J = 1$ is achieved in case the quark spins align ($\uparrow\uparrow, \downarrow\downarrow$) and the mesons are called vector mesons. The $J = 0$ and $J = 1$ even parity states are called scalar and pseudovector (axial vector) mesons. As they have no decays with an e^+e^- in the final state they are not further discussed here.

The decays listed in Tab. 2.1 show that the dominant decay of the vector mesons is directly into an e^+e^- pair; the decays of pseudoscalar mesons with an e^+e^- pair in the final state is then always accompanied at least one additional particle. This is a result of the respective quantum numbers, J^{PC}, that need to be conserved in the decay. The vector mesons have the same quantum numbers as the photon and can directly couple to a virtual photon which again can decay direct into an e^+e^- pair. The pseudoscalar mesons however decay predominantly into $\gamma\gamma$ or in the case of the η' the final state of $\gamma\pi^+\pi^-$ is relevant which can be seen as a decay of η' to $\gamma\rho$. The dominant decays of the pseudoscalar mesons do not have an e^+e^- pair in the final state. However, through the process of internal conversion, a photon can with

a certain probability decay into an e^+e^- pair [36]. The probability of producing a dielectron with a mass m_{ee} per real photon can be expressed as

$$\frac{1}{N_\gamma}\frac{\mathrm{d}N_{ee}}{\mathrm{d}m_{ee}} = \frac{2\alpha}{3\pi}\frac{1}{m_{ee}}\sqrt{1-\frac{4m_{e^2}}{m_{ee}^2}}\left(1+\frac{2m_e^2}{m_{ee}^2}\right)|F(m_{ee}^2)|^2\left(1-\frac{m_{ee}^2}{M_h^2}\right)^3. \tag{2.4}$$

Here N_γ and N_{ee} denote the number of photons and e^+e^- pairs respectively. The probability for internal conversion then depends on the electron mass (m_e) and the invariant mass of the e^+e^- pair (m_{ee}). The last term in Eq. 2.4 illustrates the limited phase space due to the mass of the decaying hadron (M_h). In case the internal conversion happens in a decay other than $h \to \gamma\gamma^*$ like in $\eta' \to \omega\gamma^*$ the phase space factor needs to be modified to $M_{\eta'} \to M_{\eta'} - M_\omega$ to account for the reduction of the phase space. The electromagnetic transition form factor $|F(m_{ee}^2)|$ needs to be taken into account. For a point-like interaction, the form factor would be unity. The interaction of the photon with the decaying particle however can be described by the interaction with an intermediate vector meson as described in the VDM [31–34]. In the pole approximation, the form factor for the transition of a state A to B can then be parameterised as

$$F_{AB}(q^2) = \frac{1}{1-\frac{q^2}{\Lambda^2}}, \tag{2.5}$$

with the momentum transfer q^2 and a the characteristic mass $\Lambda \approx m_\rho$ [37]. In the discussed cases, q^2 is given by the invariant mass of the dielectron pair. The value of Λ^2 can then be derived from parameterisations in the measurements of the three-body decays like it was done by the Lepton-G [37, 38] or the NA60 [39, 40] collaborations. The impact of $|F(m_{ee}^2)|^2$ is visualised in Fig. 2.2. Here, the calculations from Eq. 2.4 are shown for the masses of the π^0 and the η meson. The solid lines show the result neglecting the form factor while the dashed lines show the calculation including the measured form factors.

The mass shapes of the e^+e^- pairs show a maximum at very small masses and then fall off steeply and vanish at the pole masses of the respective mesons due to the available phase space in the decay. This indicates that in most cases of the three-body decay (or Dalitz decay [41]) the real photon carries most of the energy and momentum. The effect of the form factors is small at lower masses while the modulation of the mass shape becomes sizable at masses of about 0.3 GeV/c^2. In the measurement of dielectron production, the light-flavour mesons then

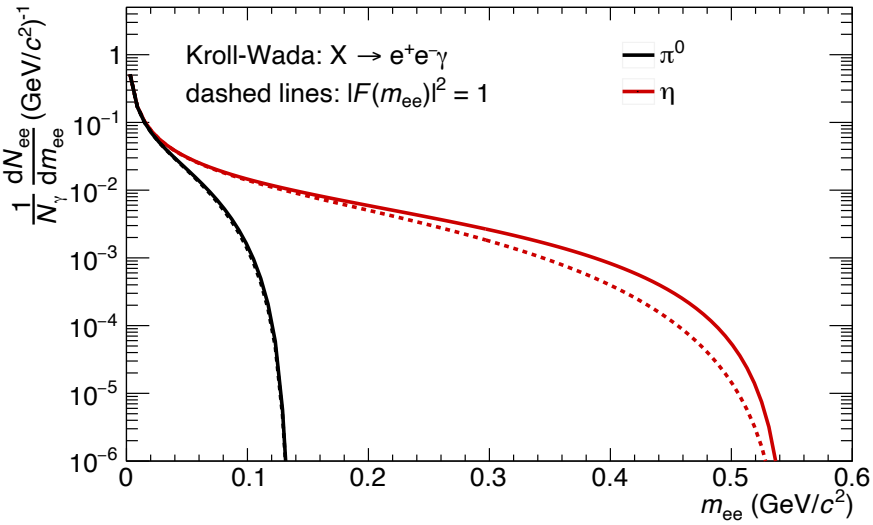

Figure 2.2.: Mass distribution of e^+e^- pairs from π^0 and η decays calculated with the Kroll-Wada equation [36]. Dashed lines show the effect of not including the electromagnetic transition form factor as measured by Lepton-G and NA60 [37–40].

contribute to masses below m_ϕ. While the Dalitz decays follow the wide distribution indicated in Fig. 2.2, the decays of the vector mesons show a peak-like structure around the respective pole masses since all products of the decays are included in the reconstruction of m_{ee}.

2.3.2 Heavy-Flavour Hadrons

After the discussion of the contributions of the decays of light-flavour hadrons to the dielectron measurements, the following section discusses the contributions from the decays of heavy-flavour hadrons. Their production can be described within uncertainties by calculations that apply the so-called factorisation theorem. It states that the cross-section of different heavy-flavour hadron species can be calculated as the convolution of three independent terms:

- The probability for two partons in the projectiles and the target to interact, which is encoded in the parton distribution functions (PDFs)
- The probability for the two interacting partons to produce a pair of heavy quarks
- The probability for the produced heavy quark to form the respective hadron, the so-called fragmentation functions (FFs)

The cross-section to produce a certain hadron species H is then given by:

$$\sigma_H = PDF(p_1(x_1)) \times PDF(p_2(x_2)) \otimes \sigma(p_1(x_1)p_2(x_2) \to Q\overline{Q}) \otimes D_{Q\to H}. \quad (2.6)$$

The first term gives the probability that parton p_1 with a given momentum fraction x_1 of the incoming projectile interacts with parton p_2 with x_2 of the other projectile. The second term gives the partonic cross-section for the two partons to produce a heavy quark-antiquark pair $Q\overline{Q}$, which can be calculated in perturbative QCD (pQCD) for the case of heavy quarks. The third term gives the probability that a heavy quark hadronises into meson species H. As the name factorisation theorem implies, the underlying assumption is that the three terms are independent from each other and factorise. This makes it possible to treat each term independently. The PDFs are based on measurements that can be extrapolated to the required scale (momentum tranfer Q^2 and x) using evolution equations like DGLAP [42–44]. The partonic cross-sections can be calculated in perturbative QCD as a series in the running coupling α_s, while the corrections to the resulting cross-section are on the order of α_s evaluated at the mass of the heavy quarks [45]. The fragmentation of the heavy quarks is typically based on parametrisations of measurements in ee or ep collisions [46]. Models like FONLL calculate the cross-sections as a function of p_{T} for a given heavy-flavour hadron species [47, 48].

The probability of the decay of a heavy-flavour hadron with an electron in the final state is about 10%. Table 2.2 summarises the branching ratios of the different mesons and baryons in the beauty and the charm sector.

As the flavour of the quark is conserved in the strong and electromagnetic interactions the only possible decay is via a weak interaction and moderated with a $W^{\pm}$ boson that decays into a lepton and a neutrino, conserving the lepton number:

$$Q \overset{W^+}{\to} q l^+ \nu_l. \quad (2.7)$$

As the decay is mediated by the weak force, the time scale in which it occurs is larger than decays via the strong or electromagnetic forces. This leads to a finite distance the heavy-flavour hadron travels before it decays. The decay lengths ($c\tau$) are of the order of 100 μm. Table 2.2 gives an overview of the values of the semi-leptonic branching ratios and the decay lengths for different hadron species. In both cases, the branching ratio into electrons as well as the decay length dependent on the hadron species is displayed in the charm case, while no large variation is visible

Decay	BR [%]	$c\tau$ [μm]
Charm		
$D^+ \to e^+$ anything	16.07 ± 0.3	309.8
$D^0 \to e^+$ anything	6.49 ± 0.11	123.01
$D_s^+ \to e^+$ anything	6.33 ± 0.15	150.3
$\Lambda_c^+ \to e^+$ anything	3.95 ± 0.35	60.75
$\Xi_c^+ \to e^+$ anything	7 ± 4	135.8
$\Xi_c^0 \to e^+$ anything	1.04 ± 0.24	45.1
Beauty		
$B^+ \to e^+\nu_e X_c$	10.8 ± 0.4	491.1
$B^0 \to e^+\nu_e X_c$	10.1 ± 0.4	454.8
$B_s^0 \to e^+\nu_e X_c$	9.1 ± 0.8	455.7
$\Lambda_b^0 \to l^-\nu_l \Lambda_c^+ X$	10.1 ± 0.4	441.0

Table 2.2.: Branching ratios of heavy-flavour hadrons with electrons in the final state. Values are taken from [3].

in the beauty case. The dominant decays have in the final state always one electron and the respective neutrino accompanied by hadrons. They are from now on referred to as semi-leptonic decays. In the measurements of dielectrons the decay of a single heavy-flavour hadron in the semi-leptonic channels will of course not contribute to the dielectron measurement. However, as the heavy quarks are produced in pairs, there will also be a second heavy-flavour hadron which can decay semi-leptonically. As they are produced as charge conjugates the resulting lepton pair will be of opposite sign in most cases. A sketch illustrating the hadronisation of a $c\bar{c}$ pair to D-mesons which decay in a semi-leptonic channel is shown in Fig. 2.3. The

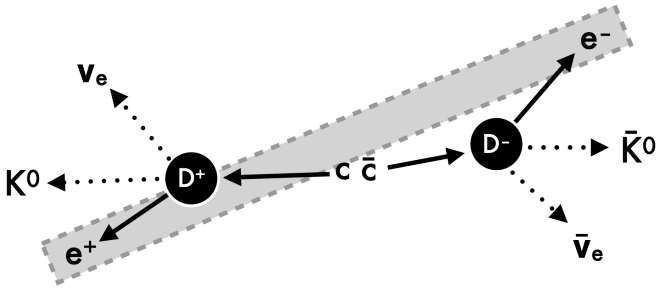

Figure 2.3.: Sketch of a $c\bar{c}$ quark pair hadronising into D-mesons which decay semi-leptonically with an e^+e^- pair in the final state.

pair reconstructed from this type of decay will only carry a residual correlation and produce a continuous mass spectrum. However, it shows the importance of the frag-

mentation functions to calculate the contribution of dielectrons from heavy-flavour decays. As described above, the factorisation theorem states that the fragmentation of the heavy quark into a hadron should be independent of the production of the quark. In this logic, the relative contributions of different species should not change across collision energies or systems. In recent measurements of the ALICE collaboration, this was put to the test. The spectra of many charm mesons and baryons were measured in pp collisions at $\sqrt{s} = 13$ and 5.02 TeV to extract the fragmentation fractions as shown in Fig. 2.4 (left) [49].

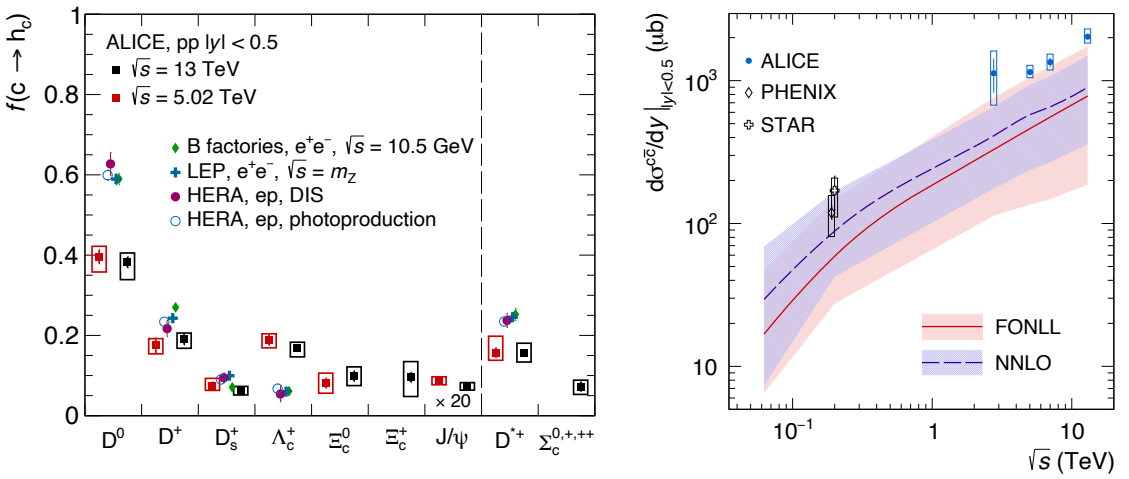

Figure 2.4.: Left: The charm fragmentation fraction $f(c \to \mathrm{h}_c)$ measured at midrapidity ($|y| < 0.5$) by ALICE in pp collisions at $\sqrt{s} = 5.02$ and 13 TeV [49]. For better visibility, the J/ψ values are scaled up by a factor of 20. The ALICE measurements are compared to $\mathrm{e^+e^-}$ and ep results [50]. Right: The charm production cross-section per unit rapidity at midrapidity is shown as a function of the collision energy. The measurements are compared to FONLL [47, 48, 51, 52] and NNLO [53–55] calculations.

The ALICE measurements are compared with different measurements in $\mathrm{e^+e^-}$ and ep collisions at smaller collision energies. The comparison shows a tension between the results obtained at the LHC with the other measurements. Namely, the enhancement of the baryon production which then reduces the fraction of the mesons. Until now, no clear explanation has been found for this tension. The impact of this measurement on dielectron analyses that extracted the charm cross-section is discussed in detail in Appendix A. The measurement of the wide range of charm hadrons, including the baryons, gives the possibility to calculate the total charm cross-section as shown in Fig. 2.4 (right) as a function of the collision energies. The data are compared to FONLL [47, 48, 51, 52] calculations which predict a similar $\sqrt{s}$ dependence as the data. A set of calculations performed at next-to-next-to-leading

order (NNLO) [53–55] shows the same trend as a function of $\sqrt{s}$ with slightly higher values. However, in both calculations, the central values underestimate the measurements. This has been observed also in measurements of the p_{T} spectra of fully reconstructed charm mesons. The large increase in the production cross-section with the collision energy shows the importance of understanding the production of charm hadrons and their contribution to the dielectron spectrum at LHC energies.
Taking a closer look at the beauty decay topologies, some additional features with respect to the charm sector should be mentioned. The decay of the beauty quark results in a charm quark as indicated in the entries in Tab. 2.2. This gives two configurations of decays as shown in Figures 2.5 and 2.6. While in the case of charm

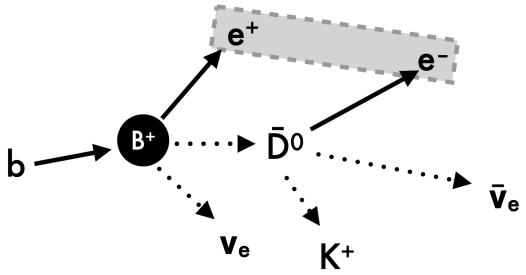

Figure 2.5.: Sketch of a $c\bar{c}$ quark pair hadronising into D-mesons which decay semi-leptonically with an e^+e^- pair in the final state.

hadrons, both hadrons need to decay in semi-leptonic channels, a single beauty hadron may produce an e^+e^- pair. This happens when the charm hadron that was produced in the semi-leptonic decay also decays with an electron in the final state. Due to the sign change on the quark level, the second lepton also changes sign compared to the first lepton. This way an e^+e^- pair can be produced from one open-flavour beauty hadron as indicated in Fig. 2.5. The decay of the beauty hadron into

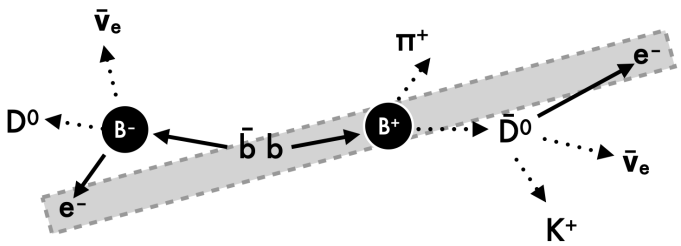

Figure 2.6.: Sketch of a $c\bar{c}$ quark pair hadronising into D-mesons which decay semi-leptonically with an e^+e^- pair in the final state.

a charm hadron is also the case illustrated in Fig. 2.6. Here one beauty hadron decays

semi-leptonically, while the second decays in a purely hadronic channel. The charm hadron produced in the hadronic decay then decays in the semi-leptonic channel. In this case, again a sign change occurs, leading to the production of a same-sign pair, i.e. e^+e^+ or e^-e^-. In addition to the decay topology that can produce a same-sign pair, also the oscillation of beauty hadrons into their anti-particle can produce a same-sign pair. While oscillation was also observed in the charm sector, the effect there is too small to make a significant contribution.

2.3.3 Modification of heavy-flavour Dielectron Production in Heavy-Ion Collisions

The above discussion is valid for the description of the production of heavy-flavour hadrons and the decay dielectrons in vacuum. However, when moving to heavy-ion collisions, modifications of the spectra of decay electrons are expected. The reasons for this are two-fold. The heavy quarks interact with the hot and dense medium created in the collision, thereby losing energy by induced gluon radiation and scattering of the medium. Energy loss is a so-called hot-nuclear matter effect, as it is due to the interaction with the hot medium. In addition to this, we have so-called cold nuclear matter effects. These refer to modifications that have their origin in the fact that the parton distribution or structure function (F_2) changes in the nucleus with respect to the free proton. In other words, the parton distribution in the nucleus is not a superposition of its constituents. These effects arising from the binding of the nucleon in the nucleus can be encoded in the so-called nuclear parton distribution functions (nPDFs) [56,57]. The modification of F_2 as a function of x is illustrated in Fig. 2.7 taken from [58].

The modification is shown as the ratio of the modified structure function of the nucleon bound in nucleus A to the free proton structure function (R^A). At small x, a depletion is visible that is referred to as shadowing. This depletion reflects a reduction in the cross-section for processes in the small x region. Going up in x, R^A grows to values above unity referred to as antishadowing. The EMC collaboration measured another reduction in R^A, named the EMC effect. Towards values of $x = 1$ a steep rise occurs due to the Fermi motion of the nuclei. As in the case of the PDFs discussed above, the evolution of the nPDF with Q^2 can be calculated using the DGLAP equations. However, the x-dependence needs to be measured experimentally. The first measurements used to constrain the R^A were based on deepinelastic scattering of leptons and the Drell-Yan production of dileptons. Since

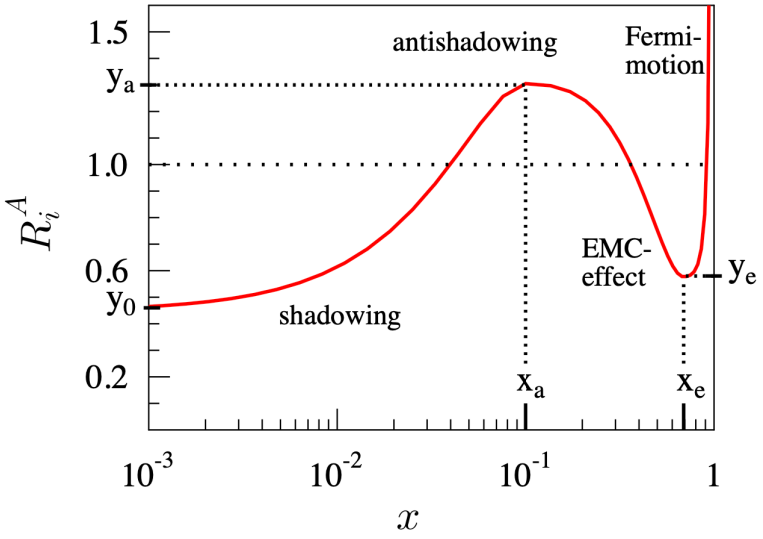

Figure 2.7.: Dependence of the nuclear modification factor of the parton distribution function on x as used in the EPS09 set [58].

then, a plethora of measurements were included in the estimation of the effects of the cold nuclear matter on the parton distributions. An overview of the Q^2 and x regions covered by the different data is given in Fig 2.8 [59]. The reach of

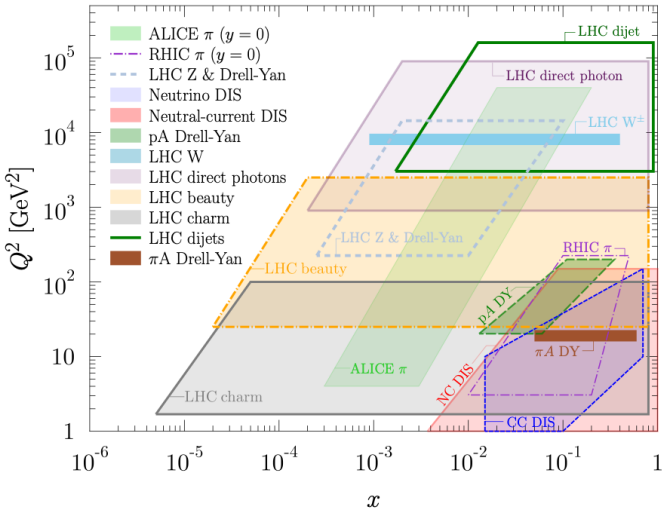

Figure 2.8.: Sensitivity of measurements to x and Q^2 regions [59].

charged current DIS, neutral current DIS, Drell-Yan production in proton-nucleus and pion-nucleus collisions, as well as pion production at RHIC, is limited to values of about $x > 10^{-2}$ and $Q^2 < 10^2$ $(\mathrm{GeV}/c)^2$. A large range of measurements like the electroweak boson production, Drell-Yan, dijet and direct photon measurements at

LHC extend the range of the measurements to about $10^3 < Q^2 < 10^5$ $(\mathrm{GeV}/c)^2$ and down to $x \approx 10^{-4}$. The region below $Q^2 \approx 10^2$ $(\mathrm{GeV}/c)^2$ and down to $x = 10^{-5}$ is shown to be sensitive to heavy-flavour quark production at LHC energies. The LHC data of the last decade extended the x and Q^2 reach significantly to smaller x and higher Q^2 values. The approach to quantify the modifications in the nPDFs is a global analysis of the data and essentially a fit of all the data. Here, the modification of the free proton PDFs are the varied parameters to best fit the set of global data. These analyses have different free parameters, such as the free proton PDF that is used or the choice of the parameterisation. While the groups responsible for the nCTEQ and the EPPS sets use analytic parameterisations the NNPDF family of nPDF is based on a neural network approach. This is also reflected in the number of free parameters in the fits which are 19(24) for the latest nCTEQ15HQ [60] (EPPS21 [61]) and 256 for nNNPDF3.0 [62]. The modification factors for the u, d, s, $\bar{u}$, $\bar{d}$ quarks and the gluons in ^{208}Pb are shown in Fig. 2.9 as a function of x at $Q^2 = 10$ GeV for the three approaches. Overall the different parameterisations of the

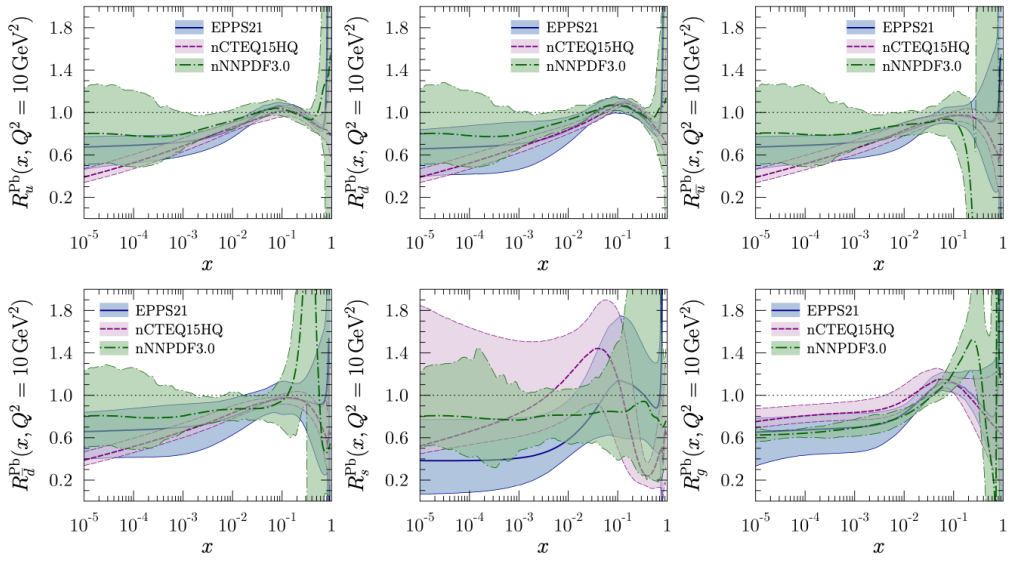

Figure 2.9.: Comparison of the EPPS21 [61], nCTEQ15HQ [60] and nNNPDF3.0 [62] nPDF parameterisations of ^{208}Pb [59].

nPDFs agree well within their uncertainties. The best constraints are given by NC DIS data for the quarks and anti-quarks at $x \approx 0.1$. However, in particular at small x, the central values differ as well as the uncertainties of the various implementations. These variations have several reasons. As discussed above, the model choices differ

for the three implementations, however, the choice of the input data and the range used for the parameterisation of the respective data also vary.

Chapter 3

Previous Measurements

After the discussion of different dielectron sources, the following chapter will give an overview of previous measurements. A short discussion of the different experimental setups is given, and when necessary also experimental techniques are discussed. However, the focus should be on the results and their interpretation.

3.1 The good old days at the SPS

The CERN Super Proton Synchrotron (SPS) with its 7 km circumference is the second largest accelerator in the CERN accelerator complex and reaches a top energy of 450 GeV for the proton beams circulating in it. In addition to protons, it is able to accelerate many more particles like sulfur, oxygen, lead ions or electrons. While the most famous discovery achieved at the SPS was the discovery of the W and Z bosons after converting the machine into a proton anti-proton collider, this chapter will focus on experiments that studied the production of dileptons. Up to today the SPS delivers proton and ion beams to the fixed target experiments in the North Area (NA) at CERN's Prévessin site.

The first measurement discussed here concerns the production of dielectrons and was performed by the CERES/NA45 collaboration in S on Au collisions at 200 GeV/u (per nucleon) beam energy [63]. The CERES spectrometer identified electrons using a setup with two Ring Imaging Cherenkov (RICH) detectors. The experiment's silicon drift detectors used for tracking and vertex reconstruction could in addition be employed to suppress photon conversions and Dalitz decays. A magnet system was used to deflect charged particles and measure the momentum of the particles.

In addition to S-Au, measurements of dielectron production were performed in smaller collision systems (p-Be, p-Au) to establish a baseline for the contributions from hadronic decays. The results could be well reproduced by expectations of hadronic decay contributions. The measurement in S-Au collisions is shown in Fig. 3.1 (left) together with the different contributions from hadronic decays.

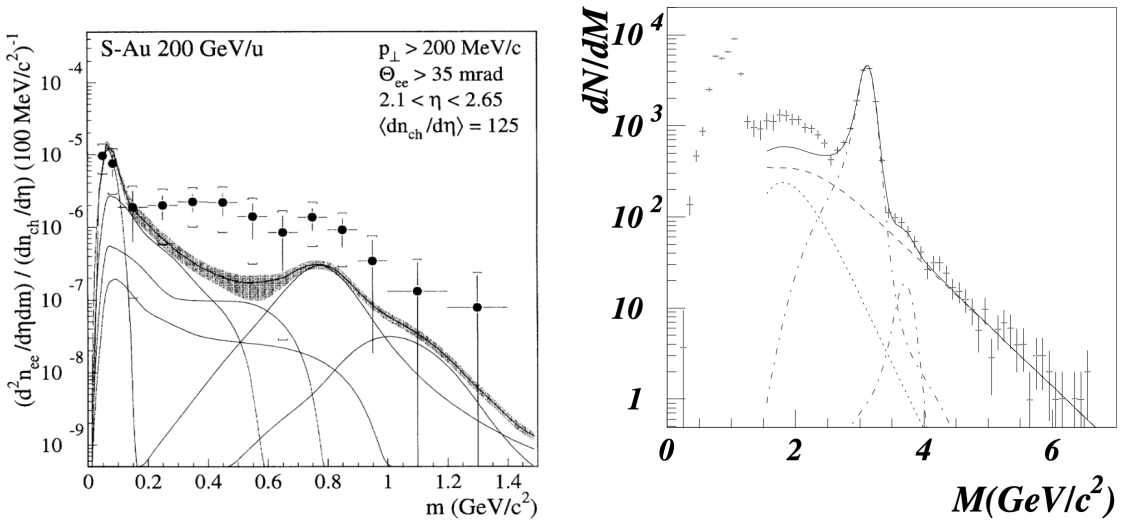

Figure 3.1.: Measurement of dilepton production at 200 AGev in S-Au collisions by the CERES collaboration (left) [63] and in Pb-Pb collisions at 158 AGeV by the NA38/NA50 collaborations (right) [64]. The measurements are compared to calculations of the expected hadronic contributions.

The grey band indicates the uncertainty on the hadronic contributions, while the uncertainties on the data are shown as bars (statistical) and rectangles (systematic). An excess of the production rate above the expected hadronic contribution is observed and quantified as a factor $5 \pm 0.7(\text{stat.}) \pm 2.0(\text{syst.})$ as the integral of the yield divided by the integral of the expected hadronic decays in the mass region $0.2 < m_{ee} < 1.5$ GeV/c^2. The onset of the excess at $m_{ee} \approx 2m_\pi$ together with a measurement of the HELIOS-3 (NA34) [65] collaboration at a different charged-particle multiplicity or energy density were interpreted as a signal of two-pion annihilation ($\pi\pi \to e^+e^-$). An contribution from vacuum ρ ($\pi\pi \to \rho \to e^+e^-$) could be excluded already. While it was clear there was a medium modification, but not clear what kind, i.e. a shifting mass described by the Brown-Rho scaling [66–68] or a collisional broadening of the spectral function [69–71]. Due to the limited momentum resolution of the CERES detector, it was not possible at the time to further conclude on the shape of the additional signal.

A second measurement that should be introduced is the one of the dimuon production at the SPS by the NA38/NA50 collaborations [64]. The NA38 apparatus consisted of a muon spectrometer with two sets of Multi-Wire-Proportional Chambers (MWPCs) in front and behind a toroidal air-gap magnet. The hadrons produced in the collision as well as beam particles that did not interact were absorbed in a carbon dump with an additional central W/U plug. The spectrometer was upgraded by the NA50 collaboration to be capable of measuring Pb-Pb collisions at higher trigger rates and radiation levels. A detailed description of the detector is found in [72]. The NA38 and NA50 experiments focused on measuring Drell-Yan and charm production, so a higher mass region than the CERES/NA45 experiment. The mass spectrum measured in central Pb-Pb collisions ($\langle N_{\mathrm{part}} \rangle = 381$) with an incident beam energy of 158 GeV/nucleon is shown in Fig. 3.1 (right). The dashed-dotted line shows the J/ψ expectation, the dotted line the contribution from open charm hadron decays and the dashed line the expected dimuon contribution from the Drell-Yan process. The contributions were scaled from the measurements in p–A collisions assuming they scale with the mass numbers of the projectile and target as $A_{\mathrm{P}} \times A_{\mathrm{T}}$. Details can be found in Ref. [72]. The striking result is that the sum of the Drell-Yan and the open-charm contributions is not able to describe the results in the intermediate mass region where it systematically undershoots the data. One possible explanation at the time was the enhancement of the charm cross-section, which in the publication was tested by scaling the expected charm contribution up. This led to a good result, assuming an enhancement of the charm contribution by a factor of about four in central collisions. However, there is the possibility that the enhancement could be due to an additional thermal source as theoretical work on this was just being developed [70, 73, 74].

To further investigate the measured enhancements both seen in the low-mass region by CERES and in the intermediate-mass regions by the NA50/NA38 collaborations both experiments implemented new detectors to refine the measurements. To improve the momentum resolution of the apparatus the CERES collaboration installed a time projection chamber (TPC) [75]. This radial-drift TPC allowed to improve the relative momentum resolution to a few per cent resulting in a mass resolution of the ϕ-meson peak of 3.8%. In addition to the improved resolution, the specific energy loss per unit length ($\mathrm{d}E/\mathrm{d}x$) measurement could be used to reject pions in the measurement of dielectron pairs. To distinguish between the contribution of open heavy-flavour decays and a possible thermal source of dimuons the NA60 collaboration set out to upgrade the muon spectrometer prior used by the NA10, NA38

and NA50 with a silicon pixel tracker [76, 77]. This would allow the collaboration to better match tracks to the primary collision vertex, and in addition measure the displacement of muons from heavy-flavour decays from the primary vertex. The measurement of the excess in the low-mass region by both experiments [78, 79] is shown in Fig. 3.2. The CERES measurement presented in Fig. 3.2 (left) was ob-

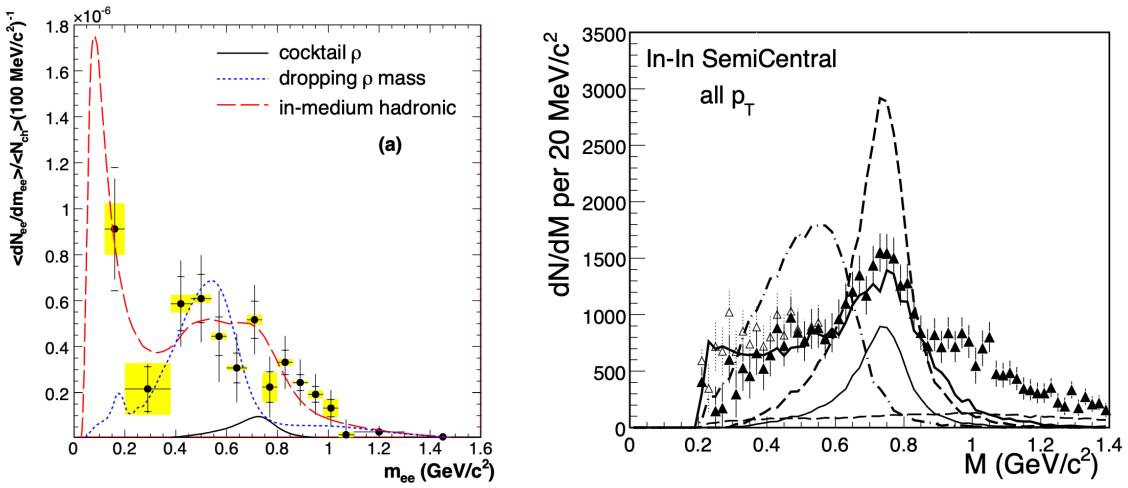

Figure 3.2.: Measurement of dilepton production in Pb-Au collisions by the CERES collaboration (left) [78] and in In-In collisions by the NA60 collaboration (right) [79]. Both measurements are compared to the vacuum ρ contribution as well as models including a thermal production of ρ mesons. Both models include the modification of the ρ mass shape. The dropping mass or Brown-Rho scaling [66–68] is shown as a blue dashed line (left) or a dash-dotted line (right) and the broadening of the mass shape by collisions in the hadronic medium [69–71] is shown as a red dashed line (left) or a thick solid black line (right).

tained from a 158 AGeV Pb beam on gold targets. From the inclusive measurement of dielectron pairs the expected hadronic contributions except the ρ were subtracted to derive the excess spectrum. The excess can not be explained by the vacuum contribution of the ρ (black solid line). The data are compared to two model calculations. Both assume an additional production of the ρ meson via $\pi\pi$-scattering. The difference of the two models manifests in the treatment of the mass of the ρ and its modification to restore chiral symmetry in a hot and dense hadronic medium. The so-called Brown-Rho (dashed blue line) scaling predicts a drop of the pole-mass of the ρ [66–68] while the model proposed by Rapp and Wambach implements a broadening of the ρ due to its scattering in the hadronic medium [69–71]. While the CERES result favours the broadening scenario, it is not able to distinguish between the two. Figure 3.2 (right) shows a similar measurement by the NA60 collaboration in In-In collisions with a 158 AGeV beam in the dimuon channel [79]. The event mul-

tiplicity was measured in the vertex tracker and corresponds to a charged-particle density of $110 < \mathrm{d}N_{\mathrm{ch}}/\mathrm{d}\eta < 170$. The data are shown in solid triangles, the open triangles correspond to the systematic uncertainty related to the subtraction of the η contribution. The expected contribution from ρ is shown by the thin black line, a calculation that includes thermal production of the ρ without modifying its shape is shown by the thick dashed line. Again, calculations assuming Brown-Rho scaling (thick dash-dotted line) and a broadening of the ρ (thick solid line) are compared to the data. It can be concluded that the modification of the ρ will affect its width, while the drop in mass can be ruled out from this measurement. In the mass region beyond 1 GeV/c^2, the NA60 results however are not consistent with the broadened ρ contribution.

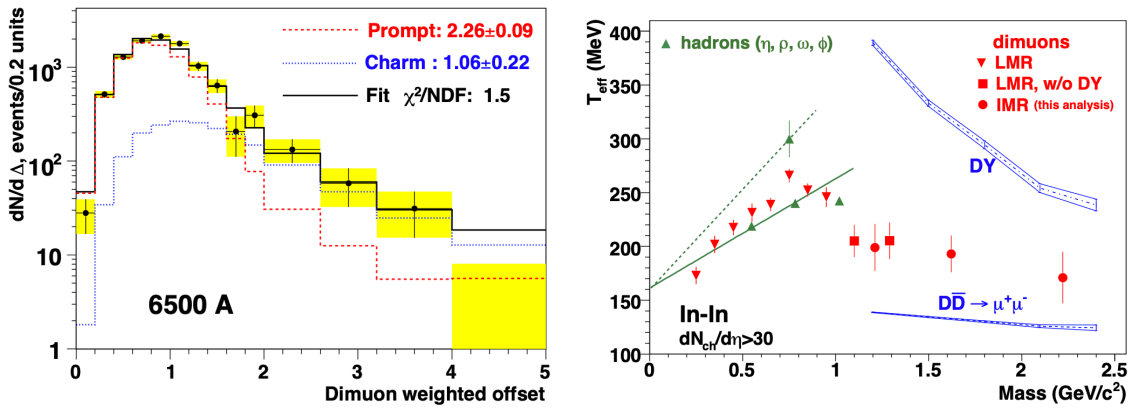

Figure 3.3.: Dimuon weighted offset measured by the NA collaboration in the mass region of $1.16 < m_{\mu\mu} < 2.56$ GeV/c^2 parameterised with a prompt and a charm contribution (left) and the inverse slope parameter as a function of m_{ee} extracted by an exponential fit to the transverse mass m_{T} spectra [80].

As discussed above one of the motivations for including a vertex tracker downstream of the hadron absorber of the NA60 experiment was the measurement of the enhancement on the intermediate-mass region of the NA38/NA50 experiments. In the analysis of the In-In data, the NA60 collaboration observes again an enhancement of dimuons in the mass range of $1.16 < m_{\mu\mu} < 2.56$ GeV/c^2 which could be explained by scaling up the expected charm contribution derived from different p-A measurements. However, the new vertex tracker enabled the introduction of the so-called weighted dimuon offset $\Delta_{\mu\mu}$

$$\Delta_{\mu\mu} = \sqrt{(\Delta_{\mu 1}^2 + \Delta_{\mu 2}^2)/2}. \tag{3.1}$$

Here $\Delta_{\mu i}$ is calculated as the distance of the propagated muon track to the primary vertex in the plane transverse to the beam normalised to the respective resolution in x and y. The distribution of $\Delta_{\mu\mu}$ in the mass range of $1.16 < m_{\mu\mu} < 2.56$ GeV/c^2 is shown in Fig. 3.3 (left). The data is parameterised with a prompt contribution and a charm contribution. The shape of the prompt contribution is evaluated in the J/ψ and ϕ peaks while the charm contribution is based on Monte Carlo simulations including additional detector resolution. The excess dimuons are located in the prompt region of the weighted dimuon offset excluding the hypothesis of an enhanced production of charm as a source of the excess. After subtraction of the backgrounds from Drell-Yan and charm and an acceptance correction, a further study of the excess focused on the transverse mass (m_{T}) spectra in different m_{ee} intervals. It was found that besides a normalisation factor all spectra could be described by an exponential function. This supports the hypothesis that the excess is from thermal dimuon pairs. The inverse slope parameter (T_{eff}) was extracted as a function of m_{ee} and is shown in Fig. 3.3 (right). The red points show T_{eff} extracted for the measured dimuon excess in the intermediate-mass region (full circles) and in the low-mass region with and without subtracting the Drell-Yan contribution in squares and triangles, respectively. For $m_{\mathrm{ee}} > 1$ GeV/c^2 the slope seems independent of the mass, while at lower masses a rise in the slope parameter with rising mass is observed. This can be interpreted as a shift in the m_{T} spectrum due to radial flow that would be present in a hadronic medium while at $m_{\mathrm{ee}} \approx 1$ GeV/c^2 a drop in T_{eff} is observed. This loss of flow can be explained by the transition of the medium to a qualitatively different source of partonic nature and marks the first observation and measurement of thermal radiation from a partonic medium or the QGP with a temperature averaged over the spacetime evolution of about 190 MeV.

3.2 Charming backgrounds at RHIC

The Relativistic Heavy-Ion Collider (RHIC) at the Brookhaven National Laboratory in Upton, New York started its operation in 2000 and was at that point the largest collider for heavy ions. Surprising measurements that came out of RHIC: the strong elliptic flow of hadrons [81] and suppression of hadrons at high p_{T} in central heavy-ion collisions [82]. As the energy of the colliding nuclei went up by about a factor of ten from the SPS, it was one of the milestones of the program to discover the QGP

in high energy Au-Au collisions.[1] One of the probes discussed for the discovering the QGP was the thermal radiation measurement in the dielectron channel. The two most recent measurements by the STAR and the PHENIX collaborations in Au-Au collisions at top RHIC energies are presented in Fig. 3.4 left and right, respectivly [83,84]. In both cases, measured yield in the respective detector acceptance

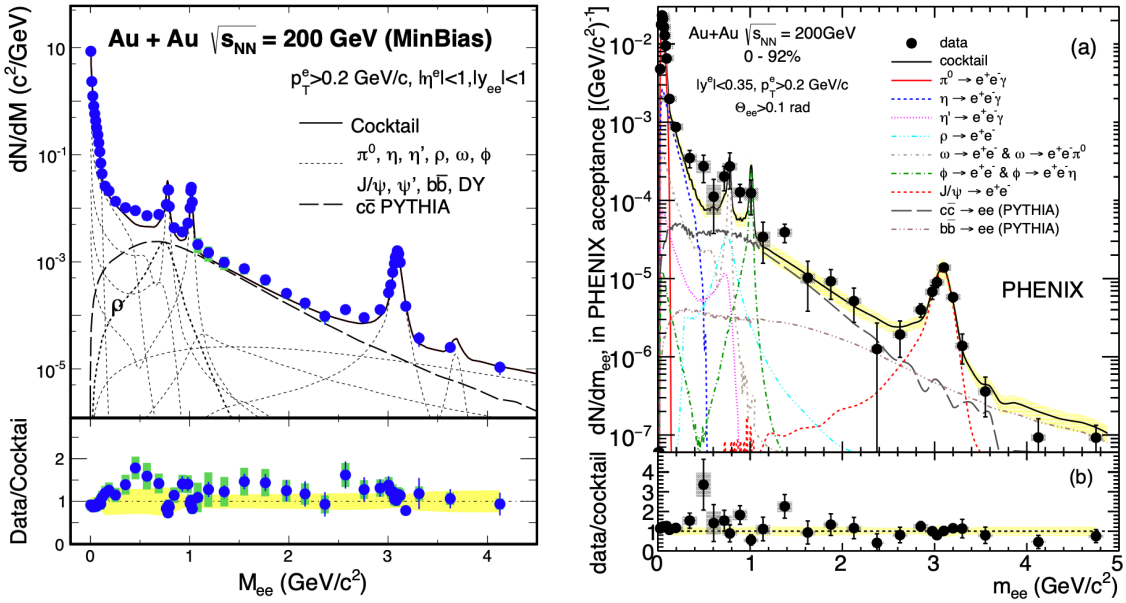

Figure 3.4.: Dielectron measurements in minimum bias Au-Au collisions at $\sqrt{s_{\mathrm{NN}}} = 200$ GeV by the STAR (left) [83] and the PHENIX (right) [84] collaborations. In both cases, the measured yield as a function of m_{ee} is compared to the expected contribution from hadron decays.

is shown as a function of m_{ee} and the data are compared to the estimation of the hadronic decays. What becomes obvious, specially investigating the invariant mass region between the ϕ and the J/ψ mesons, is the large contribution from the open-charm decays that also contribute significantly at about 0.5 to 0.7 GeV/c^2. Both experiments base their calculations of the charm contributions on measurements in smaller systems. The STAR collaboration uses a tune of the PYTHIA event generator that well describes the measurement of heavy-flavour hadron production in pp collision [85] and scales with the number of binary nucleon-nucleon (N_{coll}) collisions. The PHENIX collaboration uses the measurement of $\mathrm{e^+e^-}$ pairs from charm decays in d-Au collisions extrapolated with the PYTHIA event generator [86] which

[1] It should be pointed out that, while the planning and first data taking of the RHIC detectors was ongoing, the above discussed measurements by the NA60 and CERES collaborations were carried out and analysed.

is found to be in agreement with a measurement in pp collisions extrapolated to Au-Au collisions using binary-collision scaling [87].
Both experiments find an excess of dielectron production in the mass region around the ρ mass that can be described by models including the broadening of the ρ resonance. This indicates that despite the factor of 10 higher energy in the centre of mass system of the collision the late stage of the collision shows the same features. However, the intermediate-mass region can be described using charm production cross-sections measured in small systems and scaling with the number of binary collisions, indicating no additional contribution. This is addressed in the case of the PHENIX measurement. Assuming an interaction of the heavy quarks with the QGP medium produced it should be expected that the energy loss is accompanied by a deflection of the quark in the medium which would result in a decorrelation of the final state particles, in this case, the electrons. To investigate this effect, the charm contribution is constructed by randomly sampling the direction for both electrons of the pair while conserving a realistic p_{T} distribution based on the measurement of electrons from heavy-flavour decays [87]. This leads to a reduction of the yield in the expected contribution to about 60% in the case without any modification. As both scenarios represent an extreme case the truth should be somewhere between.

3.3 It's getting hot in here – LHC

Moving up another order of magnitude in $\sqrt{s_{\mathrm{NN}}}$ from RHIC to the LHC, one would expect the situation to become even more complicated regarding the analysis of dielectron production. While it is expected that the medium produced in the collisions is hotter and longer lived at the LHC [88] it is also expected that the charm cross-section grows by one order of magnitude as predicted by calculations [47, 48] and confirmed by ALICE measurements [49]. The measurements of dielectron production in the kinematic range relevant to the study of thermal radiation from a hot medium formed in the ultra-relativistic collisions of Pb nuclei at the LHC are solely carried out by the ALICE collaboration. The ATLAS[2] [89] and CMS[3] [90] detectors are not able to measure leptons in the p_{T} range of a few hundred MeV/c, while the LHCb [91] experiment could in principle measure electrons and muons in the relevant range. However, the tracking of LHCb in the current setup is limited to peripheral Pb–Pb collisions.

[2] A Toroidal LHC ApparatuS
[3] Compact Muon Spectrometer

In the following, the approach in ALICE concerning the description of the charm backgrounds is discussed. In the previous sections, two different approaches were described. The NA60 collaboration used a topological separation using the finite decay length of the open heavy flavour mesons. Lacking the vertexing capabilities of the NA60 detector the STAR and PHENIX collaborations relied on a description of the charm background using measured cross-sections in small systems scaled by $\langle N_{\mathrm{coll}} \rangle$. In ALICE both approaches are found and will be discussed in the following.

The first measurements of dielectron production from the ALICE collaboration were performed in pp collisions at $\sqrt{s} = 7$ and 13 TeV [92, 93]. In both analyses, the $\sigma_{\mathrm{c\bar{c}}}$ cross-section was measured by parameterising the two-dimensional m_{ee}-$p_{\mathrm{T,ee}}$ spectrum in the mass region of $1.1 < m_{\mathrm{ee}} < 2.7$ GeV/c^2. In addition to the analysis in m_{ee} and $p_{\mathrm{T,ee}}$ a second analysis was carried out in the 7 TeV data following the idea of the weighted dimuon offset used by NA60. The ALICE measurement uses the sum of the distance-of-closest approach to the primary vertex of both tracks forming the pair ($\mathrm{DCA_{ee}}$). A fit using the observable in the IMR gives consistent results with the cross sections extracted in the m_{ee}-$p_{\mathrm{T,ee}}$ analysis. The $\mathrm{DCA_{ee}}$ distribution in the low mass region is shown in Fig. 3.5 (left). The upper panel shows the data compared to templates of the $\mathrm{DCA_{ee}}$ distributions of light-flavour, charm and beauty. In this case, the charm and beauty cross sections are normalised to independent measurements of the cross-sections as done by STAR and PHENIX before. A good description of the data is possible using all three contributions, which is indicated by the pulls of the template sum and the data points shown in the lower panel.

This figure demonstrates the possibility of separating heavy-flavour decay contributions from contributions that stem directly from the interaction point like the light-flavour decays, but also a possible thermal source. A third measurement was performed on a dataset of pp collisions at $\sqrt{s} = 5.02$ TeV taken in particular as a reference for the Pb–Pb data-taking campaigns at the same energy. In the analysis the extraction of the heavy-flavour cross sections was again performed using a two-dimensional parameterisation of the m_{ee}-$p_{\mathrm{T,ee}}$ distribution in the mass range $1.1 < m_{\mathrm{ee}} < 2.7$ GeV/c^2. The result is shown in Fig. 3.5 (right) as a function of m_{ee}. The data are compared to two different cocktail sums. One is based on the PYTHIA [94], the other on the POWHEG [95–98] event generator coupled to the shower algorithm of PYTHIA. While the contributions of charm and beauty are different depending on the used generator (driven by the different $p_{\mathrm{T,ee}}$ distributions) the sum of both describes the data equally well for each generator.

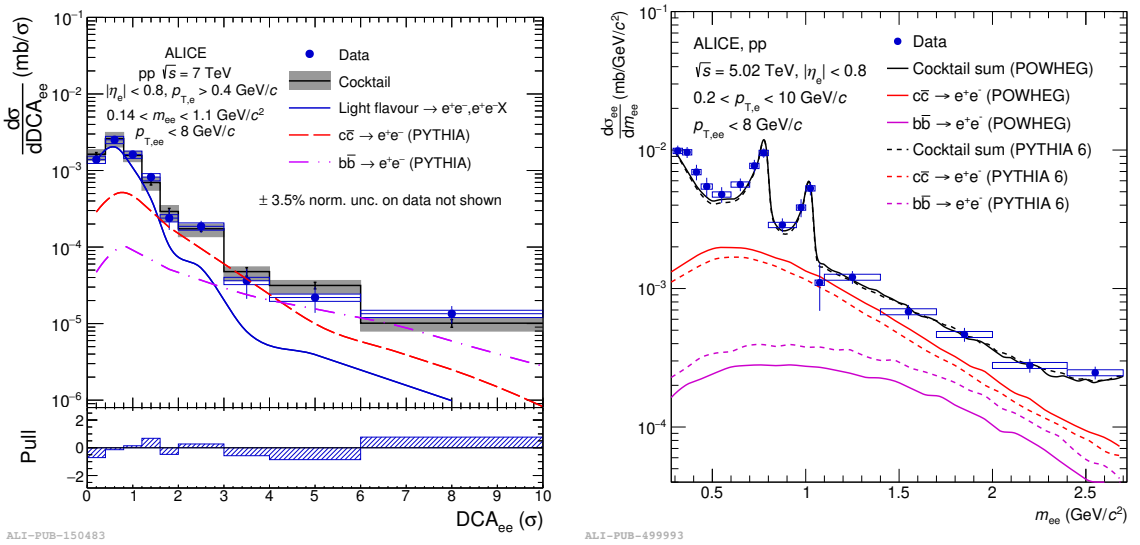

Figure 3.5.: Dielectron production cross section as a function of $\mathrm{DCA_{ee}}$ measured in pp collisions at $\sqrt{s} = 7$ TeV in the $0.14 < m_{\mathrm{ee}} < 1.1$ GeV/c^2 mass range (left) compared to expected contributions and as a function of m_{ee} measured in pp collisions at $\sqrt{s} = 5.02$ TeV after a two-dimensional parameterisation of the IMR with heavy-flavour contributions based on PYTHIA [94] and POWHEG [95–98].

The cross-sections extracted in the 5.02 TeV pp analysis were then used to construct a charm and beauty contribution for the measurement of dielectron production in central Pb–Pb collisions [99]. The dielectron yield as a function of m_{ee} measured in the 10% most central Pb–Pb collisions at $\sqrt{s_{\mathrm{NN}}} = 5.02$ TeV is shown in Fig. 3.6 (left).

The data are compared to several different cocktail assumptions. Cocktail1 includes the contributions from the light-flavour hadron decays and the J/ψ. The charm and beauty contributions are based on the measurements of the respective cross sections for dielectrons in pp collisions at $\sqrt{s} = 5.02$ TeV as described above. The advantage of using directly the measurement of dielectrons is that uncertainties on the fragmentation functions of heavy quarks to hadrons and their branching ratios into electrons can be omitted under the assumption they are unchanged from pp to Pb–Pb collisions. This way the only uncertainty entering is the one of the measurement itself as well as the uncertainty of $\langle N_{\mathrm{coll}} \rangle$ used for the scaling. Cocktail1 is shown as a solid blue line with a light blue band indicating the uncertainty. A second cocktail (cocktail2) calculation indicated by the black dashed line includes expected modifications of the heavy-flavour contributions related to the suppression of the charm and beauty production due to cold nuclear matter effects as well as energy loss of the heavy quarks when traversing the hot medium. For this the

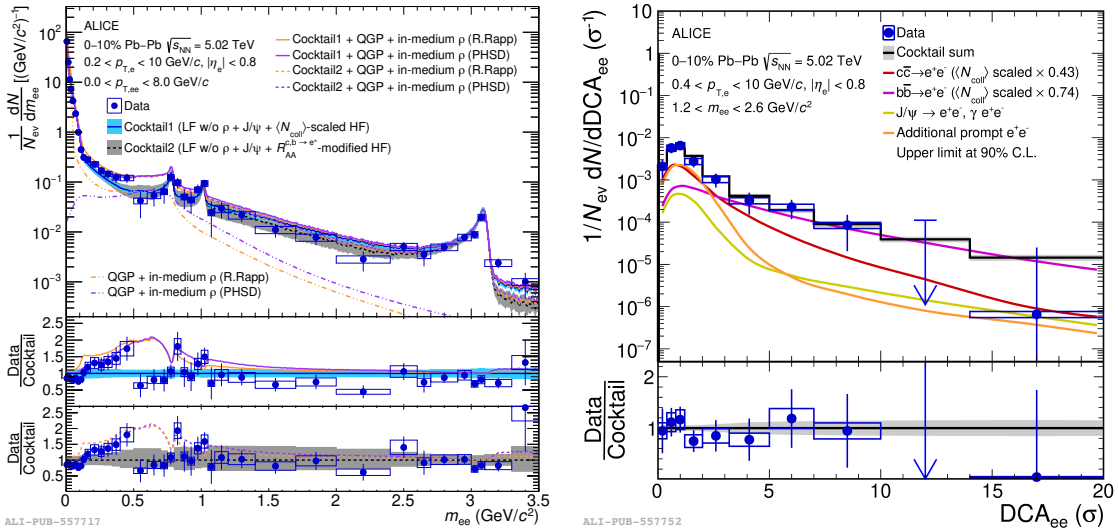

Figure 3.6.: Dielectron yield as a function of m_{ee} measured in the 10% most central Pb–Pb collisions at $\sqrt{s_{NN}} = 5.02$ TeV compared to the expectations of known hadronic decays (left), including two estimations of the heavy flavour contributions as well as two predictions for thermal radiation. The parameterisation of the inclusive dielectron yield as a function of DCA_{ee} in the $1.2 < m_{ee} < 2.6$ GeV/c^2 mass range (right).

measured heavy-flavour electron nuclear modification factor $R_{AA}^{c,b\to e}$ [100] is used together with the expected suppression of the HF production based on the EPS09 nuclear PDF [58]. The single electron modification is propagated to the dielectron pair level using a MC simulation. The uncertainties of the measured $R_{AA}^{c,b\to e}$ as well as the CNM parameterisation are propagated as well and indicated as the grey band. The two bottom panels of Fig. 3.6 show the ratio of the data to the two different cocktail calculations. In addition to the cocktail contributions two model calculations of thermal radiation from hadronic matter are shown and compared to the data. One model is based on the expanding fireball model by R. Rapp [69, 101], the other on the Parton-Hadron-String-Dynamics model (PHSD) [102]. Both models include an enhanced thermal production and broadening of the ρ meson. As expected the modification of the heavy-flavour contributions by including the energy-loss and CNM effects enlarges the uncertainties significantly, however, especially in the intermediate-mass region the description of the data improves. The large uncertainties limit any further interpretation of the data in the mass region beyond the ϕ-meson. In the mass region below 0.5 GeV/c^2 the data show a hint of an excess with a significance of about 2 σ that is described by both model calculations. No strong conclusions can be drawn.

An alternative approach to studying an additional thermal source in the intermediate-mass range is presented in Fig. 3.6 (right). Here, the dielectron production in the mass range of $1.2 < m_{\mathrm{ee}} < 2.6$ GeV/c^2 is shown as a function of $\mathrm{DCA}_{\mathrm{ee}}$. In addition to the data, the contributions of charm, beauty, J/ψ and an additional prompt contribution are shown, as well as the sum of all three. As the shapes in $\mathrm{DCA}_{\mathrm{ee}}$ are mainly sensitive to the decay length of the source, the systematic uncertainties are small compared to the cocktails in the mass analysis. The normalisation of the single contributions (except the J/ψ) is based on a parameterisation of the data. The best parameterisation is achieved with a charm contribution that is scaled to 43% of the yield expected from N_{coll} scaling and the beauty to 73%. This is consistent with the expectation that both heavy-flavour contributions are suppressed with a stronger suppression in the charm sector. In addition to the heavy-flavour contributions the minimum χ^2 of the parameterisation is achieved by including an additional prompt source that can be interpreted as thermal radiation from the QGP. It should be mentioned that, while the systematic uncertainties of this measurement can be reduced to about 10%, the statistical uncertainties for the charm and prompt contributions are 100%, which means a similar description of the data can be achieved without an additional prompt source. It should be underlined that the reduction of systematic uncertainties can be seen as a milestone for these measurements at the LHC. A statistical limitation can be overcome by taking more data, this is not the case for the systematic limitation.

As illustrated in the above discussion a clear understanding of the contribution of dielectrons from heavy heavy-flavour hadron decays is crucial for the measurement of thermal radiation from the early phases of ultra-relativistic heavy-ion collisions. One of the pieces to the puzzle are the modification of the heavy-flavour production cross sections by CNM effects and how they propagate to the dielectron spectrum. The presented thesis tries to contribute to the understanding of this by investigating the production of dielectrons in p–Pb collisions at $\sqrt{s_{\mathrm{NN}}} = 5.02$ TeV. The expectation is, that no additional thermal source is present in the small system, however, the CNM effects are present in the Pb nucleus.

Chapter 4

The Large Hadron Collider at CERN

Founded in 1954, the European Center for Nuclear Research (CERN) is the largest nuclear and particle physics laboratory in the world and houses the Large Hadron Collider (LHC). The LHC with a length of about 27 km was constructed in the prior existing tunnel of the Large Electron-Positron collider (LEP) and is the last accelerator and collider in a chain as shown in Fig. 4.1. In the LHC, different species of nuclei can be brought to collision that start their journey in the two linear accelerators LINAC 3 and LINAC 4 depending on the species. LINAC 3 is a special accelerator for heavier ions, while LINAC 4 and its predecessor LINAC 2 are responsible for the acceleration of protons[1]. In the case of the protons they transition from the linear accelerator into the proton synchrotron booster to be accelerated to up to 2.0 GeV before the injection into the proton synchrotron (PS). Heavier nuclei such as lead, but also xenon or oxygen that start their journey in LINAC 3 are first injected into the low energy ion ring (LEIR) where the Pb ions are accelerated and the beam is shaped into bunches before their injection into the PS. After further acceleration the final stage of the detector complex before the LHC is the Super Proton Synchrotron (SPS). While it serves as a pre-accelerator for the LHC, the SPS can also deliver proton beams of up to 450 MeV or heavy ions at lower energies according to the charge/mass ratio to the experiments in the experimental caverns of the North Area. The last stage of the accelerator complex is the 27 km long LHC, with a maximum energy for protons of 7 TeV. The energy of a nucleon in a Pb ion

[1]The acceleration in LINAC 4 is done with negatively charged hydrogen H^- which is then stripped of the electrons in the next acceleration stages.

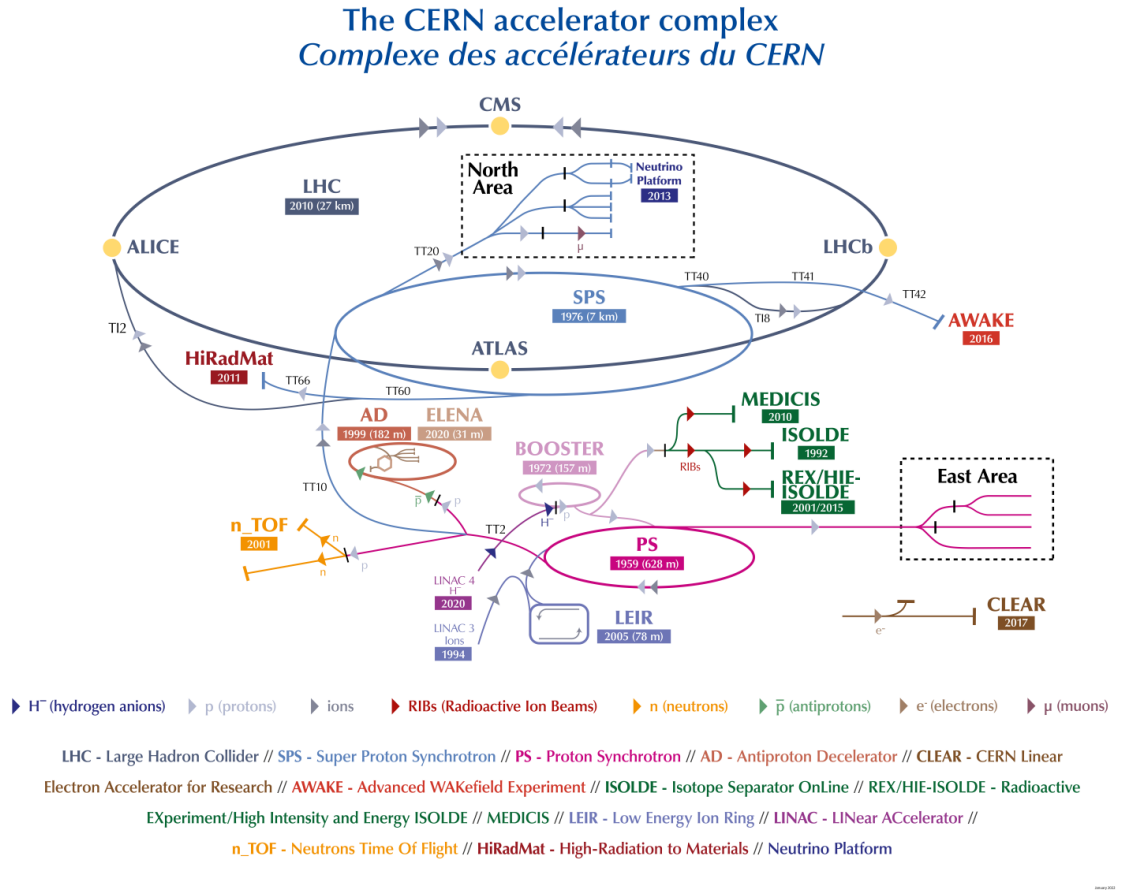

Figure 4.1.: The CERN accelerator complex

in the beam is then given by 7 TeV * 82/208 ≈ 2.75 TeV. As this is the energy of one of the 208 nucleons in the ion the total energy is about 574 TeV. The energy to which the particles can be accelerated is limited by the radius of the LHC. To steer the protons and ions and keep them from colliding with the accelerator strong magnetic dipole fields are required. The LHC dipole magnets are superconducting magnets that are operated at 1.9 K and provide a magnetic field of 8.3 T. In addition to the dipole magnets the LHC contains higher-order magnets such as quadrupole, and sextupole magnets for the transverse and longitudinal focusing of the beams.

In the procedure of filling the LHC, the particles are not injected in a continuous beam, but in packets or bunches that circulate in two separated tubes. The beams are then crossed at four interaction points to bring the circulating bunches to collisions that can be recorded by the installed experiments. Overall there are eight experiments installed that record the particles that are produced in the collisions. Two smaller specialised experiments to search for physics beyond the standard

model are MoEDAL [103], designed to measure highly ionising particles that might be related to magnetic monopoles, and FASER [104] searching for new elementary particles that are light and weakly coupled as well as the measurement of high energy neutrinos. The TOTEM [105] collaboration is a dedicated experiment to measure the full cross-section of pp collisions as well as the inner structure of the proton while the LHCf experiment [106] wants to use the collisions at LHC to better understand the production in the interaction of high-energy cosmic rays with the earth's atmosphere. All four experiments are placed away from the nominal interaction points and measure the produced particles in forward directions.
Four other large-scale multi-purpose detectors are installed at the nominal interaction points of the collider. Probably the two most famous after their discovery of the Higgs boson [107–114] are the ATLAS [89] and CMS [90] experiments. After the discovery of the particle, the experiments are still measuring the particle and its coupling to better understand the standard model of particle physics, while at the same time searching for possible indications for physics beyond the standard model, mainly connected to searches for new particles [115,116]. A slightly different approach is taken by the LHCb experiment [91] which is specialised in the measurement of the precise decays of heavy flavour hadrons like B and D mesons. In the precise measurement of, for example, the decay branching ratios and comparison with theory, the experiment could be sensitive to interference from BSM particles that would alter the branching ratios.
The last of the big four experiments is the ALICE [117] detector which is designed in particular for the precise characterisation of Pb-Pb collisions at LHC energies. The design is chosen to provide excellent particle tracking and identification down to very low momenta in an environment of several thousand particles that are produced in a single collision.

4.1 A large Ion collider Experiment - ALICE

The layout of the ALICE experiment is shown with all its detector systems in Fig. 4.2. The experiment consists of two parts: the so-called central barrel is housed inside the L3 magnet (3) that provides measurements of identified particles at mid rapidity and the muon spectrometer at forward rapidity. The muon spectrometer [118, 119] consists of a hadron absorber (11) made from carbon followed by a set of tracking stations (12). To determine the momentum of the measured tracks a dipole magnet is installed delivering a nominal field of 0.7 T. A muon trigger (14)

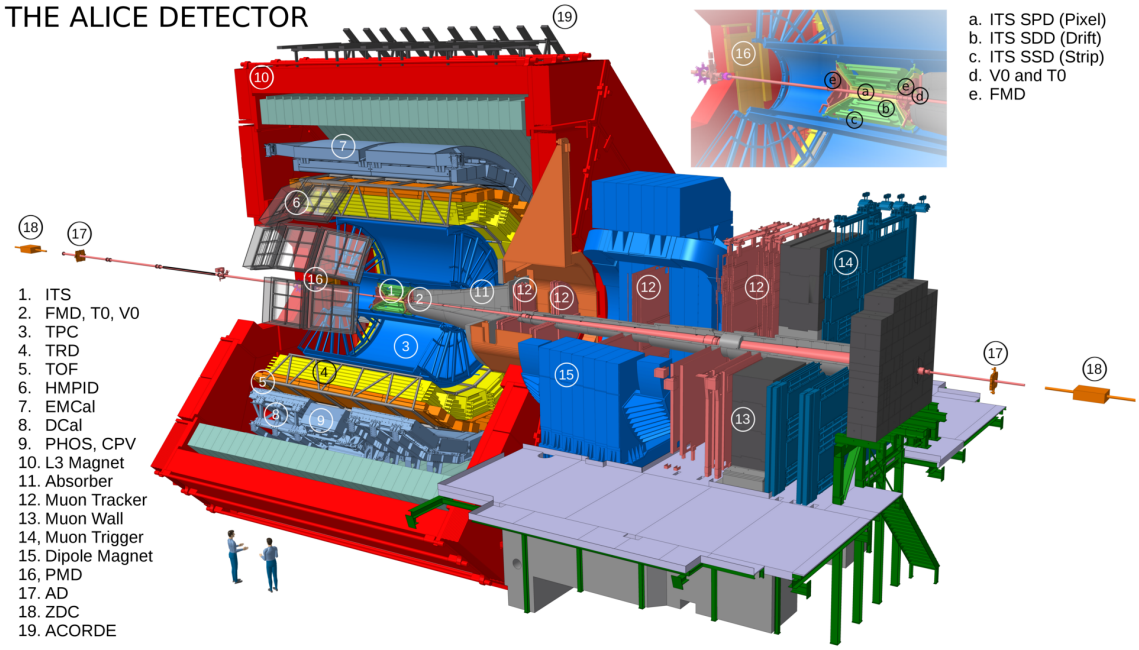

Figure 4.2.: The ALICE detector system with its subdetectors during the Run 2 data-taking. The inlay on the top right shows a zoom-in of the inner part of the detector.

is operated behind an additional absorption wall (13). The main focus of the muon system is the measurement of quarkonia states in the dimuon channel.

The innermost detectors in the central barrel are the inner tracking system (ITS) (1) and the forward detectors, the forward multiplicity detector (FMD), the T0 and the V0 [120] (2). The ITS is a six-layer silicone tracking detector specialised in the reconstruction of the primary vertex of the occurring collisions as well as the measurement of decays of weak decays see 4.1.1. The forward detectors provide additional information on the event properties like the timing information (T0) or the multiplicity (FMD, V0) in different rapidity ranges.

Moving outwards the ITS is followed by the time projection chamber (TPC) [121] (3) and then the transition radiation detector (TRD) [122] (4). The large gas-filled TPC provides excellent tracking and particle identification information via the measurement of $\mathrm{d}E/\mathrm{d}x$ (see Sec 4.1.2) while the TRD is supposed to extend the electron-pion separation that is deteriorating in the TPC's $\mathrm{d}E/\mathrm{d}x$ measurement at high momenta. This way the measurement of quarkonia can be performed in the dielectron channel and extended to larger momenta. Additional information to identify particles is provided by the time-of-flight [123, 124] (5), see Sec. 4.1.3. Particle identification at a limited rapidity, but at high momenta can be performed by the high momentum PID (HMPID) [125] detector. The proximity-focusing RICH

detector covers about 5% of the ALICE acceptance and provides π/K and K/p separation up to 3 and 5 GeV/c respectively.
The outermost detectors in the central barrel are the electromagnetic calorimeters EMCal (7) [126], DCal (8) [127] and PHOS (9) [128]. The EMCal and the DCal are two Shashlik-style lead-scintillator calorimeters that cover independent regions in the azimuth at midrapidity as shown in Fig. 4.2. Their main task is the measurement of high-energy photons and electrons to study jet-quenching in heavy-ion collisions or to reconstruct mesons at high momenta that can be used to study the fragmentation of quarks in vacuum. Since the energy resolution of these calorimeters is limited in addition the PbW-glass based PHOS is installed covering a small area. It provides measurements of highly energetic photons with a better resolution as the EMCal and Dcal. Due to the setup on opposite azimuthal areas, the detectors can be used to study dijet events.
Surrounding the full central barrel is the L3 magnet which provides a 0.5 T magnetic field to bend the charged tracks inside it. This way by measuring the curvature of the tracks, their momentum can be determined. On top of the magnet, the cosmic ray detector ACORDE (19) is installed providing a trigger for cosmic rays used for the detector alignment. In the far forward/backward direction, at 17 and 19.5 m, respectively, the ALICE diffractive detectors AD [129] (17) are installed. The two scintillators are used to trigger diffractive events. Further away from the interaction point at $\pm$112.5 m the two zero-degree calorimeters ZDC (18) [130] are installed. They measure the collision centrality via the measurement of non-interacting fragments of the heavy-ion collision and monitor the luminosity.
With all the different detector system ALICE is equipped to carry out a versatile physics program. In the following the detectors most relevant for the analysis presented in this thesis will be discussed in more detail.

4.1.1 The Inner Tracking System

The detector system closest to the interaction point is the Inner Tracking System (ITS), which consists of six layers of silicon detectors. The ITS covers the pseudo-rapidity range of $|\eta| < 0.9$, while the innermost layers extend to almost $|\eta| < 2$ to provide measurements of the charged particle density over a broader range. The ITS uses three different technologies [117]. The two innermost layers are based on hybrid silicon pixels called the Silicon Pixel Detector (SPD). The primary task of the SPD is the determination of the position of the primary collision vertex as well

as the measurement of the impact parameters of tracks originating in the decays of heavy-flavour and strange hadrons [131]. For this purpose, the detector is placed as close as possible to the interaction point (IP) where the charged particle density is the highest, which again requires the highest spatial resolution of the active elements (pixels) of the detector. A summary of the dimensions and the parameters of the different layers is presented in Tab.4.1. The two middle layers of the ITS are the silicon drift detector (SDD) and the two outer layers are based on silicon strip detectors (SSD). The four outer detector layers are equipped with analogue readout which gives them the possibility to measure the specific energy loss ($\mathrm{d}E/\mathrm{d}x$) of particles in the detector material.

		Spatial pos. (cm)		Spatial res. (μm)		
Layer	Type	r	$\pm z$	$r\varphi$	z	X_0 (%)
1	SPD	3.9	14.1	12	100	1.14
2	SPD	7.6	14.1	12	100	1.14 (+0.52)
3	SDD	15.0	22.2	35	25	1.13 (+0.25)
4	SDD	23.9	29.7	35	25	1.26
5	SSD	38.0	43.1	20	830	0.83 (+0.53)
6	SSD	43.0	48.9	20	830	0.86

Table 4.1.: Dimensions of the ITS and parameters of the six layers [117, 132]. The material budget in parenthesis corresponds to support structures and thermal shielding.

To minimise the impact of multiple scattering of charged particles in the detector the material budget of each layer was kept as low as possible. The radiation length per layer is listed in Tab. 4.1. The values in parenthesis account for additional material from thermal shielding and support structures. A total material budget of 7.26% X_0 could be reached for tracks traversing the detector perpendicular in the azimuthal. Due to the ITS, the measurement of the impact parameter of secondary tracks is possible with a precision better than 100 μm for tracks with $p_{\mathrm{T}} > 1$ GeV/c. Additionally, the p_{T} resolution including the ITS can be improved to be less than 2%.

4.1.2 The Time Projection Chamber

The main purposes of the time projection chamber are the tracking of charged particles traversing it and to provide information to identify the particle species [133]. While traversing the detector a charged particle will ionise the gas inside the detector and create electron-ion pairs along its trajectory. Due to the application of

an external electric field, electrons will then drift towards the readout chambers. Here they are amplified and registered. By connecting the signals of many primary electrons the trajectory of the primary particle can be reconstructed. The drift chamber of the ALICE experiment is a 5 m long cylindrical drift chamber with an inner radius of 0.85 and an outer radius of 2.5 m for the active volume. Overall, the detector's active volume is 88 m^3. The layout of the detector is shown in Fig. 4.3. The volume is separated in the middle by the central high-voltage electrode which

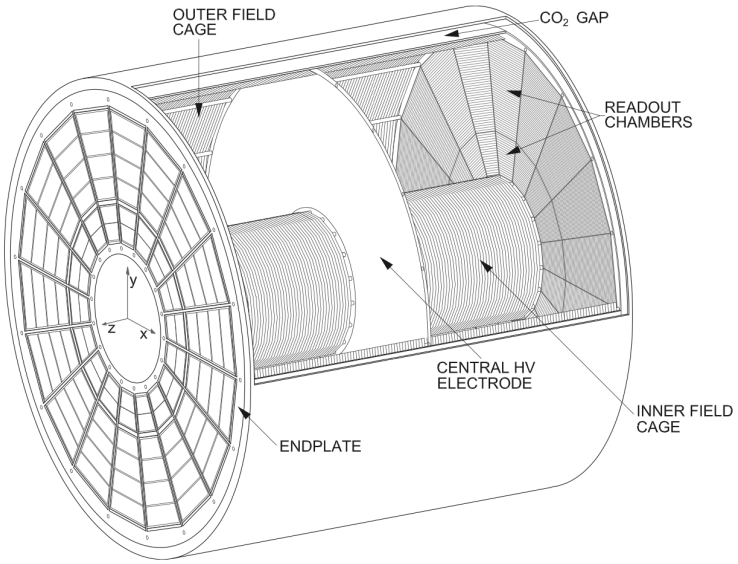

Figure 4.3.: Specific energy loss of charged particles in the ALICE TPC as a function of momentum. The data was recorded in pp collisions at $\sqrt{s} = 13$ TeV with a magnetic field of 0.2 T.

provides a voltage of 100 kV that results in a drift field of 400 V/cm that points outwards to the readout chambers. The inner and outer field cage guarantees a homogeneous field over the whole length. The amplification and registration are realised with multi-wire proportional chambers (MWPC). In the ALICE setup, the reconstruction of the primary electrons gives information about the transverse trajectory of the charged particle. The choice of the a high drift field however leads to a constant drift velocity due to a balance of the acceleration of the primary electron by the field and interactions with the gas in the active volume. The arrival time of the primary electron in the MWPCs is then used to estimate the length of the drift in the gas volume, allowing to reconstruct the three-dimensional trajectory of the charged particle. Applying an external magnetic field leads to a curved trajectory of the charged particles relative to their momentum. This means that by measuring the trajectory of the particle, its momentum can be measured by determining the

curvature. The geometry of the readout planes in the ALICE TPC was chosen to cope with charged-particle densities of up to several thousand tracks in the active volume. One important limitation of the TPC should be mentioned. The amplification of the primary electrons ($\mathcal{O}(10000)$) also produces positively-charged ions in the MWPCs. Without any measures, these ions would drift back into the active volume of the TPC — the so-called ion backflow (IBF). A local accumulation of positively charged ions in the active volume would lead to a distortion of the drift field and leading to a deflection of the primary electrons. To suppress the IBF, the MWPCs are equipped with a layer of wires that can be set to alternating potentials, so field lines will all end on the wires. When closed, this so-called gating grid will prevent ions from drifting into the active volume and primary electrons entering the MWPCs. As the ion drift velocity is much slower than that of the electrons, the operation of the MWPCs with a gating grid limits the detector's readout rate significantly.

In addition to the particle trajectory also the absolute charge that is registered in the readout is used. Taking into account the known amplification of the primary electrons in the MWPCs this is directly connected to the number of primary ionisations along the trajectory which is proportional to the specific energy loss per unit length ($\mathrm{d}E/\mathrm{d}x$) of the charged particle in the gas.

The specific energy loss is described by the Bethe-Bloch formula [134]

$$\frac{\mathrm{d}E}{\mathrm{d}x} = \frac{4\pi N e^4}{mc^2}\frac{z^2}{\beta^2}\left[\ln\frac{\sqrt{2mc^2E_{\max}}\beta\gamma}{I} - \frac{\beta^2}{2} - \frac{\delta(\beta)}{2}\right], \tag{4.1}$$

with N denoting the number density of electrons in the given gas, the elementary charge e, mc^2 the electron energy at rest, the speed of light c, the charge of the traversing particle z, the velocity relative to the speed of light β with $\gamma = \sqrt{1/(1-\beta^2)}$, and I the ionization energy of the gas. The average excitation energy I is a gas property and needs to be estimated empirically. An additional correction term that depends on the medium and takes into account medium polarisation and screening effects is given by $\delta(\beta)$. The $E_{\max}$ is a cut-off energy. Processes above the threshold are statistically not relevant due to the small probability of occurrence. Equation 4.1 is valid for $\beta\gamma$ in the range of $E_{\max}$ is smaller than the knimatic limit and $\gamma^2 \gg E_{\max}/mc^2$. By introducing $E_{\max}$ the equation becomes solely dependent on the velocity of the particle and holds for electrons and heavier particles. In the

ALICE experiment a parameterisation of equation 4.1 is used following the ALEPH collaboration

$$f(\beta\gamma) = \frac{P_1}{\beta^{P_4}\left(P_2 - \beta^{P_4} - \ln\left(P_3 + \frac{1}{(\beta\gamma)^{P_5}}\right)\right)}, \tag{4.2}$$

with five free parameters P_i. This parameterisation is performed on the measured particles as a function of $\beta\gamma$. To use the measured $\mathrm{d}E/\mathrm{d}x$ for particle identification additional information on the momentum is necessary as shown in Fig. 4.4 [3]. The

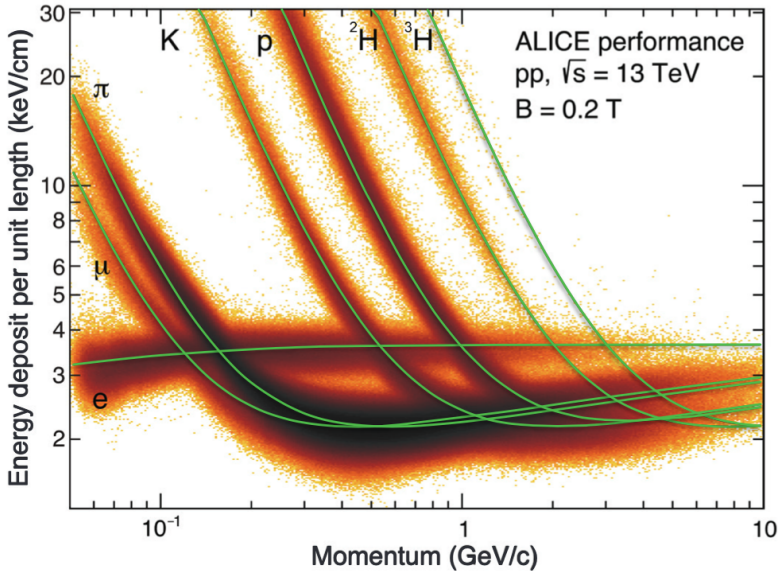

Figure 4.4.: Specific energy loss of charged particles in the ALICE TPC as a function of momentum. The data was recorded in pp collisions at $\sqrt{s} = 13$ TeV with a magnetic field of 0.2 T.

measured $\mathrm{d}E/\mathrm{d}x$ is shown for pp collisions at $\sqrt{s} = 13$ TeV and with operating the ALICE detector at a magnetic field of 0.2 T. As discussed above the energy loss depends on velocity so a separation of the particles depending on the respective mass shows when plotting the distribution as a function of the measured particle momentum. The parameterisation of Eq. 4.2 under different particle mass hypotheses is shown as the green lines. They correspond well with the measured bands, that are labeled with the respective particle hypothesis. Using the measured $\mathrm{d}E/\mathrm{d}x$, the momentum and particle hypothesis, a different representation that is simpler to handle in the analysis can be constructed. The so-called $n\sigma_{\mathrm{x}}$ distribution relates the expected specific energy loss for a given particle hypothesis x ($\mathrm{d}E/\mathrm{d}x_{\mathrm{x}}^{\mathrm{expc}}$) with

the measured $\mathrm{d}E/\mathrm{d}x^{\mathrm{meas}}$ in units of the width of the distribution determined by the parameterisation σ:

$$n\sigma_{\mathrm{x}}^{\mathrm{TPC}} = \frac{\mathrm{d}E/\mathrm{d}x_{\mathrm{x}}^{\mathrm{expc}} - \mathrm{d}E/\mathrm{d}x^{\mathrm{meas}}}{\sigma}. \tag{4.3}$$

This representation allows a more convenient selection of the desired particle in the analysis than using the direct measurement of the $\mathrm{d}E/\mathrm{d}x$.

4.1.3 The Time-Of-Flight Detector

The ALICE Time-Of-Flight (TOF) detector is based on Multi-Gap Resistive-Plate chambers (MRPC) with 10 gaps of 250 μm each. The main purpose of the detector is to provide information about the arrival time of the particles in the active volume (t_{TOF}). The TOF covers the range of $|\eta| < 0.9$ and the full azimuth. The detector is installed behind the TRD with an inner and outer radius of 370 and 399 cm, respectively [123, 124]. Due to its radial position tracks need at least a transverse momentum of 0.3 GeV/c to reach the detector. To calculate the velocity of the particle, in addition to the arrival time also the time at which the collision occurred, the start time or event time (t_{ev}) needs to be measured. Then together with the reconstructed track length the velocity can be calculated. Consisting of two arrays of Cherenkov counters, positioned at opposite sides of the interaction point (IP) at $-3.28 < \eta < -2.97$ and $4.61 < \eta < 4.92$, respectively, the T0 detector provides the start time for the TOF measurement (t_{ev}). In addition t_{ev} can be estimated using the arrival times of the particles at the TOF detector. A combinatorial algorithm compares the measured times in the TOF with the expected time of the tracks under the assumption of a common event time. For all possible combinations of masses ($m_{\mathrm{i}} = \pi, \mathrm{K}, \mathrm{p}$) the χ^2 is calculated for a given track by using all other n tracks

$$\chi^2 = \sum_{n_{\mathrm{tracks}}} \frac{((t_{\mathrm{TOF}} - t_{\mathrm{ev}}) - t_{\mathrm{exp}})^2}{\sigma_{\mathrm{TOF}}^2 + \sigma_{t_{\mathrm{exp}}}^2}. \tag{4.4}$$

The combination that gives the minimum χ^2 is used to determine t_{ev} for the respective track.

This algorithm can be used if at least three particles reach the TOF detector. Using it at a larger multiplicity can increase resolution and efficiency. The estimation of the start time in this manner is particularly useful for events in which the T0 signal is not present due to only a few particles reaching the T0 detector in low multiplicity events. If neither of these two methods is available, an average TOF start time for

the run is used instead [135]. If the signal generated in the TOF is matched with a reconstructed track, the track length together with the start and arrival time can be used to calculate the velocity of the particle. The velocity (β) is presented in Fig. 4.5 as a function of the particle's momentum.

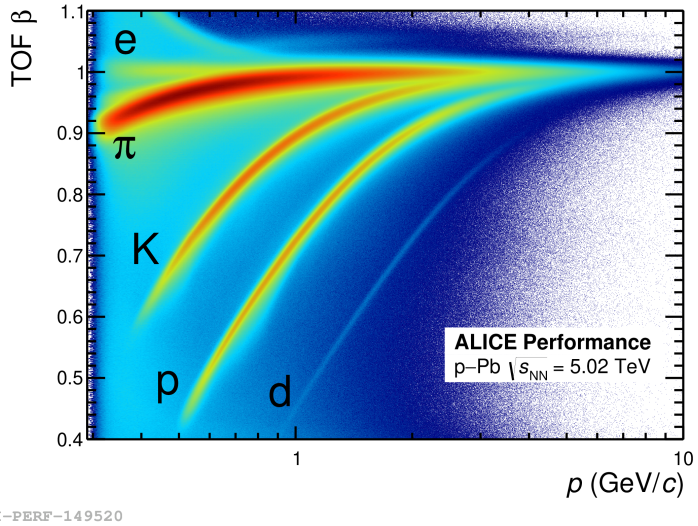

Figure 4.5.: Velocity β as a function of momentum of charged particles in the TOF measured in p–Pb collisions at $\sqrt{s_{\mathrm{NN}}} = 5.02$ TeV.

Similar to the TPC, the detector response can then be calculated in the $n\sigma$ representation:

$$n\sigma_{\mathrm{x}}^{\mathrm{TOF}} = \frac{t_{\mathrm{TOF}} - t_{\mathrm{ev}} - t_{\mathrm{exp}}(m_{\mathrm{x}}, p, L)}{\sigma_{\mathrm{tot}}(p, m_{\mathrm{x}}, t_{\mathrm{ev}})}. \tag{4.5}$$

With the arrival time measured in the TOF (t_{TOF}), the event or start time (t_{ev}), the expected time for a particle with a given momentum p, track length L under the mass hypothesis m_{x} and the total timing resolution $\sigma_{\mathrm{tot}}(p, m_{\mathrm{x}}, t_{\mathrm{ev}})$ which again depends on the particle hypothesis, the momentum, and the resolution of the start time. Especially the latter is affected by the availability of the estimators as discussed above. For low multiplicity, the value is about 80 ps and can improve down to 20 ps in Pb-Pb collisions. In case of no availability of the T0 or the time estimate from the TOF, the LHC clock information on the bunch crossings can be used. Here the resolution can be as high as 200 ps.

4.1.4 The V0 Detector

The ALICE V0 detector consists of two segmented plastic scintillator counters. The segmented discs as shown in Fig. 4.6 are placed at 340 cm (V0A) and -90 cm (V0C) covering a pseudo rapidity range of 2.8 to 5.1 and -1.7 to -3.7, respectively [120]. The detector system provides several functions. In Pb–Pb collisions the amplitude

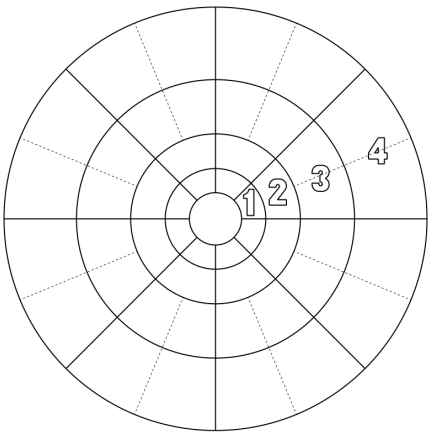

Figure 4.6.: Segmentation of the V0 discs.

measured in the detector can be directly related to the number of produced particles and such be used to determine the collision centrality. Due to its segmentation also an estimate of the orientation of the reaction plabe can be provided. In pp collisions, the detector can also be used for the estimation of the charged-particle multiplicity as well as a trigger on high multiplicity collisions. The placement of the detector at forward/backward rapidity limits the auto-correlation with multiplicity-dependent measurements performed at mid rapidity. In addition, the system can provide a fast trigger for the selection of inelastic pp events and veto asymmetric events, for example from beam-gas interactions.

Chapter 5

Analysis

In the following, the data analysis is described. Starting with a description of the data-taking conditions and the selection of collisions of interest to the details of the analysis concerning the identification of electrons and the extraction of the dielectron signal. Furthermore, the procedure to correct for inefficiencies introduced by all the selections is described and systematic biases are quantified. The last section of the chapter shows the construction of a baseline to compare with the measured spectra.

5.1 Description of the data set and the selected collisions

The data of interest in this analysis was recorded during the heavy-ion data-taking campaign of the LHC at the end of 2016. The running scenario was to collide a proton beam at 4 TeV with a lead beam at 2.76 TeV, resulting in a centre of mass energy of $\sqrt{s_{\mathrm{NN}}} = 5.02$ TeV. This asymmetry in the beam energies introduces a shift of the centre of mass rapidity $y_{CM} = 0.465$ wrt the laboratory frame.
Collision candidates were recorded in case a simultaneous signal in the two V0 scintillator arrays was registered. The used data set of the 2016 data-taking period has the speciality of consisting of two different trigger conditions in addition to the coincidence in the V0 detectors. In general, the collision data can only be recorded in case of all relevant detectors and their front-end electronic read-out (FERO) are able to process the data. In the data-taking campaigns after the year-end technical stop (YETS) of 2015 it was realised that the data acquisition rate was substantially reduced to the SDD FERO still processing events prior to the V0 coincidence while all other detectors were able to process a new event. In earlier data-taking periods,

the bottleneck was in the TPC readout. This was replaced in the YETS with the so-called read-out control unit 2 (RCU2) featuring a second data-detector link and thus a faster data acquisition rate than the previous model. While in the pp reference data-taking campaign of 2015, the lost data (all central detectors ready but SDD) would have been 2/3 of the data, in the 2016 p–Pb data taking it would have been 1/2. To mitigate this problem an additional trigger configuration was implemented, namely the 'fast' trigger. This trigger logic would record the data, in case of a V0 coincidence signal and all central barrel detectors in a READY state, except the SDD. The complementary trigger, with also the SDD present is called the `cent` trigger. To have the possibility to analyse the data, without running separate analyses, the data sample collected in the `cent` trigger was reconstructed in a second iteration in which the SDD signal was ignored, we call this reconstruction the `cent_woSDD`. This way the data collected and reconstructed in the `fast` and in the `cent_woSDD` samples should be equivalent in detector performance. The main disadvantage of not having the SDD information is that, on top of missing space points, it contains information on the specific energy loss. Losing the two potential $\mathrm{d}E/\mathrm{d}x$ measurements, the reconstruction software is not able to provide an estimation of the $\mathrm{d}E/\mathrm{d}x$ in the ITS. While the $\mathrm{d}E/\mathrm{d}x$ measurement of the ITS was used in previous measurements to reduce the hadron contamination of the electron sample [92], in this analysis it was not used in order to double the number of analysed events, while keeping the detector conditions the same over the whole analysed sample.

5.1.1 Event selection

In the first step to clean up the triggered events, and to reject collisions of beam particles with residual gas in the LHC vacuum, a centrally provided algorithm is used. It correlates signals of the forward detectors as well as the SPD while taking into account the central timing information of the LHC bunch crossings. Furthermore, to ensure optimal analysis conditions, events are selected on specific selection criteria. Triggered events, which did not get a primary vertex assigned are rejected, while the reconstructed vertex is required to be based on the information of the SPD. Asking for at least one contributor to the vertex fit in addition to the used information of the LHC beams poses a minimum requirement. To guarantee a homogeneous acceptance in the central barrel detectors, only events with a reconstructed vertex within ± 10 cm from the nominal collision point in the direction along the beam (z) are

considered for analysis. Events with multiple reconstructed vertices are discarded to reject possible pile-up events, in which more than one collision occurred. With these selection criteria, the analysed number of events is 274M in the `fast` data sample and 273M in the `cent_woSDD` sample.

5.1.2 Monte Carlo simulations

For this analysis centrally produced MC samples are used. These are based on two different event generators. The produced outputs of these are then used as an input for the GEANT 3 [136] software which transports them through the full ALICE geometry, produces secondary particles, and simulates hits in the sensitive areas of the detector. The generated hits are then used together with the full reconstruction software as it is used in the data to generate reconstructed Monte-Carlo samples. To best describe the conditions during the data taking, the state and performance of all detectors is mapped to the reconstruction, for example to account for single modules being switched off. For this analysis, two different central productions are used. A so-called general-purpose production based on the DPMJET-III event generator [137, 138] and a heavy-flavour enhanced production based on EPOS-LHC [139]. The DPMJET production is done in a 1:1 sampling and has 300M events based on the different trigger conditions of the detector.
For the enhancement of heavy flavour electrons in the EPOS-LHC MC an embedding technique is used. PYTHIA6 [94] events are generated until a certain condition is found, then the particles produced in this event are placed in the EPOS-LHC event. In the case of this particular production, we are interested in events containing electrons from charm and beauty quarks. The three different criteria that are employed are:

1. The event contains two electrons at $-1.2 < y < 1.2$ which stem from a $c\bar{c}$ pair. The charmed mesons are forced to decay semi-leptonically via the PYHTIA configuration.

2. The event contains two electrons at $-1.2 < y < 1.2$ which stem from a $b\bar{b}$ pair. The beauty mesons are forced to decay semi-leptonically via the PYHTIA configuration.

3. An electron at $-1.2 < y < 1.2$ is required which is the result of either a charmed or beauty meson decay.

The different event classes are sampled in a ratio of 1/1/3, respectively. In the last category of events, the decays of the heavy mesons are not forced to contain an electron. This is necessary to have decays of the type $B \rightarrow D \rightarrow e(e)$ in the final state possible. Otherwise, the purely hadronic decays of the B would be forbidden. A total of 50M events per trigger class were produced which amounts to about 100M events used for analysis.

5.2 Track selection and electron identification

This section will describe the approach that is used in this analysis to select tracks that are seen as good for the analysis. Furthermore, the approach of how to filter the tracks to arrive at a sample of electrons is explained.

5.2.1 Track selection

From all reconstructed tracks measured in the detector, only those that are of good reconstruction quality and that belong to particles created in the primary collision should be used for analysis. To ensure this, a set of track selection criteria is applied to all tracks. These criteria have been used in previous analyses and were proven useful. Since analysis is performed on the `analysis object data` format, or short AOD, minimal requirements were already applied to the reconstructed tracks. The AOD format is a product of filtering information from the original `event summary data` or ESD which contains the full information collected by the detectors but is not in every case necessary to perform analysis. In addition to the AOD filtering criteria in this analysis, tracks were required to contain the complete information from the ITS and the TPC that was matched to each other and considered in the inward and outward fitting of the Kalman filter. We refer to such tracks as global tracks. A refit of the ITS, as well as the TPC information, is required in addition. More specific requirements in the TPC are that the track has at least 80 space points that were used in the reconstruction of which not more than 40% should be shared with other reconstructed tracks. Furthermore, tracks are required to have crossed at least 100 pad rows, which serves as an additional length requirement of the track in the TPC. To take areas with no readout instrumentation (between neighbouring sectors) or segments in the readout chamber that are switched off into account the fraction of crossed rows with respect to findable clusters needs to be between 0.6 and 1.1. To reject bad fit results a minimum χ^2 per cluster of the track parameterisation

is required to be less than 4. In addition at least 3 hits in the ITS need to be associated with the track, of which one should be in the first layer of the SPD. The space points in the ITS can not be shared with other reconstructed tracks. The χ^2 per hit is not allowed to be larger than 5.5. On top of these detector-specific criteria, the tracks are required to be in a fiducial window of $p_{\mathrm{T}} > 0.2$ GeV/c and $|\eta| < 0.8$. Additionally, the tracks need to be as close as at least 1 cm (3 cm) to the reconstructed primary vertex in the xy-plane (beam direction) after propagating the measured track to the vertex. All selections on the tracks are summarised in Tab. 5.1.

Track observables	Selection requirement
Fiducial selection	
p_{T}	$p_{\mathrm{T}} > 0.2$ GeV/c
η	$\|\eta\| < 0.8$
ITS requirements	
ITS refit	yes
Number of clusters	≥ 3
χ^2 per cluster	≤ 5.5
No shared cluster	yes
Hit in the 1st layer	yes
DCA_{xy}	≤ 1 cm
DCA_{z}	≤ 3 cm
TPC requirements	
TPC refit	yes
Number of TPC clusters	≥ 80
Number of crossed rows	≥ 100
Ratio of crossed rows / findable clusters	≤ 0.6
Fraction of shared clusters	≤ 0.4
χ^2 per cluster	≤ 4.0

Table 5.1.: Track selection criteria in the ITS and TPC as well as the fiducial selection.

While most selections are in general to improve the track quality, two should be specially highlighted in their ability to suppress tracks that belong to particles which are not originating in the primary collision. The requirement of a hit in the very first sensitive detector layer, the SPD, should be sufficient to reject all particles that are produced beyond the first layer by the decay of neutral unstable particles or in the interaction with the detector material like the conversion of a photon into an $\mathrm{e}^+\mathrm{e}^-$ pair since these particles can not produce a hit in the first SPD layer. However, it is possible that either the tracking algorithm picks up a space point that was produced

by a primary particle, or the origin of the secondary track is the beam pipe, in which for example the photon conversion is possible. In both cases, rejecting tracks that share their clusters in the inner tracking system will suppress the contributions of conversions, or secondary tracks assigned hits from primary tracks. Additionally, the rejection of tracks that share clusters in the ITS suppresses the contributions from conversions. A conversion has a vanishing opening angle because the photon is massless. If the conversion happens in the inner layers of the ITS or the beam pipe there is a high chance that the electron and the positron will traverse the next layer of the tracker close to each other. As a consequence, the two particles produce only one cluster in the detector. Further bending of the tracks by the magnetic field would then split them up and they would produce clusters independently. The tracking algorithm will then reconstruct two tracks, but the first cluster will be shared between them.

5.2.2 Electron identification

This section explains the electron identification strategy in this analysis. The detectors used are the TPC and the TOF. Their complementary information is used to arrive at a high-purity electron sample while keeping the selection efficiency as high as possible. In addition to the selection procedure itself, also the calibration of the electron response of the TPC is explained.

5.2.2.1 Calibration of the TPC PID response

The main detector to select electrons in this analysis is the TPC. As described in Sec. 4.1.2 the particle identification does explicitly not use the measured specific energy loss. Instead the difference of the signal from the expected signal ($\langle \mathrm{d}E/\mathrm{d}x \rangle_{\mathrm{exp}}$) under a given mass hypothesis (i) to the measured signal ($\langle \mathrm{d}E/\mathrm{d}x \rangle_{\mathrm{meas}}$) normalised to the expected standard deviation (σ_i) is used:

$$n\sigma_i = \frac{\langle \mathrm{d}E/\mathrm{d}x \rangle_{\mathrm{meas}} - \langle \mathrm{d}E/\mathrm{d}x \rangle_{\mathrm{exp}}(i)}{\sigma(i)}. \tag{5.1}$$

A clean sample of a given particle species should then always be centred around 0, and distributed following a gaussian with a width of 1. In the Monte-Carlo simulations used for this analysis, the PID response is generated under exactly these assumptions. From experience it is however known that this is not necessarily true for electrons. To check the distribution and to calibrate for residual mismatches

between data and MC simulations a clean sample of electrons is needed. To generate a clean sample of electrons the decay topology is used to select electrons from conversions in the detector material. This is done with the so-called V0 finder, a centrally provided algorithm that selects pairs of particles that stem from decays of long-lived neutral particles. The algorithm is configured to specifically search for electrons from photon conversions in the detector material in front of the TPC. It is observed that this helps to generate clean samples of electrons for $p < 0.8$ GeV/c. For larger momenta, a sizable contamination of protons is observed. To suppress this contribution the information from the TOF was used. Only tracks that comply with the electron hypothesis in the TOF within $\pm 3\sigma$ were used for the TPC calibration. In the next step the distribution of the electrons as a function of $n\sigma_e$ is parameterised with a gaussian in intervals of pseudorapidity and the momentum as it is reconstructed at the inner wall of the TPC. Figure 5.1 shows two examples.

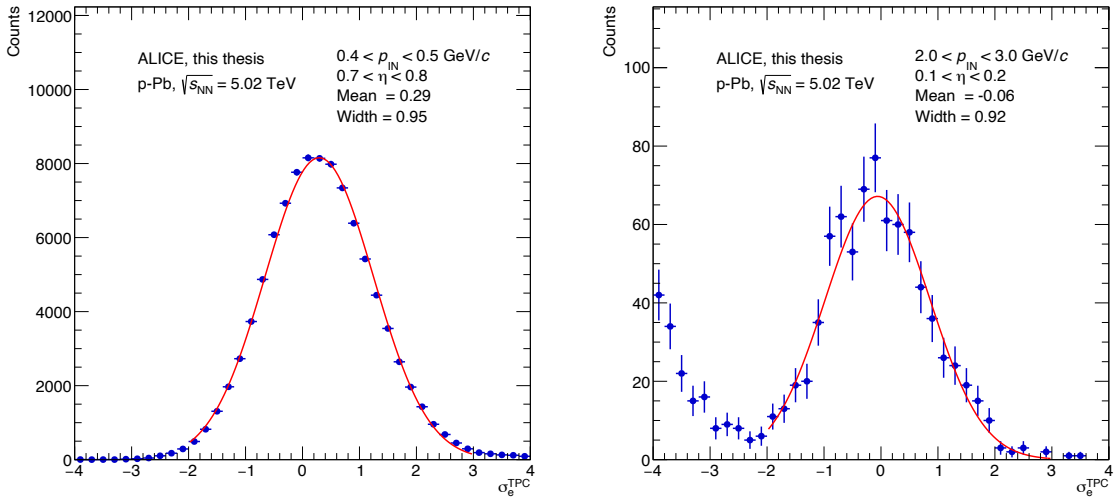

Figure 5.1.: Selection of electron candidates in $0.4 < p_{\mathrm{T}} < 0.5$ GeV/c and $0.7 < \eta < 0.8$ (left) as well as $2.0 < p_{\mathrm{T}} < 3.0$ GeV/c and $0.1 < \eta < 0.2$ (right). The number of candidates is shown as a function of the deviation from the expected electron signal in orders of standard deviations $n\sigma_{\mathrm{e}}$ in the TPC. Both distributions are parameterised with a normal distribution to extract the mean and width of the electron signal.

In Fig. 5.1 (left) the distribution of electrons is shown in the interval of $0.4 < p_{\mathrm{IN}} < 0.5$ GeV/c and $0.7 < \eta < 0.8$. A parameterisation based on a Gauss function is performed in the range of $-2 < \sigma_{\mathrm{e}}^{TPC} < 3$. The values extracted are a mean (μ) of 0.29 and a width (σ) of 0.95. The bias of this deviation from the nominal values ($\mu = 0$ and $\sigma = 1$) can be calculated by comparing the integrals of two Gauss functions in the region of $\pm 3\sigma$ and is about 5%. Fig. 5.1 (right) show the same

parameterisation for the $2.0 < p_{\mathrm{IN}} < 3.0$ GeV/c and $0.1 < \eta < 0.2$ interval. At negative $n\sigma$ values a rise of the distribution is observed. These entries observed at larger momenta are the reason the parameterisation is performed in the $[-2, 3]$ interval. The extracted values show that while the distribution is closer to the mean, it is also narrower than in the previous interval. The bias without recalibration is estimated to be about 8%. These parameterisations are performed for the full range of the measurement of $|\eta| < 0.8$ and up to a momentum of 10 GeV/c. The extracted values of mean and width as a function of p_{IN} and η are shown in Fig. 5.2 left and right, respectively.

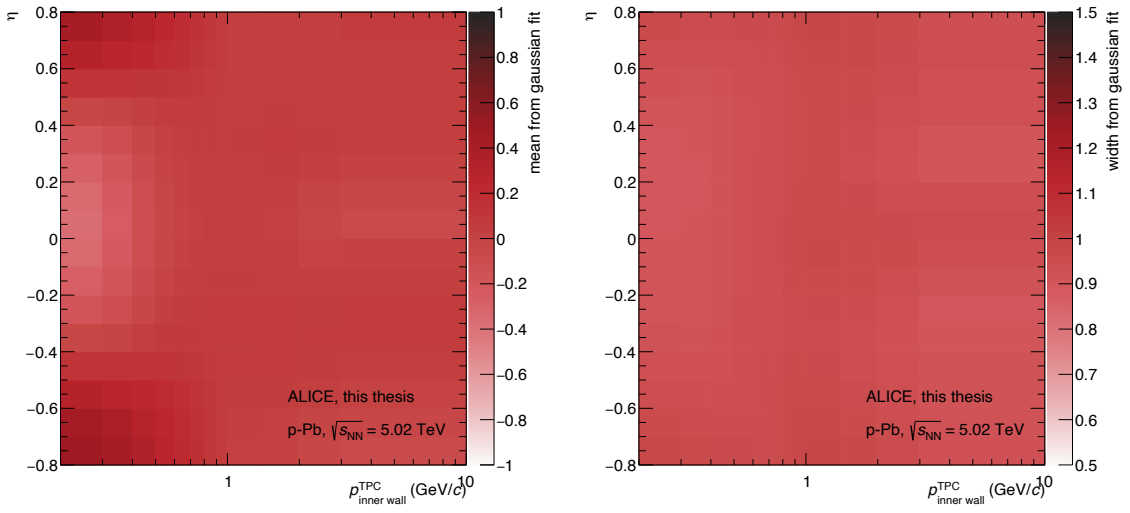

Figure 5.2.: Mean (left) and width (right) extracted from a parameterisation of the TPC particle identification response with a Gauss function as a function of the momentum at the inner wall of the TPC ($p^{\mathrm{TPC}}_{\text{inner wall}}$) and pseudorapidity ($\eta$). Electrons were selected based on the decay topology of photon conversions and the signal in the TOF.

It is observed that the main deviation of the mean is at low momenta. At midrapidity the values tend to be negative, while at the higher absolute values of η the values are positive. The total differences from 0 are up to 0.4. The width shows that the values are consistently smaller than unity and scatter around values of 0.9 over the measured range. The values in each interval are then used to recalibrate the PID response in data by:

$$n\sigma_{\mathrm{cal}} = \frac{n\sigma_{\mathrm{meas}} - \mu_{\mathrm{fit}}}{\sigma_{\mathrm{fit}}}. \tag{5.2}$$

With the PID response after calibration $n\sigma_{\mathrm{cal}}$, before calibration $n\sigma_{\mathrm{meas}}$, the mean and width from the parameterisation μ_{fit} and σ_{fit}. To validate the procedure the

correction was used on the same data sample and the correction maps were extracted in the same procedure.

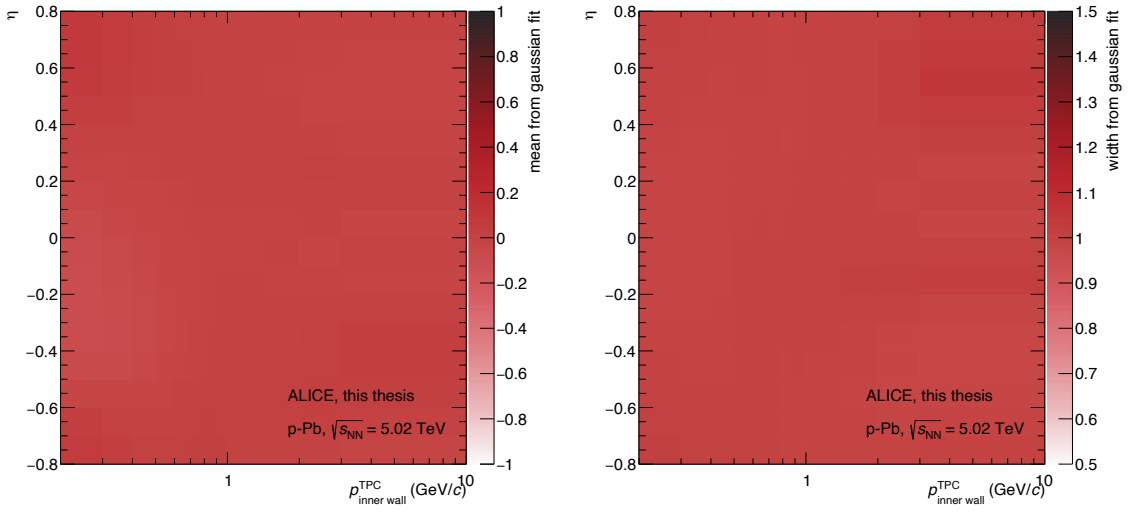

Figure 5.3.: Mean (left) and width (right) extracted from a parameterisation of the TPC particle identification response with a Gauss function as a function of the momentum at the inner wall of the TPC ($p^{\mathrm{TPC}}_{\mathrm{inner\ wall}}$) and pseudorapidity ($\eta$). Electrons were selected based on the decay topology of photon conversions and the signal in the TOF. A correction on the electron response of the TPC was applied as described in the text.

It is observed that overall there are no more structures in the mean visible as shown in Fig. 5.3 (left) and the value is at zero. In the case of the width shown in Fig. 5.3 (right) also a big improvement is observed. The values are at unity. However, some small deviations from unity can be observed in the highest momentum intervals. By construction, this should not be the case. However, the failure rate when rerunning the analysis was higher (6%) than when the initial correction was extracted (1.5%). While this is not expected to change the results in the intervals with many contributing electrons at higher momenta this can introduce statistical fluctuations. The calibration procedure is then used for the analysis of primary electrons.

5.2.2.2 Electron selection

Electrons are selected in the TPC and TOF based on complementary information provided by both detectors. The selection is applied to the detector particle identification response expressed as the number of standard deviations of the measured signal compared to the expected signal for a given particle species for the respective detector σ_i^{det} as a function of momentum. The PID response of TPC and TOF for the electron hypothesis are shown in Fig. 5.4 left and right, respectively.

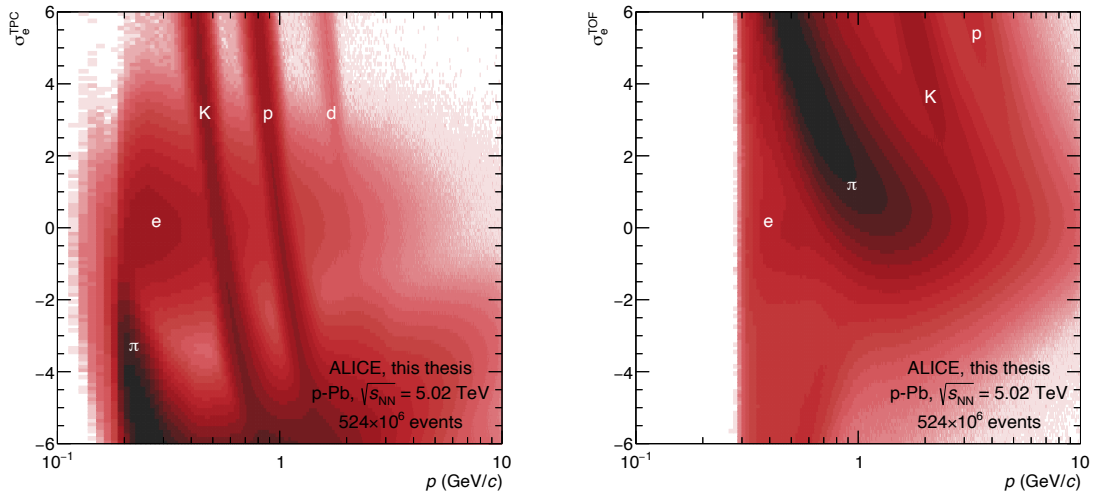

Figure 5.4.: Particle identification response for the TPC (left) and TOF (right) as a function of momentum p for the electron hypothesis.

In this representation of σ_e^{det} the electron mass hypothesis is used. Logically the difference between the measured signal in the detector and the expected signal for electrons then shifts the signal of real electrons to 0. Indicated in Fig. 5.4 are the different species (e,$\pi^{\pm}$,$K^{\pm}$,p and d in the TPC) as they are expected. While in the case of the TPC, the particles can be well identified and show distinctive bands the case in the TOF is not so clear. In the TPC however, the particle bands cross and an unambiguous identification of electrons is not possible. One possibility, that was used in the first ALICE publication [92] is to remove K and p in cases where a TOF signal is available and they are identified unambiguously. Due to inefficiencies this however can leave a significant contamination of hadrons in the analysis sample, which then leads to a deterioration of signal-to-background and significance since the hadronic contamination contributes to the background alone. In later analyses as well as this one a more sophisticated approach was chosen, that reduces the contamination, while not losing more electrons. The basic principle is, that two samples of pure electrons are selected in the TPC and the TOF. In the first sample, a clean electron sample is achieved by selecting electrons in the TPC and rejecting hadrons in the TPC. The PID response of this selection is shown in Fig. 5.6 left and right for the TPC and TOF, respectively.

While this approach gives a very clean electron sample with a high efficiency it has a clear disadvantage of introducing holes in the electron spectrum in the momentum region where K and p bands cross the electron band. To overcome this issue, a

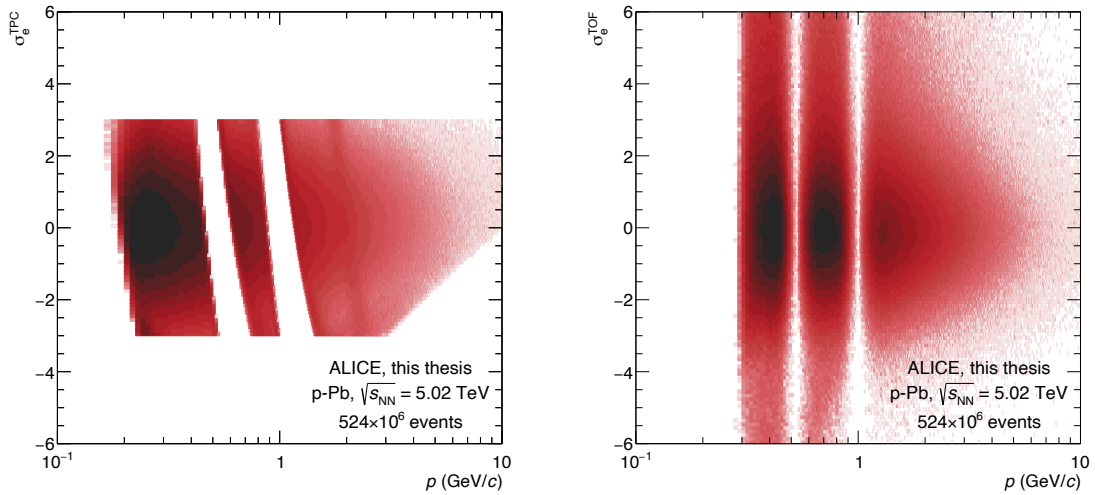

Figure 5.5.: Particle identification response for the TPC (left) and TOF (right) as a function of momentum p for the electron hypothesis. Electrons are selected in a $\pm 3\sigma$ interval in the TPC. Protons, Kaons, and Pions are rejected in the TPC.

second sample is generated in which the electrons are unambiguously identified in the TOF system. In this case, pions are rejected in the TPC, while K and p are rejected in the TOF. Electrons are then selected in the TPC and TOF as well. As shown in Fig. 5.5 a clean sample of electrons which have an associated signal in the TOF can be achieved. This approach has the disadvantage that the selection efficiency drops due to a lower matching efficiency of the tracks to the TOF hits. The exact selection criteria for both samples are summarised in tab. 5.2. Electrons

	I		II	
Selection	TPC	TOF	TPC	TOF
Electron inclusion	$\lvert n\sigma_{\mathrm{e}}\rvert < 3$		$\lvert n\sigma_{\mathrm{e}}\rvert < 3$	$\lvert n\sigma_{\mathrm{e}}\rvert < 3$
Pion rejection	$n\sigma_{\pi} > 3.5$		$n\sigma_{\pi} > 3.5$	
Kaon rejection	$\lvert n\sigma_{\mathrm{K}}\rvert > 3$			
Proton rejection	$\lvert n\sigma_{\mathrm{p}}\rvert > 3$			

Table 5.2.: Summary of selection criteria in the two different approaches to identify electrons and reject hadrons using the TPC and TOF.

for analysis must fulfil either one or the other condition. The PID response of the final electron sample is shown in Fig. 5.7. It is clear that the holes introduced by the hadron rejection in the TPC can be recovered partially using the TOF, leading to a structure in the response, which then translates to the electron efficiency and pair efficiency, however in the full phase space with finite values. The electron iden-

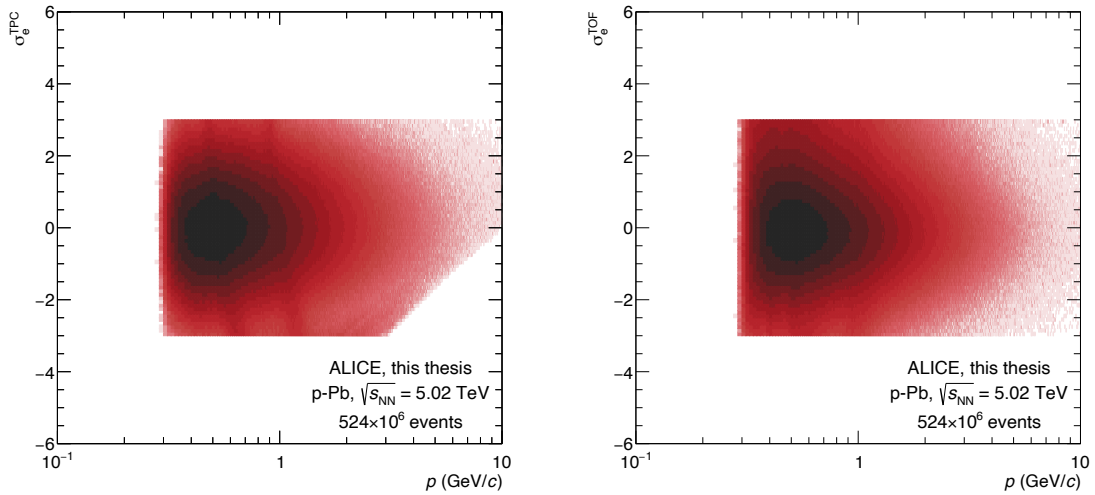

Figure 5.6.: Particle identification response for the TPC (left) and TOF (right) as a function of momentum p for the electron hypothesis. Electrons are selected in a $\pm 3\sigma$ interval in the TPC as well as in the TOF. A signal is required in both detectors.

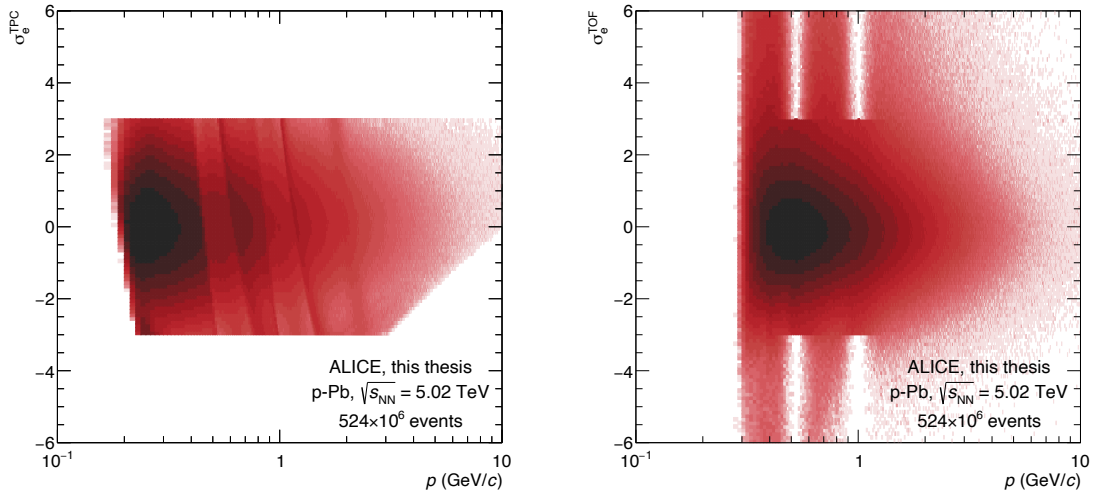

Figure 5.7.: Particle identification response for the TPC (left) and TOF (right) as a function of momentum p for the electron hypothesis. Electrons are selected in a $\pm 3\sigma$ interval in the TPC. Protons, Kaons, and Pions are rejected in the TPC. In case of availability the TOF signal is used to recover electrons in the TPC crossing regions.

tification efficiency (ϵ_{eID}) in this approach was studied in the general-purpose MC simulation based on the DPMJET event generator as described above. To determine the electron identification efficiency, electrons were selected unambiguously via their MC information but after passing the general selection criteria of the analysis. To calculate the electron identification efficiency, the different selections as discussed

above were applied and the fraction of surviving electrons gives the efficiency as shown as a function of momentum in Fig. 5.8.

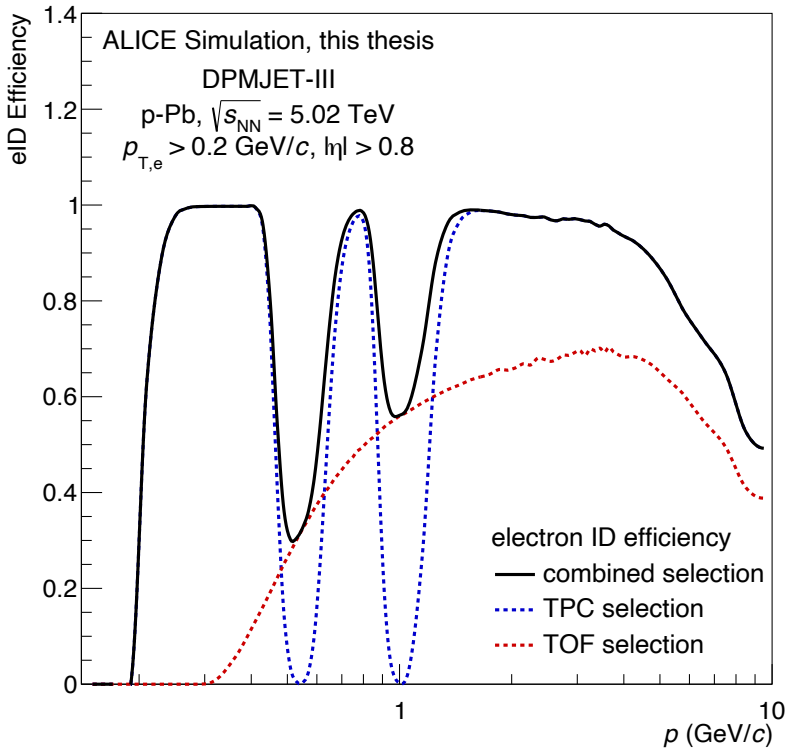

Figure 5.8.: Electron identification efficiency for the single and combined selection criteria estimated using MC simulations based on the DPMJET-III event generator [137, 138] and the GEANT3 transport code [136].

The features of the distribution are well visible. The dashed blue line shows the ϵ_{eID} using the TPC to reject hadrons. The rejection of the kaon and proton band at the relevant p shows a drop of the efficiency to 0. The TOF selection does not show specific structures, but the later and slower turn-on of the TOF efficiency, which can be related to the radial position of the detector itself and the matching of a track to a signal in the TOF. The latter is expected to be worst for tracks with large inclination angles, which can explain the rise of efficiency with momentum. In addition the material in front of the TOF, namely the TRD and multiple scattering therein can prohibit a matching of the track to the measured TOF signal. In both selections, the TPC is used to reject pions, so in both efficiencies a drop above 3 GeV/c is observed. The combination of both efficiencies leads to an overall purity of the electron sample of 98% as determined by integrating the spectra extracted from the MC simulations. This shows that in this novel approach of combining

different detector capabilities, the lack of hadron rejection utilising the ITS $\mathrm{d}E/\mathrm{d}x$ measurement can be mitigated.

5.3 Dielectron signal extraction

After identifying and selecting the electron candidates they need to be paired to dielectrons and the signal needs to be extracted. We call an electron-positron pair a signal pair if it is originating in the same decay, like the Dalitz or resonance decays. In addition, the pairs that stem from the semi-leptonic decays of heavy-flavour hadrons of a $\mathrm{Q\overline{Q}}$ pair that was created in the same process are considered signal pairs. A priori it is not possible to identify an electron and positron that belong to the same pair. The approach followed in this analysis is the most common one, the so-called Unlike-sign (ULS) method. The idea is that all electrons in an event are paired with all positrons. In this approach, every signal pair, of which both daughters are measured, is found. This however introduces a combinatoric background, since also non-correlated electrons and positrons are paired. To estimate this background the like-sign (LS) method is used. Figure 5.9 shows a sketch to illustrate the procedure.

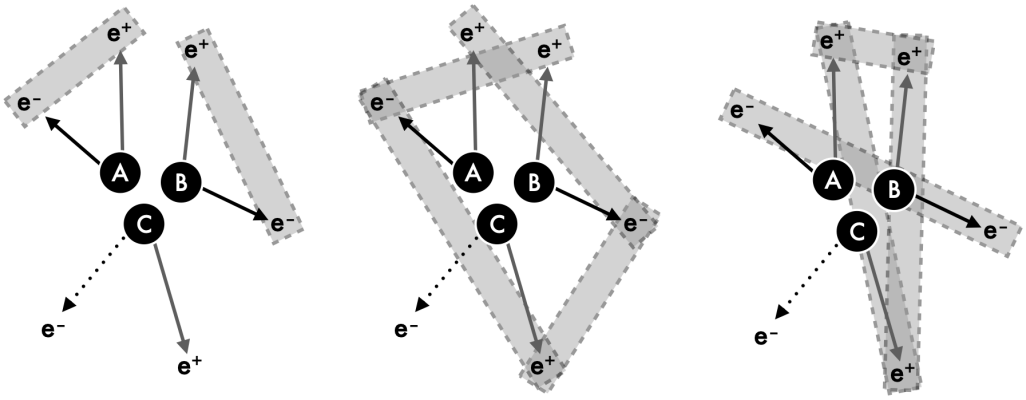

Figure 5.9.: Sketch of three particles (A,B,C) decaying into an $\mathrm{e^+e^-}$ pair. The electron of the decay of particle C is not measured in the detector. The true signal pairs are indicated in grey boxes in the left. The middle shows all combinations of unlike-sign pairs that are no signal pairs. The right sketch indicates the possible like-sign pairs.

We assume three particles A, B, and C all decay in an electron-positron pair. The electron of particle C will be neglected to indicate a finite detector acceptance and particle detection efficiency. The real signal pairs are indicated by the grey boxes in the left panel of Fig. 5.9. Since we form all ULS pairs, we will also get all pairs indicated by the grey boxes in the middle panel. Note that now also the single

positron from particle C contributes since it still produces a background pair with every charge conjugate particle. To estimate the number of background pairs we can now pair all same or like-sign particles, as shown in the right panel. Looking at the different combinations we then have two real signal ULS pairs, four 'fake' ULS pairs, and four LS pairs. So by subtracting the LS pairs from all ULS pairs, we can recover the number of real signal pairs. In this simple example, the number of LS pairs is simply calculated as $N_{++} + N_{--}$. However, the average of the real background $\langle \mathrm{B}_{+-} \rangle$ is given by the geometric mean of the like-sign background ($2\sqrt{\langle N_{++} \rangle \times \langle N_{--} \rangle}$), not the arithmetic. See for example Ref. [140] for more details. In the above case, this would be $2\sqrt{3} = 3.46$, which directly shows a problem. Namely, that in the case of small numbers, the fluctuations in the background can lead to an underestimation of the background when using the geometric mean. The assumptions on the background are only valid in the case of large N and on average. To mitigate the problem of systematically underestimating the background when using small N, the binning of the LS and ULS spectra is chosen to be as large as possible when doing the subtraction.

The subtraction is not done event by event but for the pairs measured in all events. This can lead to a subtraction of two large numbers, which can introduce rather large statistical fluctuations. One way to quantify the statistical precision of a measurement is the statistical significance of a measurement. It is given by its amplitude relative to its statistical uncertainty:

$$s = \frac{S}{\Delta S}. \tag{5.3}$$

In the case of the dielectron measurement the statistical uncertainty can be evaluated as the uncertainty of the unlike-sign spectrum, which consists of the true signal (S_{T}) and the true background (B_{T}). Assuming that both are statistically independent, i.e. follow Poissonian statistics, we can write the uncertainty as:

$$\Delta S = \sqrt{{\Delta S_{\mathrm{T}}}^2 + {\Delta B_{\mathrm{T}}}^2}. \tag{5.4}$$

In our analyses, we however estimate the true background via the like-sign spectrum introducing a second uncertainty term for the background:

$$\Delta S = \sqrt{{\Delta S_{\mathrm{T}}}^2 + {\Delta B_{\mathrm{T}}}^2 + {\Delta B_{\mathrm{LS}}}^2}. \tag{5.5}$$

By construction the like-sign background has the intrinsic right normalisation, i.e. the same statistical uncertainty as the true background. This leads to the conclusion that both have the same statistical uncertainty (${\Delta B_{\mathrm{T}}}^2 = {\Delta B_{\mathrm{LS}}}^2$). With $\Delta X^2 = X$ (Poissonian Statistics) we can then simplify the signal uncertainty to $\Delta S = \sqrt{S + 2B}$. So the significance s of the dielectron measurement, using the like-sign background estimation can be written as:

$$s = \frac{S}{\sqrt{S + 2B}}. \tag{5.6}$$

A different method to estimate the background which is used in other analyses is the mixed-event approach. Here electrons and positrons from different reconstructed events that show similar features are paired to estimate the background. This approach has advantages and disadvantages compared to the like-sign method, which should be discussed briefly. The major advantage of the mixed-event approach is that it is possible to pair an electron with positrons from a large pool of events. By this, the statistical precision of the background would be significantly better than in the like-sign approach. Looking at Eq. 5.5 this would remove the uncertainty ΔB_{LS} and consequently reduce the denominator in Eq. 5.6 to $\sqrt{S + B}$. The significance can be boosted by a factor of $\sqrt{2}$ depending on the relevant signal-to-background ratio. However, the mixed-event method does not provide a background that is normalised to the real background. This problem can not be circumvented easily, since as shown before, there is no signal-free region suited to normalise the background which would then introduce additional complications. This is why this analysis uses the LS background.

An additional effect that needs to be taken into account for the LS background estimation is that the LS and ULS pairs with the same m_{ee} and $p_{\mathrm{T,ee}}$ can have different acceptance. In the analysis, a relative acceptance factor R is calculated from mixed events. The event mixing was done by pairing electrons and positrons from two different events to create mixed-event like-sign and unlike-sign spectra ($LS^{\mathrm{mix}}_{++}, LS^{\mathrm{mix}}_{--}, ULS^{\mathrm{mix}}$). To ensure that the detector acceptance is similar for both events that are used in the mixing procedure and that no artificial modulations are introduced, the events were grouped based on their vertex position in the z-direction. Eight groups for the z vertex from -10 cm to +10 cm with each 2.5 cm width are then filled with 20 reconstructed events. Within these 20 events, all possible combinations of pairs are formed while electrons and positrons are only considered if they fulfil the

analysis selections discussed above. Then, the relative acceptance can be calculated as

$$R = \frac{ULS^{\text{mix}}}{2\sqrt{LS^{\text{mix}}_{++} \times LS^{\text{mix}}_{--}}}. \tag{5.7}$$

The calculation is done two-dimensional as a function of m_{ee} and $p_{\text{T,ee}}$, in Fig. 5.10 the one-dimensional calculations after projections to the m_{ee} (left) and the $p_{\text{T,ee}}$ (right) are shown to illustrate the effects. The relative acceptance is smaller for

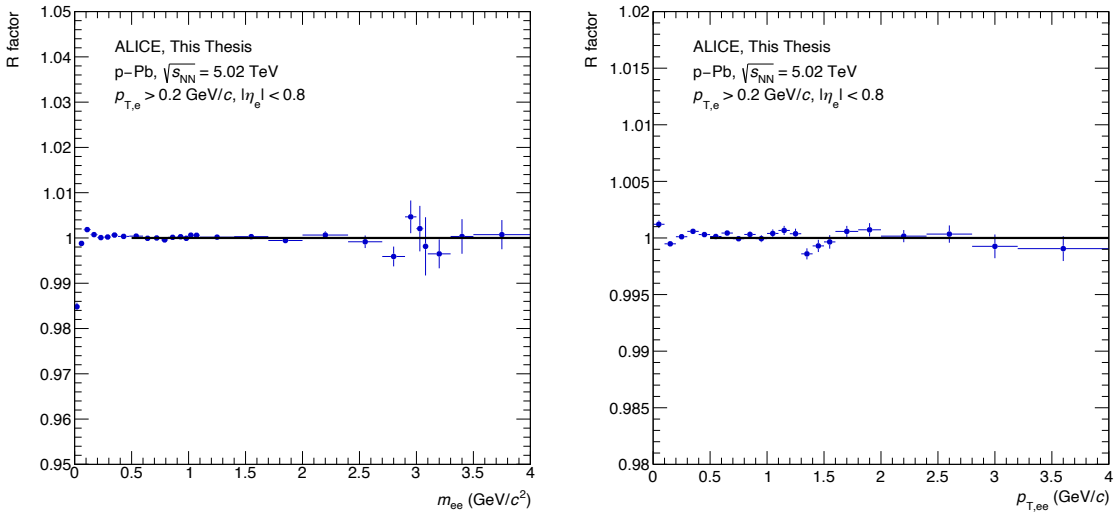

Figure 5.10.: Relative acceptance correction factor for the construction of the background from the LS spectra estimated from mixed events as a function of m_{ee} (left) and $p_{\text{T,ee}}$ (right).

ULS pairs at very small masses and slightly larger than unity when going up in mass and then saturates at unity already above a few hundred MeV/c^2. In the case of the R factor as a function of $p_{\text{T,ee}}$ also modulations can be seen for small values of $p_{\text{T,ee}}$ while we see a saturation at larger values. In both cases, we observe statistical fluctuations when going to larger m_{ee} or $p_{\text{T,ee}}$. While in principle there should be no limit to the statistical precision when using the mixed event technique the limitation in the number of events that are mixed (20) is limited by the resources such as the computing time available. To not include these fluctuations in the background estimations the R factor is set to unity for a circle with $\sqrt{m^2_{\text{ee}} + p^2_{\text{T,ee}}} > 0.5$. With the relative correction factor, we can then calculate the background in the ULS from the LS spectrum as $R \times LS$ and thus the raw signal as $S = ULS - R \times LS$. The unlike-sign spectrum, the background, and the raw signal are all shown in Fig. 5.11. The differences in the unlike-sign spectrum and the background visible in the mass regions below 140 MeV/c^2 where the Dalitz decay of the π^0 dominates the spectrum,

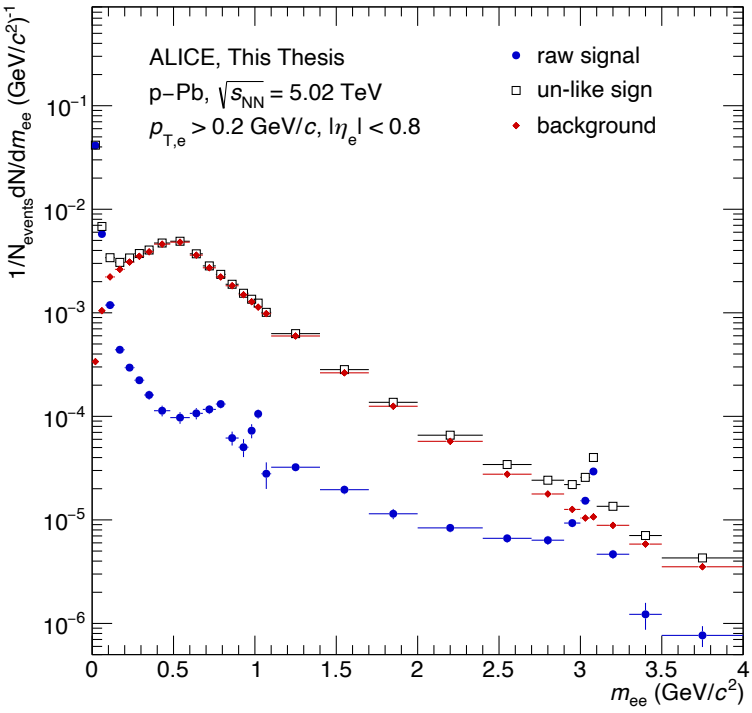

Figure 5.11.: Raw signal as a function of m_{ee} extracted in this analysis compared to the unlike-sign spectrum as well as the background estimated in the LS method corrected for relative acceptance differences of ULS and LS pairs using mixed events.

as well as around the J/ψ mass of about 3.1 GeV/c^2 are most pronounced. More structures become then visible in the subtracted spectrum or raw signal. The steeply falling shape of the π^0 Dalitz decay transitions smoothly into a slightly harder but still smooth spectrum, mainly the Dalitz decay of the η meson. Going further up in m_{ee} we can then see the peak of the ω and ρ decays at about 780 MeV/c^2 is then followed by the ϕ decay which produces a peak at about 1 GeV/c^2. The resonance peaks sit on a wide and smooth contribution produced from the semi-leptonic decays of correlated charm and beauty hadrons. This contribution then also fills the spectrum up to even higher m_{ee}. At around 3.1 GeV/c^2 we can see the J/ψ peak on top of the correlated heavy-flavour spectrum. With the raw signal and the background we can then calculate the signal-to-background (S/B) ratio and the statistical significance as a function of m_{ee} as shown in Fig. 5.12 left and right, respectively. In the S/B ratio, structures that are also seen in the raw data and the ULS spectrum repeat. The mass regions where the decays of π^0 and J/ψ are dominant show the highest S/B. In the region around 500 MeV/c^2 the S/B has a minimum where the S/B is only a few percent. While the raw signal is here at a

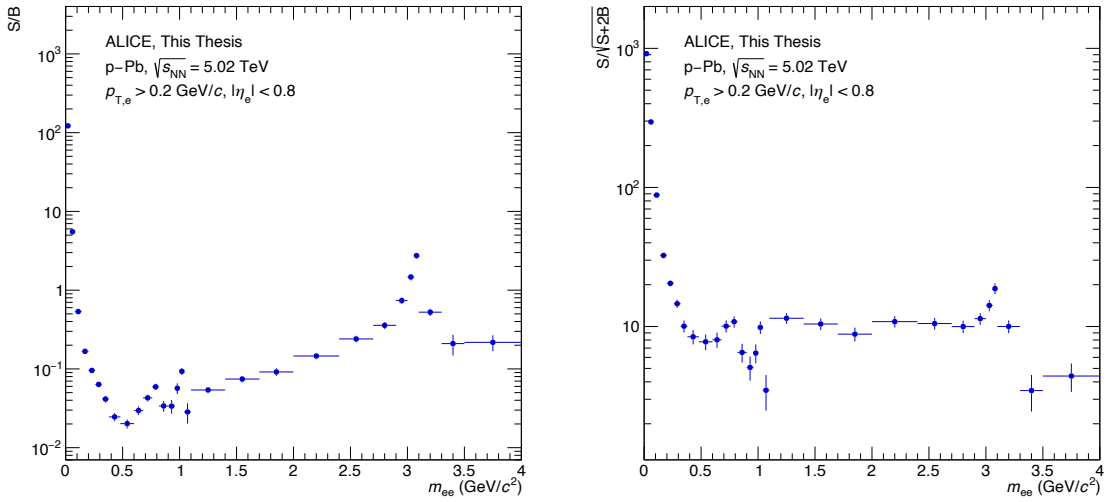

Figure 5.12.: Signal-to-background (S/B) ratio (left) and statistical significance (right) as a function of m_{ee} of the dielectron measurement in p–Pb at $\sqrt{s_{NN}}$5.02 TeV presented in this analysis.

local minimum the background peaks exactly here. In the masses of the ω, ρ, and ϕ mesons the S/B also gets better. In the m_{ee} region between the ϕ and the J/ψ the S/B rises with m_{ee}. Here the background drops faster than the signal which can be attributed to the momentum spectra of the electrons and positrons that contribute here. While the background has a significant contribution by electrons from light-flavour meson decays (π^0, η) the signal is dominated by heavy-flavour hadron decays. The electrons from the latter decay have harder p_T spectra which then translates to harder (softer) m_{ee} spectra for the signal (background). The significance is presented in Fig. 5.12. It is important to add that, in the case of this observable, the spectra are not normalised to the number of events, nor the width of the bins. This means the value of the significance given here is directly the inverse of the expected statistical precision of the data point. The values of the significance are again high in the m_{ee} region of the π^0 and J/ψ even though here the binning is very fine. In the regions where the raw signal is smooth, the binning was adjusted to give values around 10. However, this is not possible in all mass regions without losing the resolution of the peak structure in the spectrum. This leads to lower values around the ω, ϕ and beyond the J/ψ masses.

5.4 Correction for Efficiency

In the following the corrections for losses of real signal due to the selections discussed in section 5.2 are discussed. To estimate the efficiency, Monte Carlo simulations are used. In these simulations, the full ALICE detector is implemented in the GEANT 3 transport code [136]. In this way the passage of particles produced by the event generators and the full detector response is simulated to produce the final observable signal. In the next step, the full reconstruction used for real data is applied to the generated output of the simulations. The result of this is referred to as the reconstructed information, while the original information from the event generator is referred to as the generated MC information. The efficiency with which the signal in an analysis can be selected can then be estimated by repeating the full analysis on the reconstructed MC data and evaluating how much signal is lost in the analysis by comparing it to the generated MC information.

In the terminology, it is differentiated between the corrections for losses due to the fiducial or kinematic observables that could also include the limited acceptance of the used detector, and corrections that are necessary due to the selections in the analysis procedure to select the particle species of interest or ensure a good quality of the reconstructed tracks. The former is the acceptance correction while the latter is the efficiency correction. Following the practices of previous dielectron analyses, no acceptance correction is applied in the dilepton analyses and also in this analysis no correction for the fiducial selection ($p_{\mathrm{T,e}} > 0.2$ GeV/c and $|\eta| < 0.8$) is applied. A correction for acceptance effects would need an assumption about the rapidity distribution and polarisation of the respective spectrum.

The efficiency of a single electron to be measured can then be expressed as the ratio of reconstructed electrons over generated electrons. The fiducial selection is applied in both cases to avoid the acceptance correction. The whole procedure to arrive at the reconstructed MC tracks also introduces resolution effects to the original quantity. Furthermore, the passage of the electron through the detector material will lead to an energy loss of the electrons due to bremsstrahlung [3]. This effect is, in particular, relevant for electrons since their mass is very small compared to the masses of other charged particles measured in the detector ($m_{\mathrm{e}}/m_{\pi^{\pm}} \approx 0.4\%$). The effect of bremsstrahlung losses is not symmetric and can lead to an electron that was generated within the fiducial acceptance to fall below the p_{T} threshold. To take this into account for the calculation of the reconstruction efficiency, the generated kinematic observables of the particle are modified following the detector

response matrix derived from MC simulations. An observable modified in this way is referred to as the measurable observable. Details on the procedure are explained in the description of the hadronic cocktail in section 5.6. Then the efficiency to measure a single electron as a function of an observable x is defined as

$$\epsilon(x) = \frac{N_{\mathrm{e}}(x^{\mathrm{rec}})}{N_{\mathrm{e}}(x^{\mathrm{meas}})}. \tag{5.8}$$

The difference between $N_{\mathrm{e}}(x^{\mathrm{rec}})$ and $N_{\mathrm{e}}(x^{\mathrm{meas}})$ is that in the latter case, no selections on the track properties or particle identification response are applied. In addition, a loss can occure due to the efficiency of the reconstruction algorithm itself. A priori, the efficiency of measuring a primary electron at a given p_{T} and region of the detector should not depend on the source of the electron. An electron from the decay of a charmed hadron or a π^0 should have the same probability to be measured if they have the same kinematic variables. The efficiency for single electrons depending on their source, light flavour or charm, is shown as a function of p_{T}, η, and ϕ in Fig. 5.13.

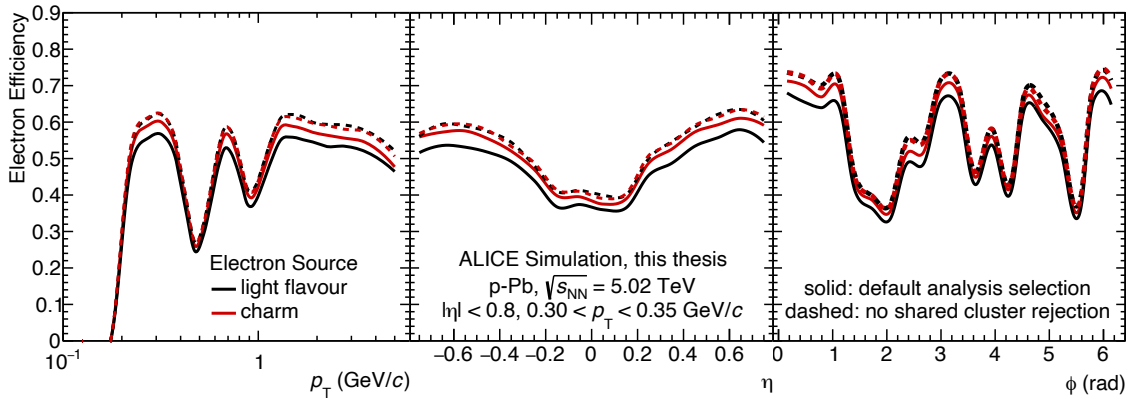

Figure 5.13.: Selection efficiency of electrons after track and particle identification requirements as a function of p_{T} (left), η (middle), and ϕ (right). The efficiency is shown for electrons originating in the decays of light flavour mesons (black) and in charm hadron (red) decays. The default selection (solid lines) is compared with a selection that does allow for shared clusters in the ITS is shown in the dashed lines.

In all three cases, it is observed that the general shape as a function of the relevant observable is independent of the source. However, the efficiency of electrons originating in the decay of a charmed hadron is higher than that of the ones from light flavour-hadron decays. This difference could be traced back to the requirement of rejecting all tracks with a shared cluster in the ITS. When removing this requirement the efficiencies are the same as shown in the dashed lines. In all three represen-

tations of the efficiencies, structures are visible. In the case of the efficiency as a function of p_{T} two minima at $0.4-0.5$ GeV/c and around 1 GeV/c occur. These are the consequences of the particle identification scheme as discussed in section 5.2.2. The slight drop at higher momenta can then be attributed to the pion rejection in the TPC. In the case of the efficiency as a function of η a minimum at midrapidity is observed. The efficiency then grows when going to the edges of the distribution in positive and negative directions. At midrapidity, the path length of the electron in the active volume in the detector is the shortest. With an inclination in η the length of the trajectory in the gas increases. The effect can be up to 30% ($\cosh(0.8)$) going from $\eta = 0$ to $\eta = 0.8$. This can affect the particle identification response. In addition, the primary produced electrons from these tracks have the longest drift in the TPC volume, which also means they have the largest possible diffusion. However, details of the detector geometry and the tracking algorithm complicate this simple explanation and can then introduce additional dependencies, but the overall shape of the efficiency can be understood. The prominent dips in the efficiency as a function of ϕ were investigated and are due to inactive segments of the SPD layers of the ITS. In Fig. 5.14 the modules of the inner (left) and outer (right) layers are mapped in ϕ and z coordinates. The colour code indicates if the respective module was active during the whole data-taking period (green), was switched off during the whole data-taking period (red) or was active in a fraction of the data-taking period (yellow). In the case of the inner SPD layer it is observed that at negative z or η the half-staves in $1.2 < \phi < 2.2$ are not available. In the same η interval also half-staves around $\phi = 4.2$ were switched off. The inactive areas on the positive z side were fortunately in different ϕ regions. This leads to a finite efficiency when integrating in the longitudinal direction. In the outer layer, only 4 half staves were inactive during the data-taking period and for a total of two runs, two more were switched off. This is a small effect compared to the inactive zones in the inner layer. Beyond the larger area that was inactive, the analysis also requires a hit in the inner layer. Therefore the impact on the efficiency is much larger here. Since the inner layer modules were not switched off over the full length in the longitudinal direction there are no areas in which the efficiency drops to zero. Overall, values of the single electron efficiency of up to 50% can be achieved in the analysis setting. The minima are as low as 30% around $p_{\mathrm{T}} = 450$ MeV/c. The difference between the electrons from light flavour and the charm decays that is introduced by the rejection of tracks with a shared cluster in the ITS shows us that we would expect different pair efficiencies from the different sources. While this is in general not expected for electrons or pairs that

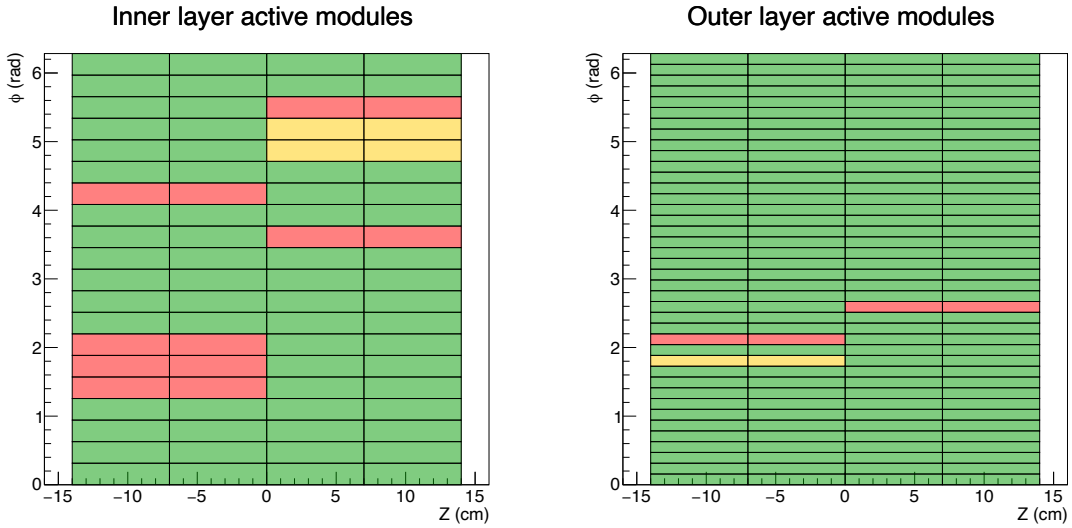

Figure 5.14.: Activity of the modules of the inner (left) and outer (right) layer of the ITS SPD during the data-taking period analysed. The color code indicates the activity as: available during the full data-taking period (green), available during parts of the data-taking period (yellow), not available during the data-taking period (red).

have the same kinematic properties, it is plausible when looking at the decays that are most probable for both sources. The heavy-flavour hadron decays are in most cases semi-leptonic decays in which the electron is accompanied by a kaon and a neutrino. Since the heavy-flavor hadrons are heavy, the electron and the kaon tend to have large opening angles at low momenta. This means the chance that charged kaon hits the innermost layer of the ITS close to the electron is small and only given at high momenta. For the light flavour decays this changes. Here the dominant decays are the Dalitz decays with and e^+e^- pair and an additional photon in the final state, at least for the most abundant particles, the π^0 and the η meson. Due to the small masses of the light flavour mesons compared to the heavy-flavour hadrons the opening angles between the e^+e^- pair and the photon are smaller than in the case of the electron and the kaon in the heavy-flavour decay. If this photon converts into an e^+e^- pair in the beam pipe, there is a chance that one of the electrons produced in the conversion hits the ITS close to one of the primary electrons in the decay. This would then lead to a rejection of the primary track of the original Dalitz pair and a reduction in the efficiency. Due to this feature in the MC simulations the reconstruction efficiency was calculated separately for pairs that originate in the same decay, or from the same mother (SM), pairs that originate in the decays of charmed mesons, as well as pairs that originate in the decays of beauty mesons. The three different pair efficiencies ($\epsilon_{X\to e^+e^-}$) are shown in Fig. 5.15.

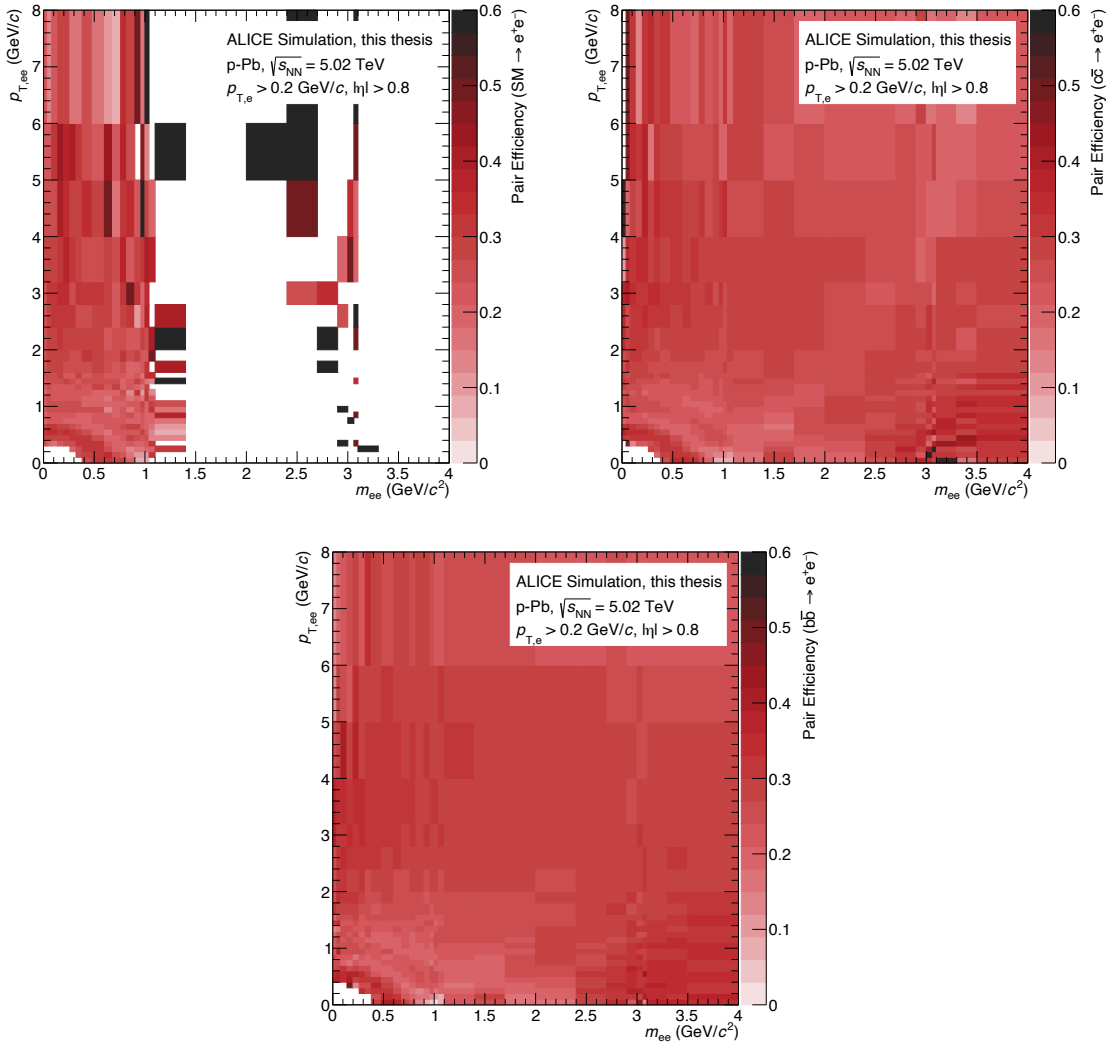

Figure 5.15.: Dielectron pair efficiency ($\epsilon_{e^+e^-}$) as a function of m_{ee} and $p_{T,ee}$ calculated for electrons that were selected in the fiducial selection of the analysis. The $\epsilon_{e^+e^-}$ is shown for different dielectrons that originate in the decay of the same mother particle (top left), dielectrons that are the result of correlated decays of open charm hadrons (top right), and those pairs that stem from the decays of correlated open beauty hadrons (bottom).

The pair efficiency is calculated as a function of m_{ee} and $p_{T,ee}$ in all cases. The procedure used to calculate ϵ_{ee} follows the same selection for generated and reconstructed electrons as described for the single electron efficiency discussed above. In addition, the source of the pair is defined on the MC level. The top left panel shows the efficiency for e^+e^- pairs that originate in the same decay, or from the same mother (SM). It is visible that there are no entries between the ϕ and the J/ψ. This is expected as no resonances exist with a mass between 1 and 3 GeV/c^2 that have a decay into a dielectron in the final state. The top right and bottom panel

of the figure show the efficiency of pairs from correlated $c\bar{c}$ and $b\bar{b}$ decays, respectively. All three efficiencies show a hole at $m_{ee} < 0.4$ GeV/c^2 and $p_{T,ee} < 0.4$ GeV/c which is understood due to the fiducial selection of electrons to fulfil $p_T > 0.2$. This requirement rejects all pairs in the region which is also referred to as the 'acceptance hole'. In addition, structures arching from $m_{ee} = 0$ and $p_{T,ee} \approx 0.8$ GeV/c to $p_{T,ee} = 0$ and $m_{ee} \approx 0.8$ GeV/c in an almost quarter circle are observed. In this region the efficiency shows a minimum. This is understood as a minimum due to the kaon rejection in the TPC and the minimum in the single electron efficiency in Fig 5.13 (left). Further structures are then due to the interplay of the different hadron rejections. In addition we see a slight rise in the efficiency at low $p_{T,ee}$ and higher masses. This can be identified as a structure due to the dip in the efficiency at midrapidity. In general it can be stated that high m_{ee} and low $p_{T,ee}$ are constellations of the decay products with large opening angles. The efficiency as a function of η would result in a higher efficiency for larger $\Delta\eta$ which is also a larger opening angle of the tracks forming the pair. The same could be said for the efficiency as a function of ϕ. However, here only a very small modification is observed. Due to the enhancement of the heavy-flavour contribution in the dedicated MC simulations (see section 5.1) the heavy-flavour contributions have sufficient statistics to fill the whole phase space of the measurement. However, it is not possible to simply combine the HF enhanced MC simulations and the general-purpose MC simulation. This would bias the efficiency towards the value of the HF simulations. Instead the efficiency is calculated as the weighted sum of all three source dependent efficiencies:

$$\epsilon_{ee} = w_{\mathrm{SM}} \times \epsilon_{\mathrm{SM}\to ee} + w_{c\bar{c}} \times \epsilon_{c\bar{c}\to ee} + w_{b\bar{b}} \times \epsilon_{b\bar{b}\to ee}. \tag{5.9}$$

Here the w_X denotes the weights that are assigned to the different sources based on hadronic cocktail calculations (details on these calculation are found in section 5.6). The weights represent the relative contribution to the yield in the respective m_{ee} and $p_{T,ee}$ interval. It is ensured that the sum of all three weights is unity and that fluctuations in the efficiency are suppressed. The final resulting pair efficiency ϵ_{ee} as a function of m_{ee} and $p_{T,ee}$ is shown in Fig. 5.16.

The same structures of the efficiency as in the source-dependent efficiencies in Fig 5.15 are visible, as it is expected. Overall, some statistical fluctuations are still observed in the efficiency. The only way to overcome these would be to use wider intervals in m_{ee} and $p_{T,ee}$ for the corrections, however, in this case the structures that are visible here would be washed out. In case of an ideal matching of

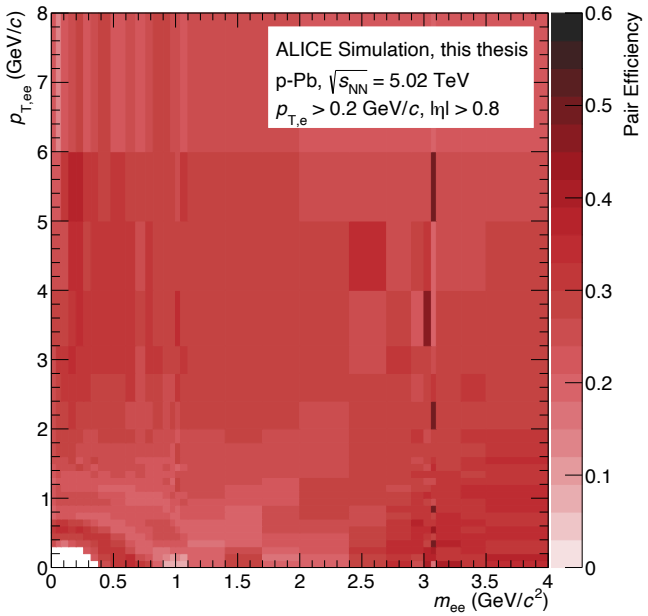

Figure 5.16.: Dielectron pair efficiency ($\epsilon_{e^+e^-}$) as a function of m_{ee} and $p_{T,ee}$. The $\epsilon_{e^+e^-}$ is calculated as the weighted sum of separately calculated efficiencies for dielectrons that originate in the decay of the same mother particle, dielectrons that are the result of correlated decays of open charm hadrons, and those pairs that stem from the decays of correlated open beauty hadrons.

the m_{ee} and $p_{T,ee}$ spectra in data and MC this would not be a problem. However, if there is a mismatch in the spectral shape in MC this would lead to a bias in the efficiency which would be larger for wider intervals. The efficiency correction is then applied as a two dimensional correction to the raw spectrum to arrive at the corrected spectrum. Figure 5.17 shows projections of the corrected spectra as a function of m_{ee} and integrated over $p_{T,ee}$ (left) and as a function of $p_{T,ee}$ in a selection of m_{ee} intervals (right).

In the m_{ee} spectrum we can see the expected features of the spectrum. At low masses, the spectrum falls steeply and changes into a slightly less steep fall-off around the mass of the π^0. In the mass region between 0.5 GeV/c^2 and 1.1 GeV/c^2 the peaks of the vector mesons ω and ϕ are pronounced and at the pole mass of the J/ψ, also a peak is visible. All these structures are on top of a continuum that can be attributed to the correlated semi-leptonic decays of open heavy-flavour hadrons. In Fig. 5.17 (right) $p_{T,ee}$ spectra are shown for different intervals of invariant mass. In blue the interval is shown that is predominantly populated by electron pairs that originate from π^0 decays. Due to the yield being much larger in this interval compared to the

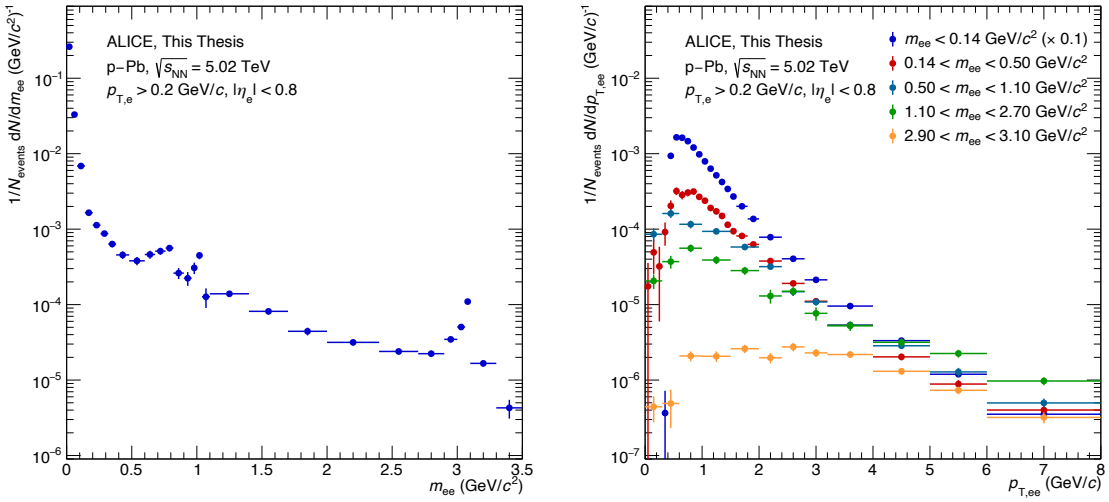

Figure 5.17.: The fully corrected dielectron spectrum in p–Pb collisions at $\sqrt{s_{\mathrm{NN}}}$ = 5.02 TeV as a function of m_{ee} and integrated in $p_{\mathrm{T,ee}}$ (left) and as a function of $p_{\mathrm{T,ee}}$ in different m_{ee} intervals (right). No correction for the fiducial correction is applied.

others it was scaled down by a factor of 10 to be able to better compare the spectra. The other mass regions were chosen based on the sources of dielectrons expected as discussed for the m_{ee} spectrum. There are no structures in the $p_{\mathrm{T,ee}}$ spectra visible for $p_{\mathrm{T,ee}} > 0.4$ GeV/c. Below this value a sharp drop of the blue spectrum is observed and a in the red spectrum also a rather steep decline of the spectrum is present. These are due to the fiducial selection of the electrons that lead to a loss of acceptance as discussed before. Comparing the spectral shape in the different mass intervals we mainly observe that for lower m_{ee} intervals the spectra fall off steeper. The yields in this representation can not directly be compared since the width of the mass intervals are varying drastically. For further interpretation additional inputs to compare to are necessary. However, with the corrected spectra it is not possible to present the efficiency correction in a more intuitive way than the two dimensional figures shown above. As the efficiency is a ratio of two falling spectra, we can not average over the ratio without introducing a bias within the range in which it was averaged. This can only be overcome by weighting the efficiency with the right underlying spectrum. This is done by calculating the so-called effective efficiency ($\epsilon_{\mathrm{ee}}^{\mathrm{eff}}$):

$$\epsilon_{\mathrm{ee}}^{\mathrm{eff}} = \frac{N_{\mathrm{ee}}^{\mathrm{raw}}}{N_{\mathrm{ee}}^{\mathrm{corr}}} \tag{5.10}$$

where $N_{\mathrm{ee}}^{\mathrm{raw}}$ and $N_{\mathrm{ee}}^{\mathrm{corr}}$ are the raw and corrected yield, respectively. The result is shown in Fig. 5.18 as a function of m_{ee} (left) as a function of $p_{\mathrm{T,ee}}$ for different m_{ee} intervals (right).

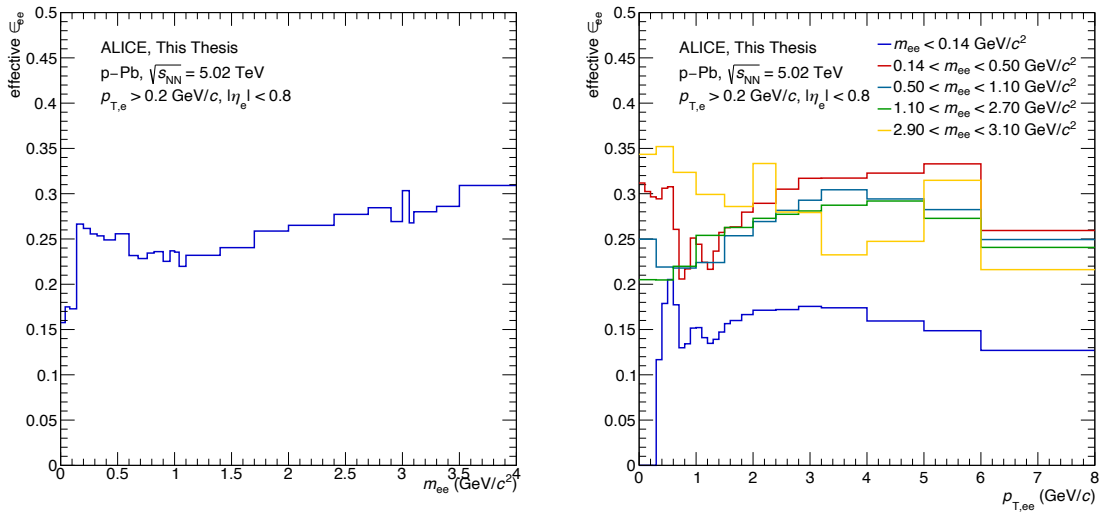

Figure 5.18.: The effective efficiency calculated as the ratio of the measured raw spectrum of dielectrons over the fully corrected spectrum as a function of m_{ee} and integrated in $p_{\mathrm{T,ee}}$ (left) and as a function of $p_{\mathrm{T,ee}}$ in different m_{ee} intervals (right). No correction for the fiducial correction is applied.

The effective efficiency as a function of m_{ee} shows a jump from about 17% to over 25% at small masses. This is the effect of the conversion rejection with the selection in ϕ_{v}. Otherwise, there are no significant structures visible. The effective efficiencies as a function of $p_{\mathrm{T,ee}}$ which are shown for different m_{ee} intervals in Fig. 5.18 (right) show more structures. A general observation is that the efficiency in the lowest m_{ee} interval (< 0.14 GeV/c^2) is lower than the other m_{ee} intervals. This is due to the ϕ_{v} selection which is performed in this m_{ee} interval and over the full $p_{\mathrm{T,ee}}$ range. We can also see a "turn-on" of the efficiency at 0.4 GeV/c related to the fiducial selection. The two dips present at about 0.8 and 1.2 GeV/c are the result of the kaon and proton rejection in the TPC. Above about 4 GeV/c the efficiency then starts to go down again towards higher $p_{\mathrm{T,ee}}$ due to the $\pi^{\pm}$ rejection in the TPC. The mass interval of $0.14 < m_{\mathrm{ee}} < 0.5$ then shows similar features. No "turn-on" is observed since a part of this interval is already outside the acceptance hole. The dips observed in the smaller m_{ee} region however are also present. The m_{ee} intervals of $0.5 < m_{\mathrm{ee}} < 1.1$ GeV/c^2 and $1.1 < m_{\mathrm{ee}} < 2.7$ GeV/c^2 show very similar behaviour. No dips in the efficiency are observed anymore, however, in the lower of the two mass regions, one could still expect a structure since they are present in the

representation of the pair efficiency as a function of m_{ee} and $p_{T,ee}$ as shown above. There are two reasons we can not observe them here: 1) The projection onto the $p_{T,ee}$ axis washes out the sharp structures in this case and 2) it is now necessary to present the spectrum in wider $p_{T,ee}$ intervals to suppress statistical fluctuations in the data. In case of the $2.9 < m_{ee} < 3.1$ GeV/c^2 region there are still fluctuations present, however, suppressed compared to the two-dimensional representation.

5.5 Estimation of systematic biases

As described above there are several corrections needed to derive the fully corrected spectrum from the raw signal that is measured. These corrections always come with certain assumptions and rely in most cases on the quality of the description of reality in the Monte-Carlo simulations. In the following section, different approaches are described to estimate the biases or uncertainties introduced by these corrections and assumptions.

5.5.1 Monte-Carlo description

The efficiency correction relies on the correct description of different contributions of the track properties in the MC simulations. To check the overall description, the full analysis was repeated using different selection criteria for the reconstructed tracks. This was done coherently in data and MC and all steps described before are done. All in all, 30 different sets of selection criteria were chosen. When choosing the different values for the selection it was always checked that there are no unreasonable values selected for the analysis. The different sets of variations are summarised in Tab. 5.3. It should be highlighted that not all track selection criteria are varied.
In particular, the track selections that help in the suppression of electrons from conversions like the requirement of a hit in the first layer of the SPD, or the rejection of tracks that share clusters in the ITS, are not varied. Since these selections are very powerful to reject the conversion background, changing them is not seen as a reasonable variation. For each set of variations, the full analysis is repeated and the reconstructed spectra are compared. The result is shown in Fig. 5.19. The default selection in this analysis is shown in blue markers while the other 29 variations are shown in grey markers. In order to suppress statistical fluctuations the binning used is much coarser then the default analysis binning. It is apparent that there is a systematic offset of a subset of the variations. All the variations that group at

	ITS		TPC			
Set	min. $N_{cls.}$	max. χ^2/cls.	min. N_{CR}	CR/FC [%]	max. SC [%]	max. χ^2/cls.
1	3	5.5	100	60	40	4.0
2	2	4.5	120	60	40	3.0
3	3	6.5	120	60	40	3.0
4	2	6.5	100	70	40	3.0
5	3	4.5	120	50	40	4.0
6	3	6.5	140	70	40	3.0
7	2	5.5	140	70	40	5.0
8	3	5.5	120	60	40	4.0
9	3	4.5	140	60	40	3.0
10	3	5.5	140	70	40	4.0
11	4	4.5	100	50	60	4.0
12	4	5.5	140	60	60	5.0
13	4	5.5	160	70	60	5.0
14	3	6.5	140	60	60	5.0
15	3	6.5	100	70	60	5.0
16	2	5.5	120	50	60	4.0
17	4	4.5	120	60	60	5.0
18	2	6.5	140	60	60	5.0
19	2	6.5	140	70	60	4.0
20	4	6.5	120	60	60	5.0
21	2	5.5	140	60	80	4.0
22	2	6.5	140	70	80	5.0
23	3	6.5	100	50	80	3.0
24	3	4.5	100	70	80	5.0
25	2	4.5	120	60	80	5.0
26	4	5.5	140	70	80	5.0
27	3	6.5	100	70	80	4.0
28	4	6.5	140	50	80	4.0
29	4	4.5	100	70	80	5.0
30	2	6.5	100	60	80	5.0

Table 5.3.: Summary of selection sets that vary the track selection criteria in the ITS and TPC. The variations include the minimum number of clusters (min. $N_{cls.}$) and the maximum χ^2 per cluster (max. χ^2/cls.) for tracks in the ITS. The criteria in the TPC are varied for the minimum number of crossed rows (min. N_{CR}), the fraction of crossed rows with respect to the number of findable clusters (CR/FC) the maximal allowed fraction of clusters shared with other tracks (max. SC) and the maximum χ^2 per cluster assigned to the track (max. χ^2/cls.). The default set used for analysis is Nr. 1

systematically different value can be identified to have the requirement of four hits in the ITS in common. It was then decided that this seems not to be a reasonable

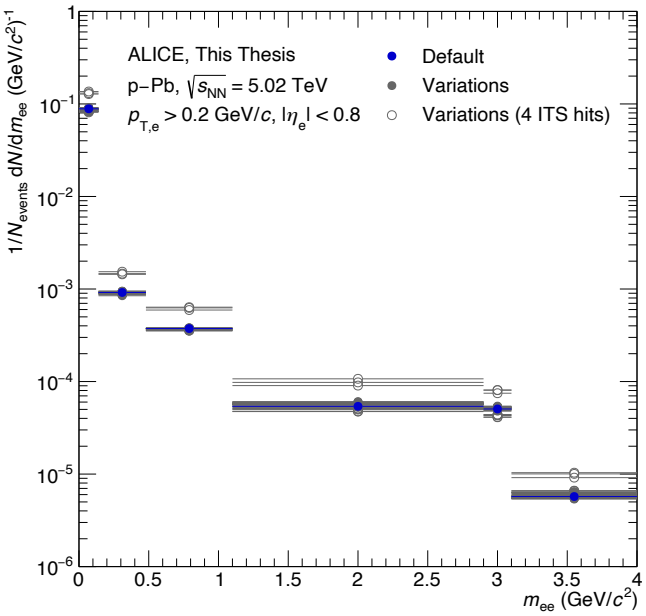

Figure 5.19.: Fully corrected spectra of dielectron production in p–Pb collisions at $\sqrt{s_{\mathrm{NN}}} = 5.02$ TeV using 30 different selections for the electron candidates. The default spectrum for the analysis is shown in blue, the variations are shown in grey. Variations that require four hits in the ITS are shown with open markers.

variation as the description of the distribution in data is not well described in the MC simulations. The variations that include this strong requirement are not taken into account further. It should be pointed out that since the data do not use the information of the two middle layers of the ITS (the SDD) a requirement of four hits requires a hit in every available layer of the detector. Comparing the default and the variations in the solid grey markers we can see that in case of requiring two or three hits in the ITS the default spectrum and the one obtained with different variations of the selection criteria agree well. In order to make sure that the default spectrum is not an outlier in any respect also the S/B and the statistical significance of the default selection and the variations is compared in Fig. 5.20 left and right, respectively. In S/B as well as statistical significance the variation from the default distribution is up to 20% with some larger deviations in the regions where the statistical precision is limited. It is apparent, that the default selection shows a larger signal-to-background and statistical significance when compared to most distributions. This is reassuring, since no out-layer was picked and a spectrum with above average performance is used for the analysis. If the MC implementations were a perfect description of the data, no difference between the fully corrected spectra

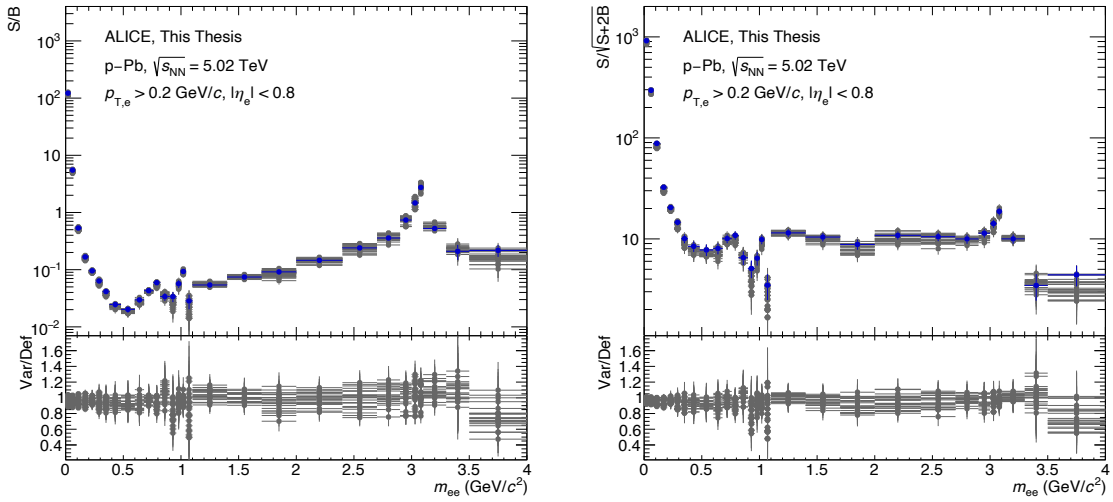

Figure 5.20.: Signal-to-background ratio (left) and statistical significance of the default track selection and the variations that do not include a requirement of four hits in the ITS. The lower panel of each figure shown the ratio of the variations to the default selection.

would be expected. However, since small deviations are observed it is necessary to assign an uncertainty to this mismatch of the data description in the MC simulation. The distribution of the corrected yields of all the variations in the different m_{ee} intervals is presented in Fig. 5.21. The histograms are chosen to have bins with a width of approximately 1.5% of the default value and the default value is always located in the central bin. The default value is indicated by the blue vertical line. In all cases, the deviations are observed to be moderate and the default value is close to the mean value of the distribution which is indicated by the black vertical line. A slight difference is seen in the interval from 1.1 to 2.9 GeV/c^2. Here the default value is slightly below the mean value. The uncertainty is then given by the standard deviation calculated as the RMS of all entries with respect to the mean. The uncertainty is indicated as the blue hatched area in Fig. 5.21. It ranges from about 2% in the lower mass regions up to about 5% in the highest mass interval.

5.5.2 ITS TPC matching efficiency

A different observable that needs to result in the same value in data and MC is the so-called ITS-TPC matching efficiency. It refers to the ability of the tracking algorithm to connect the space points and the partially reconstructed track in the ITS with the equivalent in the TPC. The two track segments need to be matched over the insensitive distance between the last ITS layer and the first pad row which is about

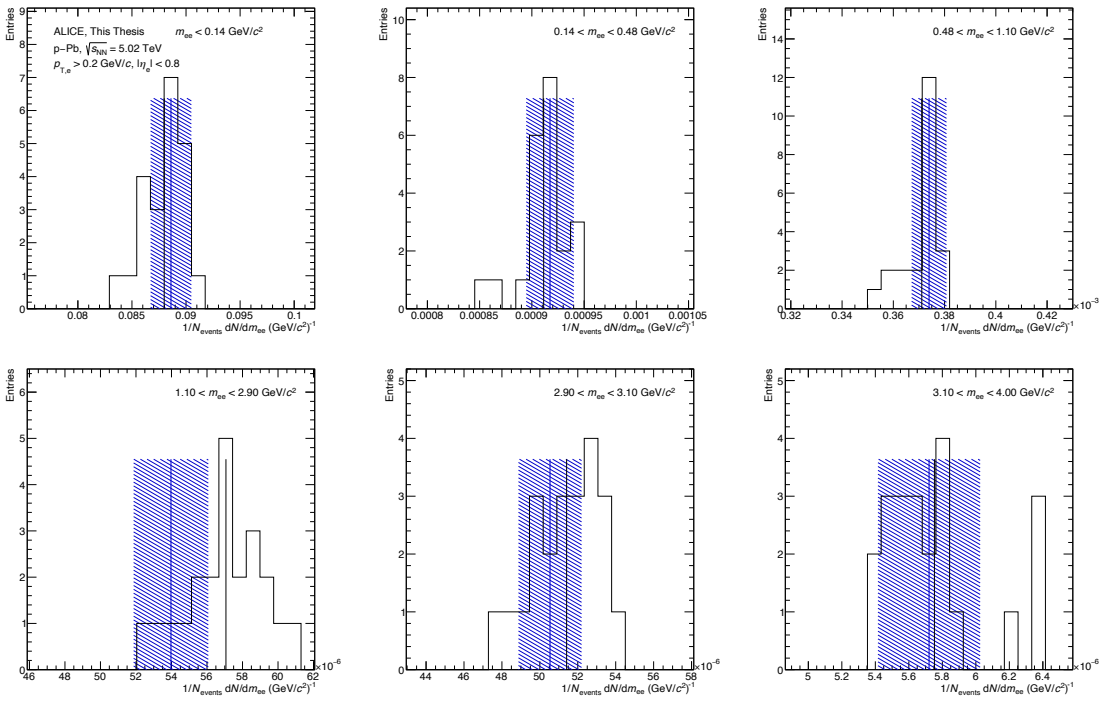

Figure 5.21.: Distribution of yields in the different m_{ee} bins used for the estimation of systematic uncertainties. The blue vertical line indicates the value of the default selection. The hatched area indicates the width of the distribution calculated as its RMS.

41 cm. Overall it is about 90% over a large p_T range and could be improved from 80% in the Run 1 data taking campaign by repairing parts of the SPD cooling. However, this needs to be properly modeled in the used MC simulations and the central quality assurance provided by the DPG found small deviations. The relative difference of the ITS-TPC matching efficiency between data and MC is shown in Fig. 5.22 (left). This is done for charged tracks, not electrons, since it is not possible to collect a clean sample of primary electrons on the single track level without suffering from large contributions from conversions which are expected to have a different (worse) matching efficiency. It is assumed that the relative difference of charged particles in data and MC is the same as for electrons and positrons. Since the uncertainty is given on the track level, a propagation to the dielectron pairs is needed. To do so, a Monte Carlo code was developed that takes the single track uncertainty as an input. In a first step, the phase space (m_{ee} and $p_{T,ee}$) of the measurement is divided into 25000 cells with widths of $\Delta m_{ee} = 0.02$ GeV/c^2 and $\Delta p_{T,ee} = 0.1$ GeV/c. In each cell 1000 particles with the corresponding m_{ee} and $p_{T,ee}$ are generated while the value in the center of the interval is taken for all particles. Each particle then

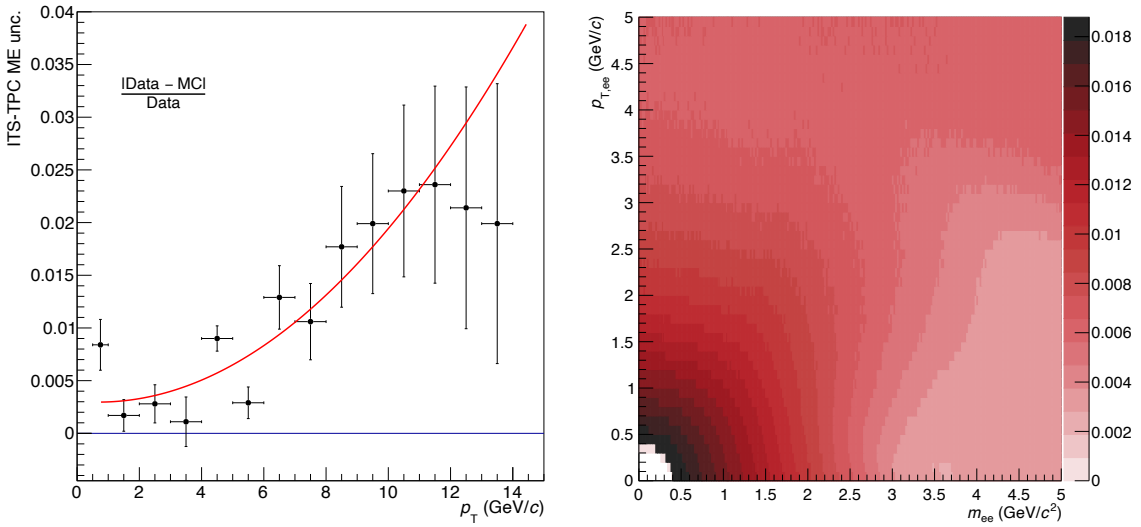

Figure 5.22.: Uncertainty of the ITS-TPC matching efficiency in data and MC simulations as provided by the ALICE DPG (left) and resulting pair uncertainty simulated in each phase space cell (right).

decays into an electron and a positron. The uncertainty is calculated in each phase space cell as:

$$\frac{1}{N}\sum_{i}^{N}\sqrt{\delta(p_{T,1,i})^2+\delta(p_{T,2,i})^2}. \tag{5.11}$$

With $\delta(p_{T,1,i})$ and $\delta(p_{T,3,i})$ the uncertainty of the two decay products of the i-th particle which is given by the ratio shown in Fig. 5.22 (left). In the case of p_{T} below 0.5 GeV/c the same value as for 1 GeV/c is used. The decay products are filtered through the fiducial acceptance that is also used in the analysis. The resulting uncertainties as a function of m_{ee} and $p_{\mathrm{T,ee}}$ are shown in Fig. 5.22 (right). The structure represents that the uncertainty is large (about 1 %) for the lower p_{T} intervals and then slightly drops between 1 and 4 GeV/c. The smallest values of the resulting pair uncertainty are for masses above 3 GeV/c^2 and small to intermediate $p_{\mathrm{T,ee}}$ since here the kinematics will lead to back-to-back decays with little Lorentz boost which leads to a symmetric distribution in the track p_{T}. These will then in most cases get the uncertainty in the minimum of the distribution shown in Fig. 5.22 (left) assigned. The uncertainties of up to 2% for the single track will not contribute significantly in the relevant phase space of the measurement and the simulation. In the last step, the uncertainty needs to be calculated for the binning in which the final systematic uncertainties are applied. Since the m_{ee} and $p_{\mathrm{T,ee}}$ spectra are steeply falling it is not possible to simply average since this would bias the values to larger m_{ee} and $p_{\mathrm{T,ee}}$ and most probably underestimate the uncertainties. Using the cocktail

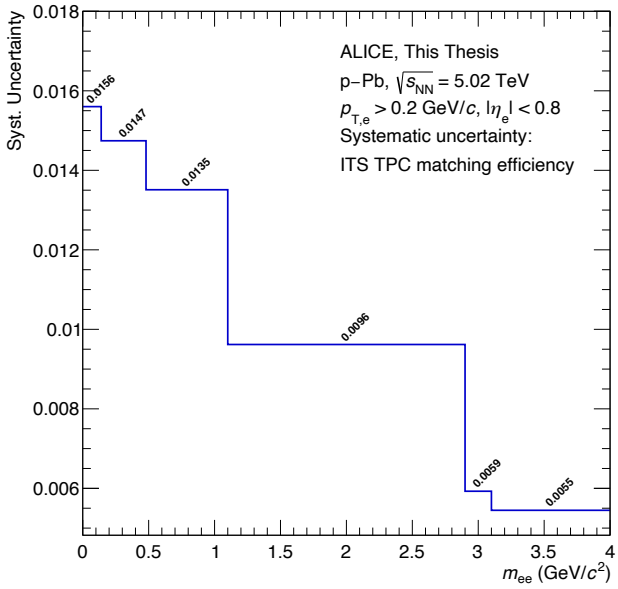

Figure 5.23.: Systematic uncertainty for ITS-TPC matching evaluated from single tracks and propagated to the pair level using a MC approach together with a realistic m_{ee} and $p_{T,ee}$ distribution based on cocktail calculations.

calculations discussed in section 5.6 we can reweight the uncertainties to a realistic distribution. The final assigned uncertainty is shown in Fig. 5.23. It is apparent that the maximum of the uncertainty is at low m_{ee} and then drops with higher masses to values that are rather negligible compared to the uncertainty assigned from the data MC matching as discussed above.

5.5.3 Hit in first SPD layer

As described above, the requirement of a reconstructed track having a hit in the first layer of the SPD is not varied in the different selection sets, so a mismatch of the data and the Monte-Carlo simulations is also not included in these variations. To investigate a possible bias in the analysis that could be introduced by this selection a similar approach as in the case of the ITS-TPC matching efficiency is used. It is not possible to perform this study with electrons, since an unambiguous selection of primary electrons is challenging due to the large contribution from electrons originating from conversions. However, it is possible to select a sample of primary pions with high purity by selecting pions with a small DCA. In this analysis, a maximum of 5 mm in the transverse plane and a maximum of 10 mm in the direction

longitudinal to the beam axis was chosen. In this sample, the selection of the hit in the 1st layer in the SPD was then varied and the efficiency of the selection is calculated as:

$$\epsilon^{\text{SPD 1st}}(p_{\text{T}}) = \frac{N_{\pi^{\pm}}^{\text{SPD 1st}}(p_{\text{T}})}{N_{\pi^{\pm}}(p_{\text{T}})}. \tag{5.12}$$

The same procedure is used in MC simulations to calculate the $\epsilon_{\text{MC}}^{\text{SPD 1st}}(p_{\text{T}})$. Both results are shown in the top panel of Fig. 5.24 (left). Overall, no strong dependence

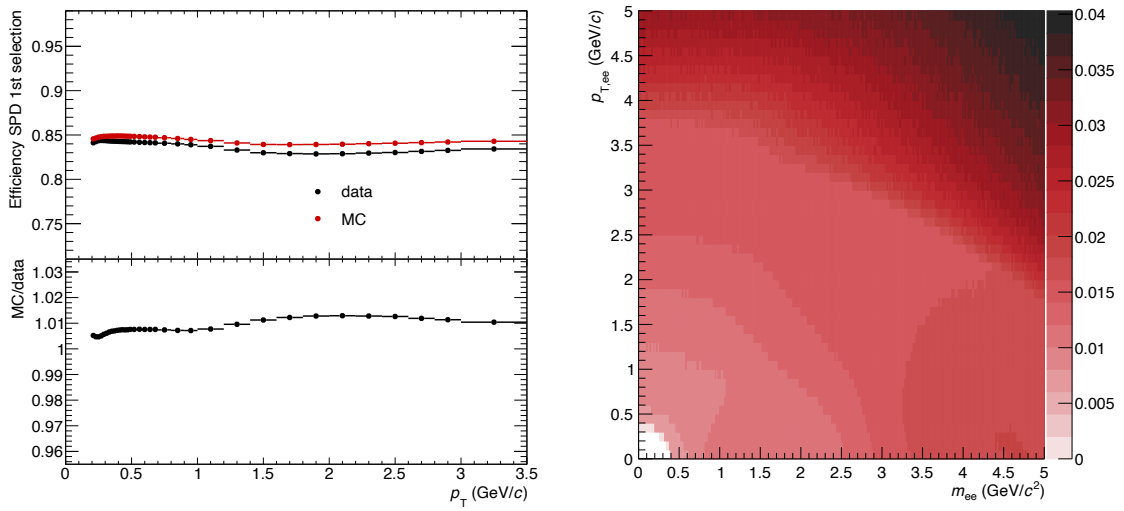

Figure 5.24.: Efficiency of the requirement of a hit in the 1st SPD layer in data and MC (left, top) and the relative difference of in data and MC simulations (left, bottom) as a function of p_{T}. The resulting uncertainty on the dielectron pair as a function of m_{ee} and $p_{\text{T,ee}}$ is calculated based on a phase space generator MC simulation (right).

of the efficiency as a function of p_{T} is observed. In order to quantify the difference of data and MC the ratio of the efficiencies $\epsilon_{\text{MC}}^{\text{SPD 1st}}(p_{\text{T}})/\epsilon^{\text{SPD 1st}}(p_{\text{T}})$ is calculated. As shown in the lower panel of Fig. 5.24 (left) the divergence of MC from data is small and shows a slight dependence on p_{T}. This ratio was then used to quantify the uncertainty of a single track at a given p_{T}. To propagate the uncertainty to dielectron pairs the Monte Carlo approach described above was used to calculate the uncertainty in a given phase space cell. The result is shown in Fig. 5.24 (right). It is again necessary to transform the result in fine m_{ee}-$p_{\text{T,ee}}$ cells to the same that is used in the analysis. As in the previous approach to estimate the ITS-TPC matching efficiency uncertainty, the hadronic cocktail is used to reweight the flat m_{ee} and $p_{\text{T,ee}}$ spectrum to a realistic distribution before rebinning the spectrum and extracting the uncertainty in the coarse m_{ee} bins. The result is presented in Fig. 5.25. The

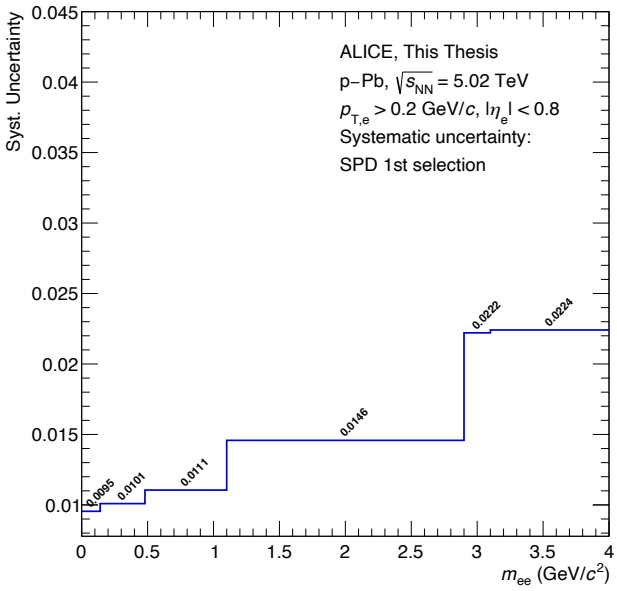

Figure 5.25.: Systematic uncertainty for the requirement of a hit in the 1st SPD layer evaluated from single tracks and propagated to the pair level using a MC approach together with a realistic m_{ee} and $p_{T,ee}$ distribution based on cocktail calculations.

uncertainty is about 1% in the low mass region and grows to about 2-2.5% at masses of the J/ψ or larger.

5.5.4 Shared cluster in the ITS

To estimate the uncertainty of the shared cluster rejection, the approach using a single-track distribution to estimate the uncertainty as a function of p_T and then propagate it to the m_{ee} and $p_{T,ee}$ distribution with the previously described MC simulation was chosen again. In this case, the single track distribution is based on electrons that were selected within a DCA window of ± 1 mm in the transverse plane and with a maximum DCA of 10 mm along the beam direction. As in the case of the requirement of a hit in the 1st layer of the SPD, the efficiency is calculated as the ratio of electron candidates with and without the selection applied. The efficiencies are calculated in data and MC simulations as shown in the top panel of Fig. 5.26 (left) as a function of p_T.

To quantify the relative uncertainty as a function of p_T the ratio of MC over data is used as it is shown in the bottom panel of Fig. 5.26 (left). The resulting uncertainty as a function of m_{ee} and $p_{T,ee}$ in fine cells is shown in Fig. 5.26 (right). A maximum

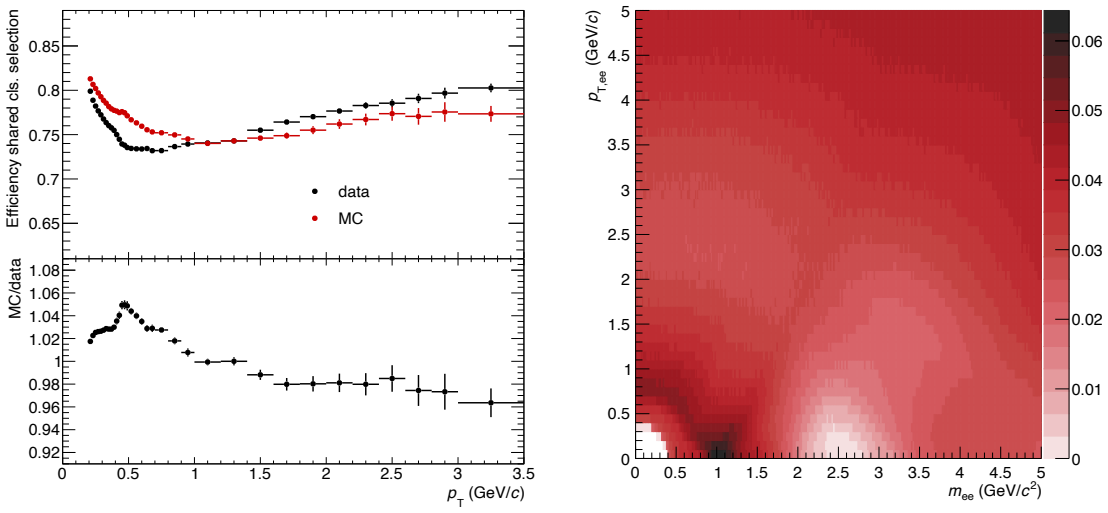

Figure 5.26.: Efficiency of the rejection of tracks with shared clusters in the ITS in data and MC (left, top) and the relative difference of in data and MC simulations (left, bottom) as a function of p_T. The resulting uncertainty on the dielectron pair as a function of m_{ee} and $p_{T,ee}$ is calculated based on a phase space generator MC simulation (right).

of about 6% uncertainty is seen as a quarter circle in the area below 1 GeV/c^2 in m_{ee} and 1 GeV/c in $p_{T,ee}$ which is the result of the small peak in the ratio of the two efficiencies at about 0.5 GeV/c. It should be noted that above 1.5 GeV/c the ratio shows values smaller than unity. In this case no "negative uncertainty is applied, but the uncertainty is always given as the absolute difference between the ratio and unity. To adjust the fine binning in the MC simulation to the analysis binning that is used for the estimation of the systematic uncertainties the cocktail distributions are used to reweight the two dimensional uncertainties to match a realistic m_{ee} and $p_{T,ee}$ distribution before rebinning.
The resulting uncertainties are presented in Fig. 5.27. The maximum around 6% that was observed in the two-dimensional representation is now reduced to about 4% at masses below 1 GeV/c^2 which shows the effect of the averaging.

5.5.5 ϕ_v correction

The correction in ϕ_v is applied assuming a flat distribution in ϕ_v for the signal pairs. To correct for possible modulations in the uniform distribution that could be introduced by the difference in the resolution in the xy and the z direction of the detector, it was studied in MC if the shape of a distribution of $\pi^0 \rightarrow e^+e^-\gamma$ decays with all analysis selections applied is compatible with a flat distribution. The

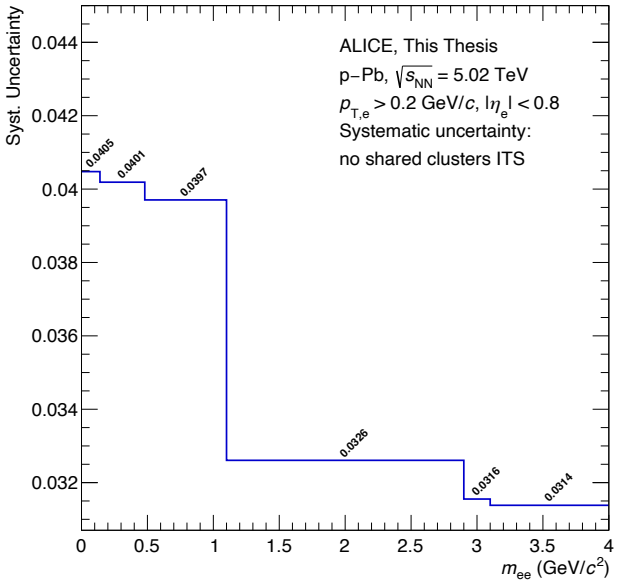

Figure 5.27.: Systematic uncertainty for the rejection of tracks that have shared clusters in the ITS evaluated from single tracks and propagated to the pair level using a MC approach together with a realistic m_{ee} and $p_{T,ee}$ distribution based on cocktail calculations.

nominal selection value of $\phi_v < 2.0$ results in the flat correction into an efficiency of $\frac{2}{\pi} = 0.637$. From the MC simulation, a correction factor of 0.615 is estimated. The relative difference of the two values is considered as a systematic uncertainty of 3.5%. Since the selection in ϕ_v is only applied in the lowest mass bins, we only assign this uncertainty in the first bin of the estimation of the systematic uncertainties.

5.5.6 Summary systematic uncertainties

The systematic uncertainties related to different selections and rejections in the analysis were estimated. To estimate uncertainties based in differences in the detector response implemented in Monte-Carlo simulations and data, 30 different track selection sets are created and the full analysis is carried out for each selection set. It is found that when requiring the maximum of 4 possible hits in the ITS a systematic shift in the corrected spectra is observed. This led to the decision to not include these variations in the data analysis. The RMS of the remaining spectra was used to estimate the uncertainty. This uncertainty includes the mismatch of data and MC implementation and in addition a component from the background estimation. The S/B was changed by up to 40% within the different selections. Nevertheless,

the resulting uncertainties are in the few per cent range. For selections that are not suited to vary because the result would be unreasonable for the analysis different approaches to estimate were explored. The uncertainty on the single track level was used as provided by the data preparation group for the ITS-TPC matching efficiency, while the relative differences of the rejection of tracks with shared clusters in the ITS and the requirement of a hit in the 1st SPD layer were extracted from the difference in data and MC simulations. For this, a topological selection was applied to only select tracks that originated in the primary vertex. A novel MC approach was developed to propagate the single-track uncertainties as a function of p_{T} to the invariant mass bins used to estimate the systematic uncertainties. The uncertainty of the rejection of pairs with ϕ_V was studied in MC simulations and the divergence of the shape of primary pairs with respect to a flat distribution was assigned as an uncertainty. All uncertainties are summarised in Tab. 5.4. The total uncertainty

m_{ee} [GeV/c^2]	data-MC	ITS-TPC ME	no ITS sh. cls.	SPD 1$^{\mathrm{st}}$	ϕ_{v}	total unc.
< 0.14	2.1%	1.6%	4.1%	1.0%	3.5*	5.0 (6.0*)%
0.14 - 0.48	2.5%	1.5%	4.0%	1.0%	–	5.1%
0.48 - 1.10	1.8%	1.4%	4.0%	1.1%	–	4.7%
1.10 - 2.90	3.9%	1.0%	3.3%	1.5%	–	5.3%
2.90 - 3.10	3.3%	0.6%	3.1%	2.2%	–	5.1%
3.10 - 4.00	5.3%	0.5%	3.1%	2.2%	–	6.6%

Table 5.4.: Summary of systematic uncertainties from different sources estimated in different invariant mass bins. The ϕ_{v} uncertainty is only applied to masses smaller than 100 MeV/c^2.

is then given as the quadratic sum of the single contributions. Overall the uncertainties are about 5% and the total uncertainty shows no strong dependence on the mass. To better judge the relative contribution in each m_{ee} bin, the fractions of the different contributions to the systematic uncertainties are presented as a stacked bar chart in Fig. 5.28. The two dominating sources of systematic uncertainty in the first mass bin are the rejection of shared clusters in the ITS and the ϕ_{v} selection. While the ϕ_{v} uncertainty is only relevant in the first mass bin, the second and third bin (< 1.1 GeV/c^2) are then dominated by the ITS shared cluster rejection. For higher masses, the MC description of the detector response becomes the biggest uncertainty. Overall the uncertainty connected to the ITS-TPC matching efficiency and the requirement of a hit in the first SPD layer are rather small compared to the other uncertainties.

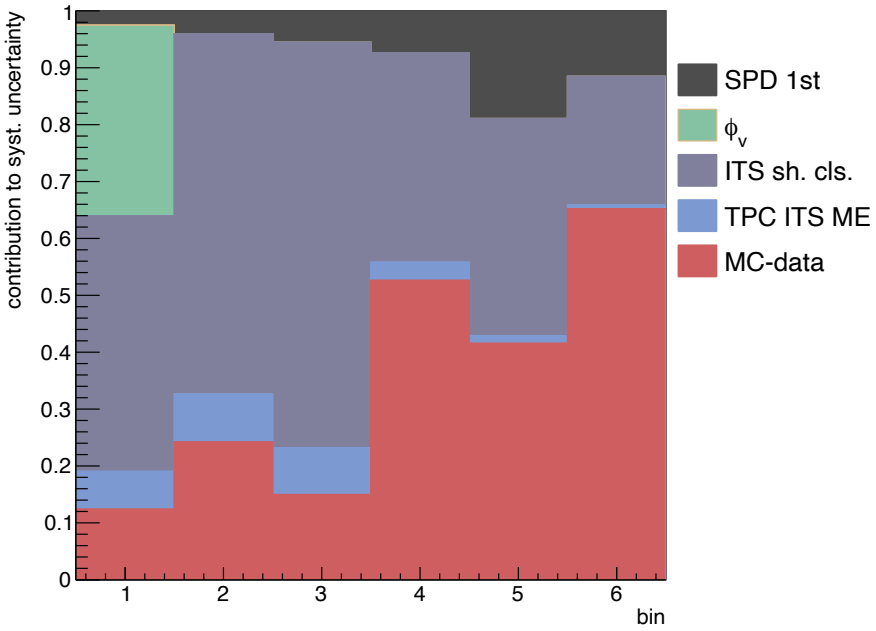

Figure 5.28.: Relative contribution of systematic uncertainties to the quadratic sum of all sources of uncertainties.

5.6 Hadronic Cocktail

The so-called hadronic cocktail is one of the main tools to interpret the measured dielectron spectra. The cocktail method uses MC simulation techniques to estimate the expected sources of dielectrons from hadronic decays. This includes the Dalitz decays of the π^0 and η, the resonant decays of the ω and ϕ as well as their Dalitz decays, but also the decays of open-heavy flavour mesons that produce dielectrons in the final state. Comparing the measured spectra with this cocktail can then indicate modifications of the dielectron spectrum with respect to the "trivial" hadronic contributions. This can be an additional contribution like a thermal photon source or a modification of the hadronic contributions.

In the following, the simulations used to describe the contribution of hadrons decaying with a dielectron in the final state are described. The general strategy is to use a data-driven approach where possible. This means to parameterise measured particle spectra and feeding these into an MC simulation that generates the relevant particle species and lets them decay, following the best knowledge available. In case no direct measurement of the relevant particles is available in the considered collision system or at the relevant energy, other information is used. This can be ratios of particle production in similar systems and collision energies or information from event gen-

erators like PYTHIA. From these so-called inputs, the final state dielectron pairs are estimated in a MC simulation that generates the hadrons based on the input spectra, decays them in the relevant channels and filters the decay products based on fiducial experimental selections, as they are used in the data analysis. Since the measured spectra are not unfolded, the simulation also accounts for the resolution effects of the detector. This was done by using MC simulations that include the full detector simulation. To estimate the resolution, the generated and reconstructed kinematic p_{T}, η, φ variables of electrons are compared. In Fig. 5.29 the relative p_{T} resolution of primary electrons estimated in MC simulations is shown as a function of the generated transverse momentum $p_{\mathrm{T}}^{\mathrm{gen}}$. The resolution is calculated as the difference of the

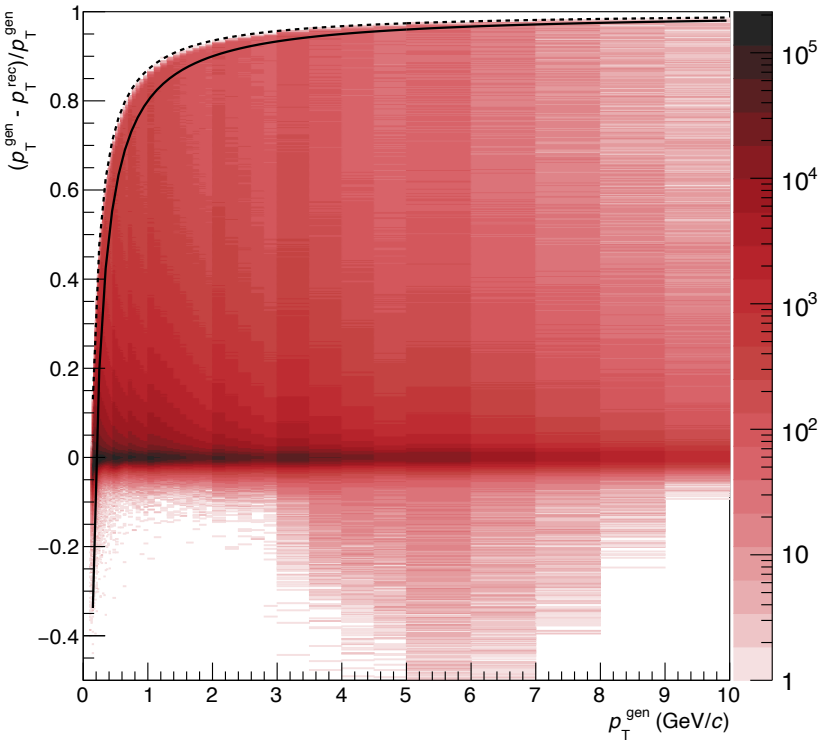

Figure 5.29.: Relative p_{T} resolution for primary electrons as a function of the generated p_{T} estimated from MC simulations. Positive values on the y-axis indicate $p_{\mathrm{T}}^{\mathrm{rec}} < p_{\mathrm{T}}^{\mathrm{gen}}$. A cut-off towards positive values on the y-axis is observed. This can be described by a fixed value of $p_{\mathrm{T}}^{\mathrm{rec}} \approx 0.13$ GeV/c which is indicated by the black dashed line. This indicates an implicit minimum p_{T} selection which is introduced by the track requirements discussed above. The analysis selection of $p_{\mathrm{T}} > 0.2$ GeV/c is indicated by the black solid line.

reconstructed and the generated transverse momentum $p_{\mathrm{T}}^{\mathrm{rec}}$ and $p_{\mathrm{T}}^{\mathrm{gen}}$ as a function of $p_{\mathrm{T}}^{\mathrm{gen}}$. Generated refers to the pure MC information while the reconstructed p_{T} is the p_{T} that is reconstructed when propagating the particle through the full MC chain

including the reconstruction algorithm. The well-pronounced tails towards positive values are a consequence of the Bremsstrahlung of the electrons in the detector material. For large values of the relative resolution, a cut-off is observed. This can be described by the black dashed curve which assumes a $p_{\mathrm{T}}^{\mathrm{rec}}$ threshold of 0.13 GeV/c. Since there is no explicit cut on the reconstructed momentum, this is considered a result of track selection criteria that lead to an implicit p_{T} cut-off. It can be traced back to the required number of pad rows crossed in the TPC. The corresponding radius to the $p_{\mathrm{T}} = 0.13$ GeV/c can be calculated by

$$0.3 \cdot B[\mathrm{T}] \cdot \varrho[\mathrm{m}] = p_{\mathrm{T}}[\mathrm{GeV}/c] \tag{5.13}$$

with the magnetic field B and the bending radius of the track ϱ which is equivalent to half the maximum radius reached in the detector R. The maximum radius reached by a track with $p_{\mathrm{T}} = 0.13$ GeV/c and $B = 0.5$ T can be calculated as

$$R = \frac{2 \cdot 0.13}{0.3 \cdot 0.5} = 1.73 \text{ m}. \tag{5.14}$$

The OROC inner radius is 135 cm [133], while the inner pads have a length of 10 mm. With the 63 pad rows of the IROC, a track needs to cross 37 more pad rows in the OROC to fulfil the track requirement of 100 applied in this analysis. This means it reaches a radius of 135 cm + 37 · 1 cm = 172 cm. This neglects the effects of the track crossing sector boundaries which would lead to a larger radius and momentum. In the analysis, only electron candidates with a reconstructed $p_{\mathrm{T}} > 0.2$ GeV/c are accepted. This selection is indicated by the black solid line in Fig. 5.29.

The smearing in η and φ is performed in absolute values also estimated from MC simulations as the difference between reconstructed and generated values. The distributions of $\varphi^{\mathrm{gen}} - \varphi^{\mathrm{rec}}$ as a function of $p_{\mathrm{T}}^{\mathrm{gen}}$ for e^+ and e^- are shown in Fig. 5.30 top left and right, respectively. It is apparent that the charge sign is relevant in this case, since electrons and positrons show shifts in opposite directions, however, with the same magnitude. This can be understood in the same way as the asymmetry in the p_{T} resolutions. An electron or positron can only lose energy due to bremsstrahlung. This leads to a smaller curvature. In the reconstruction, this leads to a bias in the curvature towards smaller values which leads to a shift in the pointing in the φ direction that depends on the sign of the curvature, which again is defined by the charge sign. In Fig. 5.30 bottom the difference of the generated and reconstructed η

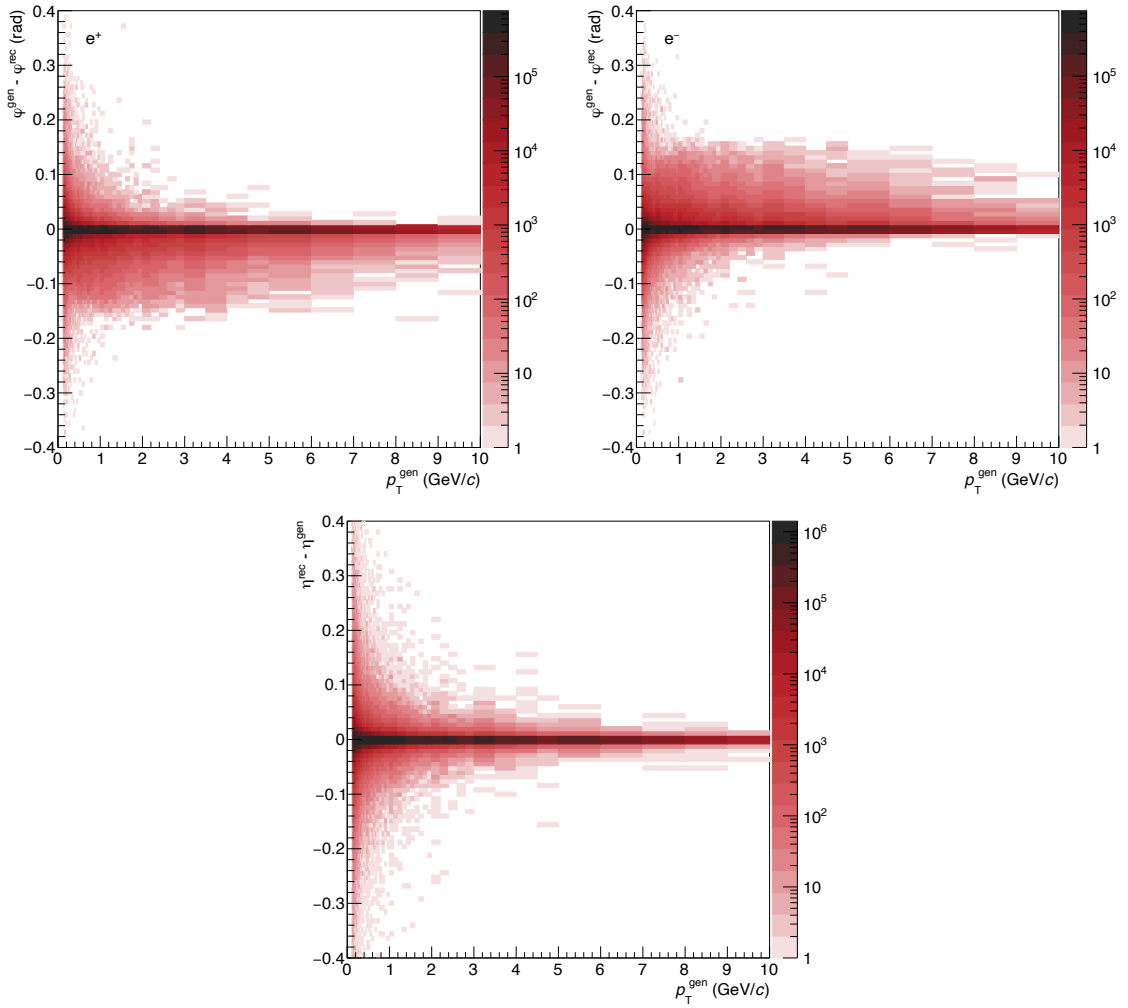

Figure 5.30.: The difference of reconstructed and generated azimuthal angle φ for positrons (top left) and electrons (top right) as well as the difference of generated and reconstructed η (bottom). All distributions are shown as a function of the generated p_T.

as a function of p_T^{gen} is shown. Again a narrow distribution around 0 with strongly suppressed tails is seen. No difference depending on the charge was observed.

The smearing is then applied to p_T^{gen}, φ^{gen} and η^{gen} by adding random number generated from the respective distributions (σ) to derive the smeared kinematic quantities p_T^s, φ^s and η^s of the decay products of the original particle:

$$p_T^s = p_T^{gen} + \sigma_{p_T} \cdot p_T^{gen}, \tag{5.15}$$

$$\varphi^s = \varphi^{gen} + \sigma_\varphi, \tag{5.16}$$

$$\eta^s = \eta^{gen} + \sigma_\eta. \tag{5.17}$$

The smeared quantities are used to calculate the m_{ee} and $p_{\mathrm{T,ee}}$ distributions. By applying this procedure, the cocktail calculations include the detector resolution and can be compared directly to the measured spectra. The inputs used for the generation of the particles will be discussed in the following.

5.6.1 Light-Flavour Dielectron Cocktail

The contributions of light-flavour hadron decays to the dielectron spectrum are generated with the phenomenological event generator EXODUS [140] which uses parameterised hadron p_{T} spectra to simulate Dalitz and resonance decays. In the case of this analysis, the starting point of the light-flavour cocktail is the spectra of $\pi^{\pm}$ and ϕ mesons. The spectra were measured in minimum bias p–Pb collisions at $\sqrt{s_{\mathrm{NN}}} = 5.02$ TeV by the ALICE collaboration [141, 142]. To use them in the cocktail creation both spectra are parameterised as shown in Fig. 5.31.

The top panel shows the measured data as well as a parameterisation based on a modified Hagedorn function with five free parameters defined as [143]:

$$\frac{\mathrm{d}N}{\mathrm{d}p_{\mathrm{T}}} = p_{\mathrm{T}} \cdot A \cdot \left[\exp(B \cdot p_{\mathrm{T}} + C \cdot p_{\mathrm{T}}^2) + \frac{p_{\mathrm{T}}}{D}\right]^{-E}. \tag{5.18}$$

Here p_{T} indicated the transverse momentum of the particle while A, B, C, D and E are the free parameters of the function. In the middle and bottom panel of Fig. 5.31 the ratio of the measured data and the corresponding parameterisation is shown for the $\pi^{\pm}$ and the ϕ spectrum, respectively. Both measurements are described well in this approach. To propagate the systematic uncertainty of the measurement to the final cocktail, the data are coherently shifted up and down within the given point-by-point correlated uncertainties and the parameterisations are repeated.

These parameterisations are then used further to estimate the contributions of light-flavour hadron decays with a dielectron in the final state. The relevant hadrons and their decays are listed in Tab. 5.6. The table lists also the respective branching ratios with their uncertainties, as well as additional ingredients that are used to construct the relevant spectrum from the $\pi^{\pm}$ parameterisation. In the following, the way these additional ingredients for the cocktail calculations are used are discussed in detail.

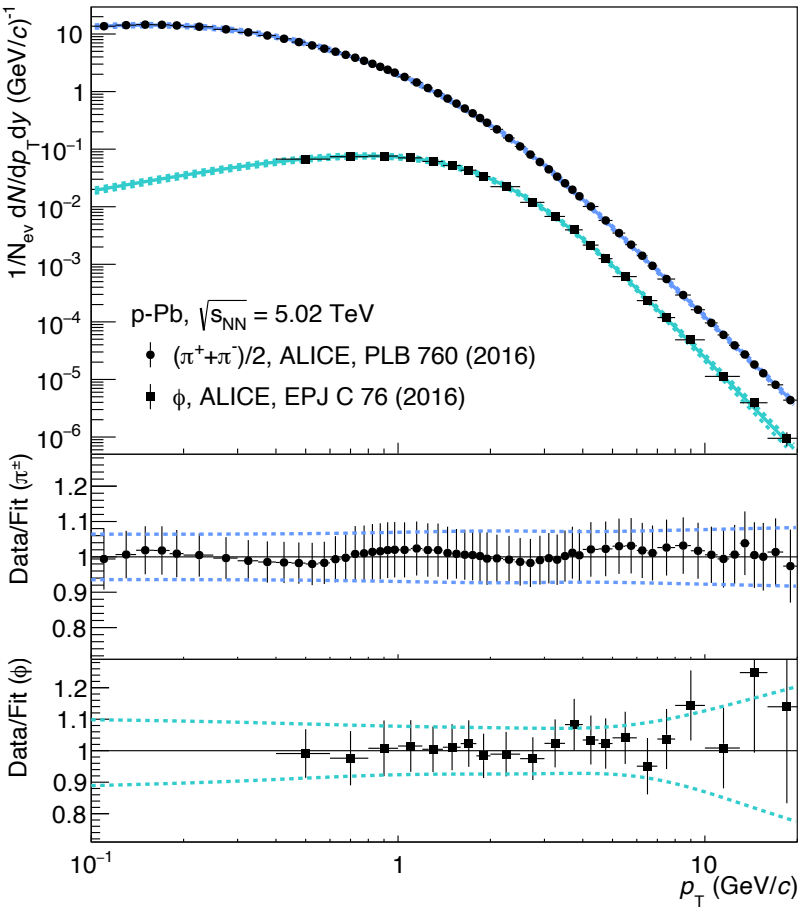

Figure 5.31.: Top panel: Measurements of $\pi^{\pm}$ and ϕ-meson p_{T} spectra in p–Pb collisions at $\sqrt{s_{\mathrm{NN}}} = 5.02$ TeV [141, 142]. The quadratic sums of systematic and statistical uncertainties are indicated by the vertical bars. The data are parameterised with a modified Hagedorn function that contains five free parameters as described in the text. The uncertainty is estimated by coherently shifting the data points up and down within the given systematic uncertainties. Middel (bottom) panel: Ratio of the measured $\pi^{\pm}$ (ϕ) p_{T} spectrum to the parameterisation, the uncertainty evaluated as described is indicated in the dashed lines.

5.6.1.1 Neutral Pions

The contribution of neutral pions to the dielectron spectrum is estimated by fitting the measured charged pion spectrum. The reasoning is that most of the yield is located at small p_{T} where the neutral pion measurements lack precision, if data is available at all. There is no measurement available in p–Pb collisions at $\sqrt{s_{\mathrm{NN}}} = 5.02$ TeV. Given isospin-symmetry the production of charged and neutral pions should be the same. However, contributions from isospin-violating decays, mainly of η mesons [3], lead to an imbalance in the measured spectra. Since the

Parameter	$\pi^{\pm}$	ϕ
A	$286.143^{+18.592}_{-18.618}$	$0.198^{+0.02}_{-0.024}$
B	$-0.252^{+0.001}_{-0.001}$	$-0.508^{+0.005}_{-0.006}$
C	$-0.148^{+0.003}_{-0.004}$	$-0.018^{+0.007}_{-0.014}$
D	$0.635^{+0.001}_{-0.001}$	$1.738^{+0.04}_{-0.079}$
E	$6.155^{+0.008}_{-0.009}$	$6.466^{+0.097}_{-0.173}$

Table 5.5.: Parameters of a modified Hagedorn function as defined in eq. 5.18 to describe p_{T}-differential spectra of $\pi^{\pm}$ and ϕ mesons in p–Pb collisions at $\sqrt{s_{\mathrm{NN}}} = 5.02$ TeV as measured by the ALICE collaboration [141, 142]. The uncertainties are estimated by coherently shifting the data up and down within the given point-by-point correlated uncertainties.

particle	decay	branching ratio	input
π^0	$\mathrm{e^+e^-}\gamma$	$(1.2 \pm 0.4) \times 10^{-2}$	$\pi^{\pm}$ [141] + correction
η	$\mathrm{e^+e^-}\gamma$	$(7 \pm 0.4) \times 10^{-3}$	η/π^0 (World data [144–150])
η'	$\mathrm{e^+e^-}\gamma$	$(4.73 \pm 0.27) \times 10^{-4}$	m_{T} scaling
	$\mathrm{e^+e^-}\omega$	$(2 \pm 0.4) \times 10^{-4}$	
ρ	$\mathrm{e^+e^-}$	$(4.7 \pm 0.05) \times 10^{-5}$	$\rho/\pi^{\pm}$ [151]
ω	$\mathrm{e^+e^-}$	$(7.4 \pm 0.15) \times 10^{-5}$	$\omega/\pi^{\pm}$ ratio (PHENIX [152])
	$\mathrm{e^+e^-}\pi^0$	$(7.7 \pm 0.6) \times 10^{-4}$	
ϕ	$\mathrm{e^+e^-}$	$(2.97 \pm 0.034) \times 10^{-4}$	measurement [142]
	$\mathrm{e^+e^-}\pi^0$	$(1.3 \pm 0.1) \times 10^{-5}$	
	$\mathrm{e^+e^-}\eta$	$(1.08 \pm 0.04) \times 10^{-4}$	

Table 5.6.: Summary of light flavour hadrons and the decay channels with dielectrons in the final state. Each decay channel is listed with the branching ratio that was used in the cocktail calculation and the uncertainty that is based on the particle data group values [3]. In addition the

extra neutral pions stem from decays, the main difference in the spectra of neutral and charged pions is expected at low momenta where feed-down contributes. A blastwave-inspired model [153] was used to estimate the additional contribution and estimate the imbalance of $\pi^{\pm}/\pi^0$ [154]. The expected ratio is shown in Fig. 5.32. As expected, the effect does not change the ratio for momenta larger than 1 GeV/c, but shows a significant effect at small p_{T}. In addition to the correction function and its uncertainties, a dashed line at 0.4 GeV/c indicates the kinematic limit in this analysis introduced by the fiducial selection of the electron candidates of $p_{\mathrm{T}} > 0.2$ GeV/c.

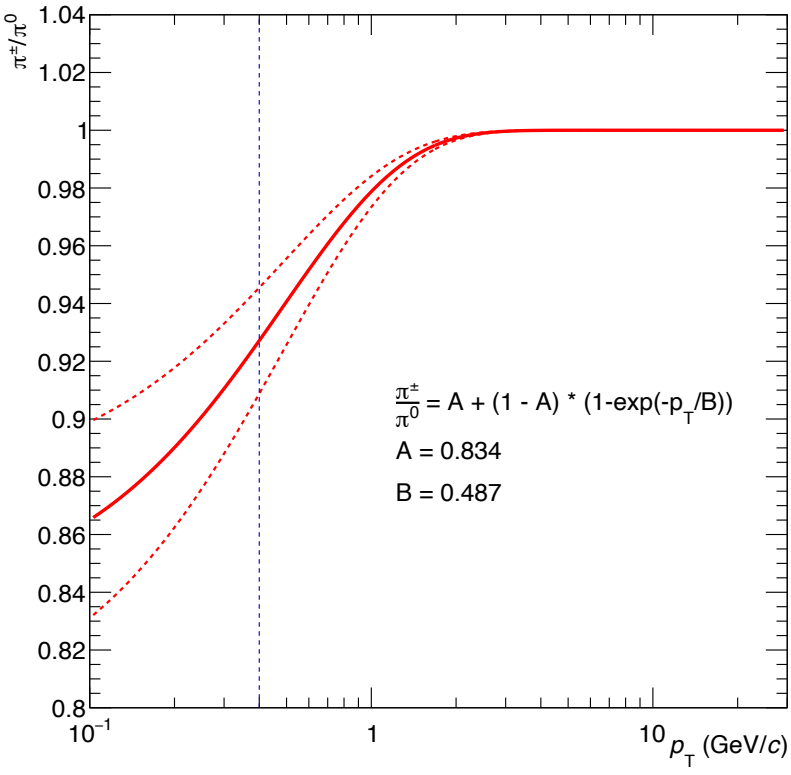

Figure 5.32.: Expected ratio of $\pi^{\pm}$ to π^{0} based on a blast wave inspired model [153] that describes hadron spectra at low p_{T}. The model includes strong and electromagnetic decays. Expected uncertainties are indicated by the dashed lines. The fiducial limit based on the selection criterion of $p_{\mathrm{T,e}} > 0.2$ GeV/c is indicated by the dashed blue line.

This, together with the kinematics of the Dalitz decay, reduces the effect on the final cocktail to a correction of about 2%.

5.6.1.2 η mesons

The parameterisation of the η meson is based on measured η/π^{0} ratios. The ratio used is a parameterisation of all available data in small collisions systems over a wide energy range [144–150]. The data are shown in Fig. 5.33 as a function of p_{T}. It can be observed that the data are well in agreement with each other. On top of the available world data the latest preliminary measurement of ALICE is shown which follows the overall trend of the world data. The ALICE and PHENIX points cover a p_{T} range from 0.4 to 30 GeV/c. The low-p_{T} range can be extended by measurements of the CERES/TAPS collaboration which measured η and π^{0} mesons in fixed target collisions at the CERN SPS. Together with the data, heuristic

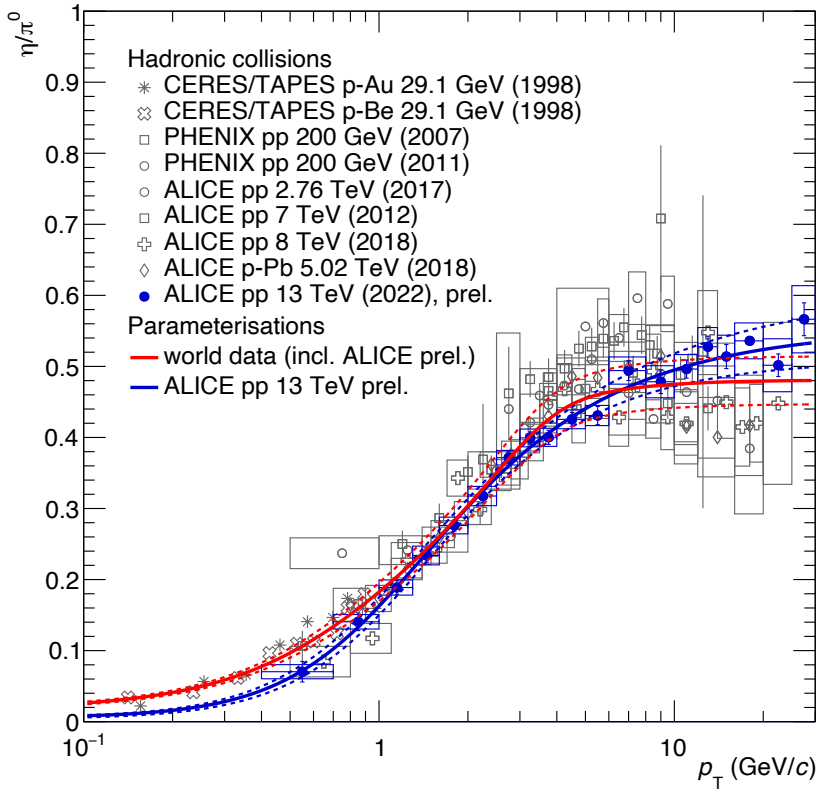

Figure 5.33.: Summary of η/π^0 measurements in hadronic collisions at different $\sqrt{s_{\mathrm{NN}}}$ [144–150] including preliminary data from the ALICE collaboration in pp collisions at $\sqrt{s} = 13$ TeV (blue markers). The data are in agreement with each other over a wide range of energies. Parameterisations inspired by m_{T} scaling of the full data set and only the preliminary measurement are shown in the red and blue curves, respectively.

parameterisations inspired by m_{T} scaling of the full available data including the preliminary measurement of ALICE and the preliminary data alone are shown in red and blue, respectively. While the two parameterisations agree for p_{T} above 1 GeV/c, at lower p_{T} a significant difference is observed, due to the constraints from the CERES/TAPS measurements. Used for this analysis is the parameterisation based on the full set of measurements. The η input spectrum for the cocktail is then constructed as:

$$\frac{1}{N_{\mathrm{ev}}}\frac{\mathrm{d}N_{\eta}}{\mathrm{d}p_{\mathrm{T}}\mathrm{d}y} = \frac{1}{N_{\mathrm{ev}}}\frac{\mathrm{d}N_{\pi^0}}{\mathrm{d}p_{\mathrm{T}}\mathrm{d}y} \times \frac{\frac{\mathrm{d}N_{\eta}}{\mathrm{d}p_{\mathrm{T}}\mathrm{d}y}}{\frac{\mathrm{d}N_{\pi^0}}{\mathrm{d}p_{\mathrm{T}}\mathrm{d}y}}. \tag{5.19}$$

The sources of uncertainties taken into account are the uncertainties on the π^0 spectrum, i. e. the uncertainty on the $\pi^{\pm}$ parameterisation and the uncertainty on the $\pi^{\pm}/\pi^0$ ratio, the uncertainty on the η/π^0 parameterisation of about $\pm 7\%$, as

well as the uncertainty of the $\eta \to \gamma e^+e^-$ branching ratio (6%). All uncertainties are assumed to be uncorrelated.

5.6.1.3 ω and ρ meson

The input parameterisations of the ρ and ω mesons are based again on ratios of measured spectra and the pion spectrum measured at different energies and collision systems. The data and parameterisations are shown in Fig. 5.34 for the $\rho/\pi^{\pm}$ and the ω/π^0 ratio left and right, respectively. The $\rho/\pi^{\pm}$ ratio was measured by the

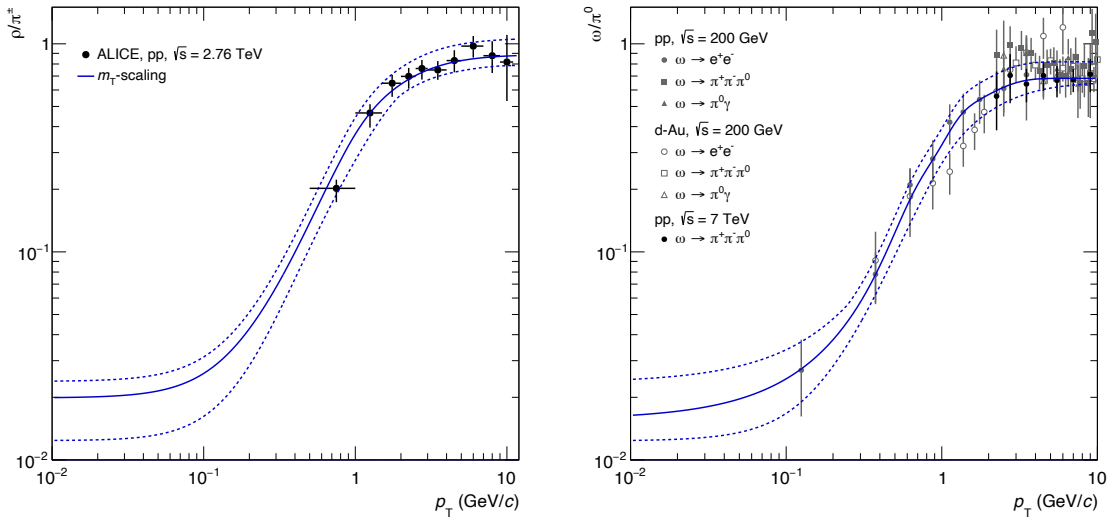

Figure 5.34.: Measurement of the $\rho/\pi^{\pm}$ ratio in pp collisions by the ALICE collaboration at $\sqrt{s} = 2.76$ TeV [151] (left). The data are parameterised using m_{T} scaling for $p_{\mathrm{T}} > 5$ GeV/c with a constant value of 0.82. The uncertainties shown in the dashed lines are based on shifting the constant value up by 20% for the upper uncertainty and by applying an ad-hoc parameterisations to the data points after shifting them down coherently within their systematic uncertainties. Measurements of ω/π^0 ratios at different energies and in pp and dAu collisions by the ALICE [155] and the PHENIX [152, 156] collaborations. The ALICE measurements were perfomed at $\sqrt{s} = 7$ TeV in pp collisions, while PHENIX measured in pp and dAu collisions at $\sqrt{s_{\mathrm{NN}}} = 200$ GeV/c. An ad-hoc parameterisation of the ALICE data together with the PHENIX pp measurement of $\omega \to e^+e^-$ was performed for the central value. For the upper uncertainty the data were shifted up coherently within their systematic uncertainty, while the lower uncertainty is given by m_{T} scaling with a high-p_{T} constant of 0.62.

ALICE collaboration in pp collisions at $\sqrt{s} = 2.76$ TeV [151] in the range of 0.5 $< p_{\mathrm{T}} <$ 11 GeV/c. A constraint at low p_{T} is missing from the data. Therefore, m_{T} scaling was chosen to parameterise the spectrum. The result of the m_{T}-scaling curve with a high-p_{T} constant of 0.82 is shown as the solid blue line in Fig. 5.34.

Following the analysis of dielectron production in peripheral Pb–Pb collisions [157] the uncertainties are estimated twofold. While the upper uncertainty is calculated by increasing the m_{T}-scaling constant by 20% the lower uncertainty is estimated by shifting the data points down coherently within their systematic uncertainties and performing a fit with an ad-hoc parameterisation. The uncertainties are shown as dashed lines.

Figure 5.34 right shows the ratio of ω/π^0 measured by the ALICE collaboration in pp collisions at $\sqrt{s} = 7$ TeV [155]. As in the case of the ρ the measurement does not provide constraints at low p_{T}. However, in this case, measurements of the PHENIX collaboration are available. The grey data points in Fig. 5.34 (right) show measurements in pp and dAu collisions at $\sqrt{s_{\mathrm{NN}}} = 200$ GeV [152, 156]. The uncertainties on the x-axis (indicating the bin width) are not shown to make the figure more readable. The measurements were performed in the $\omega \to \mathrm{e}^+\mathrm{e}^-$, $\omega \to \pi^+\pi^-\pi^0$ and the $\omega \to \pi^0\gamma$ decay channels for both systems. While all measurements align well at transverse momenta of a few GeV/c only the dielectron measurements can extend the measurement down to $p_{\mathrm{T}} = 100$ MeV/c. The parameterisation used for the cocktail calculations is then based on the PHENIX measurement in the dielectron channel in pp collisions together with the ALICE measurement in the three-pion channel. Again, a heuristic parameterisation similar to the η/π case is used as the central value. The upper uncertainty is based on the parameterisation after shifting the points up coherently within their systematic uncertainties. The lower uncertainty is given by m_{T} scaling with a high-p_{T} constant of 0.62, again following the dielectron analysis in peripheral Pb–Pb collisions.

5.6.2 Charm and beauty cocktails

In contrast to the light meson cocktail calculations, the charm and beauty contributions are not based on parameterised input spectra. While the p_{T} spectra of at least the charmed hadrons are measured with high accuracy, the nature of their appearance in the dielectron spectrum is very different. As described in the beginning, we do not see the decay of one single particle, which needs to be modelled, but a residual correlation of two semi-leptonic decays. Therefore, not only do the momenta of the single hadrons enter, but also the relative momentum vectors of two hadrons that emerge from the fragmentation of a primordial $Q\bar{Q}$ pair. To describe the contributions of the charm and beauty we use the measurements of the $\mathrm{c\bar{c}} \to \mathrm{e}^+\mathrm{e}^-$ and $\mathrm{b\bar{b}} \to \mathrm{e}^+\mathrm{e}^-$ cross-sections performed in the dielectron analysis in pp

collisions at $\sqrt{s} = 5.02$ TeV. In this publication, as well as the measurements in pp collisions at 7 and 13 TeV [92,93] the charm and beauty production cross sections at midrapidity were extracted by a two-dimensional parameterisation of the m_{ee}-$p_{\mathrm{T,ee}}$ spectrum with templates based on two different event generators in the IMR. The used generators are PYTHIA in version 6.4 with the Perugia 2011 tune [94, 158] as well as an NLO calculation of the cross-section (matrix element) of the heavy-quark production which is injected to the PYTHIA shower algorithm using the POWHEG method [95–98]. In all analyses the data in the IMR is described well by both approaches and the extrapolated cross sections using the effective branching ratios were both in agreement with FONLL calculations as well as measurements in the single HF hadron measurements in their hadronic decays. At the time it was then chosen to use the results based on POWHEG for the further dielectron analysis. With the update of the effective branching ratio described in the introduction of this thesis, I would argue, that this does not hold anymore. The cross sections estimated using the POWHEG method show tension with the measured and calculated charm cross sections as shown in Fig. A.2 (Appendix A), most likely overestimating the charm and then underestimating the beauty contributions. For this reason the cocktail is based on the PYTHIA calculations.

The MC is produced in the general framework on the grid. PYTHIA in version 6.4 is used with the Perugia 2011 tune [94, 158] and the CTEQ5 parton distribution functions calculated at leading order [159]. To enhance the statistical precision and minimize the computational time, the charmed mesons and baryons that are produced in minimum bias events are forced to decay in their semi-leptonic decay channels. The generated events are pp collisions at a centre-of-mass energy of $\sqrt{s_{\mathrm{NN}}} = 5.02$ TeV with an additional rapidity shift of $\Delta y = -0.465$ to account for the asymmetry in the p–Pb collision system. In the case of the cocktail for electrons from the decays of beauty hadrons, the only difference is that the decays of the hadrons are not forced. This is done to enable for example a B meson decay into a D meson without producing an electron in the decay, and then the D meson decays semi-leptonically. If the decays were forced to include an electron, this kind of decay would not be possible and a B meson would always lead to an ULS pair as described before. The rapidity distribution of the heavy-flavour quarks is shown in Fig. 5.35. The distributions are normalised to unity to be comparable. The maxima of both distributions are shifted to positive rapidity due to the boost of the centre of mass system with respect to the lab system by 0.465. Furthermore, the beauty distribution is more narrow than the charm distribution. This is understood

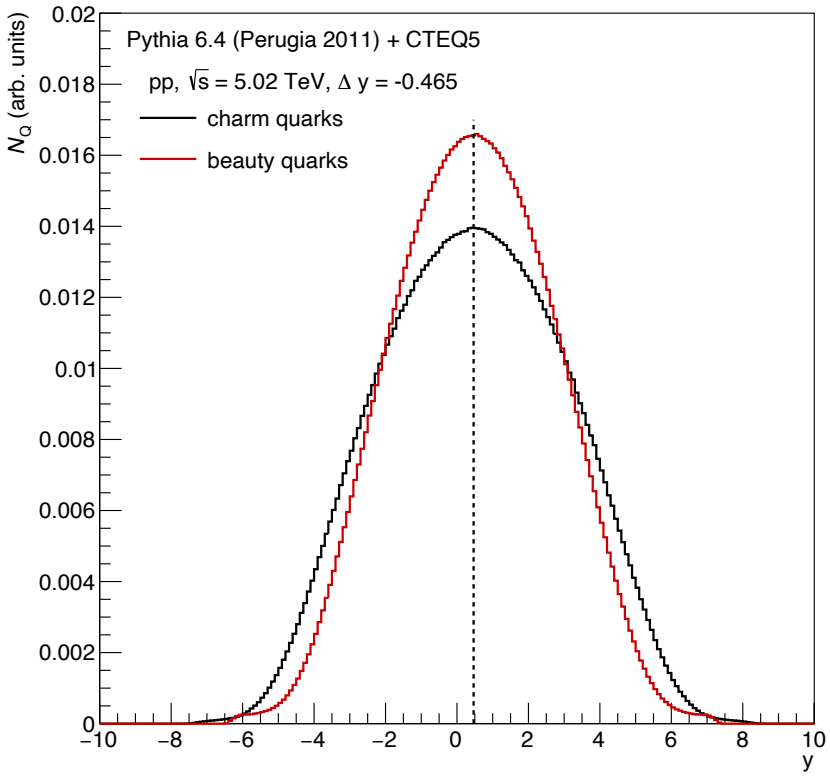

Figure 5.35.: Rapidity distributions of charm and beauty quarks generated with PYTHIA 6.4 (Perugia 2011) [94, 158] and CTEQ5 pdf at leading order [159] for pp collisions with $\sqrt{s} = 5.02$ TeV with an additional boost of the collision system of $\Delta y = -0.465$ to mimic the asymmetry in the p–Pb system.

from the different masses of the heavy quarks and the momentum transfer in the scattering needed to produce a heavy-quark pair. To normalise the generated m_{ee} and p_{T} spectra the the charm and beauty cross sections measured in pp collisions at $\sqrt{s} = 5.02$ TeV in the dielectron channel [160] are used. At midrapidity these are $\sigma_{\mathrm{c\bar{c}}}|_{y=0} = 0.524$ mb and $\sigma_{\mathrm{b\bar{b}}}|_{y=0} = 0.034$ mb. To scale the pp collisions to p–Pb collisions the nuclear overlap function for minimum bias p–Pb collisions is used with $T_{\mathrm{pA}} = 0.09923 \pm 0.0017$ [161]. To account for the forced decays in the semi-leptonic channel for the charmed hadrons, also the semi-leptonic branching ratio that was used to estimate this cross-section which is 9.6% is needed. The scaling factor for the normalisation of the spectra to the heavy quark production cross section can be calculated as:

$$S = \frac{T_{\mathrm{pA}} \cdot BR_{\mathrm{SL}}^2}{\mathcal{L}_{\mathrm{Q\bar{Q}}}}, \tag{5.20}$$

with the heavy-flavour luminosity $\mathcal{L}_{\mathrm{Q\bar{Q}}}$ given as the number of heavy quark pairs at midrapidity divided by the production cross section. The number of heavy quark pairs is calculated by the integral of the histograms shown in 5.35 as

$$\mathcal{L}_{\mathrm{Q\bar{Q}}} = \frac{1}{\sigma_{\mathrm{Q\bar{Q}}}} \int_{-0.5}^{0.5} \frac{N_{\mathrm{Q}}}{2} dy = \frac{1}{\sigma_{\mathrm{Q\bar{Q}}}} \int_{-0.5}^{0.5} N_{\mathrm{Q\bar{Q}}} dy. \tag{5.21}$$

Since this method uses the measurement of the heavy-flavour cross sections in the dielectron channel, the uncertainties on the decay branching ratios and the fragmentation fractions cancel. The uncertainty from the data in the pp at $\sqrt{s} = 5.02$ TeV as well as the uncertainty on T_{pA} of are taken into account, which leads to a total uncertainty on the charm cocktail of 12.6% and for the beauty of 13.2%.

5.6.3 J/ψ cocktail

The J/ψ input spectrum is based on the measurement of its production by the ALICE collaboration in p–Pb collisions at $\sqrt{s_{\mathrm{NN}}} = 5.02$ TeV [162]. To be consistent with other cocktail inputs, the published p_{T} differential cross sections were translated into yields using the given minimum bias cross-section in p–Pb collisions $\sigma^{\mathrm{MB}}_{\mathrm{pPb}} = 2.09 \pm 0.7$ b estimated in a van der Meer scan [163]. The data with its statistical and systematic uncertainties is shown in Fig. 5.36 together with a parameterisation that is used as input for the cocktail. The parameterisation is the same empirical function used in [162] to determine the $\langle p_{\mathrm{T}} \rangle$:

$$\frac{\mathrm{d}^2 N_{J/\psi}}{\mathrm{d}p_{\mathrm{T}}\mathrm{d}y} = C \times \frac{p_{\mathrm{T}}}{\left[1 + \left(\frac{p_{\mathrm{T}}}{p_0}\right)^2\right]^n}. \tag{5.22}$$

The dashed lines indicate the systematic uncertainties of the parameterisation which are estimated by shifting the data points up and down coherently within their uncertainties and repeating the parameterisation.

5.6.4 Cocktail uncertainties

There are several uncertainties that enter the cocktail calculations, and they exhibit different correlations. While the uncertainty of the charm is fully independent for example of the neutral pion contribution, the pion and the η contributions are correlated since the η is calculated directly from the π^0 spectrum and the η/π^0 ratio. Then again, there is for example the ρ which is derived by m_{T}-scaling from

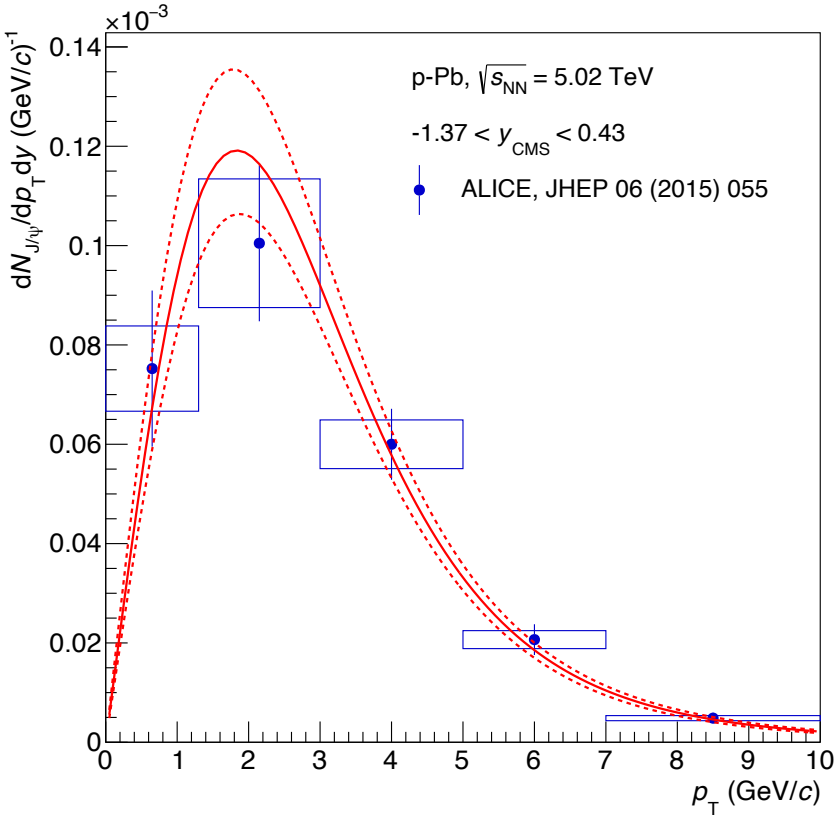

Figure 5.36.: Measurement of p_{T} differential yield of J/ψ in p–Pb collisions at $\sqrt{s_{\mathrm{NN}}} = 5.02$ TeV by the ALICE collaboration [162]. The data are parameterised with an empirical function. The dashed lines indicate the parameterisations after shifting the data coherently up and down within the systematic uncertainties.

the $\pi^{\pm}$ spectrum. In this case, the uncertainty on the $\pi^{\pm}$ needs to be propagated, while the uncertainty of the correction from $\pi^{\pm} \rightarrow \pi^{0}$ does not enter. To estimate the uncertainties on the cocktail calculations, each input is varied within its uncertainties while the other inputs are kept at their default values. From this, a complete cocktail is generated for the upper and lower uncertainties. By comparing the new cocktail with the default cocktail the uncertainties for a given variation are estimated. The uncertainties estimated for the different sources contributing to the light flavour part of the cocktail are summarised in 5.37 and presented as a function of m_{ee}. One can observe that the different uncertainties are relevant in different m_{ee} ranges. The parameterisation of the $\pi^{\pm}$ shows uncertainties up to a mass of the ω meson since the spectrum of the ω and the ρ are constructed from the measured $\omega(\rho)/\pi^{\pm}$ ratios and the parameterisation of the $\pi^{\pm}$ spectrum measured in p–Pb collisions. The $\pi^{\pm}/\pi^{0}$ correction is then relevant for the π^{0} contribution as well as the η contribution, since the η is again constructed based on the ratio of η/π^{0}. The uncertainty of the latter

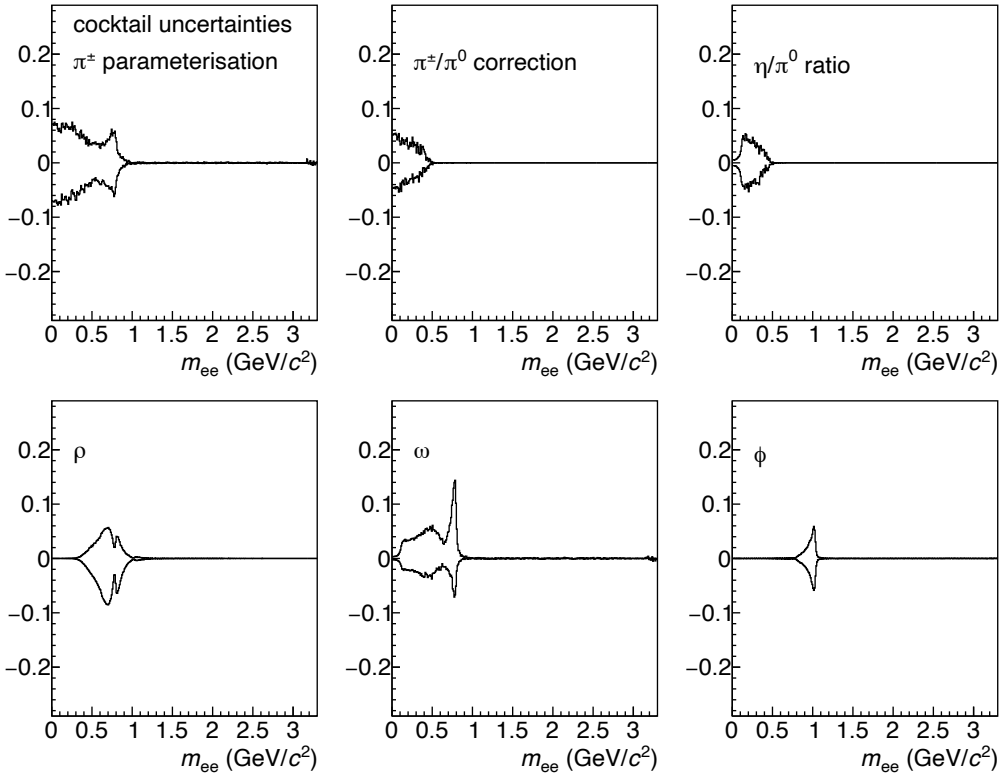

Figure 5.37.: Summary of the cocktail uncertainties as a function of the invariant mass for the different inputs for the light flavour cocktail.

is only relevant in the η mass region. At masses below the π^0 one can observe that this uncertainty drops, which is expected since the relative contribution of the η is only small. The same effect can be observed for the uncertainties from the ω which are the highest at the mass pole of the ω but not negligible at lower masses. This is due to the contribution of the $\omega \to e^+e^-\pi$ decay. The ρ and ϕ do not exhibit tails to lower masses since their Dalitz decays have very small yields compared to the other sources. The uncertainties of the charm, beauty and J/ψ contributions are shown in Fig. 5.38 as a function of the invariant mass. The structures in the $c\bar{c}$ and $b\bar{b}$ contributions are again due to the relative contribution of the respective source at a given mass. They are most pronounced for the charm contribution since the charm shows a broad continuum, and the relative contribution is then reduced at the pole masses of the ω and the ϕ and close to vanishing when going to $m_{ee} \to 0$, since here the π^0 contribution dominates. Also visible is the contribution of the J/ψ. While at masses smaller than the J/ψ nominal mass, the tail partially suppresses the charm contribution. For the beauty contribution, the same features are visible, however slightly damped, since the beauty contribution is outshined by the charm

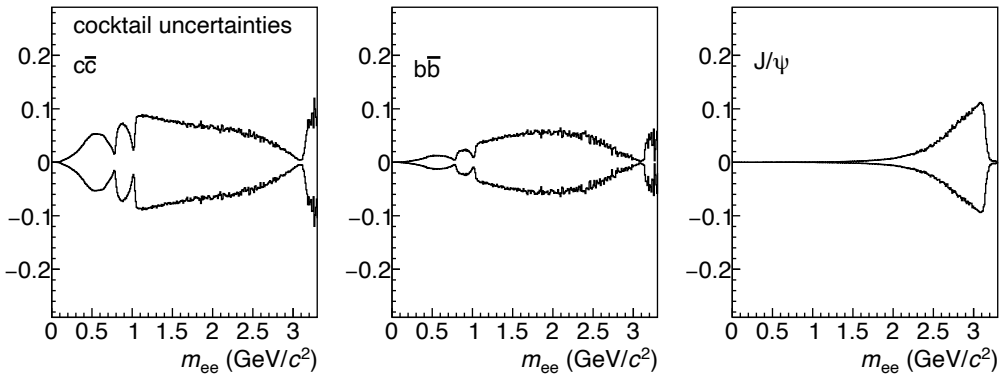

Figure 5.38.: Summary of the cocktail uncertainties as a function of the invariant mass for the different inputs for the charm, beauty, and J/ψ contribution.

contribution over the whole mass range. Finally, the uncertainties on the branching ratios of the mesons into dielectrons as listed in Tab. 5.6 are taken into account. Figure 5.39 shows the full cocktail as a function of invariant mass (left) integrated over $p_{\mathrm{T,ee}}$ and as a function of $p_{\mathrm{T,ee}}$ (right) integrated over the invariant mass. In both

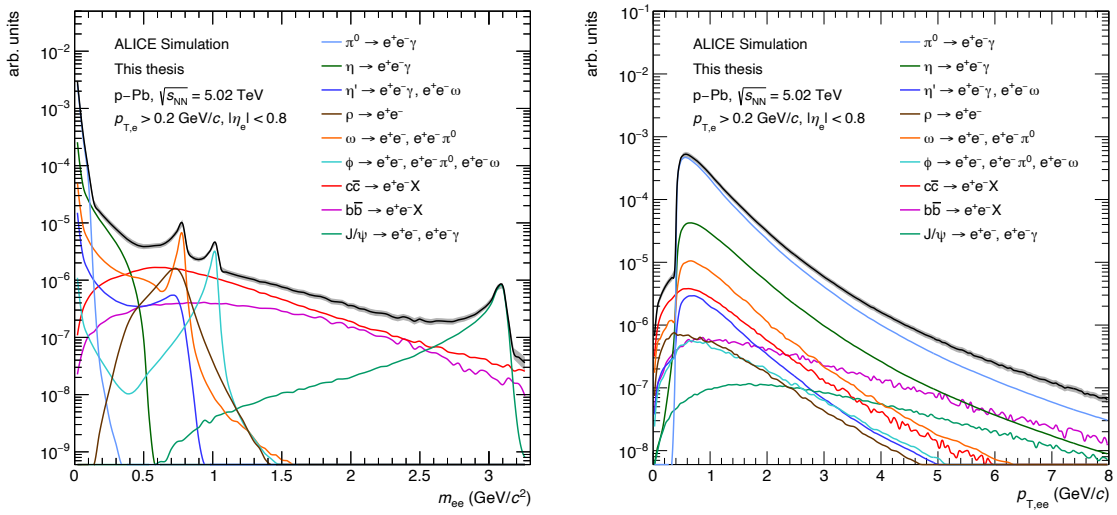

Figure 5.39.: Cocktail calculations for the contributions of known hadronic sources to the dielectron spectrum in p–Pb collisions at $\sqrt{s_{\mathrm{NN}}} = 5.02$ TeV as a function of m_{ee} (left) and $p_{\mathrm{T,ee}}$ (right). Decay electrons are smeared according to full MC simulations and filtered through the fiducial selection of the analysis.

cases, the sum of the single contributions is shown as a solid black line, with a grey band indicating the uncertainty of the sum. As described above the decay electrons are smeared and the same fiducial selection as in the analysis ($p_{\mathrm{T}} > 0.2$ GeV/c, $|\eta| < 0.8$) is applied. As expected, the peaks in the mass spectrum show slight asymmetries which are related to the energy loss due to bremsstrahlung included

in the smearing procedure. In Fig. 5.39 the pair transverse momentum spectrum integrated over all invariant masses shows a clear drop for $p_{\mathrm{T,ee}} < 0.4$ GeV/c. This is due to the selection of electron candidates with $p_{\mathrm{T}} > 0.2$ GeV/c.

Chapter 6

Model Comparisons

In the following, the measured data are compared to different expectations of the production. Starting with a cocktail comparison, the baseline is established. Furthermore, comparisons to a cocktail modified to account for charm suppression due to cold nuclear matter effects are discussed. The possibility of an additional source of dielectrons is explored by adding calculations from a fireball model to the baseline.

6.1 Cocktail comparison

The hadronic cocktail calculations are compared to the yield of dielectrons as a function of invariant mass in Fig. 6.1. As described before, the measurement is corrected for efficiency losses in the signal extraction but not for acceptance effects due to the fiducial selection of the electrons ($p_{\mathrm{T}} < 0.2$ GeV/c and $|\eta| < 0.8$) The data is represented as blue markers while the sum of the different hadronic sources estimated in the cocktail approach is shown as a black line. The statistical uncertainties of the measurement are shown as bars on the markers, while a box represents the systematic uncertainties. The uncertainty on the cocktail calculation is shown as a grey band. The upper panel of Fig. 6.1 shows the also the different cocktail contributions. In favour of readability, the single contributions of light flavour hadrons are summarised in the curve labelled "light flavour". The lower panel shows the ratio of the measured data to the cocktail calculations. Overall, a good agreement is observed within the uncertainties of the measurement and the cocktail calculations. Taking a closer look some variations are visible that could point to a systematic effect. The two data points in the mass region of the ω and ρ mesons are about 25% below the cocktail calculation. The data would suggest a less peaked spectrum in this mass

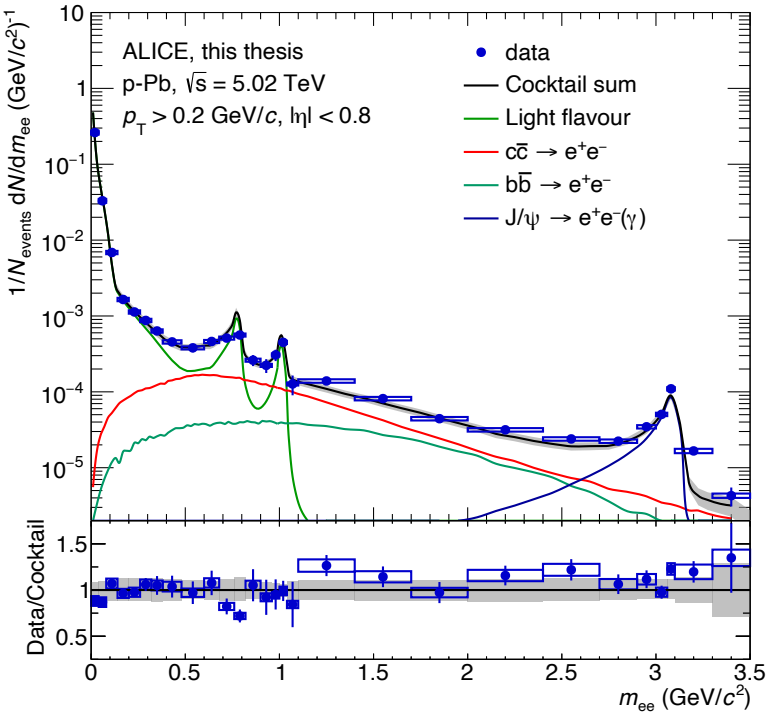

Figure 6.1.: Differential yield of dielectrons as a function of m_{ee} measured in p–Pb collisions at $\sqrt{s_{\mathrm{NN}}} = 5.02$ TeV. The data are compared to the hadronic cocktail with the gray band representing the total uncertainty on the hadronic cocktail.

region. It should be pointed out here that the cocktail calculations for both particles lack data recorded at LHC at low momenta. In addition, the ρ contribution was estimated using m_{T}-scaling which was seen to overestimate the particle yields at low p_{T} [164]. The ω/π^0 measurement used to constrain the cocktail, especially at low momenta where most yield is expected was carried out by the PHENIX collaboration in different collision systems at $\sqrt{s} = 200$ GeV [152,156,165]. While the ALICE data of the same measurement in pp collisions at $\sqrt{s} = 7$ TeV [155] tend to be on the lower edge of the PHENIX data where an overlap of the spectra is present, there is no data at lower momenta available. Also, event generators like PYTHIA or EPOS would predict a smaller ω/π ratio at higher collision energies and lower p_{T} which is the result of a larger feed-down contribution to the pions. For masses larger than the ϕ the data are on the upper edge of the systematic uncertainty of the cocktail. In the continuum between the ϕ and the J/ψ, the cocktail uncertainty is dominated by the charm contribution, which is based on the measurement of dielectrons from charm in pp collisions at $\sqrt{s} = 5.02$ TeV. Using a measurement in the same channel cancels all uncertainties that are related to the fragmentation and the branching ra-

tios. However, the precision of the data in the pp measurement is limited and leads to a finite uncertainty that is propagated to the cocktail calculations. To further investigate the spectra and better understand the contributions, in the following the $p_{\mathrm{T,ee}}$ spectra are shown in mass regions that are dominated by certain contributions.

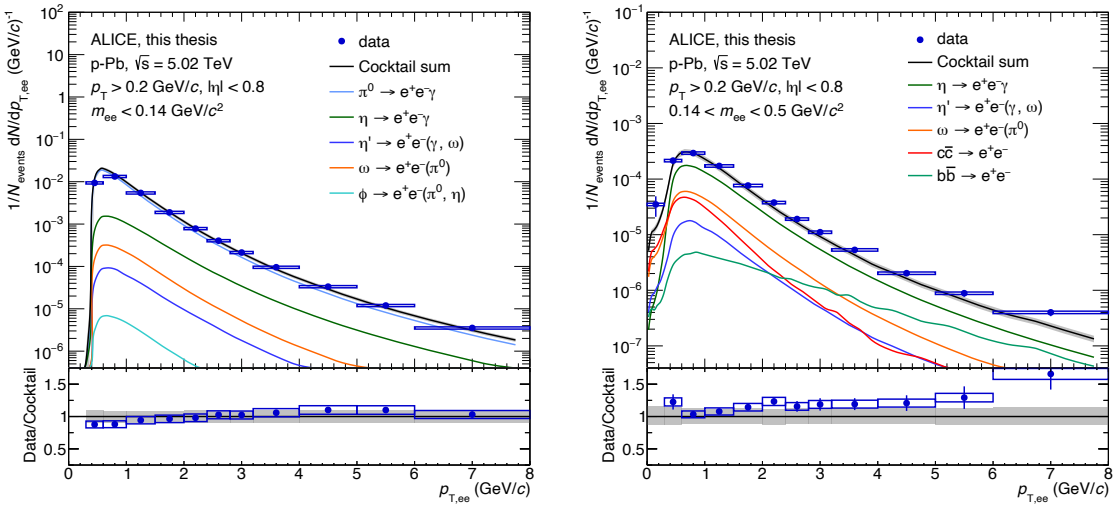

Figure 6.2.: Differential yield of dielectrons as a function of $p_{\mathrm{T,ee}}$ measured in p–Pb collisions at $\sqrt{s_{\mathrm{NN}}} = 5.02$ TeV in the ranges of $m_{\mathrm{ee}} < 0.14$ GeV/c^2 (left) and $0.14 < m_{\mathrm{ee}} < 0.5$ GeV/c^2 (right). The data are compared to the hadronic cocktail with the gray band representing the total uncertainty on the hadronic cocktail.

Figure 6.2 (left) shows the differential yield of dielectron production as a function of $p_{\mathrm{T,ee}}$ for $m_{\mathrm{ee}} < 0.14$ GeV/c^2. This mass interval is dominated by the Dalitz decays of the π^0. Overall a good agreement of the cocktail calculations is observed, while the points for $p_{\mathrm{T,ee}} < 1$ GeV/c are on the edge of the uncertainties. In Fig. 6.2 (right) the mass region is dominated mainly by the Dalitz decay of the η meson. Also, significant contributions from the $\omega \rightarrow \mathrm{e^+e^-}\pi^0$ as well as from charm and beauty are present. A similar feature as in the pion mass region is observed for the low $p_{\mathrm{T,ee}}$ points. It could point to an issue related to the acceptance boundaries of the measurement. In the ratios of both spectra, a slight slope is observed. As the cocktail contribution of the η is based on the parameterisation of $\pi^{\pm}$. It should be pointed out that the systematic uncertainties were estimated by coherently shifting the measured $\pi^{\pm}$ spectrum up and down. However, in this measurement, several different techniques depending on the p_{T} region measured are used which could also lead to an anti-correlation of the uncertainties which would explain a slope in the ratio. Another caveat is the availability of π^0 measurements at low p_{T}. While great efforts went into

the construction of the cocktail contribution it has to be pointed out that the η/π ratio is based on measurements of the π^0. However, the cocktail calculation then constructs the η spectrum based on the $\pi^{\pm}$ and an additional correction to account for the expected differences of the different charge configurations of the pion. This does not take into account previously observed differences in the charged and neutral pion measurements as they were presented in [164]. While addressing the mentioned caveats should lead to a better description of the dielectron data it should also lead to a reduction of the systematic uncertainties. However, the overall good description of the data is apparent and gives confidence that the cocktail method works.
The two mass ranges that have significant contributions from charm and beauty are the so-called low-mass region (LMR) and the intermediate-mass region (IMR) that are defined in this work as $0.5 < m_{\mathrm{ee}} < 1.1$ GeV/c^2 and $1.1 < m_{\mathrm{ee}} < 2.7$ GeV/c^2, respectively. The differential $p_{\mathrm{T,ee}}$ spectra of both are shown in Fig. 6.3. Unfortu-

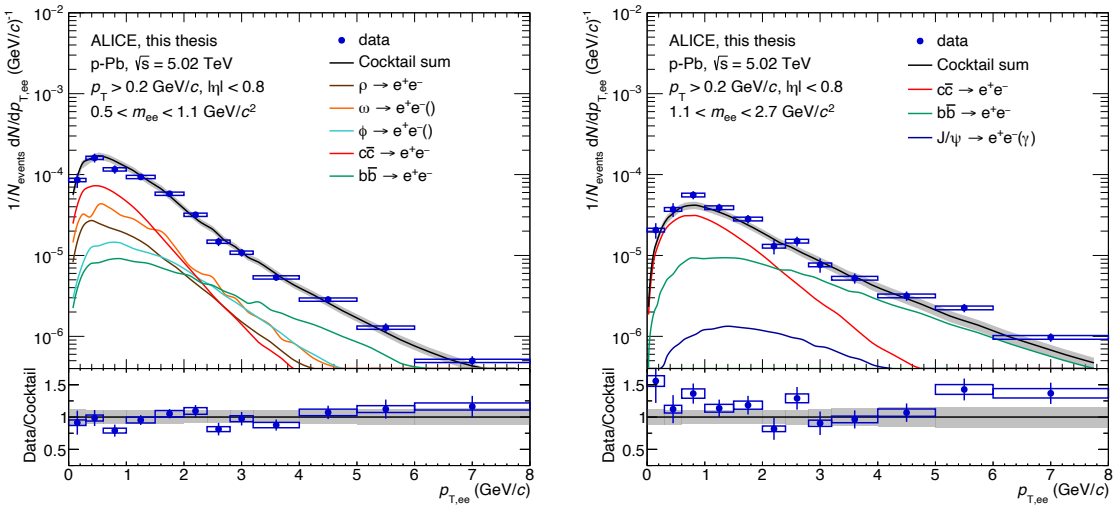

Figure 6.3.: Differential yield of dielectrons as a function of $p_{\mathrm{T,ee}}$ measured in p–Pb collisions at $\sqrt{s_{\mathrm{NN}}} = 5.02$ TeV in the ranges of $0.5 < m_{\mathrm{ee}} < 1.1$ GeV/c^2 (left) and $1.1 < m_{\mathrm{ee}} < 2.7$ GeV/c^2 (right). The data are compared to the hadronic cocktail with the grey band representing the total uncertainty on the hadronic cocktail.

nately, the data start to display sizable statistical uncertainties, which are on the order of, or larger than the systematic uncertainties. However, no large fluctuations are observed. In the mass region of $0.5 < m_{\mathrm{ee}} < 1.1$ GeV/c^2 the cocktail is overall in agreement with the data over the whole $p_{\mathrm{T,ee}}$ range. The main source of the dielectrons for $p_{\mathrm{T,ee}} < 2$ GeV/c is expected to be the decays of charmed hadrons, while for $p_{\mathrm{T,ee}} < 3$ GeV/c the beauty contribution is dominant. Less significant contributions from ω and ρ are expected in the range where the charm is dominant.

In the intermediate-mass region, the only contribution except charm and beauty is the J/ψ. Since the pole mass of the J/ψ is at larger momenta than the selected m_{ee} interval the contribution is mainly due to electrons in the decay that lost energy due to bremsstrahlung, or the radiative decay of the J/ψ including a γ in the final state. Although the most prevalent distributions in the two mass ranges are the charm and the beauty contributions, the description of the data is better in the lower mass region. In the IMR there is an indication for an underestimation of the data for $p_{\mathrm{T,ee}} < 2$ GeV/c and for $p_{\mathrm{T,ee}} < 5$ GeV/c. However, as discussed in Sec 2.3.3 a modification of the charm is expected due to cold nuclear matter effects.

6.2 Cold-Nuclear-Matter effects

To study the effect of the modified gluon content, the charm cocktail was modified according to the expectations based on sets of nuclear particle distribution functions (nPDF). A good description of the nuclear modification factor R_{pPb} of D mesons measured by ALICE [166] was achieved using pQCD NLO (MNR) calculations [167] together with the EPS09 [58] nuclear PDF set which is used in the following. This set was super-seeded by the newer EPPS16 [168] set. The main extension of the EPPS16 set is the inclusion of LHC data concerning W and Z [169–171] production as well as dijet data [172]. While there are more inclusions of data from deep inelastic scattering (DIS) and Drell Yan production, the LHC data significantly extends the reach of the fitted data to the high Q^2 and low x region. In addition to the LHC data, the treatment of the heavy quarks is changed together with the dependence of the nuclear modification on the quark flavour [168]. These changes lead to more free parameters in the global fits.

The inclusion of the nPDFs into the cocktail estimation was done by constructing the D-meson $R_{\mathrm{p}Pb}$ using the pQCD NLO (MNR) calculations [167] together with the EPS09 [58] as in [166]. To estimate the uncertainties, the 44 different sets of nPDFs provided with EPS09 were used [173]. A similar approach was followed to calculate the modification using EPPS16 [168] together with FONLL [47, 48]. The main difference is that here the $R_{\mathrm{p}Pb}$ was calculated on the charm quark level [174]. The propagation from the quark or meson to the modification as a function of p_{T} is done following a weighting procedure in the cocktail generation. The weight is calculated as

$$w_{\mathrm{ee}}(m_{\mathrm{ee}}, p_{\mathrm{T,ee}}) = \frac{R^{\mathrm{D/c}}_{\mathrm{pPb}}(p_{\mathrm{T},1}) + R^{\mathrm{D/c}}_{\mathrm{pPb}}(p_{\mathrm{T},2})}{2}, \tag{6.1}$$

with the dielectron weight for a given m_{ee} and $p_{T,ee}$ ($w_{ee}(m_{ee}, p_{T,ee})$) and the values of the nuclear modification factors at a given p_T of the original quark or meson mother ($R_{pPb}^{D/c}(p_{T,i})$) for both electrons of the pair. The resulting cocktail calculation as a function of m_{ee} is shown in Fig.6.4 (left). The solid lines show the central values of

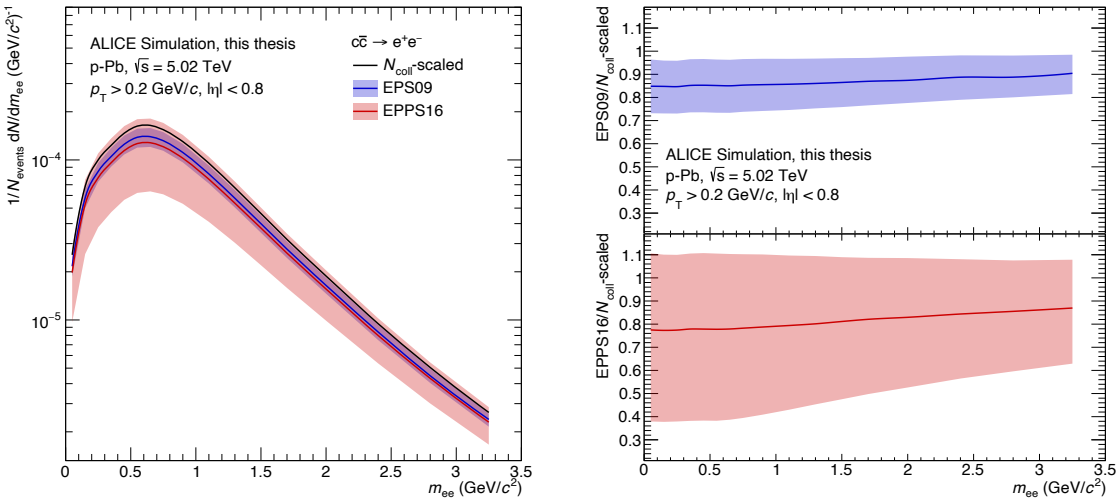

Figure 6.4.: Expected differential yield of dielectrons from charm decays as a function of m_{ee} measured in p–Pb collisions at $\sqrt{s_{NN}} = 5.02$ TeV based on cocktail calculations (left). The default hadronic cocktail is shown together with calculations in which the charm contribution is modified by the expected suppression based on nuclear particle distribution functions (nPDFs) EPS09 (blue) and EPPS16 (red). The bands represent the total uncertainty on the hadronic cocktails based on the nPDF uncertainties. Other uncertainties are not shown. The ratio of the cocktails including a modification is shown in addition to the EPS09 (top right) and the EPPS16 (bottom right) calculations

the calculations while the bands indicate the uncertainties that stem from the respective nPDF. In the case of both nPDF sets a suppression of the charm production is visible. The EPPS16 nPDF would suggest a slightly larger suppression, however, connected to a much larger uncertainty. This uncertainty is as mentioned above related to the treatment of the quarks in the parameterisation. To better quantify the size of the effects, the ratios to the charm contribution that was only scaled with the number of binary nucleon-nucleon collisions was calculated as it is shown in Fig. 6.4 (right). Both implementations of the CNM effects suggest a suppression that is slightly stronger at smaller masses. The EPS09 values range from 15% to 10% suppression, while EPPS16 indicates 20% to 15% suppression. Figure 6.5 shows the calculations as a function of $p_{T,ee}$ for the mass regions of $0.5 < m_{ee} < 1.1$ GeV/c^2 and $0.5 < m_{ee} < 1.1$ GeV/c^2. The observed features are very similar to the observations made for the mass dependence of the modifications. The larger suppression is

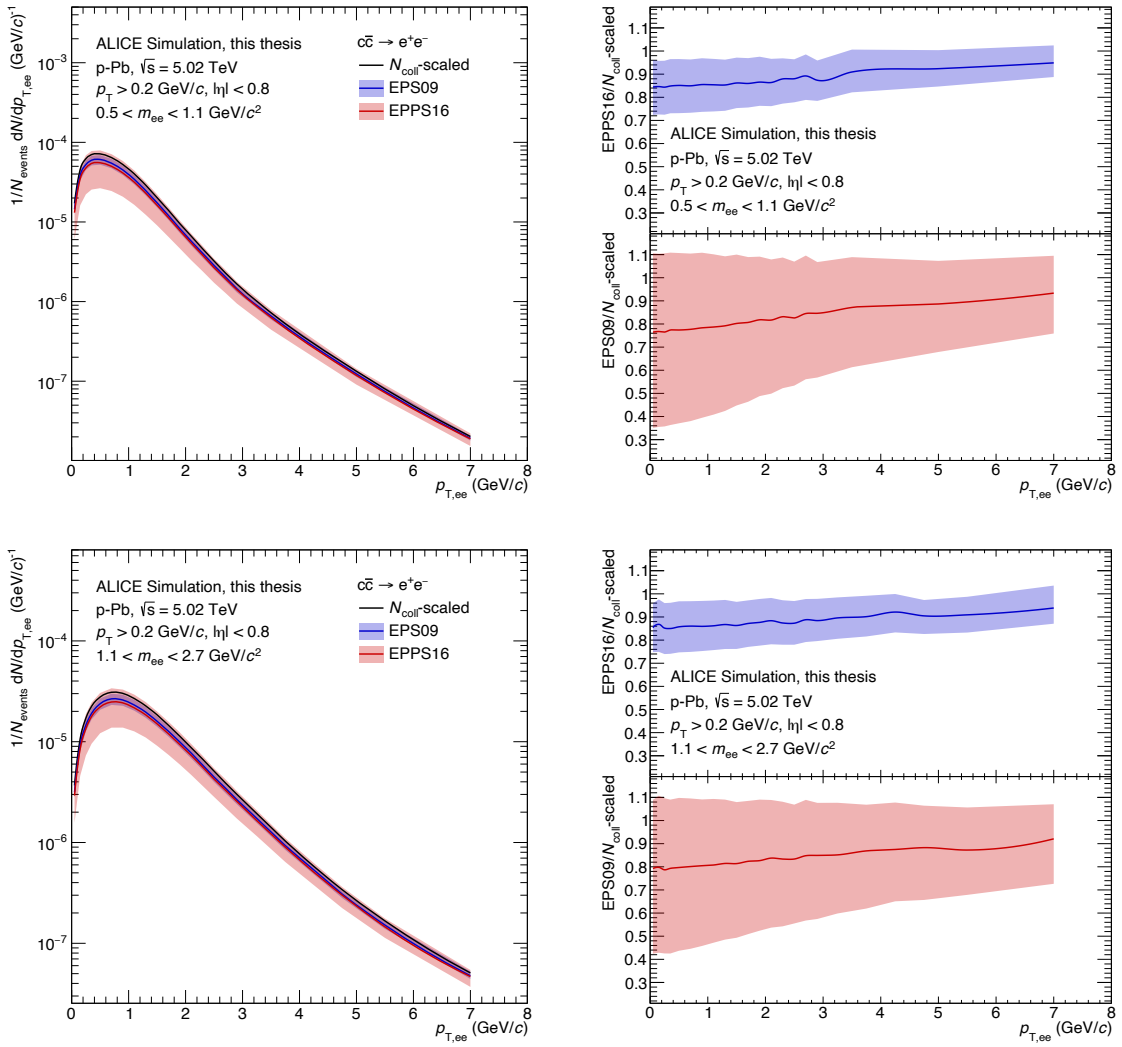

Figure 6.5.: Expected differential yield of dielectrons from charm decays as a function of $p_{\mathrm{T,ee}}$ measured in p–Pb collisions at $\sqrt{s_{\mathrm{NN}}} = 5.02$ TeV based on cocktail calculations (left) for $0.5 < m_{\mathrm{ee}} < 1.1$ GeV/c^2 (top) and $1.1 < m_{\mathrm{ee}} < 2.7$ GeV/c^2 (bottom). The default hadronic cocktail is shown together with calculations in which the charm contribution is modified by the expected suppression based on nuclear particle distribution functions (nPDFs) EPS09 (blue) and EPPS16 (red). The bands represent the total uncertainty on the hadronic cocktails based on the nPDF uncertainties. Other uncertainties are not shown. The ratio of the cocktails including a modification is shown in addition to the EPS09 and the EPPS16 calculations (right).

in both mass regions expected at low $p_{\mathrm{T,ee}}$ while the effect gradually lessens. No differences in the size of the effect depending on the relevant mass range are expected in this calculation. A comparison of the cocktail calculations including the CNM effects discussed above with the measurement of the differential dielectron yield as a function of m_{ee} is shown in Fig. 6.6 for the case using EPS09 (left) and EPPS16

(right). The main changes are as expected in the mass region between 0.5 GeV/c^2

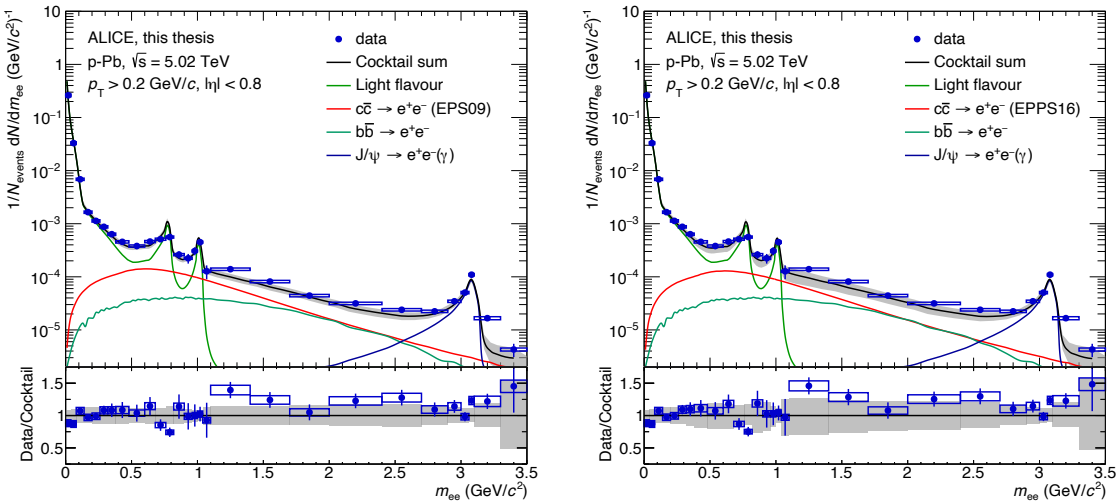

Figure 6.6.: Differential yield of dielectrons as a function of m_{ee} measured in p–Pb collisions at $\sqrt{s_{NN}} = 5.02$ TeV. The data are compared to the hadronic cocktail in which the charm contribution is modified by the expected suppression based on nuclear particle distribution functions (nPDFs) EPS09 (left) and EPPS16 (right). The grey bands represent the total uncertainty on the hadronic cocktails and include the nPDF uncertainties.

and 2.4 GeV/c^2 except around the pole masses of the ϕ and the ω/ρ. Inspecting the ratios in the lower panels it is apparent that in this region the data moves slightly above the central value of the cocktail in both cases. The effect is a bit larger for the EPPS16 case. However, since the uncertainties of the cocktail calculation now also need to take into account the model uncertainties, the effect is not more significant than in the vacuum case. The representation of the data as a function of $p_{T,ee}$ is shown in Fig. 6.7 in the mass regions of $0.5 < m_{ee} < 1.1$ GeV/c^2 (top) and $1.1 < m_{ee} < 2.7$ GeV/c^2 (bottom). In both cases, the comparison to the hadronic cocktail is shown including either modification of the charm cross section based on EPS09 (left) or EPPS16 (right). While in the lower of the two mass regions, the agreement with the cocktail seems to get better, the discrepancy of the data is larger for the intermediate-mass region at $p_{T,ee} < 2$ GeV/c as expected. While not significantly, the data are consistently above the central value of the cocktail which would indicate a possible additional source of dielectrons. This leaves room for speculation.

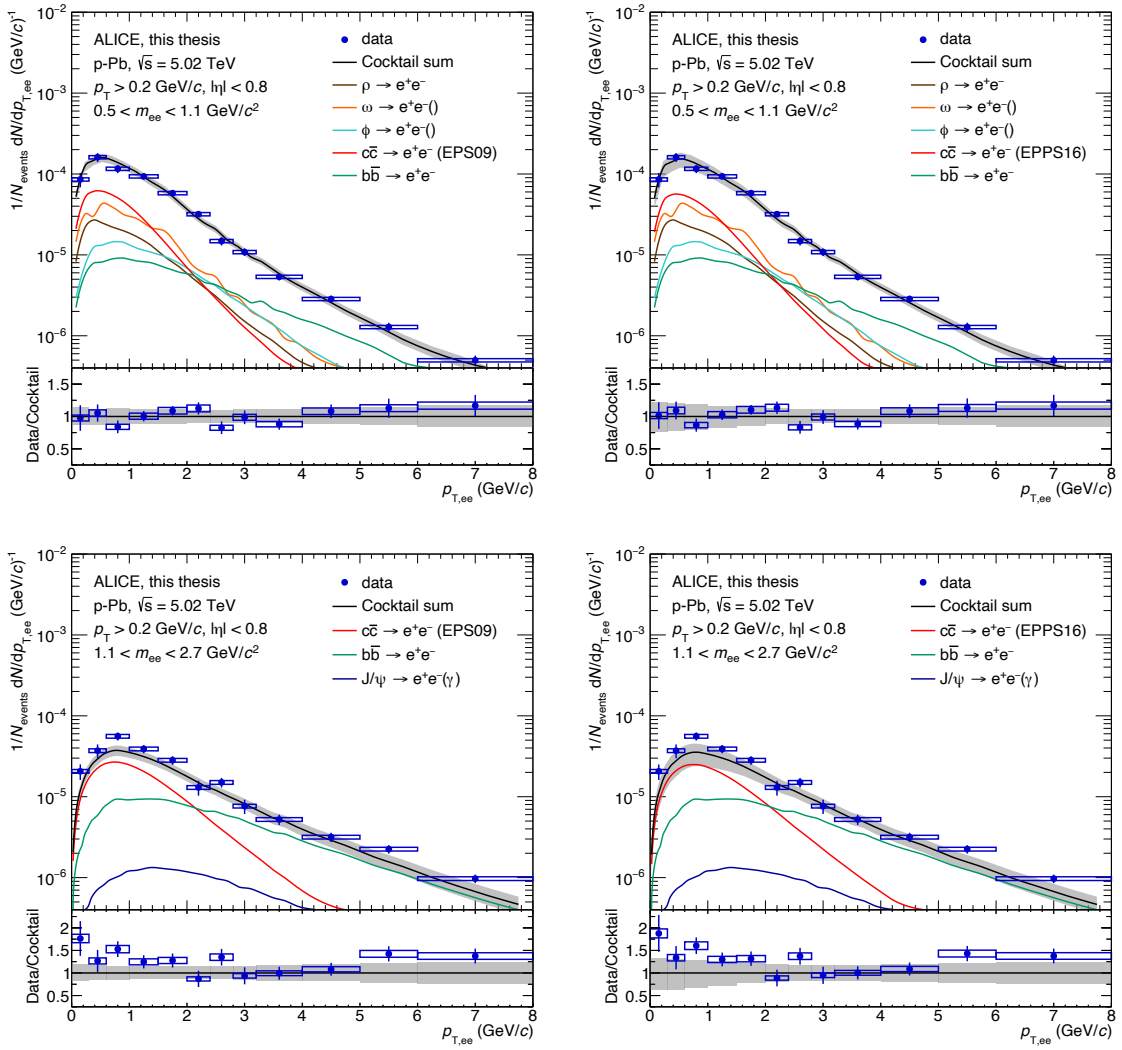

Figure 6.7.: Differential yield of dielectrons as a function of $p_{\mathrm{T,ee}}$ measured in p–Pb collisions at $\sqrt{s_{\mathrm{NN}}} = 5.02$ TeV in the ranges of $0.5 < m_{\mathrm{ee}} < 1.1$ GeV/c^2 (top) and $1.1 < m_{\mathrm{ee}} < 2.7$ GeV/c^2. The data are compared to the hadronic cocktail in which the charm contribution is modified by the expected suppression based on nuclear particle distribution functions (nPDFs) EPS09 (left) and EPPS16 (right). The gray bands represent the total uncertainty on the hadronic cocktails and include the nPDF uncertainties.

6.3 Possible Thermal Sources

In the following, the possibility of an additional source of dielectrons is explored. The measurement of probes in the pA system is thought to constrain the effects that can be attributed to cold nuclear matter. However, in recent years several experiments have measured features that were in the past attributed to the formation of a QGP in small systems. ALICE measured strangeness enhancement as a function

of multiplicity and observed an onset already in the regime of high-multiplicity pp collisions [175], the CMS collaboration measured long-range correlations in the near-side in pp collisions [176] and PHENIX observed anisotropic flow coefficients in pAu, dAu and tAu collisions that can be explained by hydrodynamic calculations that include the formation of a droplet of QGP [177]. The formation of a QGP in small systems would also indicate a signal of thermal radiation, which would lead to an additional source of dielectrons.

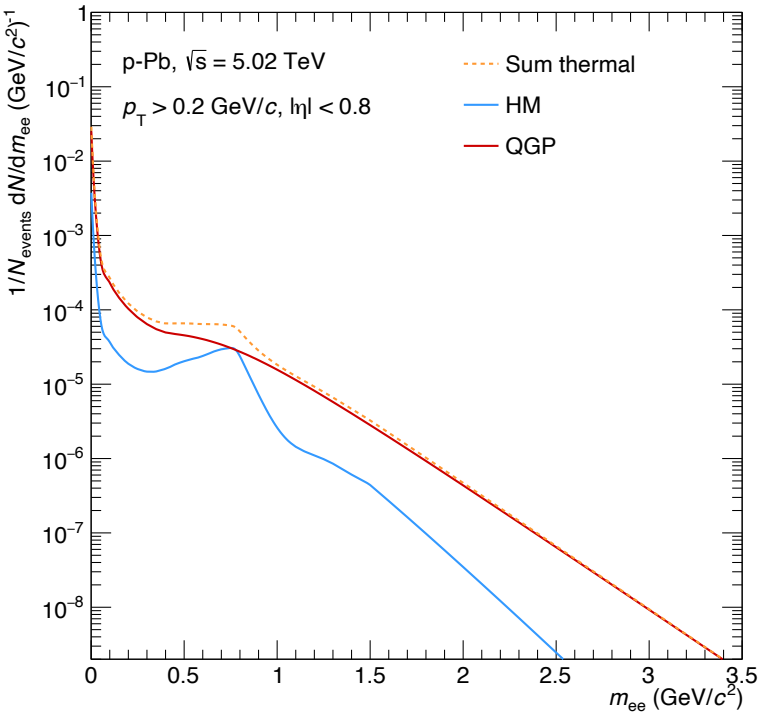

Figure 6.8.: Prediction of the thermal fireball model by R. Rapp [70, 101] as a function of m_{ee} separated for a hadronic and a partonic source. The sum is shown in the dashed orange line. All fiducial selections are applied in the same way as in the analysis.

To test the data for compatibility with an additional thermal source, a model calculation based on the expanding fireball model is used [70, 101]. The model already introduced in 2.1 contains thermal dielectrons from a partonic (QGP) and a hadronic matter (HM) phase. The initial energy density for the model calculation is derived from the $\langle dN_{ch}/dy \rangle = 20$ expected in p–Pb collisions at $\sqrt{s_{NN}} = 5.02$ TeV. The transition from the partonic to the hadronic degrees of freedom is implemented as a cross-over at a critical temperature $T_c = 170$ MeV extracted from lattice QCD calculations. The used equation of state is based on a parameterisation of an lQCD calculation which is matched to a hydrodynamic calculation. The hadro-chemical

freeze-out temperature is set to $T_{\mathrm{ch}} = 160$ MeV [178,179]. Figure 6.8 shows the result of these calculations as a function of m_{ee} for the hadronic, the partonic contributions as well as the sum. Overall the thermal radiation from the QGP phase is expected to dominate the distribution over the full mass range except around the pole mass of the ρ meson. This is slightly different than in Pb–Pb collisions where relatively larger contribution from the hadronic phase is expected. In the calculation, the same fiducial selection as in the data is applied. It should be noted, that the calculations do not include decays after the freeze-out, so a pure thermal contribution. In Figures 6.11 the expectation for the thermal yield as a function of $p_{\mathrm{T,ee}}$ is shown in the mass regions of $0.5 < m_{\mathrm{ee}} < 1.1$ GeV/c^2 (left) and $1.1 < m_{\mathrm{ee}} < 2.7$ GeV/c^2 (right). In Figures 6.9 the expectation for the thermal yield as a function of $p_{\mathrm{T,ee}}$ is shown

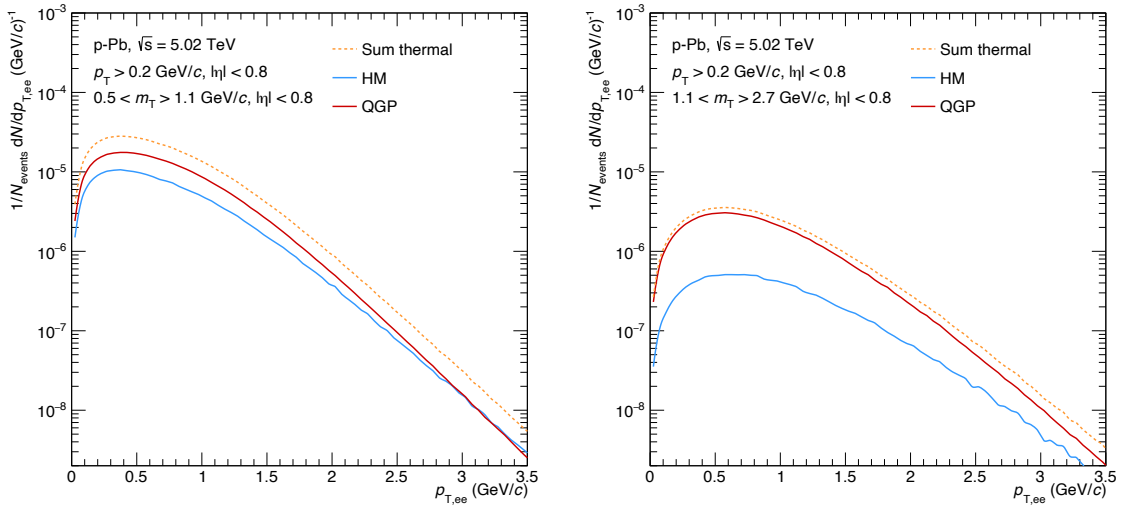

Figure 6.9.: Prediction of the thermal fireball model by R. Rapp as a function of $p_{\mathrm{T,ee}}$ in the mass regions of $0.5 < m_{\mathrm{ee}} < 1.1$ GeV/c^2 (left) and $1.1 < m_{\mathrm{ee}} < 2.7$ GeV/c^2 (right). The contributions from a hadronic and a partonic source are shown separately. The sum is shown in the dashed orange line. All fiducial selections are applied in the same way as in the analysis.

in the mass regions of $0.5 < m_{\mathrm{ee}} < 1.1$ GeV/c^2 (left) and $1.1 < m_{\mathrm{ee}} < 2.7$ GeV/c^2 (right). As expected the different mass regions show different abundances of the contributions. While the intermediate-mass region is dominated by the partonic source, the lower-mass region has a sizable contribution from hot hadronic matter. It is also observed that the slopes of the two contributions are different. While the QGP contribution has a harder spectrum as a function of m_{ee}, in the representation as a function of $p_{\mathrm{T,ee}}$ the hadronic contribution shows the harder slope. This feature is due to the inclusion of radial flow in the model. As m_{ee} is invariant under

Lorentz transformation, no effect of an additional velocity of the expanding source is expected. This is not the case for $p_{\mathrm{T,ee}}$, here the pairs should be shifted to higher momenta, depending on their mass. However, the velocity needs to build up over time, thus the boost will be larger at later times. This means the partonic contribution will be less blue-shifted than the later-produced hadronic contribution. See also the discussion of the NA60 results in Sec 3.1.

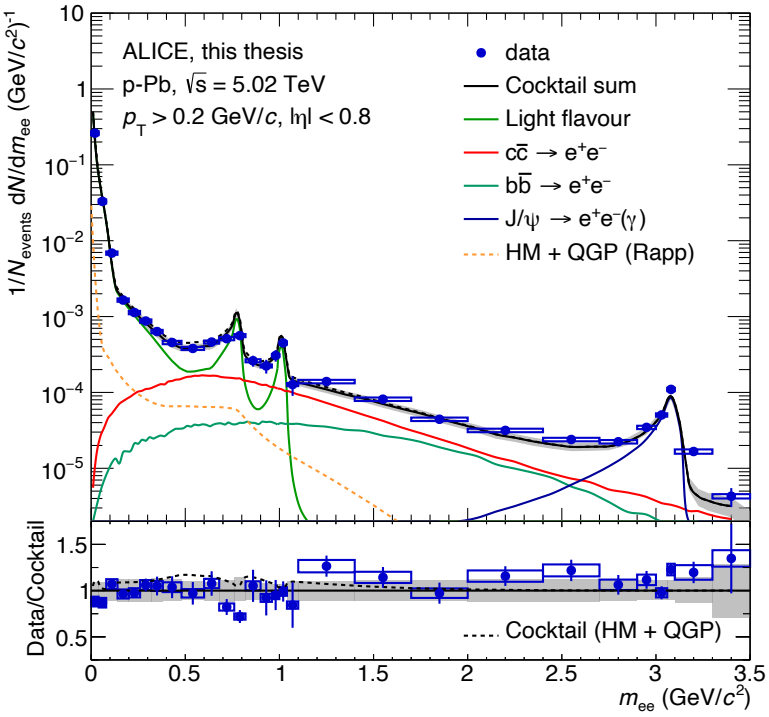

Figure 6.10.: Differential yield of dielectrons as a function of m_{ee} measured in p–Pb collisions at $\sqrt{s_{\mathrm{NN}}} = 5.02$ TeV. The data are compared to the hadronic cocktail in which an additional source of thermal dielectrons from a hadronic and partonic phase based on the thermal fireball model [70, 101, 180] are included. The grey bands represent the total uncertainty on the hadronic cocktail. No uncertainty for the theoretical calculations is added.

In Fig. 6.10 the comparison of the measured differential dielectron yield as a function of m_{ee} is shown and compared to a cocktail that now also includes the thermal radiation. The orange dashed line shows the amount of the predicted thermal radiation while the dashed black line shows the sum of the cocktail and the thermal contribution. Overall, the expected effect is small since the thermal production rate in the model calculation is small compared to the produced hadrons in a p–Pb collision at $\sqrt{s_{\mathrm{NN}}} = 5.02$ TeV as expected. The dashed line in the lower panel of the figure

indicates that a modification of up to 10% would be expected. While the addition of a thermal source would lead to a better description in the intermediate mass region between 1.1 and around 2 GeV/c^2 it would introduce a tension in the lower mass region. Also, the $p_{\mathrm{T,ee}}$ dependence is investigated. Figure 6.11 shows the differential

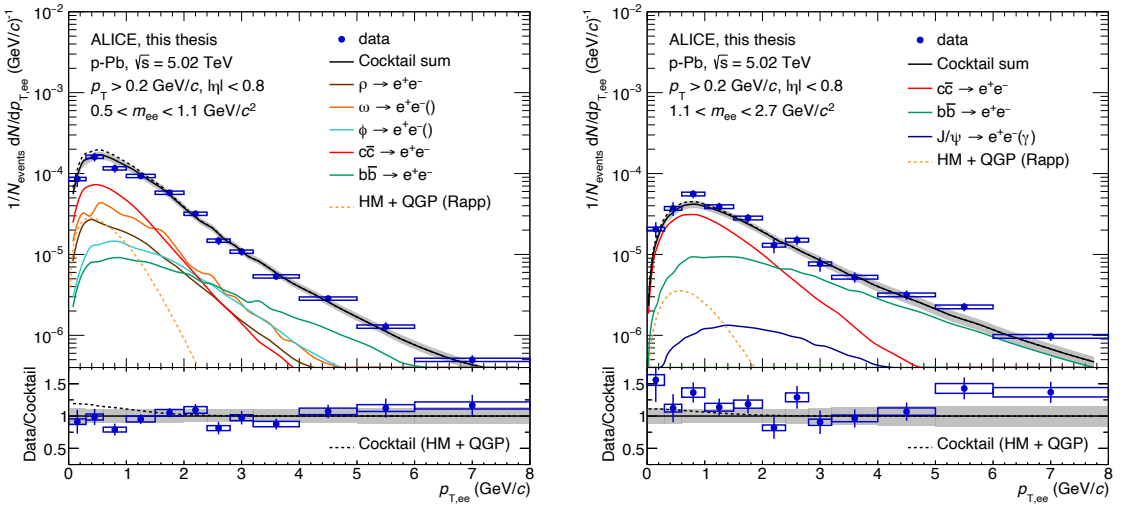

Figure 6.11.: Differential yield of dielectrons as a function of $p_{\mathrm{T,ee}}$ measured in p–Pb collisions at $\sqrt{s_{\mathrm{NN}}} = 5.02$ TeV in the range $0.5 < m_{\mathrm{ee}} < 1.1$ GeV/c^2 (left) and $1.1 < m_{\mathrm{ee}} < 2.7$ GeV/c^2 (right). The data are compared to the hadronic cocktail in which an additional source of thermal dielectrons from a hadronic and partonic phase based on the thermal fireball model [70, 101, 180] are included. The grey bands represent the total uncertainty of the hadronic cocktail. No uncertainty for the theoretical calculations is added.

yield of dielectrons as a function of $p_{\mathrm{T,ee}}$ in the mass regions $0.5 < m_{\mathrm{ee}} < 1.1$ GeV/c^2 (left) and $1.1 < m_{\mathrm{ee}} < 2.7$ GeV/c^2 (right). The thermal radiation contributes at the softer part of the spectra below about 2 GeV/c where the light flavour mesons and the charm contribution are dominant. The expected effect would be on the size of up to 20% additional dielectron yield at small $p_{\mathrm{T,ee}}$ in the lower of the two mass regions while an enhancement of about 10% would be expected in the intermediate mass region. Overall the effects are not sizable and within the precision of the measurement and the cocktail calculations. In the case of the lower mass region, the low $p_{\mathrm{T,ee}}$ description of the data would worsen, while in the intermediate mass region, the central value of the cocktail including an additional thermal source would be closer to the measurement.

6.4 The Full Picture

As the reduction of the charm cross section due to CNM effects would suppress the dielectron production with respect to a binary scaled pp cross section and the additional thermal radiation would enhance the production, both effects can compensate each other. The measured dielectron yield as a function of the invariant mass compared to a cocktail including CNM effects based on the EPPS16 nPDF set [168] together with an additional source of dielectrons from thermal radiation based on the above discussed model is shown in Fig. 6.12. The inclusion of ther-

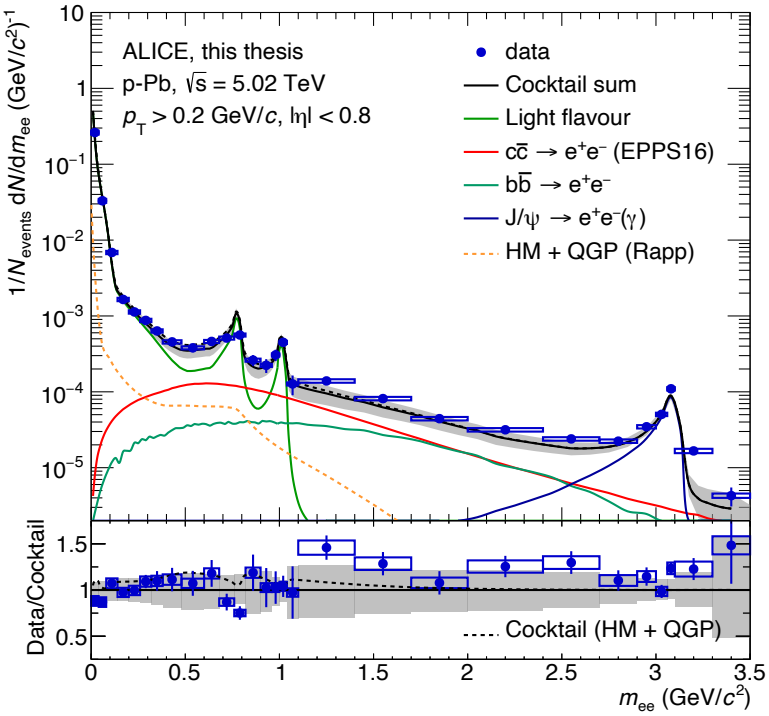

Figure 6.12.: Differential yield of dielectrons as a function of m_{ee} measured in p–Pb collisions at $\sqrt{s_{NN}} = 5.02$ TeV. The data are compared to the hadronic cocktail in which CNM effects are included in charm cocktail based on the EPPS16 nPDF set. An additional source of thermal dielectrons from a hadronic and partonic phase based on the thermal fireball model [70, 101, 180] is included. The grey bands represent the total uncertainty on the hadronic cocktail. No uncertainty for the theoretical calculations is added.

mal radiation in a cocktail incorporating CNM effects shows an improvement in the description of the data specifically in the mass region below the ϕ. In the intermediate-mass region, the data are on the upper edge of the uncertainties and the inclusion of thermal radiation would only contribute up to 1.5 GeV/c^2, while the

overall effect is still expected to be small and of the order of $10-15\%$. The same cocktail calculations are compared to the data in the $0.5 < m_{\mathrm{ee}} < 1.1$ GeV/c^2 and $1.1 < m_{\mathrm{ee}} < 2.7$ GeV/c^2 mass regions as a function of $p_{\mathrm{T,ee}}$ in Fig. 6.13 left and right, respectively. As seen before the inclusion of thermal radiation in the lower

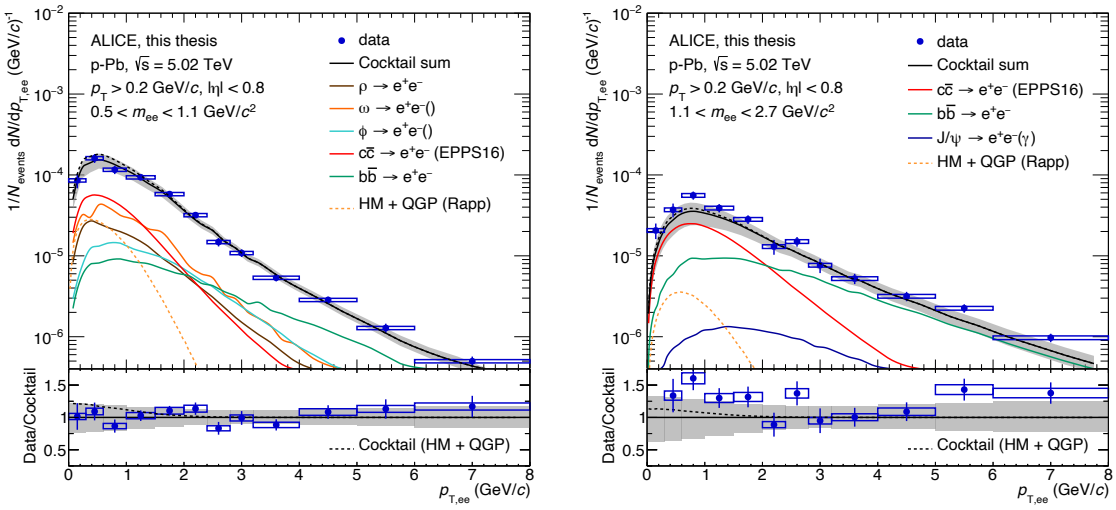

Figure 6.13.: Differential yield of dielectrons as a function of $p_{\mathrm{T,ee}}$ measured in p–Pb collisions at $\sqrt{s_{\mathrm{NN}}} = 5.02$ TeV in the range of $0.5 < m_{\mathrm{ee}} < 1.1$ GeV/c^2 (left) and $1.1 < m_{\mathrm{ee}} < 2.7$ GeV/c^2 (right). The data are compared to the hadronic cocktail in which CNM effects are included in charm cocktail based on the EPPS16 nPDF set. An additional source of thermal dielectrons from a hadronic and partonic phase based on the thermal fireball model [70, 101, 180] are included. The grey bands represent the total uncertainty on the hadronic cocktail. No uncertainty for the theoretical calculations is added.

mass region would tend to overestimate the dielectron production in the low $p_{\mathrm{T,ee}}$ regime. Combining the thermal enhancement with a suppression of charm gives a better description of the data However, below $p_{\mathrm{T,ee}} = 1$ GeV/c, the data would still be slightly below the central value of the prediction including thermal radiation and CNM effects. It should however be mentioned here that the ρ and ω are relevant sources in this mass region. As the comparison as a function of mass shows, there might be an overestimation of these two sources in the cocktail calculation. It is not implausible that the cocktail calculations could overestimate the contributions. In the case of the ρ, data is scarce and essentially no constraints are available at $p_{\mathrm{T}} < 0.4$ GeV/c. In the case of the ω measurements of the ω/π^0 are available from RHIC down to low p_{T}. However, this has to be taken with a grain of salt, as no effects due to the much higher energies at LHC are taken into account. A reduction of the ρ and ω as suggested by the mass distribution would then favour a scenario

that includes thermal radiation. Measurements of both, the ω and ρ mesons down to low p_{T} at LHC energies would greatly improve the possibility of interpreting this data.

In the intermediate-mass region, the data is above the cocktail calculations below $p_{\mathrm{T,ee}} = 1$ GeV/c as seen before and the inclusion of thermal radiation is not capable of significantly improving the description of the data. It seems that while a reduction of the charm cross section helps in the description of the low-mass region, the opposite is the case for the intermediate-mass region. It should be mentioned here that previous measurements of the nuclear modification of fully reconstructed heavy flavour mesons by the ALICE collaboration [181, 182] in p–Pb collisions showed no significant suppression for D mesons or Λ_{c} (See Fig. B.1 in B). Especially in the kinematic regime of p_{T} between 2 and 3 GeV/c of the charm hadrons an enhancement could be imagined. This is the momentum range of charmed hadrons which mainly feeds into the intermediate-mass region, while lower momenta of D mesons and Λ_{c}, where a suppression is observed, contribute to lower mass regions. From this fact, it would be plausible that the suppression in both regions is different while the functional shape that is used in the EPPS16 parameterisation might not be able to catch this. Another explanation could be that the QGP radiation is underestimated in the model calculations. A possibility to clarify this ambiguity is the analysis using a topological separation of the two sources.

Chapter 7

Summary and Conclusion

This thesis presents the measurement of dielectron production in p–Pb collisions at $\sqrt{s_{\mathrm{NN}}} = 5.02$ TeV recorded with the ALICE experiment at the CERN LHC in the 2016 data taking campaign. The measurement is carried out two-dimensionally as a function of the dielectron invariant mass (m_{ee}) and the pair transverse momentum ($p_{\mathrm{T,ee}}$). The maximum m_{ee} and $p_{\mathrm{T,ee}}$ reach of the analysis is 3.5 GeV/c^2 and 8 GeV/c, respectively. The $p_{\mathrm{T,ee}}$ integrated m_{ee} spectrum shows the expected features of the π^0 and η meson Dalitz decays, the decays of ρ, ω, ϕ peaks at the respective pole masses as well as a broad continuum contribution expected from the correlated semi-leptonic decays of open charm and beauty hadrons.

As guidance of the interpretation of the data, a hadronic cocktail calculation is prepared that uses the available measurements of hadron production to estimate the expected contributions in the dielectron spectrum. While the cocktail estimates for light-flavour hadron and J/ψ production is in principle based on measurements in the same collision system as the presented analysis, the contribution from open heavy-flavour decays utilises the measurements at the same energy, but in pp collisions. The comparison of the cocktail calculations without any further modification shows an overall good agreement with the measurements as a function of m_{ee} as well as a function of $p_{\mathrm{T,ee}}$ in different m_{ee} intervals. A slight tension in the intermediate mass region dominated by the decays of open charm hadrons is observed. The data is slightly above the cocktail calculations. This is surprising as the expected modification of the charm production due to binding effects of the protons in the nucleus is a suppression. In order to further investigate this, a cocktail for the charm contribution is constructed in which cold nuclear matter effects are included. The expected suppression of the charm contribution is observed in the cocktail, as it is

constructed. No strong m_{ee} or $p_{\mathrm{T,ee}}$ dependence of the suppression is expected, however, the uncertainties should be more reliable when using the CNM modifications. Overall the data are still in agreement with the cocktail calculations when including the modification of the charm production. An additional study is performed in which a source of thermal radiation based on a model calculation is added to the cocktail contributions. The highest sensitivity to this additional source of dielectrons is expected in the m_{ee} region around 0.5 GeV/c^2 and just above 1.1 GeV/c^2. Combining the extra thermal radiation with the CNM-modified cocktail shows a good description for $m_{\mathrm{ee}} < 1$ GeV/c^2 and a moderate description for higher masses while both effects show a behaviour that would compensate each other. Overall, the interpretation of the data is very dependent on the reliability of the different calculations that do not necessarily give a consistent picture when confronted with the measurements. A possible way to circumvent at least the model dependence on the implementation of the CNM effects could be to construct a cocktail based directly on measurements of the open charm hadrons in p–Pb collisions at the same energy. This however comes with its own limitations as no correlations of the hadrons are measured and the spectra themselves have sizable experimental uncertainties. However, the statistical precision of the dielectron measurement is also a limiting factor in its interpretation.

Nevertheless, the presented thesis shows that a modification of dielectron production due to cold nuclear matter effects, if present is small. In the future, the only way for an unambiguous interpretation of dielectron measurements at LHC energies will be high statistics combined with the possibility of experimentally separating the overwhelming heavy-flavour contributions from the possible thermal sources.

Chapter 8

Quo vadis dielectrons?

In the last part of this thesis opportunities for future dielectron measurements with ALICE at the LHC are presented. This is not a review or a summary of every aspect of the matter but should give pointers to developments that will have the potential to usher in a new era of dielectron measurements at the highest collision energies possible in the laboratory.

8.1 ALICE Run 3 and Run 4

As discussed before, the two main challenges of dielectron measurements are the small cross section of this rare probe and at LHC energies the large production of heavy-flavour hadrons. Their correlated semi-leptonic decays populate the phase space that is in particular of interest to study thermal radiation originating in the partonic and hadronic phases of the medium created in the ultra-relativistic heavy-ion collisions.

Being aware of these issues, the ALICE collaboration started a huge upgrade program including tremendous R&D efforts [183,184] targeted to enable unprecedented measurements of dielectron production. This led to the construction of a new inner tracking system (ITS) based solely on monolithic active pixel sensors (MAPS) [185] and a completely new readout system for the TPC [186–188] based on gas electron multipliers (GEMs) [189]. These major upgrades, completed in time for the 2022 data taking, together with a completely new system of the data acquisition, enables the operation of the detector in a continuous readout mode. In the heavy-ion data-taking campaign of 2023 it was possible to record Pb–Pb events at a rate of more than 40kHz, limited mainly by the operation of the LHC, not the detector.

This gives the possibility to record datasets one hundred times larger than what was recorded by the collaboration until now. Thus, overcoming the limitations imposed by the statistical precision of the data.

Furthermore, the pointing resolution of the newly installed ITS is improved by factors of three to six compared to its predecessor. This is mainly due to the smaller size of the used pixel matrix, but also factors in the proximity of the first layer to the interaction point which was reduced. This gives significantly better handles on the heavy-flavour contribution and the possibility to separate the directly produced dielectrons from a thermal medium from those stemming from delayed decays of the heavy-flavour hadrons.

Another upgrade of the Inner Tracking System (ITS3) is planned during the long shutdown phase of the LHC from 2026 to 2028. In the three year period, the inner barrel of the tracker will be replaced with almost massless silicon tracking layers [190]. This is achieved by reducing the detector to essentially the active silicon wafer. By thinning of the wafer sized chip to a few tens of nanometers the material becomes flexible enough to be bent to an arch. This way the detector does not rely on additional support structures beyond a bare minimum to hold it in place. The expected improvement in the DCA resolution is a factor of two in the $r\varphi$ as well as in the z direction. This will benefit the measurement of dielectrons by improving the separation of the signal of interest from the heavy-flavour decay background.

8.2 ALICE 3 – A Next Generation Heavy-Ion Experiment

While the data-taking with the upgraded ALICE detector is ongoing and the analyses are in full swing, the plans for the further future are forged. In 2022 the ALICE collaboration published a letter of intent for a next generation heavy ion experiment [191]. The planned ALICE 3 detector concept is based on a pure silicon tracker with a size of about 50 m^2 complemeted with particle identification via time of flight measurements and a Cherenkov detector. The innermost layers of the detector will be a continuation of the developments for the cylindrical ITS installed for Run 4. The main feature of the new detector will be its installation in a secondary vacuum inside the beam pipe. This has two major advantages. On the one hand, the material budget in front of the first layer is reduced significantly which in turn reduces multiple scattering effects of low momentum electrons. On the other hand,

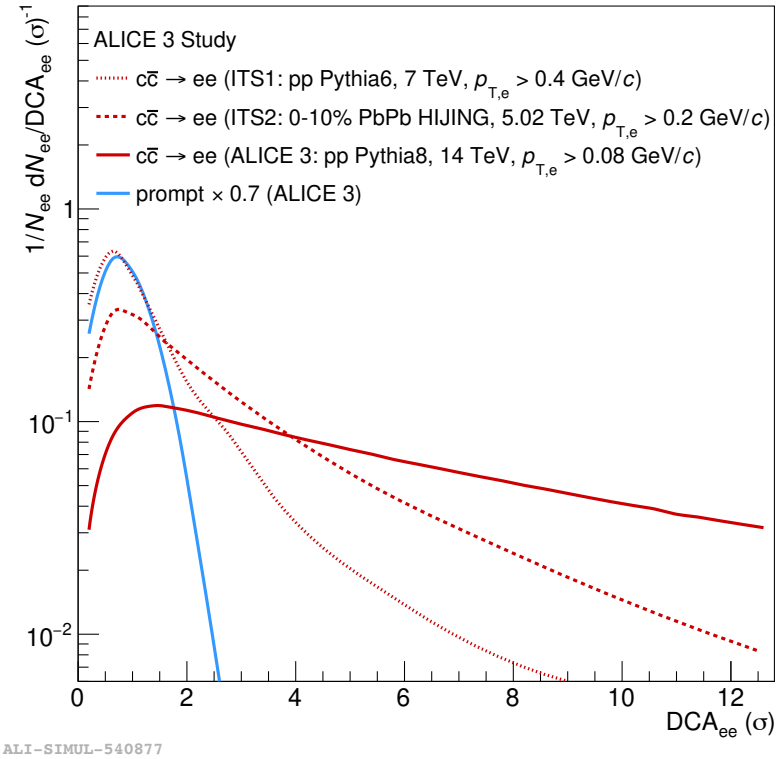

Figure 8.1.: Comparison of DCA_{ee} templates for charm contribution for the Run 1, 3 and 5 setup and a prompt contribution based on different MC simulations.

it is possible to bring the detector as close as 5 mm to the interaction point (ITS3: 19 mm). Since the aperture of the LHC beams at injection is about 16 mm, the inner layers of the detector will be installed in a movable IRIS layout which can be opened at injection. The development of the separation of prompt and charm dielectrons from Run 1 and 2 to the expected performance of the Run 3 setup and ALICE 3 is illustrated in Fig. 8.1 based on MC simulations. The templates for charm extracted from MC simulations are compared to a prompt contribution which by construction should not depend on the detector layout. It is clear that while in Run 1 and 2 the charm distribution still has a large similarity with the prompt contribution due to the pointing resolution of the detector, the separation power gets better with the subsequent improvements of the detectors.

These improvements will make the measurement of thermal radiation close to independent on many model calculations and assumptions. In a purely data-driven manner the charm contribution can be subtracted from the measured spectra to extract the thermal signal in the region where the QGP radiation dominates the

spectral function. In the context of dielectron measurements at LHC, it is safe to say that there is a bright future ahead.

Appendix A

Charm to electron fragmentation

A.1 Inputs

In this section the inputs used for the reevaluation of the effective branching ratio are described. Namely these are the fragmentation fractions of a charm quark to different charmed hadrons H_c measured by the ALICE collaboration [192] and the decay branching ratios of these hadrons into electrons. The latter will mainly be based on inclusive values given by the particle data group (PDG) [3]. If a different value is used, or no inclusive value is available, the reasoning will be explained.

A.1.1 Fragmentation fractions

The fragmentation fractions for charm quarks into hadrons were measured by the ALICE collaboration and are listed in Tab. A.1 together with the corresponding statistical and systematic uncertainties. The systematic uncertainties include the uncertainties on the meson and baryon measurements which include the following sources: (1) extraction of yields, (2) prompt fraction estimation, (3) tracking and selection efficiency, (4) particle identification efficiency, (5) sensitivity of the efficiencies to the hadron p_{T} shape generated in the simulations, (6) p_{T}-extrapolation for the hadrons not measured down to $p_{\mathrm{T}} = 0$.
In the calculation of the cross-section of $\mathrm{c\bar{c}}$ at midrapidity an additional contribution of Ω_c was neglected. A contribution of the size of the Ξ_c was assumed to estimate an uncertainty. The assumption of similar contributions from the two types of baryons is based on calculations of the Catania model. The uncertainty of this contribution leads to an asymmetric uncertainty.

H_c	$f(c \to H_c)[\%]$
D^0	$39.1 \pm 1.7(\text{stat})^{+2.5}_{-3.7}(\text{syst})$
D^+	$17.3 \pm 1.8(\text{stat})^{+1.7}_{-2.1}(\text{syst})$
D_s^+	$7.3 \pm 1.0(\text{stat})^{+1.9}_{-1.1}(\text{syst})$
Λ_c^+	$20.4 \pm 1.3(\text{stat})^{+1.6}_{-2.2}(\text{syst})$
Ξ_c^0	$8.0 \pm 1.2(\text{stat})^{+2.5}_{-2.4}(\text{syst})$

Table A.1.: Charm-quark fragmentation fractions into charmed hadrons H_c measured in pp collisions at $\sqrt{s} = 5.02$ TeV. Statistical and systematic uncertainties are reported separately. The complete fragmentation should also include a contribution from Ξ_c^+ which is assumed to be the same as Ξ_c^0 assuming isospin symmetry. Contributions of Σ_c and D^* are omitted since they are included via their feed-down to the other H_c.

A.1.2 Decay branching ratios of charmed hadrons

The inclusive decay branching fractions of D^0, $D^\pm$, D_s, and Λ_c are listed in the latest edition of the PDG [3] to be $(6.94 \pm 0.11)\%$, $(16.07 \pm 0.30)\%$, $(6.33 \pm 0.15)\%$, and $(3.95 \pm 0.35)\%$, respectively. For the cases of the Ξ_c and the Ω_c, however, there are no inclusive values available. In the case of the Ξ_c^+ and Ξ_c^0 there are only measurements of the exclusive channel with $\Xi e\nu$ in the final state available. In the case of the Ω_c the situation is more dire, since here no "full" BR is measured. The $\Omega_c \to \Omega e\nu$ is only measured relative to the decay $\Omega_c \to \Omega\pi$. In the following, the different decay branching ratios are discussed.

A.1.2.1 $\Xi_c^+ \to \Xi^0 e^+ \nu$

The value of this exclusive decay branching ratio is given by the PDG as $(7 \pm 4)\%$ [3]. This is the only listed decay that includes an electron or lepton at all. The decay can be seen as the decay of the charm quark in the baryon decaying under the emission of a W boson into a strange quark, and the W decays into a lepton + lepton neutrino. In the Cabibbo-Kobayashi-Maskawa (CKM) matrix, this decay corresponds to the V_{cs} element on the diagonal. A second possible weak decay could happen if, instead of the c, the s quark in the Ξ_c^+ transitions into a u. This would then correspond to the V_{su} element in the CKM-matrix, which is not on the diagonal of the matrix. The relative probability of the two different transitions can be estimated by comparing the squares of the two elements $V_{su}/V_{cs} \sim 0.05$. So the decay of the s quark is suppressed by a factor 20. Taking this into account, the decay of the Ξ_c baryons is very similar to the Λ_c. In case of the Λ_c the difference of the exclusive decay

$\Lambda_c^+ \rightarrow \Lambda e^+ \nu_e$ $(3.6 \pm 0.4)\%$ to the inclusive $\Lambda_c^+ \rightarrow e^+ X$ $(3.95 \pm 0.35\%)$ is about 10%. Based on these observations we decide to use the measured exclusive decay branching ratio since the expected difference to an inclusive measurement is small compared to the uncertainties.

A.1.2.2 $\Xi_c^0 \rightarrow \Xi^- e^+ \nu$

In the case of the Ξ_c^0 decay into electrons, all the arguments above are applicable as well. In this case, the PDG gives a value for the exclusive decay of $(1.04 \pm 0.24)\%$. However, a value of $(1.94 \pm 0.55)\%$ is used. The reason for this is that the latter value was measured and used by the ALICE collaboration to estimate the visible cross-section of Ξ_c^0 $\mathrm{d}\sigma^{\Xi_c^0}_{pp,5.02TeV}/dy|^{2<p_\mathrm{T}<8\mathrm{GeV}/c}_{|y|<0}$ from a measurement in the semi-leptonic channel [193]. This cross-section was again used to calculate the fragmentation fraction. By using this value, the uncertainty on the branching ratio can be used properly, while using a different value, an additional uncertainty needs to be taken into account.

A.1.2.3 $\Omega_c^0 \rightarrow \Omega^- e^+ \nu$

The fragmentation fraction only includes a possible contribution of Ω_c as part of the systematic uncertainties. To estimate these uncertainties equal values for Ω_c and Ξ_c^0 production were assumed, which is motivated by model calculations. In the estimation of the BR($c \rightarrow e$) we will follow this approach. Together with the fragmentation also a decay branching ratio into electrons needs to be taken into account. As for the Ξ_c states, no inclusive measurement is available, assumptions enter. In addition, no absolute branching fraction is measured, but the relative decay branching fraction to the $\Omega_c \rightarrow \Omega^- \pi^+$ is given by the PDG. The value is 2.4 ± 1.2. Up to now, there are no experimental measurements of the BR of $\Omega_c \rightarrow \Omega\pi$. The analysis that measured this channel in ALICE for the first time on pp collisions at $\sqrt{s} = 13$ TeV [194] evaluated a branching ratio of $(0.51^{+2.19}_{-0.31})\%$ from the theoretical estimate in [195] with the uncertainties based on the envelope and uncertainties of different calculations [195–199]. The semi-leptonic branching ratio can then be calculated as $\mathrm{BR}(\Omega_c^0 \rightarrow \Omega^- e^+ \nu) = (2.4 \pm 1.2) \times (0.51^{+2.19}_{-0.31})\% = (1.22^{+4.32}_{-0.79})\%$.
In this section we describe how the different inputs discussed prior are used to determine the effective branching ratio of charm quarks into electrons and the resulting effect on the extracted cross sections of charm pair production at midrapidity. Dif-

ferent considerations for the sources of systematic uncertainties are described and estimated.

A.1.3 Putting together the ingredients

In this section we describe step-by-step how the inputs mentioned in sec. A.1 are used to determine the effective branching ratio of charm quarks into electron BR(c $\rightarrow$ e) and the associated uncertainties. The general approach is that BR(c $\rightarrow$ e) is the sum of the products of the different fragmentation fractions of a c quark into a given hadron $f(\mathrm{c} \rightarrow \mathrm{H_c})$ and their respective decay branching ratios into electrons BR($\mathrm{H_c} \rightarrow$ e):

$$\mathrm{BR}(\mathrm{c} \rightarrow \mathrm{e}) = \sum_{\mathrm{H_c}} f(\mathrm{c} \rightarrow \mathrm{H_c}) \times \mathrm{BR}(\mathrm{H_c} \rightarrow \mathrm{e}). \tag{A.1}$$

As mentioned before, the fragmentation fraction in teb. A.1 include an asymmetric systematic uncertainty that considers a sizable Ω_c fraction. To estimate this uncertainty a fraction of Ω_c the size of Ξ_c^0 was assumed. In order to estimate the uncertainty of this Ω_c contribution it is not sufficient to simply propagate the uncertainty, since the BR($\Omega_c \rightarrow \Omega e\nu$) needs to be included in the uncertainty propagation. To do so, in a first step the uncertainty that was assigned for the Ω_c fraction is subtracted from the values in Tab. A.1. For this we first calculate the difference in fragmentation fractions without and with an Ω_c fraction the same size as the Ξ_c^0 fraction and calculate the differences as listed in Tab. A.2. This uncertainty can then be subtracted from the lower systematic uncertainty listed in Tab. A.1.

As an example the lower systematic uncertainty of the D^0 fraction is listed as -3.7 [192]. Assuming that the other systematic uncertainties are independent of the one connected to the Ω_c the reduced systematic uncertainty can be calculated as $\sqrt{3.7^2 - 2.9^2} = 2.3\%$. All fragmentation fractions, with their statistical and reduced systematic uncertainties are listed together with the corresponding decay branching ratio in Tab. A.3. The decay branching ratios correspond either to inclusive values listed in the latest edition of the PDG booklet or, where not available, to the values discussed above.

The product of $f\mathrm{c} \rightarrow \mathrm{H_c}$ and BR($\mathrm{H_c} \rightarrow$ e) with the propagated uncertainties is given in the last column. The sum over all contributions with its uncertainties is given in the last row. This value is the effective branching ratio of a charm quark into an electron BR(c $\rightarrow$ e), neglecting a possible fragmentation of the c quark into an Ω_c. To estimate this uncertainty, the BR(c $\rightarrow$ e) is calculated again, this time assuming

Appendix A. Charm to electron fragmentation

H_c	$f(c \to H_c)$[%]	$f(c \to H_c)_{\Omega_c}$[%]	Δf
D^0	39.1	36.2	−2.9
D^+	17.3	16.0	−1.3
D_s^+	7.3	6.8	−0.5
Λ_c^+	20.4	18.9	−1.5
Ξ_c^0	8.0	7.4	−0.6
Ξ_c^+	8.0	7.4	−0.6
Ω_c^0	–	7.4	–

Table A.2.: Charm-quark fragmentation fractions into charmed hadrons H_c measured in pp collisions at $\sqrt{s} = 5.02$ TeV with and without the assumption of an Ω_c contribution the same size as the Ξ_c^0 contribution. The Ξ_c^+ contribution was not measured but considering isospin symmetry assumed the same as the Ξ_c^0. A second set of fragmentation fractions was calculated assuming a contribution of Ω_c the same size as Ξ_c^0 as predicted by the Catania model [200]. The difference in the fragmentation fractions with and without an Ω_c fraction is listed in the last column.

H_c	$f(c \to H_c)$[%]	$BR(H_c \to e)$[%]	$f \times BR$[%]
D^0	$39.1 \pm 1.7(\text{stat})^{+2.5}_{-2.3}(\text{syst})$	6.49 ± 0.11	$2.54^{+0.20}_{-0.27}$
D^+	$17.3 \pm 1.8(\text{stat})^{+1.7}_{-1.7}(\text{syst})$	16.07 ± 0.3	$2.78^{+0.40}_{-0.45}$
D_s^+	$7.3 \pm 1.0(\text{stat})^{+1.9}_{-0.1}(\text{syst})$	6.33 ± 0.15	$0.46^{+0.14}_{-0.09}$
Λ_c^+	$20.4 \pm 1.3(\text{stat})^{+1.6}_{-1.6}(\text{syst})$	3.95 ± 0.35	$0.81^{+0.11}_{-0.12}$
Ξ_c^0	$8.0 \pm 1.2(\text{stat})^{+2.5}_{-2.3}(\text{syst})$	$1.94 \pm 0.55(0.0)$	$0.16^{+0.05}_{-0.05}$
Ξ_c^+	$8.0 \pm 1.2(\text{stat})^{+2.5}_{-2.3}(\text{syst})$	7 ± 4	$0.56^{+0.37}_{-0.37}$
			$7.30^{+0.61}_{-0.66}$

Table A.3.: The charm quark fragmentation functions into charmed hadrons $f(c \to H_c)$ from [192] are listed together with the respective branching ratios of the hadrons into electron $BR(H_c \to e)$, as well as their product. The systematic uncertainties were reduced by the uncertainty asigend for a sizable Ω_c contribution. For $f(c \to \Xi_c^+)$ the same central value as for $f(c \to \Xi_c^0)$ is listed, assuming isospin symmetry. For the branching ratios the inclusive values into electrons were used where available. In case of Ξ_c^+ and Ξ_c^0 no inclusive measurements are available, only one decay with an electron in the final state are measured. In these cases, the BR for the respective channel was used. For the Ξ_c^+ value from [3] is used while in the case of Ξ_c^0 a measurement of ALICE [193] is used as explained above.

the fragmentation fractions in the 3rd column in Tab. A.2 and the branching ratio of $\Omega_c^0 \to \Omega^- e^+ \nu_e$ discussed in sec. A.1.2.3. Since the uncertainties on the decay branching ratio are so large we take the two extremes into account. Using the upper

edge of the uncertainty $(1.224 + 5.29)\% = 6.514\%$ we derive a value of 7.24%, at the lower edge of the uncertainty (0.264%) the effective branching ratio is 6.77%. Since both values are smaller, we assign the larger difference of -0.53% as the uncertainty. This leads to a final value of $\mathrm{BR}(\mathrm{c} \to \mathrm{e}) = 7.3^{+0.61}_{-0.84}\%$. This corresponds to a relative uncertainty of $^{+8.4}_{-9.0}\%$.

To derive the effective branching ratio of a pair of charm and anticharm quarks to both lead to an electron/positron and thus be measured in the dielectron channel, we then take the square of the $\mathrm{c} \to \mathrm{e}$, $\mathrm{BR}(\mathrm{c} \to \mathrm{e})^2 = \mathrm{BR}(\mathrm{cc} \to \mathrm{ee})$. Using gaussian propagation of uncertainties:

$$\delta f(x, \delta x) := \sqrt{\left(\frac{\partial f(x)}{\partial x}\right)^2 \delta x^2}, \tag{A.2}$$

with the absolute uncertainty δx and $f(x) = x^2$ we can then evaluate the uncertainty to be:

$$\delta f(x, \delta x) := 2 \cdot x \cdot \delta x. \tag{A.3}$$

This leads to an effective branching ratio for pairs of $\mathrm{BR}(\mathrm{cc} \to \mathrm{ee}) = (0.53^{+0.09}_{-0.12})\%$, which corresponds to an upper (lower) uncertainty of 16.8(23)%. Comparing this with the $\mathrm{BR}(\mathrm{cc} \to \mathrm{ee}) = (9.6)^2\% = 0.92\%$ used in previous analysis measurements [92, 93, 160], shows a difference of a factor 1.73. This means the extracted $\sigma_{\mathrm{c\bar{c}}}|_{y=0}$ should be higher by 74%, while the uncertainty of the $\mathrm{BR}(\mathrm{cc} \to \mathrm{ee})$ becomes more asymmetric. The significant change of the extracted branching ratio would not be covered by the prior assigned uncertainties. While only taking the change of the Λ_c fraction is covered by the assigned uncertainties, the additional fraction of Ξ_c is not. The impact of the change in the normalisation will be discussed in the following section.

A.1.4 Results

The detailed description of the procedure to extract $\sigma_{\mathrm{c\bar{c}}}|_{y=0}$ from a measurement of the dielectron mass and pair p_{T} spectrum can be found in the publications [92, 93, 160]. The general idea is that the spectrum is parameterised in the intermediate mass region IMR ($1.1 < m_{\mathrm{ee}} < 2.7$ GeV/c^2) in which only HF contributions are expected. Two templates for $\mathrm{cc} \to \mathrm{ee}$ and $\mathrm{bb} \to \mathrm{ee}$ are used for this. After fitting in the IMR the templates are used to extrapolate the fiducial cross section for heavy-flavour dielectrons to full phase space. We use templates from the event generators PYTHIA

and POWHEG to do so. To then evaluate the charm cross section at midrapidity, the cross section for dielectrons from charm decays is divided by BR(cc $\rightarrow$ ee). The extracted cross sections at midrapidity, with the prior used and newly evaluated BR(cc $\rightarrow$ ee) are listed in Tab. A.4 for both event generators with the corresponding statistical and systematic uncertainties for the different collision energies.

$\sqrt{s}$ (TeV)	$\sigma_{c\bar{c}}\|_{y=0}$ (μb)	
	PYTHIA	POWHEG
	published (old)	
5.02	$524 \pm 26(\text{stat}) \pm 61(\text{syst})$	$756 \pm 38(\text{stat}) \pm 80(\text{syst})$
7	$854 \pm 145(\text{stat}) \pm 123(\text{syst})$	$1251 \pm 213(\text{stat}) \pm 155(\text{syst})$
13	$974 \pm 140(\text{stat}) \pm 138(\text{syst})$	$1417 \pm 204(\text{stat}) \pm 184(\text{syst})$
	updated (new)	
5.02	$906 \pm 45(\text{stat}) \pm 105(\text{syst})$	$1307 \pm 66(\text{stat}) \pm 138(\text{syst})$
7	$1477 \pm 251(\text{stat}) \pm 213(\text{syst})$	$2163 \pm 368(\text{stat}) \pm 268(\text{syst})$
13	$1684 \pm 242(\text{stat}) \pm 239(\text{syst})$	$2450 \pm 353(\text{stat}) \pm 318(\text{syst})$

Table A.4.: Charm cross sections at midrapidity extracted at different collision energies using the event generators PYTHIA and POWHEG with an effective branching ratio of charm quarks to electrons based on fragmentation functions at LEP [3] (published) and including the latest measurements by the ALICE collaboration [192] (updated). Not included in the table are the uncertainties based on the effective branching ratio discussed in the text.

The table includes the $\sigma_{c\bar{c}}|_{y=0}$ with the statistical and systematic uncertainties, which did not change relative to the central values. The uncertainties on the effective branching ratios of 22% ($^{+23}_{-17}$%) for the old(new) estimate of the effective branching ratio are not listed in the table.

The extracted data points are shown in Fig. A.1 left and right as a function of $\sqrt{s}$ for PYTHIA and POWHEG, respectively. The data are represented with their statistical (bars), systematic (box), and branching ratio (area) uncertainties. The data are compared to FONLL [47, 48, 51, 52] calculations (black line) that used the CTEQ6.6 [201] particle distribution functions (PDF). As observed in previous measurements of identified heavy-flavour hadrons, the data are compatible with the model calculations, while the data tend to be on the upper edge of the uncertainties. This is also true for the $\sigma_{c\bar{c}}|_{y=0}$ extracted combining several such measurements. The large uncertainties in the FONLL calculations (dashed line) include the uncertainties in the model that depend on the PDF, the scale uncertainty, and the uncertainty on the mass of the c quark. A second calculation that extends the FONLL calculations

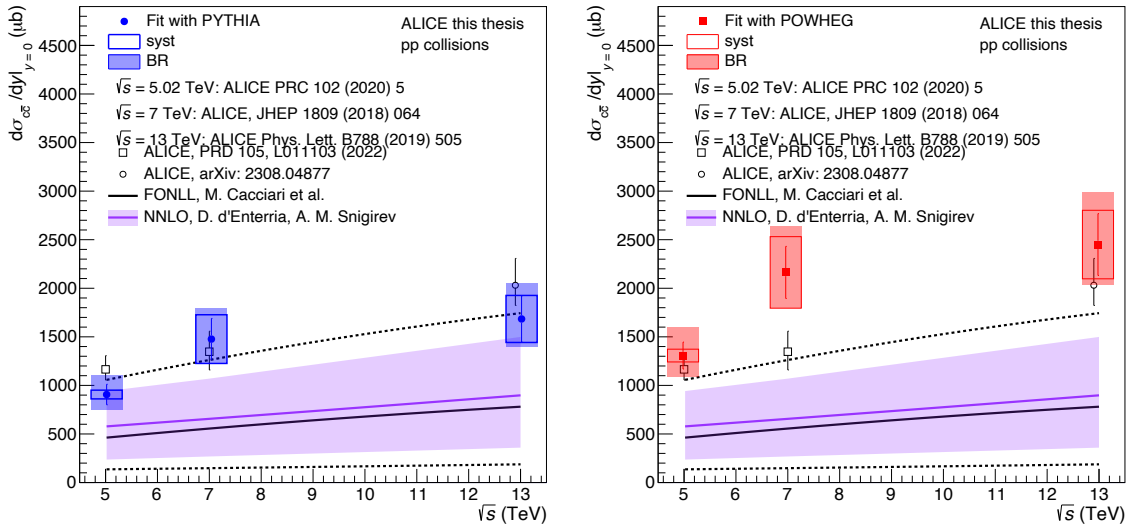

Figure A.1.: The charm cross section at midrapidity $\sigma_{c\bar{c}}|_{y=0}$ measured by ALICE vs $\sqrt{s}$. The measurements in the dielectron channel utilising PYTHIA (left) and POWHEG (right) are shown together with the complementary measurements in the identified charm hadron channels. The data are in agreement with calculations at FONLL and NNLO within the large uncertainties.

to NNLO [53, 54] is shown as well. Extending the order leads to a slightly higher central value of the calculation, and to smaller uncertainties. Given the precision of the data, no conclusion on the model description beyond the discussed can be drawn. An updated version of the plot shown in [160] now including also the NNLO calculations and $\sigma_{c\bar{c}}|_{y=0}$ measurements by the ALICE collaboration is presented in Fig. A.2. The common branching ratio uncertainties were updated in the legend, but for readability not included in the graphical representation.

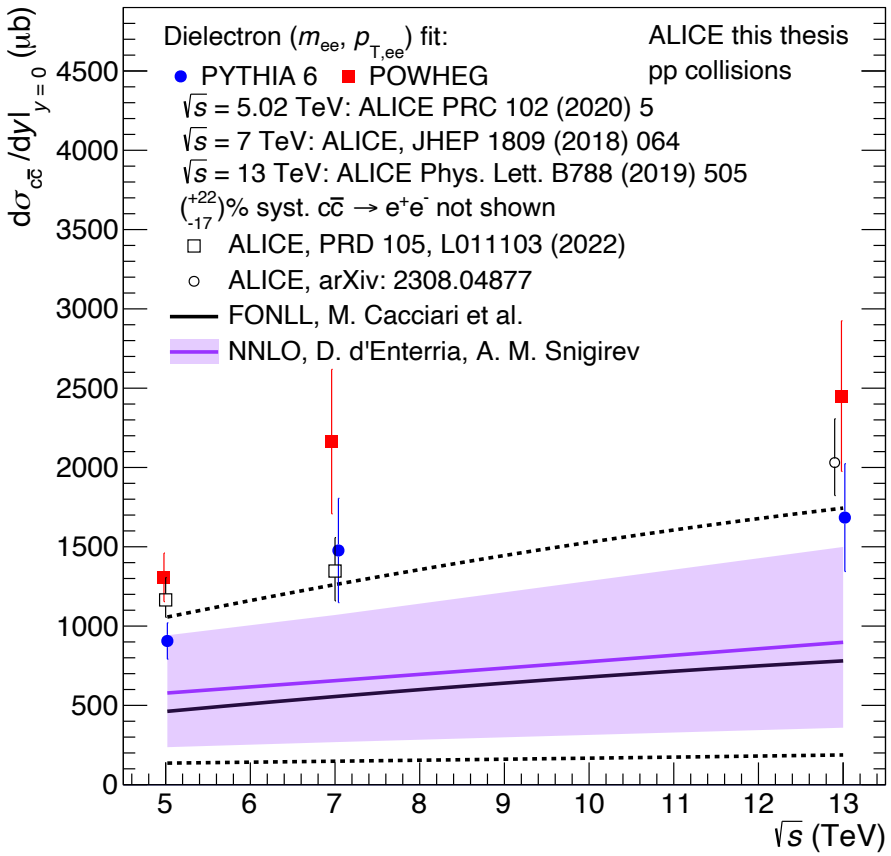

Figure A.2.: Charm production cross section at midrapidity based on measurements in the dielectron channels and extrapolated to the quark cross section using fragmentation fractions measured by ALICE and decay branching ratios published by the particle data group.

Appendix B

Nuclear modification of Prompt Charm Hadrons

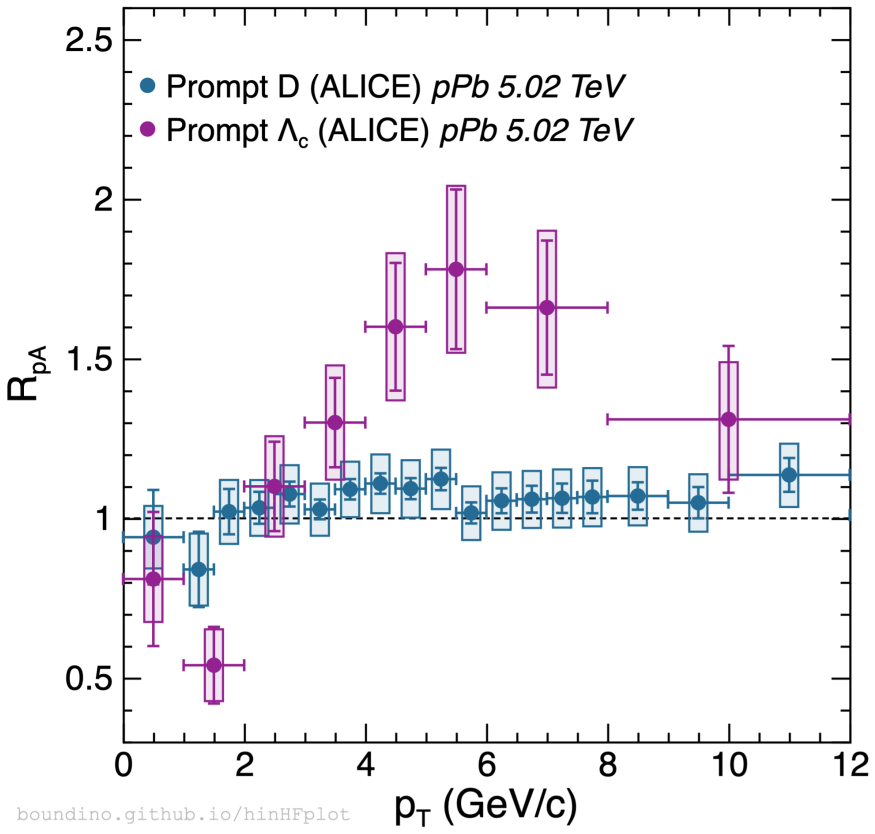

Figure B.1.: Nuclear modification factor R_{pPb} for prompt D mesons and Λ_{c} measured by the ALICE collaboration [181, 182]. Prompt D mesons are an average of D^0, D^+ and D^{*+}.

Appendix C

Kinematic Variables

The full kinematic information of a particle can be written as a four-momentum vector with its energy (E)and the three momentum components in the spatial directions (p_x, p_y, p_z)

$$p_\mu = (E, p_x, p_y, p_z). \tag{C.1}$$

The momentum can be separated in a transverse and a longitudinal component, $\vec{p_{\mathrm{T}}} = (p_x, p_z)$ and p_z, respectively. For particles created in a collision, the p_{T} needs to be created in the collision itself. The magnitude of the transverse momentum is connected to the production of the particle in the collision and can be calculated as $p_{\mathrm{T}} = \sqrt{p_x^2 + p_y^2}$. The transverse momentum is Lorentz invariant under boost in the z direction. Another quantity that is invariant under lorentz transformation in the longitudinal direction is the transverse mass, $m_{\mathrm{T}} = \sqrt{m^2 + p_{\mathrm{T}}^2}$, with the rest mass of the particle, m.

It is useful in relativistic calculations to use the rapidity (y) defined as

$$y = \frac{1}{2} \ln \left(\frac{E + p_z}{E - p_z} \right). \tag{C.2}$$

As the rapidity uses the energy of the particle and in the experiment we usually measure the momentum, the mass of the particle is also needed. This is not always known, and commonly the pseudo-rapidity (η) is used which is defined as

$$\eta = \frac{1}{2} \ln \left(\frac{p + p_z}{p - p_z} \right) = -\ln \left(\tan \left(\frac{\theta}{2} \right) \right). \tag{C.3}$$

Here θ denotes the angle between the z-axis and $\vec{p}$. For momenta much larger than the particle mass ($\vec{p} \gg m$) the pseudo-rapidity converges with the rapidity. It is common to then instead of p_x, p_y, p_z write the three-momentum of a particle as $(p_\mathrm{T}, \varphi, \eta)$, with the angle in the transverse plane (φ).
The invariant mass of a particle or rest mass is given by

$$p_\mu^2 = m_0^2 c^2 = \left(\frac{E}{c}\right)^2 - |\vec{p}|^2. \tag{C.4}$$

The invariant mass of a two particle system in natural units ($c = 1$) is then

$$\begin{aligned} m_{1,2}^2 &= (E_1 + E_2)^2 - |\vec{p_1} + \vec{p_2}|^2 \\ &= m_1^2 + m_2^2 + 2(E_1 E_2 - \vec{p_1} \cdot \vec{p_2}). \end{aligned} \tag{C.5}$$

In the case of massless particles or if $E \gg m$ the mass of the particles can be neglected and the equation simplifies to

$$m_{1,2}^2 = 2p_1 p_2 (1 - \cos\theta) \tag{C.6}$$

with the angle θ between the two momentum vectors. Neglecting the mass is justified in the case of electrons as their rest mass ($\mathcal{O}(100)$ keV) is much smaller than the energies that are measured in high energy experiments ($\mathcal{O}(100)$ MeV). Using the above introduced notation this can be expressed as

$$m_{1,2}^2 = 2p_{\mathrm{T},1} p_{\mathrm{T},2} (\cosh(\eta_1 - \eta 2) - \cos(\phi_1 - \phi_2)). \tag{C.7}$$

The transverse momentum of the system is calculated as the sum of the two particles

$$p_{\mathrm{T},1,2} = p_{\mathrm{T},1} + p_{\mathrm{T},2}. \tag{C.8}$$

Appendix C. Kinematic Variables

Bibliography

[1] D. J. Gross and F. Wilczek, Ultraviolet Behavior of Nonabelian Gauge Theories, *Phys. Rev. Lett.* **30** (1973) 1343–1346.

[2] H. D. Politzer, Reliable Perturbative Results for Strong Interactions?, *Phys. Rev. Lett.* **30** (1973) 1346–1349.

[3] **Particle Data Group** Collaboration, R. L. Workman and Others, Review of Particle Physics, *PTEP* **2022** (2022) 083C01.

[4] H. Beker *et al.*, m(T) dependence of boson interferometry in heavy ion collisions at the CERN SPS, *Phys. Rev. Lett.* **74** (1995) 3340–3343.

[5] **NA44** Collaboration, I. G. Bearden *et al.*, Collective expansion in high-energy heavy ion collisions, *Phys. Rev. Lett.* **78** (1997) 2080–2083.

[6] **NA44** Collaboration, I. Bearden *et al.*, Strange meson enhancement in Pb Pb collisions, *Phys. Lett. B* **471** (1999) 6–12, `arXiv:nucl-ex/9907013`.

[7] **CERES/NA45** Collaboration, G. Agakichiev *et al.*, Low mass e+ e- pair production in 158/A-GeV Pb - Au collisions at the CERN SPS, its dependence on multiplicity and transverse momentum, *Phys. Lett. B* **422** (1998) 405–412, `arXiv:nucl-ex/9712008`.

[8] **NA49** Collaboration, T. Alber *et al.*, Transverse energy production in Pb-208 + Pb collisions at 158-GeV per nucleon, *Phys. Rev. Lett.* **75** (1995) 3814–3817.

[9] **NA49** Collaboration, H. Appelshauser *et al.*, Hadronic expansion dynamics in central Pb + Pb collisions at 158-GeV per nucleon, *Eur. Phys. J. C* **2** (1998) 661–670, `arXiv:hep-ex/9711024`.

[10] **NA50** Collaboration, M. C. Abreu *et al.*, Anomalous J / psi suppression in Pb - Pb interactions at 158 GeV/c per nucleon, *Phys. Lett. B* **410** (1997) 337–343.

[11] **NA50** Collaboration, M. C. Abreu *et al.*, Observation of a threshold effect in the anomalous J/ psi suppression, *Phys. Lett. B* **450** (1999) 456–466.

[12] **NA52 (NEWMASS)** Collaboration, G. Ambrosini *et al.*, Strangelet search and antinuclei production studies in Pb + Pb collisions, *Nucl. Phys. A* **610** (1996) 306C–316C.

[13] **NA52 (NEWMASS)** Collaboration, G. Ambrosini *et al.*, Baryon and anti-baryon production in lead-lead collisions at 158 A-GeV/c, *Phys. Lett. B* **417** (1998) 202–210.

[14] **WA97** Collaboration, E. Andersen *et al.*, Strangeness enhancement at mid-rapidity in Pb Pb collisions at 158-A-GeV/c, *Phys. Lett. B* **449** (1999) 401–406.

[15] **WA80** Collaboration, R. Albrecht *et al.*, Limits on the production of direct photons in 200-A/GeV S-32 + Au collisions, *Phys. Rev. Lett.* **76** (1996) 3506–3509.

[16] **WA98** Collaboration, M. M. Aggarwal *et al.*, Centrality dependence of neutral pion production in 158-A-GeV Pb-208 + Pb-208 collisions, *Phys. Rev. Lett.* **81** (1998) 4087–4091, `arXiv:nucl-ex/9806004`. [Erratum: Phys.Rev.Lett. 84, 578–579 (2000)].

[17] **WA98** Collaboration, M. M. Aggarwal *et al.*, Freezeout parameters in central 158/A-GeV Pb-208 + Pb-208 collisions, *Phys. Rev. Lett.* **83** (1999) 926–930, `arXiv:nucl-ex/9901009`.

[18] U. W. Heinz and M. Jacob, Evidence for a new state of matter: An Assessment of the results from the CERN lead beam program, `arXiv:nucl-th/0002042`.

[19] **BRAHMS** Collaboration, I. Arsene *et al.*, Quark gluon plasma and color glass condensate at RHIC? The Perspective from the BRAHMS experiment, *Nucl. Phys. A* **757** (2005) 1–27, `arXiv:nucl-ex/0410020`.

[20] **PHENIX** Collaboration, K. Adcox *et al.*, Formation of dense partonic matter in relativistic nucleus-nucleus collisions at RHIC: Experimental evaluation by the PHENIX collaboration, *Nucl. Phys. A* **757** (2005) 184–283, arXiv:nucl-ex/0410003.

[21] **STAR** Collaboration, J. Adams *et al.*, Experimental and theoretical challenges in the search for the quark gluon plasma: The STAR Collaboration's critical assessment of the evidence from RHIC collisions, *Nucl. Phys. A* **757** (2005) 102–183, arXiv:nucl-ex/0501009.

[22] **PHOBOS** Collaboration, B. B. Back *et al.*, The PHOBOS perspective on discoveries at RHIC, *Nucl. Phys. A* **757** (2005) 28–101, arXiv:nucl-ex/0410022.

[23] **HotQCD** Collaboration, A. Bazavov *et al.*, Equation of state in (2+1)-flavor QCD, *Phys. Rev. D* **90** (2014) 094503, arXiv:1407.6387 [hep-lat].

[24] E. V. Shuryak, Quark-Gluon Plasma and Hadronic Production of Leptons, Photons and Psions, *Phys. Lett. B* **78** (1978) 150.

[25] E. V. Shuryak, Quantum Chromodynamics and the Theory of Superdense Matter, *Phys. Rept.* **61** (1980) 71–158.

[26] G. Domokos and J. I. Goldman, Quark Matter Diagnostics, *Phys. Rev. D* **23** (1981) 203.

[27] K. Kajantie and H. I. Miettinen, Temperature Measurement of Quark-Gluon Plasma Formed in High-Energy Nucleus-Nucleus Collisions, *Z. Phys. C* **9** (1981) 341.

[28] K. Kajantie and H. I. Miettinen, MUON PAIR PRODUCTION IN VERY HIGH-ENERGY NUCLEUS NUCLEUS COLLISIONS, *Z. Phys. C* **14** (1982) 357–362.

[29] G. Domokos, Direct Lepton Production in High-energy Collisions of Nuclei, *Phys. Rev. D* **28** (1983) 123.

[30] L. D. McLerran and T. Toimela, Photon and Dilepton Emission from the Quark - Gluon Plasma: Some General Considerations, *Phys. Rev. D* **31** (1985) 545.

[31] J. J. Sakurai, Theory of strong interactions, *Annals Phys.* **11** (1960) 1–48.

[32] M. Gell-Mann and F. Zachariasen, Form-factors and vector mesons, *Phys. Rev.* **124** (1961) 953–964.

[33] R. P. Feynman, Photon-hadron interactions,.

[34] T. H. Bauer, R. D. Spital, D. R. Yennie, and F. M. Pipkin, The Hadronic Properties of the Photon in High-Energy Interactions, *Rev. Mod. Phys.* **50** (1978) 261. [Erratum: Rev.Mod.Phys. 51, 407 (1979)].

[35] S. D. Drell and T.-M. Yan, Massive Lepton Pair Production in Hadron-Hadron Collisions at High-Energies, *Phys. Rev. Lett.* **25** (1970) 316–320. [Erratum: Phys.Rev.Lett. 25, 902 (1970)].

[36] N. M. Kroll and W. Wada, Internal pair production associated with the emission of high-energy gamma rays, *Phys. Rev.* **98** (1955) 1355–1359.

[37] L. G. Landsberg, Electromagnetic Decays of Light Mesons, *Phys. Rept.* **128** (1985) 301–376.

[38] R. I. Dzhelyadin *et al.*, Study of the Electromagnetic Transition Form-factor in $\omega \to \pi^0\mu^+\mu^-$ Decay, *Phys. Lett. B* **102** (1981) 296.

[39] **NA60** Collaboration, R. Arnaldi *et al.*, Study of the electromagnetic transition form-factors in eta —> mu+ mu- gamma and omega —> mu+ mu- pi0 decays with NA60, *Phys. Lett. B* **677** (2009) 260–266, arXiv:0902.2547 [hep-ph].

[40] **NA60** Collaboration, R. Arnaldi *et al.*, Precision study of the $\eta \to \mu^+\mu^-\gamma$ and $\omega \to \mu^+\mu^-\pi^0$ electromagnetic transition form-factors and of the $\rho \to \mu^+\mu^-$ line shape in NA60, *Phys. Lett. B* **757** (2016) 437–444, arXiv:1608.07898 [hep-ex].

[41] R. H. Dalitz, Decay of tau mesons of known charge, *Phys. Rev.* **94** (1954) 1046–1051.

[42] V. N. Gribov and L. N. Lipatov, Deep inelastic e p scattering in perturbation theory, *Sov. J. Nucl. Phys.* **15** (1972) 438–450.

[43] Y. L. Dokshitzer, Calculation of the Structure Functions for Deep Inelastic Scattering and e+ e- Annihilation by Perturbation Theory in Quantum Chromodynamics., *Sov. Phys. JETP* **46** (1977) 641–653.

[44] G. Altarelli and G. Parisi, Asymptotic Freedom in Parton Language, *Nucl. Phys. B* **126** (1977) 298–318.

[45] P. Nason, S. Dawson, and R. K. Ellis, The Total Cross-Section for the Production of Heavy Quarks in Hadronic Collisions, *Nucl. Phys. B* **303** (1988) 607–633.

[46] E. Braaten, K.-m. Cheung, S. Fleming, and T. C. Yuan, Perturbative QCD fragmentation functions as a model for heavy quark fragmentation, *Phys. Rev. D* **51** (1995) 4819–4829, arXiv:hep-ph/9409316.

[47] M. Cacciari, M. Greco, and P. Nason, The P(T) spectrum in heavy flavor hadroproduction, *JHEP* **05** (1998) 007, arXiv:hep-ph/9803400.

[48] M. Cacciari, S. Frixione, and P. Nason, The p(T) spectrum in heavy flavor photoproduction, *JHEP* **03** (2001) 006, arXiv:hep-ph/0102134.

[49] **ALICE** Collaboration, S. Acharya *et al.*, Charm production and fragmentation fractions at midrapidity in pp collisions at $\sqrt{s} = 13$ TeV, *JHEP* **12** (2023) 086, arXiv:2308.04877 [hep-ex].

[50] M. Lisovyi, A. Verbytskyi, and O. Zenaiev, Combined analysis of charm-quark fragmentation-fraction measurements, *Eur. Phys. J. C* **76** no. 7, (2016) 397, arXiv:1509.01061 [hep-ex].

[51] M. Cacciari, S. Frixione, N. Houdeau, M. L. Mangano, P. Nason, and G. Ridolfi, Theoretical predictions for charm and bottom production at the LHC, *JHEP* **10** (2012) 137, arXiv:1205.6344 [hep-ph].

[52] M. Cacciari, M. L. Mangano, and P. Nason, Gluon PDF constraints from the ratio of forward heavy-quark production at the LHC at $\sqrt{S} = 7$ and 13 TeV, *Eur. Phys. J. C* **75** no. 12, (2015) 610, arXiv:1507.06197 [hep-ph].

[53] D. d'Enterria and A. M. Snigirev, Triple parton scatterings in high-energy proton-proton collisions, *Phys. Rev. Lett.* **118** no. 12, (2017) 122001, arXiv:1612.05582 [hep-ph].

[54] D. d'Enterria and A. M. Snigirev, Triple-parton scatterings in proton–nucleus collisions at high energies, *Eur. Phys. J. C* **78** no. 5, (2018) 359, arXiv:1612.08112 [hep-ph].

[55] M. Czakon, P. Fiedler, and A. Mitov, Total Top-Quark Pair-Production Cross Section at Hadron Colliders Through $O(\alpha_S^4)$, *Phys. Rev. Lett.* **110** (2013) 252004, arXiv:1303.6254 [hep-ph].

[56] L. L. Frankfurt and M. I. Strikman, Hard Nuclear Processes and Microscopic Nuclear Structure, *Phys. Rept.* **160** (1988) 235–427.

[57] M. Arneodo, Nuclear effects in structure functions, *Phys. Rept.* **240** (1994) 301–393.

[58] K. J. Eskola, H. Paukkunen, and C. A. Salgado, EPS09: A New Generation of NLO and LO Nuclear Parton Distribution Functions, *JHEP* **04** (2009) 065, arXiv:0902.4154 [hep-ph].

[59] M. Klasen and H. Paukkunen, Nuclear PDFs After the First Decade of LHC Data, arXiv:2311.00450 [hep-ph].

[60] P. Duwentäster, T. Ježo, M. Klasen, K. Kovařík, A. Kusina, K. F. Muzakka, F. I. Olness, R. Ruiz, I. Schienbein, and J. Y. Yu, Impact of heavy quark and quarkonium data on nuclear gluon PDFs, *Phys. Rev. D* **105** no. 11, (2022) 114043, arXiv:2204.09982 [hep-ph].

[61] K. J. Eskola, P. Paakkinen, H. Paukkunen, and C. A. Salgado, EPPS21: a global QCD analysis of nuclear PDFs, *Eur. Phys. J. C* **82** no. 5, (2022) 413, arXiv:2112.12462 [hep-ph].

[62] R. Abdul Khalek, R. Gauld, T. Giani, E. R. Nocera, T. R. Rabemananjara, and J. Rojo, nNNPDF3.0: evidence for a modified partonic structure in heavy nuclei, *Eur. Phys. J. C* **82** no. 6, (2022) 507, arXiv:2201.12363 [hep-ph].

[63] **CERES** Collaboration, G. Agakichiev *et al.*, Enhanced production of low mass electron pairs in 200-GeV/u S - Au collisions at the CERN SPS, *Phys. Rev. Lett.* **75** (1995) 1272–1275.

[64] **NA38, NA50** Collaboration, M. C. Abreu *et al.*, Dimuon and charm production in nucleus-nucleus collisions at the CERN SPS, *Eur. Phys. J. C* **14** (2000) 443–455.

[65] **HELIOS** Collaboration, M. Masera, Dimuon production below mass 3.1-GeV/c**2 in p W and S W interactions at 200-A/GeV/c, *Nucl. Phys. A* **590** (1995) 93C–102C.

[66] G. E. Brown and M. Rho, Scaling effective Lagrangians in a dense medium, *Phys. Rev. Lett.* **66** (1991) 2720–2723.

[67] G. E. Brown and M. Rho, Chiral restoration in hot and/or dense matter, *Phys. Rept.* **269** (1996) 333–380, arXiv:hep-ph/9504250.

[68] G. E. Brown and M. Rho, On the manifestation of chiral symmetry in nuclei and dense nuclear matter, *Phys. Rept.* **363** (2002) 85–171, arXiv:hep-ph/0103102.

[69] R. Rapp and J. Wambach, Chiral symmetry restoration and dileptons in relativistic heavy ion collisions, *Adv. Nucl. Phys.* **25** (2000) 1, arXiv:hep-ph/9909229.

[70] R. Rapp and E. V. Shuryak, Thermal dilepton radiation at intermediate masses at the CERN - SPS, *Phys. Lett. B* **473** (2000) 13–19, arXiv:hep-ph/9909348.

[71] H. van Hees and R. Rapp, Comprehensive interpretation of thermal dileptons at the SPS, *Phys. Rev. Lett.* **97** (2006) 102301, arXiv:hep-ph/0603084.

[72] **NA50** Collaboration, M. C. Abreu *et al.*, J / psi and Drell-Yan cross-sections in Pb Pb interactions at 158 GeV/c per nucleon, *Phys. Lett. B* **410** (1997) 327–336.

[73] K. Gallmeister, B. Kampfer, and O. P. Pavlenko, Is there a unique thermal source of dileptons in Pb(158-GeV/A) + Au, Pb reactions?, *Phys. Lett. B* **473** (2000) 20–24, arXiv:hep-ph/9908269.

[74] P. Huovinen, P. V. Ruuskanen, and J. Sollfrank, Sensitivity of hadronic and electromagnetic spectra to equation of state and initial energy density in the Pb + Pb collisions at SPS, *Nucl. Phys. A* **650** (1999) 227–244, arXiv:nucl-th/9807076.

[75] **CERES** Collaboration, D. Adamova *et al.*, The CERES/NA45 Radial Drift Time Projection Chamber, *Nucl. Instrum. Meth. A* **593** (2008) 203–231, arXiv:0802.1443 [nucl-ex].

[76] A. Baldit *et al.*, Study of prompt dimuon and charm production with proton and heavy ion beams at the CERN SPS: Proposal,.

[77] M. Keil, K. Banicz, A. David, M. Floris, C. Lourenco, H. Ohnishi, E. Radermacher, R. Shahoian, and G. Usai, The NA60 silicon pixel tracker, *Nucl. Instrum. Meth. A* **565** (2006) 55–61.

[78] **CERES** Collaboration, D. Adamova *et al.*, Modification of the rho-meson detected by low-mass electron-positron pairs in central Pb-Au collisions at 158-A-GeV/c, *Phys. Lett. B* **666** (2008) 425–429, arXiv:nucl-ex/0611022.

[79] **NA60** Collaboration, R. Arnaldi *et al.*, First measurement of the rho spectral function in high-energy nuclear collisions, *Phys. Rev. Lett.* **96** (2006) 162302, arXiv:nucl-ex/0605007.

[80] **NA60** Collaboration, R. Arnaldi *et al.*, Evidence for the production of thermal-like muon pairs with masses above 1-GeV/c**2 in 158-A-GeV Indium-Indium Collisions, *Eur. Phys. J. C* **59** (2009) 607–623, arXiv:0810.3204 [nucl-ex].

[81] **STAR** Collaboration, K. H. Ackermann *et al.*, Elliptic flow in Au + Au collisions at (S(NN))**(1/2) = 130 GeV, *Phys. Rev. Lett.* **86** (2001) 402–407, arXiv:nucl-ex/0009011.

[82] **PHENIX** Collaboration, K. Adcox *et al.*, Suppression of hadrons with large transverse momentum in central Au+Au collisions at $\sqrt{s_{NN}}$ = 130-GeV, *Phys. Rev. Lett.* **88** (2002) 022301, arXiv:nucl-ex/0109003.

[83] **STAR** Collaboration, L. Adamczyk *et al.*, Measurements of Dielectron Production in Au+Au Collisions at $\sqrt{s_{\rm NN}}$ = 200 GeV from the STAR Experiment, *Phys. Rev. C* **92** no. 2, (2015) 024912, arXiv:1504.01317 [hep-ex].

[84] **PHENIX** Collaboration, A. Adare *et al.*, Dielectron production in Au+Au collisions at $\sqrt{s_{NN}}$=200 GeV, *Phys. Rev. C* **93** no. 1, (2016) 014904, arXiv:1509.04667 [nucl-ex].

[85] **STAR** Collaboration, L. Adamczyk *et al.*, Measurements of D^0 and D^* Production in $p+p$ Collisions at $\sqrt{s} = 200$ GeV, *Phys. Rev. D* **86** (2012) 072013, arXiv:1204.4244 [nucl-ex].

[86] **PHENIX** Collaboration, A. Adare *et al.*, Cross section for $b\bar{b}$ production via dielectrons in d+Au collisions at $\sqrt{s_{NN}} = 200$ GeV, *Phys. Rev. C* **91** no. 1, (2015) 014907, arXiv:1405.4004 [nucl-ex].

[87] **PHENIX** Collaboration, A. Adare *et al.*, Heavy Quark Production in $p+p$ and Energy Loss and Flow of Heavy Quarks in Au+Au Collisions at $\sqrt{s_{NN}} = 200$ GeV, *Phys. Rev. C* **84** (2011) 044905, arXiv:1005.1627 [nucl-ex].

[88] P. Braun-Munzinger, K. Redlich, and J. Stachel, Particle production in heavy ion collisions, arXiv:nucl-th/0304013.

[89] **ATLAS** Collaboration, G. Aad *et al.*, The ATLAS Experiment at the CERN Large Hadron Collider, *JINST* **3** (2008) S08003.

[90] **CMS** Collaboration, S. Chatrchyan *et al.*, The CMS Experiment at the CERN LHC, *JINST* **3** (2008) S08004.

[91] **LHCb** Collaboration, A. A. Alves, Jr. *et al.*, The LHCb Detector at the LHC, *JINST* **3** (2008) S08005.

[92] **ALICE** Collaboration, S. Acharya *et al.*, Dielectron production in proton-proton collisions at $\sqrt{s} = 7$ TeV, *JHEP* **09** (2018) 064, arXiv:1805.04391 [hep-ex].

[93] **ALICE** Collaboration, S. Acharya *et al.*, Dielectron and heavy-quark production in inelastic and high-multiplicity proton–proton collisions at $\sqrt{s_{NN}} = 13$TeV, *Phys. Lett. B* **788** (2019) 505–518, arXiv:1805.04407 [hep-ex].

[94] T. Sjostrand, S. Mrenna, and P. Z. Skands, PYTHIA 6.4 Physics and Manual, *JHEP* **05** (2006) 026.

[95] P. Nason, A New method for combining NLO QCD with shower Monte Carlo algorithms, *JHEP* **11** (2004) 040, arXiv:hep-ph/0409146 [hep-ph].

[96] S. Frixione, P. Nason, and G. Ridolfi, A Positive-weight next-to-leading-order Monte Carlo for heavy flavour hadroproduction, *JHEP* **09** (2007) 126.

[97] S. Frixione, P. Nason, and C. Oleari, Matching NLO QCD computations with Parton Shower simulations: the POWHEG method, *JHEP* **11** (2007) 070.

[98] S. Alioli, P. Nason, C. Oleari, and E. Re, A general framework for implementing NLO calculations in shower Monte Carlo programs: the POWHEG BOX, *JHEP* **06** (2010) 043, `arXiv:1002.2581 [hep-ph]`.

[99] **ALICE** Collaboration, S. Acharya *et al.*, Dielectron production in central Pb−Pb collisions at $\sqrt{s_{\rm NN}} = 5.02$ TeV, `arXiv:2308.16704 [nucl-ex]`.

[100] **ALICE** Collaboration, S. Acharya *et al.*, Measurement of electrons from semileptonic heavy-flavour hadron decays at midrapidity in pp and Pb-Pb collisions at $\sqrt{s_{\rm NN}} = 5.02$ TeV, *Phys. Lett. B* **804** (2020) 135377, `arXiv:1910.09110 [nucl-ex]`.

[101] R. Rapp, Signatures of thermal dilepton radiation at RHIC, *Phys. Rev. C* **63** (2001) 054907, `arXiv:hep-ph/0010101`.

[102] T. Song, W. Cassing, P. Moreau, and E. Bratkovskaya, Open charm and dileptons from relativistic heavy-ion collisions, *Phys. Rev. C* **97** no. 6, (2018) 064907, `arXiv:1803.02698 [nucl-th]`.

[103] **MoEDAL** Collaboration, B. Acharya *et al.*, The Physics Programme Of The MoEDAL Experiment At The LHC, *Int. J. Mod. Phys. A* **29** (2014) 1430050, `arXiv:1405.7662 [hep-ph]`.

[104] **FASER** Collaboration, A. Ariga *et al.*, FASER's physics reach for long-lived particles, *Phys. Rev. D* **99** no. 9, (2019) 095011, `arXiv:1811.12522 [hep-ph]`.

[105] **TOTEM** Collaboration, G. Anelli *et al.*, The TOTEM experiment at the CERN Large Hadron Collider, *JINST* **3** (2008) S08007.

[106] **LHCf** Collaboration, O. Adriani *et al.*, The LHCf detector at the CERN Large Hadron Collider, *JINST* **3** (2008) S08006.

[107] F. Englert and R. Brout, Broken Symmetry and the Mass of Gauge Vector Mesons, *Phys. Rev. Lett.* **13** (1964) 321–323.

[108] P. W. Higgs, Broken symmetries, massless particles and gauge fields, *Phys. Lett.* **12** (1964) 132–133.

[109] P. W. Higgs, Broken Symmetries and the Masses of Gauge Bosons, *Phys. Rev. Lett.* **13** (1964) 508–509.

[110] G. S. Guralnik, C. R. Hagen, and T. W. B. Kibble, Global Conservation Laws and Massless Particles, *Phys. Rev. Lett.* **13** (1964) 585–587.

[111] P. W. Higgs, Spontaneous Symmetry Breakdown without Massless Bosons, *Phys. Rev.* **145** (1966) 1156–1163.

[112] T. W. B. Kibble, Symmetry breaking in nonAbelian gauge theories, *Phys. Rev.* **155** (1967) 1554–1561.

[113] **ATLAS** Collaboration, G. Aad *et al.*, Observation of a new particle in the search for the Standard Model Higgs boson with the ATLAS detector at the LHC, *Phys. Lett. B* **716** (2012) 1–29, `arXiv:1207.7214 [hep-ex]`.

[114] **CMS** Collaboration, S. Chatrchyan *et al.*, Observation of a New Boson at a Mass of 125 GeV with the CMS Experiment at the LHC, *Phys. Lett. B* **716** (2012) 30–61, `arXiv:1207.7235 [hep-ex]`.

[115] **ATLAS** Collaboration, Combination of searches for heavy resonances using 139 fb^{-1} of proton–proton collision data at $\sqrt{s} = 13$ TeV with the ATLAS detector, tech. rep., CERN, Geneva, 2022. `https://cds.cern.ch/record/2809967`. All figures including auxiliary figures are available at https://atlas.web.cern.ch/Atlas/GROUPS/PHYSICS/CONFNOTES/ATLAS-CONF-2022-028.

[116] **CMS** Collaboration, A. M. Sirunyan *et al.*, Search for a standard model-like Higgs boson in the mass range between 70 and 110 GeV in the diphoton final state in proton-proton collisions at $\sqrt{s} = 8$ and 13 TeV, *Phys. Lett. B* **793** (2019) 320–347, `arXiv:1811.08459 [hep-ex]`.

[117] **ALICE** Collaboration, K. Aamodt *et al.*, The ALICE experiment at the CERN LHC, *JINST* **3** (2008) S08002.

[118] **ALICE** Collaboration, ALICE technical design report of the dimuon forward spectrometer,.

[119] **ALICE** Collaboration, ALICE dimuon forward spectrometer: addendum to the Technical Design Report,.

[120] **ALICE** Collaboration, P. Cortese *et al.*, ALICE technical design report on forward detectors: FMD, T0 and V0,.

[121] **ALICE** Collaboration, G. Dellacasa *et al.*, ALICE: Technical design report of the time projection chamber,.

[122] **ALICE** Collaboration, P. Cortese, ALICE transition-radiation detector: Technical Design Report,.

[123] **ALICE** Collaboration, G. Dellacasa *et al.*, ALICE technical design report of the time-of-flight system (TOF),.

[124] **ALICE** Collaboration, P. Cortese *et al.*, ALICE: Addendum to the technical design report of the time of flight system (TOF),.

[125] **ALICE** Collaboration, S. Beole *et al.*, ALICE technical design report: Detector for high momentum PID,.

[126] **ALICE** Collaboration, P. Cortese *et al.*, ALICE electromagnetic calorimeter technical design report,.

[127] J. Allen *et al.*, ALICE DCal: An Addendum to the EMCal Technical Design Report Di-Jet and Hadron-Jet correlation measurements in ALICE,.

[128] **ALICE** Collaboration, G. Dellacasa *et al.*, ALICE technical design report of the photon spectrometer (PHOS),.

[129] **ALICE** Collaboration, A. Villatoro Tello, AD, the ALICE diffractive detector, *AIP Conf. Proc.* **1819** no. 1, (2017) 040020.

[130] **ALICE** Collaboration, G. Dellacasa *et al.*, ALICE technical design report of the zero degree calorimeter (ZDC),.

[131] **ALICE** Collaboration, P. Cortese *et al.*, ALICE: Physics performance report, volume I, *J. Phys. G* **30** (2004) 1517–1763.

[132] **ALICE** Collaboration, G. Dellacasa *et al.*, ALICE technical design report of the inner tracking system (ITS),.

[133] J. Alme *et al.*, The ALICE TPC, a large 3-dimensional tracking device with fast readout for ultra-high multiplicity events, *Nucl. Instrum. Meth. A* **622** (2010) 316–367, arXiv:1001.1950 [physics.ins-det].

[134] W. Blum, L. Rolandi, and W. Riegler, *Particle detection with drift chambers*. Particle Acceleration and Detection. 2008.

[135] **ALICE** Collaboration, J. Adam *et al.*, Determination of the event collision time with the ALICE detector at the LHC, *Eur. Phys. J. Plus* **132** no. 2, (2017) 99, arXiv:1610.03055 [physics.ins-det].

[136] R. Brun, F. Bruyant, F. Carminati, S. Giani, M. Maire, A. McPherson, G. Patrick, and L. Urban, GEANT Detector Description and Simulation Tool,.

[137] S. Roesler, R. Engel, and J. Ranft, The Monte Carlo event generator DPMJET-III, in *International Conference on Advanced Monte Carlo for Radiation Physics, Particle Transport Simulation and Applications (MC 2000)*, pp. 1033–1038. 12, 2000. arXiv:hep-ph/0012252.

[138] A. Fedynitch, *Cascade equations and hadronic interactions at very high energies*. PhD thesis, KIT, Karlsruhe, Dept. Phys., 11, 2015.

[139] T. Pierog, I. Karpenko, J. M. Katzy, E. Yatsenko, and K. Werner, EPOS LHC: Test of collective hadronization with data measured at the CERN Large Hadron Collider, *Phys. Rev. C* **92** no. 3, (2015) 034906, arXiv:1306.0121 [hep-ph].

[140] **PHENIX** Collaboration, A. Adare *et al.*, Detailed measurement of the e^+e^- pair continuum in $p+p$ and Au+Au collisions at $\sqrt{s_{NN}} = 200$ GeV and implications for direct photon production, *Phys. Rev. C* **81** (2010) 034911, arXiv:0912.0244 [nucl-ex].

[141] **ALICE** Collaboration, J. Adam *et al.*, Multiplicity dependence of charged pion, kaon, and (anti)proton production at large transverse momentum in p-Pb collisions at $\sqrt{s_{\mathrm{NN}}} = 5.02$ TeV, *Phys. Lett. B* **760** (2016) 720–735, arXiv:1601.03658 [nucl-ex].

[142] **ALICE** Collaboration, J. Adam *et al.*, Production of $\mathrm{K}^*(892)^0$ and $\phi(1020)$ in p–Pb collisions at $\sqrt{s_{\mathrm{NN}}} = 5.02$ TeV, *Eur. Phys. J. C* **76** no. 5, (2016) 245, arXiv:1601.07868 [nucl-ex].

[143] R. Hagedorn, Multiplicities, p_T Distributions and the Expected Hadron $\rightarrow$ Quark - Gluon Phase Transition, *Riv. Nuovo Cim.* **6N10** (1983) 1–50.

[144] **PHENIX** Collaboration, S. S. Adler *et al.*, High transverse momentum η meson production in p^+p, d^+ Au and Au+Au collisions at $S(NN)^{(1/2)}$ = 200-GeV, *Phys. Rev. C* **75** (2007) 024909, arXiv:nucl-ex/0611006.

[145] **PHENIX** Collaboration, A. Adare *et al.*, Cross section and double helicity asymmetry for η mesons and their comparison to neutral pion production in $p+p$ collisions at $\sqrt{s}$=200 GeV, *Phys. Rev. D* **83** (2011) 032001, arXiv:1009.6224 [hep-ex].

[146] **ALICE** Collaboration, S. Acharya *et al.*, Production of π^0 and η mesons up to high transverse momentum in pp collisions at 2.76 TeV, *Eur. Phys. J. C* **77** no. 5, (2017) 339, arXiv:1702.00917 [hep-ex].

[147] **ALICE** Collaboration, B. Abelev *et al.*, Neutral pion and η meson production in proton-proton collisions at $\sqrt{s} = 0.9$ TeV and $\sqrt{s} = 7$ TeV, *Phys. Lett. B* **717** (2012) 162–172, arXiv:1205.5724 [hep-ex].

[148] **ALICE** Collaboration, S. Acharya *et al.*, π^0 and η meson production in proton-proton collisions at $\sqrt{s} = 8$ TeV, *Eur. Phys. J. C* **78** no. 3, (2018) 263, arXiv:1708.08745 [hep-ex].

[149] **ALICE** Collaboration, S. Acharya *et al.*, Neutral pion and η meson production in p-Pb collisions at $\sqrt{s_{\rm NN}} = 5.02$ TeV, *Eur. Phys. J. C* **78** no. 8, (2018) 624, arXiv:1801.07051 [nucl-ex].

[150] G. Agakichiev *et al.*, Neutral meson production in p Be and p Au collisions at 450-GeV beam energy, *Eur. Phys. J. C* **4** (1998) 249–257.

[151] **ALICE** Collaboration, S. Acharya *et al.*, Production of the $\rho(770)^0$ meson in pp and Pb-Pb collisions at $\sqrt{s_{\rm NN}} = 2.76$ TeV, *Phys. Rev. C* **99** no. 6, (2019) 064901, arXiv:1805.04365 [nucl-ex].

[152] **PHENIX** Collaboration, S. S. Adler *et al.*, Production of omega mesons at Large Transverse Momenta in p + p and d + Au Collisions at s**(1/2)(NN) = 200-GeV, *Phys. Rev. C* **75** (2007) 051902, arXiv:nucl-ex/0611031.

[153] K. Reygers, A. Schmah, A. Berdnikova, and X. Sun, Blast-wave description of Υ elliptic flow at energies available at the CERN Large Hadron Collider, *Phys. Rev. C* **101** no. 6, (2020) 064905, arXiv:1910.14618 [hep-ph].

[154] K. Reygers.

[155] **ALICE** Collaboration, S. Acharya *et al.*, Production of ω mesons in pp collisions at $\sqrt{\mathbf{s}} = \mathbf{7}$ TeV, *Eur. Phys. J. C* **80** no. 12, (2020) 1130, arXiv:2007.02208 [nucl-ex].

[156] **PHENIX** Collaboration, A. Adare *et al.*, Production of ω mesons in $p + p$, d+Au, Cu+Cu, and Au+Au collisions at $\sqrt{s_N N} = 200$ GeV, *Phys. Rev. C* **84** (2011) 044902, arXiv:1105.3467 [nucl-ex].

[157] **ALICE** Collaboration, S. Acharya *et al.*, Dielectron production at midrapidity at low transverse momentum in peripheral and semi-peripheral Pb–Pb collisions at $\sqrt{s}_{\mathrm{NN}} = 5.02$ TeV, *JHEP* **06** (2023) 024, arXiv:2204.11732 [nucl-ex].

[158] P. Z. Skands, Tuning Monte Carlo Generators: The Perugia Tunes, *Phys. Rev.* **D82** (2010) 074018, arXiv:1005.3457 [hep-ph].

[159] **CTEQ** Collaboration, H. L. Lai, J. Huston, S. Kuhlmann, J. Morfin, F. I. Olness, J. F. Owens, J. Pumplin, and W. K. Tung, Global QCD analysis of parton structure of the nucleon: CTEQ5 parton distributions, *Eur. Phys. J. C* **12** (2000) 375–392, arXiv:hep-ph/9903282.

[160] **ALICE** Collaboration, S. Acharya *et al.*, Dielectron production in proton-proton and proton-lead collisions at $\sqrt{s_{NN}} = 5.02$ TeV, *Phys. Rev. C* **102** no. 5, (2020) 055204, arXiv:2005.11995 [nucl-ex].

[161] **ALICE** Collaboration, Centrality determination in heavy ion collisions,.

[162] **ALICE** Collaboration, J. Adam *et al.*, Rapidity and transverse-momentum dependence of the inclusive J/ψ nuclear modification factor in p-Pb collisions at $\sqrt{s_{N\ N}} = 5.02$ TeV, *JHEP* **06** (2015) 055, arXiv:1503.07179 [nucl-ex].

[163] **ALICE** Collaboration, B. B. Abelev *et al.*, Measurement of visible cross sections in proton-lead collisions at $\sqrt{s_{\mathrm{NN}}} = 5.02$ TeV in van der Meer scans with the ALICE detector, *JINST* **9** no. 11, (2014) P11003, arXiv:1405.1849 [nucl-ex].

[164] L. Altenkämper, F. Bock, C. Loizides, and N. Schmidt, Applicability of transverse mass scaling in hadronic collisions at energies available at the CERN Large Hadron Collider, *Phys. Rev. C* **96** no. 6, (2017) 064907, arXiv:1710.01933 [hep-ph].

[165] **PHENIX** Collaboration, A. Adare *et al.*, Measurement of neutral mesons in p+p collisions at $\sqrt{s}$= 200 GeV and scaling properties of hadron production, *Phys. Rev. D* **83** (2011) 052004, arXiv:1005.3674 [hep-ex].

[166] **ALICE** Collaboration, J. Adam *et al.*, D-meson production in p-Pb collisions at $\sqrt{s_{NN}}$ =5.02 TeV and in pp collisions at $\sqrt{s}$ =7 TeV, *Phys. Rev. C* **94** no. 5, (2016) 054908, arXiv:1605.07569 [nucl-ex].

[167] M. L. Mangano, P. Nason, and G. Ridolfi, Heavy quark correlations in hadron collisions at next-to-leading order, *Nucl. Phys. B* **373** (1992) 295–345.

[168] K. J. Eskola, P. Paakkinen, H. Paukkunen, and C. A. Salgado, EPPS16: Nuclear parton distributions with LHC data, *Eur. Phys. J. C* **77** no. 3, (2017) 163, arXiv:1612.05741 [hep-ph].

[169] **CMS** Collaboration, V. Khachatryan *et al.*, Study of W boson production in pPb collisions at $\sqrt{s_{\mathrm{NN}}} = 5.02$ TeV, *Phys. Lett. B* **750** (2015) 565–586, arXiv:1503.05825 [nucl-ex].

[170] **CMS** Collaboration, V. Khachatryan *et al.*, Study of Z boson production in pPb collisions at $\sqrt{s_{NN}} = 5.02$ TeV, *Phys. Lett. B* **759** (2016) 36–57, arXiv:1512.06461 [hep-ex].

[171] **ATLAS** Collaboration, G. Aad *et al.*, Z boson production in p+Pb collisions at $\sqrt{s_{NN}} = 5.02$ TeV measured with the ATLAS detector, *Phys. Rev. C* **92** no. 4, (2015) 044915, arXiv:1507.06232 [hep-ex].

[172] **CMS** Collaboration, S. Chatrchyan *et al.*, Studies of dijet transverse momentum balance and pseudorapidity distributions in pPb collisions at $\sqrt{s_{\mathrm{NN}}} = 5.02$ TeV, *Eur. Phys. J. C* **74** no. 7, (2014) 2951, arXiv:1401.4433 [nucl-ex].

[173] A. Dainese, "private communication".

[174] G. Bruno, "private communication".

[175] **ALICE** Collaboration, J. Adam *et al.*, Enhanced production of multi-strange hadrons in high-multiplicity proton-proton collisions, *Nature Phys.* **13** (2017) 535–539, arXiv:1606.07424 [nucl-ex].

[176] **CMS** Collaboration, V. Khachatryan *et al.*, Observation of Long-Range Near-Side Angular Correlations in Proton-Proton Collisions at the LHC, *JHEP* **09** (2010) 091, arXiv:1009.4122 [hep-ex].

[177] **PHENIX** Collaboration, C. Aidala *et al.*, Creation of quark–gluon plasma droplets with three distinct geometries, *Nature Phys.* **15** no. 3, (2019) 214–220, arXiv:1805.02973 [nucl-ex].

[178] M. He, R. J. Fries, and R. Rapp, Ideal Hydrodynamics for Bulk and Multistrange Hadrons in $\sqrt{s_{NN}}$=200\,AGeV Au-Au Collisions, *Phys. Rev. C* **85** (2012) 044911, arXiv:1112.5894 [nucl-th].

[179] R. Rapp, Dilepton Spectroscopy of QCD Matter at Collider Energies, *Adv. High Energy Phys.* **2013** (2013) 148253, arXiv:1304.2309 [hep-ph].

[180] H. van Hees and R. Rapp, Dilepton Radiation at the CERN Super Proton Synchrotron, *Nucl. Phys. A* **806** (2008) 339–387, arXiv:0711.3444 [hep-ph].

[181] **ALICE** Collaboration, S. Acharya *et al.*, Measurement of prompt D^0, D^+, D^{*+}, and D_S^+ production in p–Pb collisions at $\sqrt{s_{NN}}$ = 5.02 TeV, *JHEP* **12** (2019) 092, arXiv:1906.03425 [nucl-ex].

[182] **ALICE** Collaboration, S. Acharya *et al.*, First measurement of Λc+ production down to pT=0 in pp and p-Pb collisions at sNN=5.02 TeV, *Phys. Rev. C* **107** no. 6, (2023) 064901, arXiv:2211.14032 [nucl-ex].

[183] **ALICE** Collaboration, B. Abelev *et al.*, Upgrade of the ALICE Experiment: Letter Of Intent, *J. Phys. G* **41** (2014) 087001.

[184] **ALICE** Collaboration, S. Acharya *et al.*, ALICE upgrades during the LHC Long Shutdown 2, *JINST* **19** no. 05, (2024) P05062, arXiv:2302.01238 [physics.ins-det].

[185] **ALICE** Collaboration, B. Abelev *et al.*, Technical Design Report for the Upgrade of the ALICE Inner Tracking System, *J. Phys. G* **41** (2014) 087002.

[186] **ALICE** Collaboration, C. Lippmann, Upgrade of the ALICE Time Projection Chamber,.

[187] Addendum to the Technical Design Report for the Upgrade of the ALICE Time Projection Chamber,.

[188] **ALICE TPC** Collaboration, J. Adolfsson *et al.*, The upgrade of the ALICE TPC with GEMs and continuous readout, *JINST* **16** no. 03, (2021) P03022, arXiv:2012.09518 [physics.ins-det].

[189] F. Sauli, GEM: A new concept for electron amplification in gas detectors, *Nucl. Instrum. Meth. A* **386** (1997) 531–534.

[190] A. c. The, Technical Design report for the ALICE Inner Tracking System 3 - ITS3 ; A bent wafer-scale monolithic pixel detector, tech. rep., CERN, Geneva, 2024. https://cds.cern.ch/record/2890181. Co-project Manager: Magnus Mager, magnus.mager@cern.chds.

[191] **ALICE** Collaboration, Letter of intent for ALICE 3: A next-generation heavy-ion experiment at the LHC, arXiv:2211.02491 [physics.ins-det].

[192] **ALICE** Collaboration, S. Acharya *et al.*, Charm-quark fragmentation fractions and production cross section at midrapidity in pp collisions at the LHC, *Phys. Rev. D* **105** no. 1, (2022) L011103, arXiv:2105.06335 [nucl-ex].

[193] **ALICE** Collaboration, S. Acharya *et al.*, Measurement of the production cross section of prompt $\Xi_{\rm c}^0$ baryons at midrapidity in pp collisions at $\sqrt{s} =$ 5.02 TeV, *JHEP* **10** (2021) 159, arXiv:2105.05616 [nucl-ex].

[194] **ALICE** Collaboration, S. Acharya *et al.*, First measurement of $\Omega_{\rm c}^0$ production in pp collisions at $\sqrt{s} = 13$ TeV, arXiv:2205.13993 [nucl-ex].

[195] Y.-K. Hsiao, L. Yang, C.-C. Lih, and S.-Y. Tsai, Charmed Ω_c weak decays into Ω in the light-front quark model, *Eur. Phys. J. C* **80** no. 11, (2020) 1066, arXiv:2009.12752 [hep-ph].

[196] T. Gutsche, M. A. Ivanov, J. G. Körner, and V. E. Lyubovitskij, Nonleptonic two-body decays of single heavy baryons Λ_Q, Ξ_Q, and Ω_Q ($Q = b, c$) induced by W emission in the covariant confined quark model, *Phys. Rev. D* **98** no. 7, (2018) 074011, arXiv:1806.11549 [hep-ph].

[197] H.-Y. Cheng, Nonleptonic weak decays of bottom baryons, *Phys. Rev. D* **56** (1997) 2799–2811, arXiv:hep-ph/9612223. [Erratum: Phys.Rev.D 99, 079901 (2019)].

[198] S. Hu, G. Meng, and F. Xu, Hadronic weak decays of the charmed baryon Ω_c, *Phys. Rev. D* **101** no. 9, (2020) 094033, arXiv:2003.04705 [hep-ph].

[199] E. Solovieva *et al.*, Study of Ω_c^0 and Ω_c^{*0} Baryons at Belle, *Phys. Lett. B* **672** (2009) 1–5, arXiv:0808.3677 [hep-ex].

[200] V. Minissale, S. Plumari, and V. Greco, Charm hadrons in pp collisions at LHC energy within a coalescence plus fragmentation approach, *Phys. Lett. B* **821** (2021) 136622, arXiv:2012.12001 [hep-ph].

[201] P. M. Nadolsky, H.-L. Lai, Q.-H. Cao, J. Huston, J. Pumplin, D. Stump, W.-K. Tung, and C. P. Yuan, Implications of CTEQ global analysis for collider observables, *Phys. Rev. D* **78** (2008) 013004, arXiv:0802.0007 [hep-ph].

List of Figures

List of Tables